Karlsruhe Institute of Technology

Search for $B \to h^{(*)}\nu\bar{\nu}$ decays at Belle and development of track finding for Belle II

Zur Erlangung des akademischen Grades eines

Doktors der Naturwissenschaften

von der Fakultät für Physik des
Karlsruher Institut für Technologie (KIT)

genehmigte

Dissertation

von

Dipl.-Phys. Oksana Lutz

aus Kiew (Ukraine)

Tag der mündlichen Prüfung:	7. Dezember 2012
Referent:	Prof. Dr. Th. Müller
Korreferent:	Prof. Dr. M. Feindt

Deutsche Zusammenfassung

Das Standardmodell der Teilchenphysik beschreibt die Eigenschaften und die Wechselwirkungen zwischen den bekannten Elementarteilchen. Die aktuelle Formulierung des Standardmodells, die fast alle heutigen Beobachtungen beschreiben und erkären kann, entstand in jahrzehntelangen Zusammenarbeit von Theorie und Experiment. Die meisten theoretischen Vorhersagen des Standardmodells sind von den experimentellen Messungen im Rahmen deren Genauigkeit bestätigt worden.

Trotz des großen Erfolges des Standardmodells gibt es in der Teilchenphysik noch mehrere offene Fragen, die dieses Modell nicht beantworten kann. Wir wissen, dass unser Universum aus Materie und nicht aus Antimaterie besteht. Die CP-Verletzung im Standardmodell ist nicht groß genug um die beobachtete Baryon-Antibaryon Asymmetrie zu erklären. Gleichzeitig wissen wir aus den Rotationskurven der Galaxien, dass es eine beachtliche Masse an unsichtbarer dunkler Materie unbekannter Herkunft im Universum gibt. Darüber hinaus werfen die beobachteten Neutrinooszillationen weitere neue Fragen auf. Im Standardmodell sind Neutrinos masselos, die Oszillationen setzen jedoch eine nicht verschwindende Masse voraus.

Diese noch unbeantworteten Fragen motivieren die Teilchenphysiker zur Suche nach Neuer Physik, um das Standardmodell zu erweitern und unser Verständis vom Universum zu vervollständigen. Es gibt zahlreiche Theorien die über das Standardmodell hinaus gehen und die ungeklärten Beobachtungen, die im letzen Absatz beschrieben wurden, zu erklären versuchen. Es ist eine herausfordernde und wichtige Aufgabe der experimentellen Teilchenphysik, nach Neuer Physik außerhalb des Standardmodells zu suchen, um diese Theorien zu bestätigen oder zu widerlegen. Eine der mächtigen Methoden, um dies zu erreichen, ist die Suche nach seltenen Zerfällen.

Teilchenzerfälle werden als selten bezeichnet, wenn sie im Standardmodell stark unterdrückt oder verboten sind. Neue schwere Teilchen können zu den Zerfallsamplituden durch Schleifen beitragen und neue Kopplungen können die Zerfallsamplituden beeinflussen. Bei seltenen Zerfällen können solche Beiträge die Gesamtzerfallsamplitude größtenteils bestimmen. Die Beobachtung von seltenen Zerfällen kann also zu einer indirekten Entdeckung Neuer Physik außerhalb des Standardmodells führen.

Die Zerfälle, die in dieser Doktorarbeit analysiert wurden, $B \to h^{(*)}\nu\bar{\nu}$, sind solche seltenen

B-Mesonen-Zerfälle. Die vom Standardmodell vorhergesagte Verzweigungsverhältnisse sind sehr klein: eine bis zwei Größenordnungen kleiner als die aktuelle experimentelle Empfindlichkeit. Die Messung dieser Zerfälle wäre ein exzellenter Test der Neuen Physik.

Das dominierende experimentelle Werkzeug in der Hochenergieteilchenphysik sind Teilchenbeschleuniger, wo geladene Teilchen beschleunigt und zur Kollision gebracht werden. Ein Detektor um den Wechselwirkungspunkt zeichnet die Signale der Zerfallsprodukte der Wechselwirkung auf und erlaubt so die Rekonstruktion des Kollisionsereignisses.

Der KEKB-Beschleuniger, der sich in der High Energy Accelerator Research Organization (KEK) in Tsukuba (Japan) befindet, ist ein asymmetrischer e^+e^--Beschleuniger. Die Schwerpunktsenergie entspricht der $\Upsilon(4S)$ Resonanz, die direkt über der Produktionsschwelle von $B\bar{B}$ Paaren liegt und damit in über 96% der Fälle ein solches Paar erzeugt. Da sonst keine weiteren Zerfallsprodukte entstehen, können die B-Mesonen-Zerfälle in einer verhältnismässig untergrundarmen Umgebung untersucht werden. Da der KEKB-Beschleuniger damit auf die Produktion von B-Mesonen ausgerichtet ist, wird er auch als B-Fabrik bezeichnet. Belle ist der Name des Vielzweckdetektors am einzigen Wechselwirkungspunkt des KEKB-Beschleunigers.

Die Analyse, die im Rahmen dieser Doktorarbeit durchgeführt wurde, beruht auf dem kompletten Datensatz von 711 fb^{-1} ($\approx 771 \times 10^6$ $B\bar{B}$ Paare), aufgezeichet an der $\Upsilon(4S)$ Resonanz bei Belle. In der Analyse wurde nach den Zerfällen $B \to h^{(*)}\nu\bar{\nu}$, wo $h^{(*)}$ für K^+, K^0_S, K^{*+}, K^{*0}, π^+, π^0, ρ^+, ρ^0 und ϕ steht, gesucht. Die Signalkandidaten wurden durch eine vollständige Rekonstruktion des hadronisches Zerfalls des begleitenden B-Mesons und die Forderung nach einem einzigen verbleibenden $h^{(*)}$ Meson auf der Signalseite gebildet. Die Auswahlschnitte wurden, um eine höhere Sensitivität für einen möglichen Signalbeitrag zu erreichen, durch simulierte Experimente optimiert. Die Analyse wurde blind durchgeführt: Die Auswahlschnitte wurden festgelegt bevor das Verfahren auf die experimentellen Daten angewendet wurde. Um den Signalbeitrag zu bestimmen, wurde die verbleibende Energie im elektromagnetischem Kalorimeter, $E_{\rm ECL}$, verwendet. Da in einem Signalereignis abgesehen von zwei Neutrinos alles rekonstruiert wird, sollte es im Detektor keine weitere Aktivität geben und die Signalereignisse bei kleinen $E_{\rm ECL}$ Werten einen Peak aufweisen.

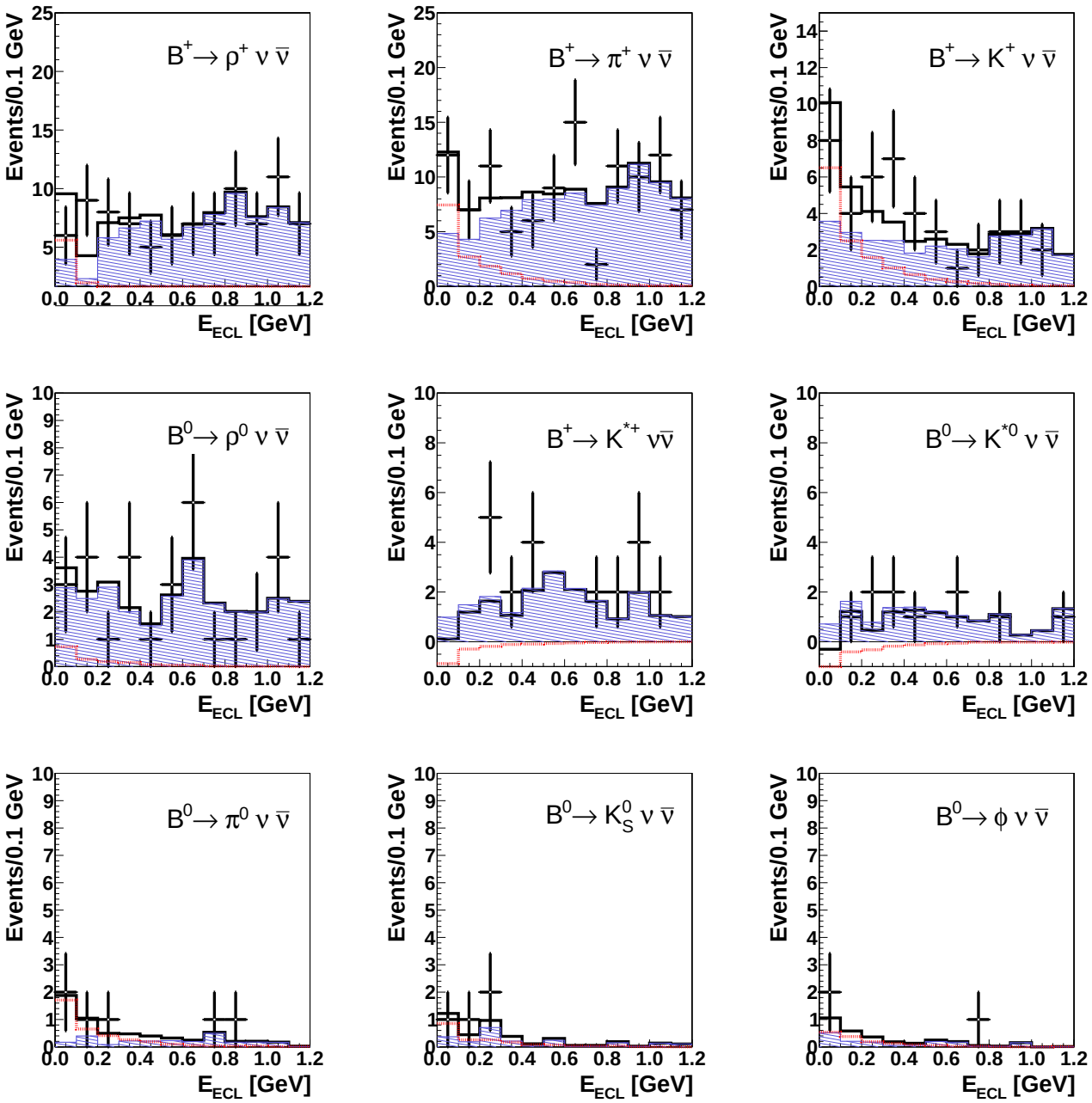

Abbildung 0.1.: Fit-Ergebnisse für die neun untersuchten $B \to h^{(*)}\nu\bar{\nu}$ Kanäle. Die Punkte mit Fehlerbalken zeigen die experimentellen Datenpunkte, während die durchgezogene schwarze Linie das Fit-Ergebnis zeigt. Der blaue kreuzschraffierte Bereich entspricht dem Untergrundanteil und die rote gestrichelte Linie dem Signalanteil.

Die Schaubilder der finalen Verteilungen mit den Fits an die Datenpunkte sind in Abbildung 0.1 zu sehen. Die endgültige Anzahl an Signalereignissen mit den dazugehörigen statistischen und systematischen Fehlern, sowie der Signifikanz des Signalbeitrags, sind für jeden Zerfallskanal in der Tabelle 0.1 aufgelistet. Obwohl Signalereignisse beobachtet wurden, sind die Signalbeiträge aufgrund der hohen statistischen und systematischen Unsicherheiten in keinem der Zerfallskanäle signifikant. Die Limits auf die Verzeiwegungsverhältnisse bei 90% Konfidenzniveau wurden bestimmt und sind in der Tabelle 0.2 aufgeführt. Obowohl der Datensatz nur das anderthalbfache des Datensatzes der vorherigen Belle Analyse betrug, konnten die meisten Limits durch das verfeinerte Analyseverfahren deutlich verbessert werden. Für vier Kanäle sind die erzielten Limits aktuell die strengsten der Welt.

Zerfallskanal	Signal	Signifikanz
$B^+ \to K^+\nu\bar{\nu}$	$13.3^{+7.4}_{-6.6}(stat) \pm 2.5(syst)$	2.0σ
$B^+ \to K^{*+}\nu\bar{\nu}$	$-1.7^{+1.7}_{-1.1}(stat) \pm 1.5(syst)$	-
$B^+ \to \pi^+\nu\bar{\nu}$	$15.2^{+7.1}_{-6.2}(stat) \pm 1.8(syst)$	2.6σ
$B^+ \to \rho^+\nu\bar{\nu}$	$11.3^{+6.3}_{-5.4}(stat) \pm 4.2(syst)$	1.7σ
$B^0 \to K^0_s\nu\bar{\nu}$	$1.8^{+3.3}_{-2.4}(stat) \pm 1.0(syst)$	0.7σ
$B^0 \to K^{*0}\nu\bar{\nu}$	$-2.3^{+10.2}_{-3.5}(stat) \pm 0.9(syst)$	-
$B^0 \to \pi^0\nu\bar{\nu}$	$3.5^{+2.6}_{-1.9}(stat) \pm 0.7(syst)$	1.9σ
$B^0 \to \rho^0\nu\bar{\nu}$	$1.6^{+5.0}_{-4.1}(stat) \pm 0.4(syst)$	0.4σ
$B^0 \to \phi\nu\bar{\nu}$	$1.4^{+2.9}_{-0.9}(stat) \pm 0.8(syst)$	0.5σ

Tabelle 0.1.: Anzahl der Signalereignisse erhalten aus dem Fit an die Daten mit den statistischen ($stat$) und systematischen ($syst$) Unsicherheiten sowie der Signifikanz des Signalbeitrags.

Die für die Verzweigungsverhältnisse bestimmten Limits können als Grenzen in der Entwicklung von Theorien der Neuen Physik dienen. Generell sind sie jedoch weiterhin etwa eine Größenordnung über den Vorhersagen des Standardmodells. Es gibt also nach wie vor Freiraum für Beiträge der Neuen Physik, die in diesen Zerfallskanälen entdeckt werden könnte. Die beobachtete Signifikanz von 2σ in K^+ und π^+ Kanälen verlangt nach weiteren Untersuchungen in den zukünftigen Experimenten.

Zerfallskanal	Verzweigungsverhältnislimit bei 90% CL	Verzweigungsverhältnislimit bei 90% CL Vorgängeranalyse bei Belle [1]	Weltbeste Verzweigungsverhältnislimits bei 90% CL [2]
$B^+ \to K^+\nu\bar{\nu}$	5.5×10^{-5}	1.4×10^{-5}	1.3×10^{-5}
$B^+ \to K^{*+}\nu\bar{\nu}$	$\mathbf{4.0 \times 10^{-5}}$	14×10^{-5}	8×10^{-5}
$B^+ \to \pi^+\nu\bar{\nu}$	$\mathbf{9.8 \times 10^{-5}}$	17×10^{-5}	10×10^{-5}
$B^+ \to \rho^+\nu\bar{\nu}$	21.4×10^{-5}	15×10^{-5}	15×10^{-5}
$B^0 \to K_s^0\nu\bar{\nu}$	9.7×10^{-5}	16×10^{-5}	5.6×10^{-5}
$B^0 \to K^{*0}\nu\bar{\nu}$	34×10^{-5}	1.2×10^{-5}	
$B^0 \to \pi^0\nu\bar{\nu}$	$\mathbf{6.9 \times 10^{-5}}$	22×22^{-5}	22×10^{-5}
$B^0 \to \rho^0\nu\bar{\nu}$	$\mathbf{20.8 \times 10^{-5}}$	44×10^{-5}	44×10^{-5}
$B^0 \to \phi\nu\bar{\nu}$	12.7×10^{-5}	5.8×10^{-5}	5.8×10^{-5}

Tabelle 0.2.: Verzweigungsverhältnisselimits bei 90% Konfidenzniveau (**C**onfidence **L**evel).

Für eine bessere statistische Empfindlichkeit ist ein größerer Datensatz mit mehr $B\bar{B}$-Paaren notwendig. Das kommende Belle-II-Experiment, mit einem erwarteten Datensatz von 50 ab^{-1} und einer verbesserten Ereignisrekonstruktion, sollte es ermöglichen, in die vom Standardmodell vorhergesagten Größenordnung für das Verzweigungsverhältnis vorzudringen und die Zerfälle zu beobachten.

Der Belle-II-Detektor wird sich am einzigen Wechselwirkungspunkt des neuen verbesserten SuperKEKB-Beschleunigers befinden und den Belle-Detektor ersetzen. Der neue Detektor wird in der Lage sein, mit den höheren Ereignisraten und dem gestiegenen Strahlungsuntergrund umzugehen und damit eine einzigartige Suche nach Neuer Physik zu ermöglichen.

Um aus den Signalen der einzelnen Subdetektoren ein Kollisionsereignis rekonstruieren zu können, wird eine durchdachte und aufwändige Rekonstruktionsoftware benötigt. Einer der wichtigsten Schritte der Ereignisrekonstruktion ist das Tracking. Es beschreibt das Verfahren, mit dem die Flugbahn eines geladenen Teilchens gefunden und sein Impuls gemessen wird. Ein effizientes, genaues und schnelles Tracking über den gesamten Impulsbereich ist entscheidend für die korrekte Rekonstruktion und damit die physikalische Interpretation der Kollisionsereignisse.

Um den neuen Belle-II-Detektor optimal zu nutzen und mit dem höheren Strahlungsuntergrund zurecht zu kommen, wird von der Belle-II-Kollaboration zur Zeit eine mehrstufige Trackingstrategie entwickelt. Im Rahmen dieser Doktorarbeit wurde ein Algorithmus, `ConformalFinder`, entwickelt, um hochenergetische Spuren in Detektorsignalen der

Belle-II-Driftkammer zu finden. Der Algorithmus basiert auf der lokalen Spurfindung und kombiniert mehrere Techniken, unter anderem den Zellulären Automat und die konforme Tranformation. Während der Integration des Algorithmus in die Belle-II-Software wurden außerdem technische Werkzeuge implementiert, die notwendig sind, um im Rahmen dieser Software die Simulation und die Rekonstruktion der Ereignisse auszuführen.

Durch Monte-Carlo-Studien mit speziellen Spurverteilungen sowie mit den realistischen $B^0 \to D^0(K^+\pi^-)\pi^+$ Ereignissen wurde gezeigt, dass der `ConformalFinder` effizient Spuren mit $p > 0.4$ GeV in der simulierten Belle-II-Driftkammer finden kann (siehe Abbildung 0.2a, 96% der Spuren konnten bei der erwarteten Durchschnittsanzahl der Spuren von 9 gefunden wuerden). Ferner konnte gezeigt werden, dass die Leistung des Algorithmus auch mit bis zu 10% Belegung der Drähte durch Untergrundteilchen stabil bleibt (siehe Abbildung 0.2b).

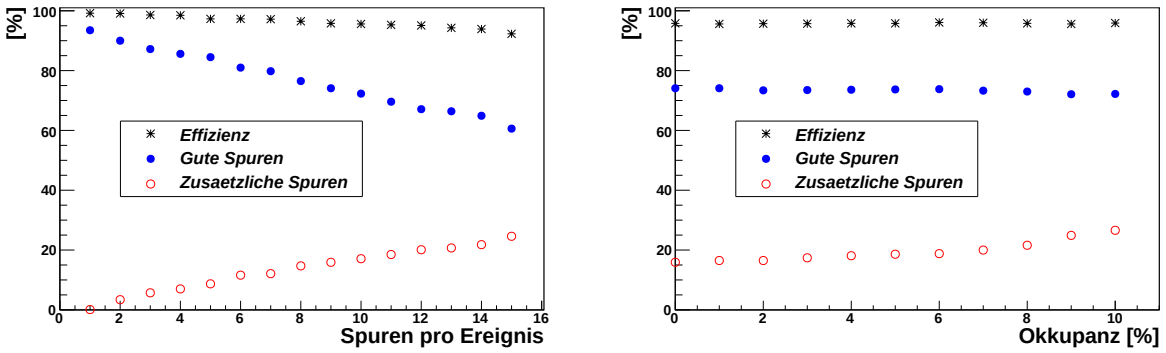

(a) Anzahl der Spuren im Ereignis

(b) Belegung der Drähte durch den Untergrund

Abbildung 0.2.: Die Leistung von `ConformalFinder` in Abhängigkeit von der Anzahl der Spuren im Ereignis (a) und in Abhängigkeit vom Untergrund für Ereignisse mit 9 Spuren (b). Der prozentuale Anteil der gefundenen Spuren (Effizienz), der Spuren mit guter Parameterbestimmung (Gute Spuren) und der zusätzlich gefundenen Spuren sind gezeigt.

Ein externes Softwarepaket `GENFIT`, welches die präzise Spurparameteranpassung durchführt, wurde in die Belle-II-Software eingegliedert und mit den Spuren, die mit dem `ConformalFinder` gefunden wurden, getestet. Es konnte gezeigt werden, dass der in `GENFIT` eingebundene `DeterministicAnnealingFilter` in der Lage ist, Untergrundhits von den Signalhits zu trennen. Die Parameterauflösung mit und ohne Undergrund ist in Abbildung 0.3 gezeigt: Es ist nur eine minimale Verschlechterung der Auflösung von $< 5\%$ zu sehen.

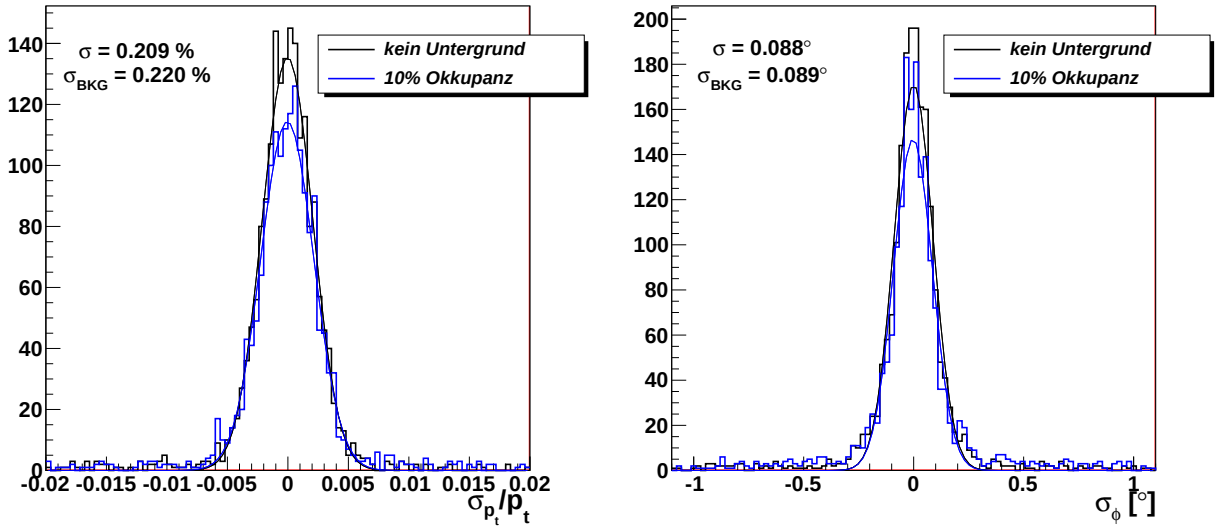

(a) p_t Auflösung (b) ϕ Auflösung

Abbildung 0.3.: Parameterauflösung der rekonstruierten Spuren nach dem Fitten mit und ohne Untergrund. Die Auflösungen des Transversalimpulses p_t und des Polarwinkels ϕ sind gezeigt.

Da der `ConformalFinder` der erste Spurfindungsalgorithmus war, der in die Belle-II-Software integriert wurde, hat seine Implementierung den Weg für die Entwicklung weiterer Rekonstruktionsschritte, wie zum Beispiel die Extrapolation der Spuren in die anderen Subdetektoren, geebnet. Überdies wurde damit ein Grundstein für die Entwicklung von weiteren, verbesserten Spurfindungsalgorithmen gelegt. Zur Zeit werden zwei weitere komplexe Algorithmen für die Spurfindung in Detektorsignalen der Driftkammer am KIT entwickelt.

Contents

1. Introduction

The Standard Model of particle physics describes properties and interactions between the known elementary particles. After decades of cooperative work of theory and experiment the current formulation of the Standard Model can describe and explain nearly all current observations within the current experimental precision.

Despite the great success of the Standard Model there are several open questions, which cannot be answered by it. We know that our universe consists of matter and not of antimatter. The CP violation within the Standard Model cannot explain the observed baryon-antibaryon asymmetry. At the same time we know from rotation curves of galaxies that there has to be more massive invisible dark matter of unknown origin in the universe. The observed neutrino oscillations also evoked new questions. In the Standard Model neutrinos are massless, the oscillations however imply that they have a non-zero mass.

These unanswered questions motivate physicists to search for New Physics to extend the Standard Model and to complete our understanding of the universe. There are many theories beyond the Standard Model that try to explain the unpredicted observations mentioned above. It is a challenging and important task for experimental particle physics to probe for New Physics beyond the Standard Model to confirm or reject these theories. One of the powerful methods to achieve this is the study of rare decays.

Decays are called rare when they are heavily suppressed or forbidden in the Standard Model. New heavy particles can contribute to the decay amplitudes via virtual loops and new couplings might affect the decay amplitude. For rare decays such a contribution might change the decay amplitude significantly and thus notably increase the probability of this decay. Observations of rare decays can therefore lead to an indirect discovery of New Physics beyond the Standard Model.

The decays analysed in this thesis, $B \to h^{(*)}\nu\bar{\nu}$, are such rare B decays. The branching fractions predicted by the Standard Model are very small, one to two orders of magnitude smaller than the current experimental sensitivity. The contributions from New Physics models can increase the branching fractions by an order of magnitude, the examination of these decays is therefore an excellent probe for New Physics.

1. Introduction

The main experimental devices in high energy particle physics are particle colliders, where charged particles are accelerated and brought to a collision. A detector build around this interaction point records signatures produced by decay products of the interaction and allows for the reconstruction of the event.

The KEKB accelerator, which is located at the High Energy Accelerator Research Organization (KEK) in Tsukuba (Japan) is an asymmetric e^+e^- accelerator. Its main purpose is the production of B mesons, and therefore it is called a B-factory. Belle is a multi-purpose detector at the sole interaction point of the KEKB accelerator, designed to perform precise measurements of B meson decays.

The analysis performed within this thesis was done using the full data sample of 711 fb^{-1} ($\approx 771 \times 10^6$ $B\bar{B}$ pairs) collected on the $\Upsilon(4S)$ resonance at Belle. A search for decays $B \to h^{(*)}\nu\bar{\nu}$, where $h^{(*)}$ stands for K^+, K^0_S, K^{*+}, K^{*0}, π^+, π^0, ρ^+, ρ^0 and ϕ was performed. Signal candidates were searched for by fully reconstructing a hadronic decay of the accompanying B meson and requiring a single $h^{(*)}$ meson to be left on the signal side. To be sensitive to the possible signal contribution the signal extraction was optimised using simulated experiments. The analysis was performed 'blind': the procedure was fixed before it was applied on experimental data.

As the expected sensitivity of this analysis is above the Standard Modell predictions for the branching fractions, new experiments will be necessary to further investige these rare decays. A higher sensitivity will be achieved in the new era of Super B factories, when the KEKB accelerator will be upgraded to SuperKEKB. The target luminosity of the new machine is $8 \times 10^{35}\text{cm}^{-2}\text{s}^{-1}$, which will increase the luminosity achieved by KEKB by a factor of 40. Important and unique measurements of New Physics processes will be possible. To cope with the high event rate and increased radiation and to achieve the physical goals, the Belle detector will be replaced by the new Belle II detector.

An elaborate reconstruction software is necessary to reconstruct a collision event from the various subdetector signals. One important step of the event reconstruction is tracking. It describes the procedure of retrieving the trajectory of a charged particle and measuring the direction and magnitude of its momentum. An efficient, precise and fast tracking performance over the whole range of particle momenta is crucial for the correct reconstruction and therefore the physical interpretation of the collision events.

A multi-stage tracking strategy to optimally use the improved Belle II detector and to cope with the expected beam background is currently being developed by the Belle II collaboration. Within this thesis an algorithm which combines different established techniques to find tracks in the central drift chamber, was developed, implemented and studied.

In the following, an overview over the flavour structure of the Standard Model and a theoretical motivation for the search for $B \to h^{(*)}\nu\bar{\nu}$ is given in chapter 2. The Belle detector, which provides the data for the analysis, and the Belle II detector, for which the tracking was developed, are describes in chapter 3. In chapter 4 a brief explanation of the full reconstruction, which is an essential analysis technique to reconstruct decays with undetectable neutrinos in the final state, is given. Chapter 5 contains the full description of the $B \to h^{(*)}\nu\bar{\nu}$ analysis. The final results of the analysis are then presented in chapter 6. In chapter 7 the tracking algorithm is described and evaluated. Finally, in chapter 8 all results are summarised and discussed.

2. Theoretical overview and motivation

In this chapter the basic concepts, such as flavour changing neutral currents, which are related to the the given analysis, are explained and the theoretical motivation for the search of the decays $B \to h^{(*)}\nu\bar{\nu}$ is given.

2.1. Flavour physics within the Standard Model

The Standard Model (SM) of particle physics describes properties and interactions between the known elementary particles. The basic principles are described in various textbooks (e.g. [3]) and the current status and the latest measurements of all parameters can be found at [2].

The elementary particles of the SM can be divided into two groups: matter particles, which are fermions, with spin 1/2, and interaction particles, which are bosons, with spin 1. The Standard Model describes three known fundamental forces: strong, electromagnetic and weak force. Weak and electromagnetic force are unified to a common description as electroweak force. The governing symmetry of the SM is the $SU(3)_{color} \times SU(2)_{weak} \times U(1)_{hypercharge}$ gauge symmetry. The $SU(3)$ symmetry determines the interactions of the strong force, while the $SU(2) \times U(1)$ controls the electroweak interactions which permit flavour changing decays of quarks. The fourth fundamental force, gravity, is not included in the Standard Model. A summary of all elementary particles is shown in fig. 2.1. The elementary fermions are divided into quarks and leptons. All fermions can also be grouped into three families or generations.

Flavour physics describes interactions that distinguish between the fermion generations. The electroweak interaction can be written in three terms: one containing the electromagnetic current, one containing the weak charged current and one containing the weak neutral current. The electromagnetic current is mediated through photons γ, while the weak currents are mediated through massive $W^{\pm}$ and Z^0 bosons. The weak charged current is a flavour changing interaction, b quarks usually decay via such processes, an example is shown in fig. 2.2(a). Neutral and electromagnetic currents do not change the flavour of quarks in the leading order interaction, which is denoted as tree level interaction. An example of neutral current is shown in fig. 2.2(b).

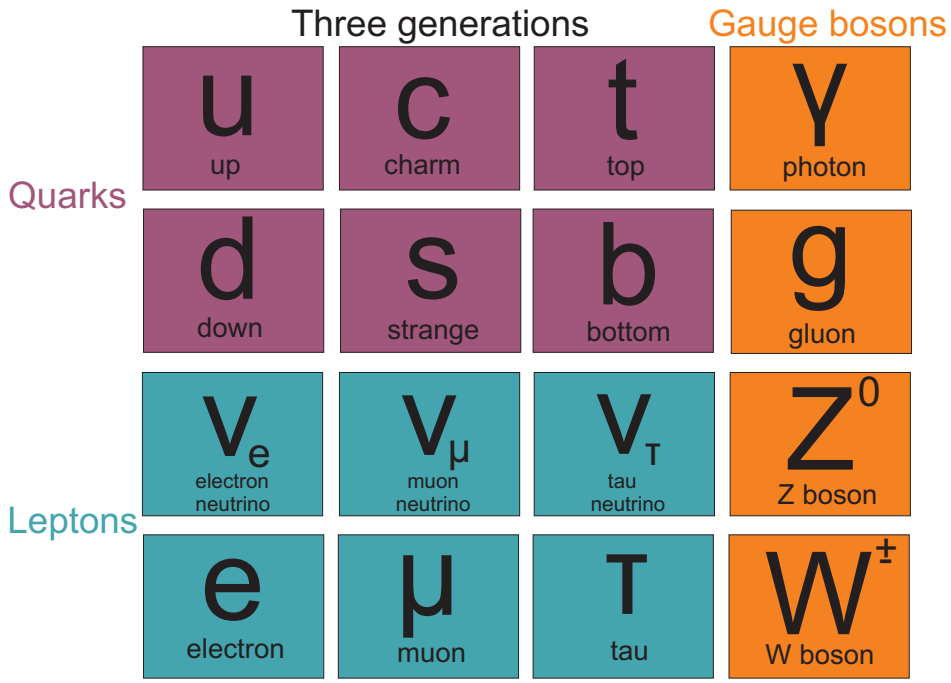

Figure 2.1.: The elementary particles of the Standard Model.

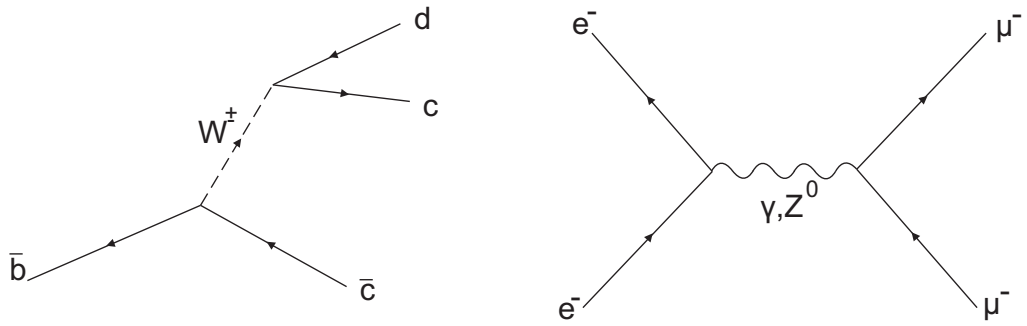

(a) Charged current (b) Neutral current

Figure 2.2.: Examples for charged and neutral currents in the Standard Model.

Another important concept in flavour physics is the helicity of a particle. It describes the relation between the spin and the momentum of the particle. If both have the same direction, the particle is denoted as left-handed. If the spin direction is opposite to the momentum direction, the particle is referred to as right-handed. Only left-handed components of particles and right-handed components of anti-particles can participate in charged

current interaction.

The description of the electroweak symmetry breaking via the Higgs mechanism can explain the heavy masses of $W^{\pm}$ and Z^0 bosons compared to the massless γ. One of the features of this mechanism is that it also gives masses to the fermions. However, the mass-eigenstates of quarks are rotated with respect to the electroweak flavour-eigenstates. The relation between these eigenstates and the flavour changing processes can be describes with the Cabbibo-Kobayashi-Maskawa (CKM) matrix [4, 5]:

$$\begin{pmatrix} d \\ s \\ b \end{pmatrix}_{\text{weak}} = V_{\text{CKM}} \begin{pmatrix} d \\ s \\ b \end{pmatrix}_{\text{mass}} \equiv \begin{pmatrix} V_{ud} & V_{us} & V_{ub} \\ V_{cd} & V_{cs} & V_{cb} \\ V_{td} & V_{ts} & V_{tb} \end{pmatrix} \begin{pmatrix} d \\ s \\ b \end{pmatrix}_{\text{mass}} \quad . \tag{2.1}$$

To convey the relative strength of the elements more intuitively, usually the Wolfenstein parametrisation [6] is used, which expands the V_{CKM} in powers of $\lambda = \sin\theta_C \approx 0.23$, where θ_C is the Cabbibo angle. Terms of $\mathcal{O}(\lambda^4)$ are neglected.

$$V_{\text{CKM}} = \begin{pmatrix} 1 - \frac{1}{2}\lambda^2 & \lambda & A\lambda^3(\rho - i\eta) \\ -\lambda & 1 - \frac{1}{2}\lambda^2 & A\lambda^2) \\ A\lambda^3(1 - \rho - i\eta) & -A\lambda^2 & 1 \end{pmatrix} \quad . \tag{2.2}$$

The V_{CKM} matrix is unitary, which allows us to set up additional constraints on the values of the matrix elements. One of these constraints is

$$\begin{array}{ccccccc} V_{ud}V_{ub}^* & + & V_{cd}V_{cb}^* & + & V_{td}V_{tb}^* & = & 0 \\ \mathcal{O}(\lambda^3) & & \mathcal{O}(\lambda^3) & & \mathcal{O}(\lambda^3) & & \end{array} \quad , \tag{2.3}$$

which is relevant to B meson decays and is known as the CKM Unitarity Triangle when represented in the complex plane.

Although the flavour changing neutral currents (FCNC) are not possible within the SM on the tree level, they still can proceed via higher order processes. $b \to s\nu\bar{\nu}$ is such a FCNC transition, the dominant first order diagrams are shown in fig. 2.3 (a) and (b).

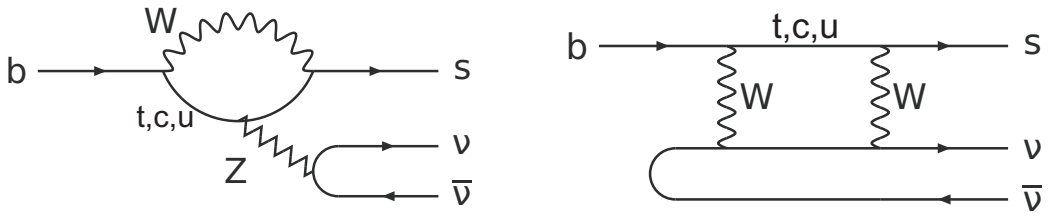

(a) Penguin diagram (b) Box diagram

Figure 2.3.: The Feynman diagrams for the $b \to s\nu\bar{\nu}$ transition in the Standard Model.

These higher order diagrams are even further suppressed through the GIM mechanism [7]. This mechanism was first described by Glashow, Iliopoulos and Mainani and is responsible for the cancellation between different diagram contributions due to the CKM mixing. For the $b \to s$ transition mention above, the total matrix element $\mathcal{M}$ of the FCNC process can be obtained from the sum of the contributions from all three loops (one for each up-type quark):

$$\mathcal{M} \propto F(x_u)V_{us}^*V_{ub} + F(x_c)V_{cs}^*V_{cb} + F(x_t)V_{ts}^*V_{tb} \quad . \tag{2.4}$$

The functions $F(x_i)$ depend on a single parameter $x_i \propto m_i^2$, where m_i are the masses of the particles present in the loop. If we now consider one of the relations resulting from the unitarity of the CKM matrix (see equation 2.1):

$$V_{us}^*V_{ub} + V_{cs}^*V_{cb} + V_{ts}^*V_{tb} = 0 \quad , \tag{2.5}$$

we can see, that the matrix element $\mathcal{M}$ for the FCNC process would vanish if the masses of the u, c and t quarks were identical. It would also vanish if the energy at which the process occurs is much greater than the masses of the quarks. GIM mechanism is a manifestation of the underlying symmetry between the electroweak and the strong interactions. However, as the quark family symmetry is broken through different quark masses and because the quarks masses are often greater than the external momenta, the cancellation between different contributions is not exact and the FCNC processes can be observed experimentally. The circumstances to observe FCNC processes in b quark decays are especially favourable, because these decays are dominated by the contribution from the t quark which is much heavier than the u and d quarks. The suppression for up-type quarks is more severe, as the mass differences between s, d and b quarks are not that large.

Although the CKM mechanism can describe the presently available data in a consistent

way, the flavour structure of the SM is not satisfactory clarified from the theoretical point of view. The search for non-standard flavour dynamics provided by FCNC is especially interesting, as their suppression ensures a large sensitivity to NP effects.

2.2. $B \to h^{(*)}\nu\bar{\nu}$ decays

The decays $B \to h^{(*)}\nu\bar{\nu}$ proceed through $b \to s\nu\bar{\nu}$ and $b \to d\nu\bar{\nu}$ higher order FCNC transitions (see fig. 2.3) and are suppressed via the GIM mechanism. The resulting SM branching fractions are very small, therefore these decays are denoted as 'rare' and offer an excellent opportunity to probe for New Physics beyond the SM. Especially the decays $B \to K\nu\bar{\nu}$ and $B \to K^*\nu\bar{\nu}$ were elaborately studied in several theory works [8–14], the main ideas and conclusions will be presented in the following.

From the theory perspective the inclusive decay $B \to X_s\nu\bar{\nu}$ would be ideal to study $b \to s$ transitions, it is however very challenging experimentally. The exclusive decays like $B \to K\nu\bar{\nu}$ belong nevertheless to the theoretically cleanest decays in the field of FCNC processes and can be studied experimentally. The advantage of the final state with $\nu\bar{\nu}$ instead of l^+l^- is the absence of long-distance electromagnetic interactions and the enhancement of the branching fractions by the summation over the three neutrino flavours. However, the study of exclusive decays requires the control of non-pertubative hadronic form factors.

In the following the summary of current theoretical results within the SM will be given, followed by the description of NP models which can contribute to the observables of the $B \to h^{(*)}\nu\bar{\nu}$ decays and the current experimental status.

2.2.1. Standard Model predictions

The differential branching fraction of the $B \to K\nu\bar{\nu}$ decay in the SM is given by

$$\frac{d\mathcal{B}(\bar{B} \to \bar{K}\nu\bar{\nu})}{ds} = \tau_B \frac{G_F^2 \alpha^2 m_B^5}{256\pi^5} |V_{ts}V_{tb}|^2 \cdot \lambda^{2/3}(s) f_+^2(s) |a(K\nu\nu)|^2 \quad , \tag{2.6}$$

with $s = q^2/m_B^2$, q is the dilepton invariant mass, m_B is the B meson mass, G_F is the Fermi coupling constant, α is the fine structure constant, $r_K = m_K^2/m_B^2$ and $\lambda_K(s) = 1 + r_K^2 + s^2 - 2r_K - 2s - 2r_K s$ [14]. The coefficient $a(K\nu\nu)$ is given by a short-distance Wilson coefficient at the weak scale and is precisely known. Wilson coefficients are widely used in the theoretical flavour physics to parametrise weak interactions. The long-distance hadronic dynamics is contained in the matrix elements, which are parametrised by the form factors f_+, f_0, f_T. f_0 drops out for small lepton masses and the ratio f_T/f_+ is

independent of unknown hadronic quantities in the limit of large kaon energy. Following approximation, valid in the entire physical domain, can be formulated:

$$\frac{f_T(s)}{f_+(s)} = \frac{m_B + m_K}{m_B} + \mathcal{O}(\alpha_s, \Lambda/m_b) \quad . \tag{2.7}$$

The calculations lead to the following prediction for the branching fraction:

$$\mathcal{B}(B^- \to K^- \nu\bar{\nu}) = (4.4^{+1.3}_{-1.1}(f_+(0))^{+0.8}_{-0.7}(a_0)^{+0.0}_{-0.03}(\mu)) \times 10^{-6} \quad .$$

To reduce the error a combined analysis of $B \to K\nu\bar{\nu}$ and $B \to Kl^+l^-$ was proposed in [14]. Although the individual branching fraction suffer from large hadronic uncertainties, their ratio R should have a significantly smaller theoretical error. Using the experimental result for $B \to Kl^+l^-$ one can obtain the following branching fraction for $B \to K\nu\bar{\nu}$:

$$\mathcal{B}(B^- \to K^- \nu\bar{\nu}) = R \cdot \mathcal{B}(B^- \to K^- l^+ l^-)_{exp} = (3.64 \pm 0.47) \times 10^{-6} \quad .$$

As NP might also have a different impact on $B \to K\nu\bar{\nu}$ and $B \to Kl^+l^-$, a good theoretical determination of the ratio will help to reveal even moderate deviations from SM expectations.

The observation of the decay including the excited kaon, $B \to K^*\nu\bar{\nu}$, would contribute to the investigation of right-handed currents due to the additional angular observables, as it is described in [10]. The angular distribution of the K^* decay products can be used to determine the polarisation of K^*. The dependence of the predicted branching fractions on the normalised neutrino invariant mass squared is shown in fig. 2.4.

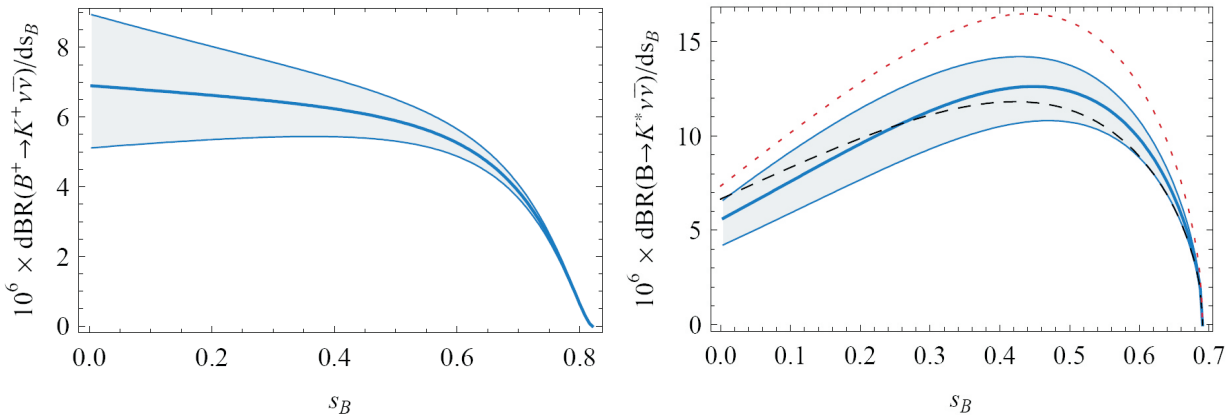

(a) $B^+ \to K^+\nu\bar{\nu}$ (b) $B \to K^*\nu\bar{\nu}$

Figure 2.4.: Dependence of the $B^+ \to K^+\nu\bar{\nu}$ and $B \to K^*\nu\bar{\nu}$ branching fractions on the normalised neutrino invariant masses squared s_B within the SM. The error bands reflect the theoretical uncertainties. The black dashed lines and dotted red lines in (b) are the results based on different sets of form factors. (Taken from [10]).

The branching fractions of $b \to s\nu\bar{\nu}$ decays are dependent on the two complex Wilson coefficients C_L^ν and C_R^ν. However, only two combinations of these complex quantities are observable:

$$\epsilon = \frac{\sqrt{|C_L^\nu|^2 + |C_R^\nu|^2}}{|(C_L^\nu)^{SM}|}, \qquad \eta = \frac{-Re(C_L^\nu C_R^{\nu *})}{|C_L^\nu|^2 + |C_R^\nu|^2} \quad , \tag{2.8}$$

such that η lies in the range $[-\frac{1}{2}, \frac{1}{2}]$. The branching fractions can be expressed as follows [10]:

$$\mathcal{B}(B \to K^*\nu\bar{\nu}) = (6.8 \times 10^{-6}) \cdot (1 + 1.31\eta)\epsilon^2 \quad ,$$
$$\mathcal{B}(B \to K\nu\bar{\nu}) = (4.5 \times 10^{-6}) \cdot (1 - 2\eta)\epsilon^2 \quad .$$

As η and ϵ can be calculated in any model, these equations can be used as fundamental formulae for any phenomenological analysis of these decays. For SM these values would be $(\epsilon, \eta) = (1, 0)$. The current constraints on the $\epsilon - \eta$ plane are shown in fig. 2.5

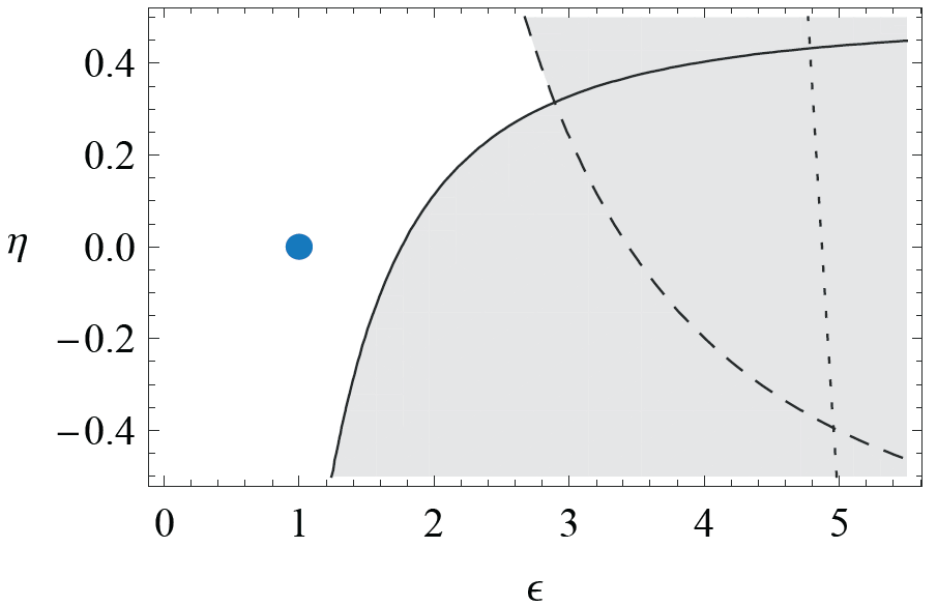

Figure 2.5.: Existing experimental constraints on ϵ and η. Dashed line: constraint from $B(B \to K^* \nu\bar{\nu})$, solid line: constraint from $B(B \to K\nu\bar{\nu})$, dotted line: constraint from $B(B \to X_s\nu\bar{\nu})$. The shaded area is ruled out experimentally at the 90% confidence level. The blue circle represents the SM point. (Taken from [10]).

Another related study was performed in [12], where the tree level contributions to the rare decays $B \to \pi^+\nu\bar{\nu}$, $B \to K^+\nu\bar{\nu}$ and $B \to K^{*+}\nu\bar{\nu}$ are analysed. For all rare charged meson decays, there is a possible long-distance contribution arising at tree-level through an intermediate lepton state. Such contributions are potentially large when the intermediate lepton is kinematically allowed to be on-shell, as can be seen in the case of $B \to K^+\nu\bar{\nu}$ by multiplying the measured branching ratios of $B \to \tau\nu$ and $\tau \to K\nu$:

$$\mathcal{B}(B^+ \to K^+\nu\bar{\nu})_{Tree} \approx \mathcal{B}(B^+ \to \tau^+\nu) \times \mathcal{B}(\tau^+ \to K^+\nu) = (1.0 \pm 0.3) \times 10^{-6} \quad ,$$

which is, after a proper calculation, about 15% of the corresponding SM short-distance FCNC contributions from which they cannot be disentangled. On the other hand, $\mathcal{B}(B \to \pi^+\nu\bar{\nu})$ is dominated by the τ lepton transition, with the contribution of short distance FCNC processes being of about 3%. The updated values which include these effects in the SM predictions are given in table 2.1.

Decay	FCNC SM prediction	Tree level τ contribution	Full SM prediction
$\mathcal{B}(B^+ \to \pi^+\nu_l\bar{\nu}_l)$	$\sim 3 \times 10^{-7}$	$(9.4 \pm 2.1) \times 10^{-6}$	$(9.7 \pm 2.1) \times 10^{-6}$
$\mathcal{B}(B^+ \to K^+\nu_l\bar{\nu}_l)$	$(4.5 \pm 0.7) \times 10^{-6}$	$(6.1 \pm 1.3) \times 10^{-7}$	$(5.1 \pm 0.8) \times 10^{-6}$
$\mathcal{B}(B^+ \to K^{*+}\nu_l\bar{\nu}_l)$	$(7.2 \pm 1.1) \times 10^{-6}$	$(1.2 \pm 3) \times 10^{-6}$	$(8.4 \pm 1.4) \times 10^{-6}$

Table 2.1.: Theoretical Standard Model predictions for some $b \to s\nu\bar{\nu}$ and $b \to d\nu\bar{\nu}$ decay modes including tree level contributions. (Adapted from [12]).

2.2.2. Supersymmetry

Supersymmetry (SUSY) is an attractive and currently common NP model. In the minimal supersymmetric extension of the SM (MSSM) the superpartners of the electroweak gauge and Higgs bosons (the gauginos and higgsinos) mix to form two electrically charged and four electrically neutral mass eigenstates: charginos $\tilde{\chi}^{\pm}_{1,2}$ and neutralinos $\tilde{\chi}^{0}_{1,2,3,4}$. In many supersymmetric models, the neutralino plays a special role in phenomenology as the lightest supersymmetric particle. Supersymmetry introduces a new symmetry described by the R-parity. All supersymmetric particles have R-parity of -1 while all SM particles have the R-parity of 1. In several models with conserved R-parity, the neutralino is stable and provides a promising dark matter candidate.

In [10] it is discussed, that the MSSM should lead to various contributions to the $b \to s\nu\bar{\nu}$ processes. However, when the existing costraints from other FCNC processes are applied, the effects of the Wilson coefficients C^{ν}_{L} and C^{ν}_{R} turn out to be quite small. A sizeable contribution can only be expected from C^{ν}_{L} through chargino contributions, which are also not strongly constrained by the existing data. Largest effects can be generated by a Z penguin with a $(\delta^{RL}_{u})_{32}$ mass insertion. The mass insertion approximation is widely used in theoretical descriptions of the supersymmetry. In this approximation a basis is chosen where all gauge couplings are diagonal and the flavour violation sources are represented via small off-diagonal mass insertion term. The Z penguin diagrams giving that contribution are shown in fig. 2.6.

Within a certain setup following ranges for the branching fractions were obtained:

$$3.5 \times 10^{-6} \lesssim \mathcal{B}(B \to K\nu\bar{\nu}) \lesssim 5.8 \times 10^{-6} \quad ,$$
$$5.3 \times 10^{-6} \lesssim \mathcal{B}(B \to K^*\nu\bar{\nu}) \lesssim 8.7 \times 10^{-6} \quad .$$

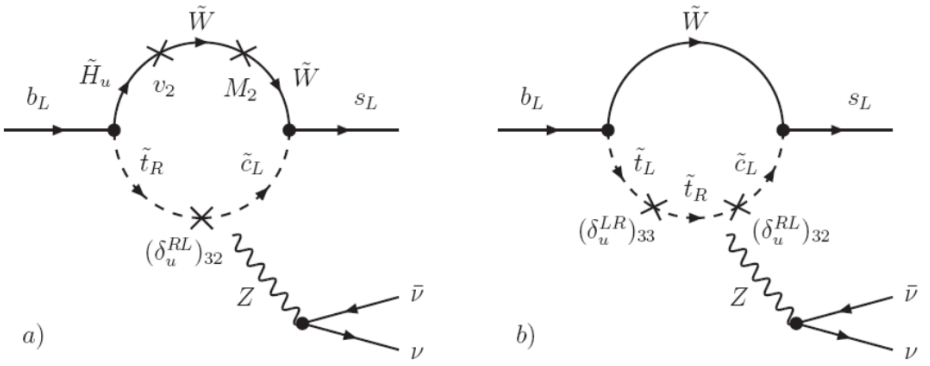

Figure 2.6.: Dominant chargino contributions to the Wilson coefficient C_L^ν in the mass insertion approximation. (Taken from [10]).

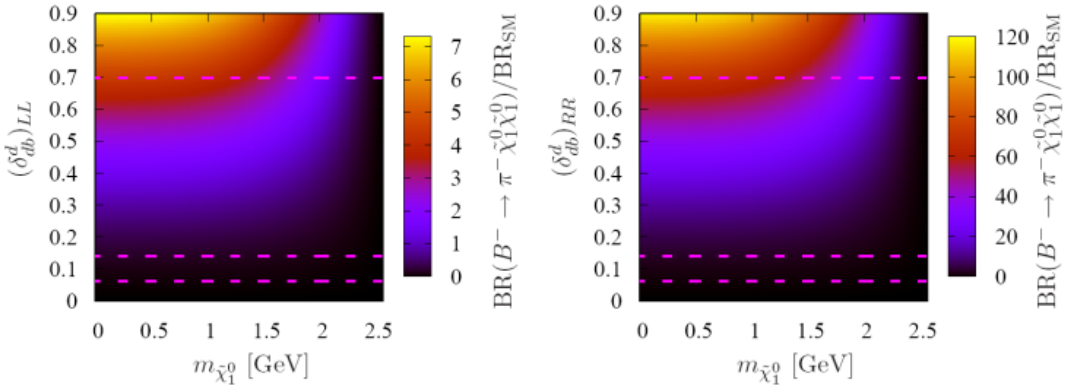

Figure 2.7.: Branching ratios for and $B^- \to \pi^- \tilde{\chi}_1^0 \tilde{\chi}_1^0$ as a function of the neutralino mass $m_{\tilde{\chi}_1^0}$ and the mass insertion $(\delta_{db}^d)_{LL}$ (left-hand side) and $(\delta_{db}^d)_{RR}$(right-hand side). The branching ratio is normalised to the calculated BR for $B^- \to \pi^- \nu\bar{\nu}$ within the SM, which is 2.2×10^{-7}. We assume an average squark mass of $\tilde{m} = 500$ GeV. The dashed lines show upper bounds on the mass insertions $(\delta_{db}^d)_{LL/RR}$ mainly obtained from $B_d - \bar{B}_d$ mixing for different ratios of squark mass to gluino mass. (Taken from [11]).

In [11] rare meson decays into very light neutralinos are analysed. Minimal flavour violation (MFV) models are defined by the requirement that all flavour violating and CP-violating transitions are described by the CKM matrix of the SM. This means that the decays like $B^- \to K^- \tilde{\chi}_1^0 \tilde{\chi}_1^0$ only have leading contributions from one-loop diagrams. The branching fraction for the decay $B^- \to K^- \tilde{\chi}_1^0 \tilde{\chi}_1^0$ in the MSSM with MFV is several orders

of magnitude smaller than the SM process.

However, considering a non-minimal flavour violation in the MSSM one can obtain larger effects. Here also the mass insertion approximation was used to estimate the branching ratio contribution. The results are shown in fig. 2.7 and fig. 2.8.

It can be concluded, that the branching ratios for decays $B^- \to K^-\tilde{\chi}_1^0\tilde{\chi}_1^0$ and $B^- \to \pi^-\tilde{\chi}_1^0\tilde{\chi}_1^0$ may be significantly enhanced when one allows for non-minimal flavour violation.

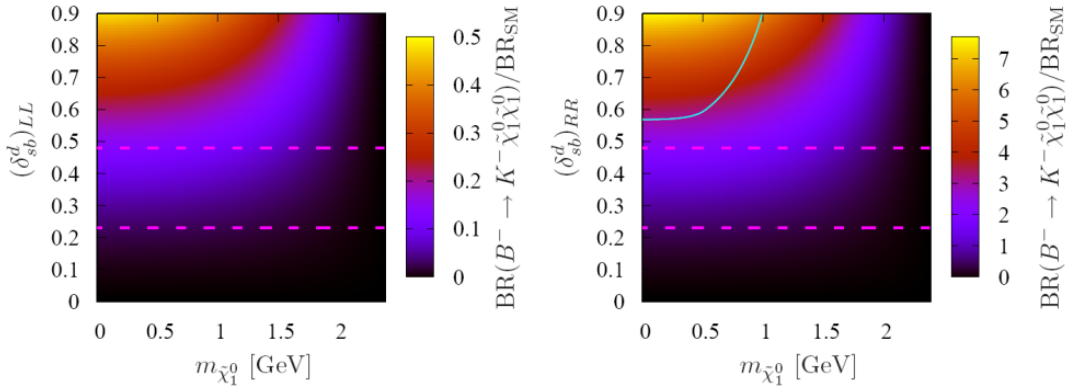

Figure 2.8.: Branching ratios for and $B^- \to K^-\tilde{\chi}_1^0\tilde{\chi}_1^0$ as a function of the neutralino mass $m_{\tilde{\chi}_1^0}$ and the mass insertion $(\delta^d_{db})_{LL}$ (left-hand side) and $(\delta^d_{db})_{RR}$ (right-hand side). The branching ratio is normalised to the calculated BR for $B^- \to K^-\nu\bar{\nu}$ within the SM, which is 4.5×10^{-6}. We assume an average squark mass of $\tilde{m} = 500$ GeV. The solid grey (turquoise) line corresponds to the experimental upper bound . The dashed lines show upper bounds on the mass insertions $(\delta^d_{db})_{LL/RR}$ mainly obtained from $B_d - \bar{B}_d$ mixing for different ratios of squark mass to gluino mass. (Taken from [11]).

2.2.3. Invisible scalars and dark matter

A transition $b \to sSS$ with an additional general gauge-singlet scalar S with mass $m_S < m_B/2$ might contribute to the observables of $b \to s\nu\bar{\nu}$ transitions, if S is stable and sufficiently long-lived to escape the detector. Both final state have the same experimental signature. However, one can analyse the resulting spectrum, as it was done in [10]. The dependence of the branching fraction on the neutrino invariant mass squared is shown in fig. 2.9. The overlap of the both distributions leads to a characteristic spectrum with a kinematical edge at $q^2 = m_S^2/4$, which would point to an additional contribution from $b \to sSS$ decays.

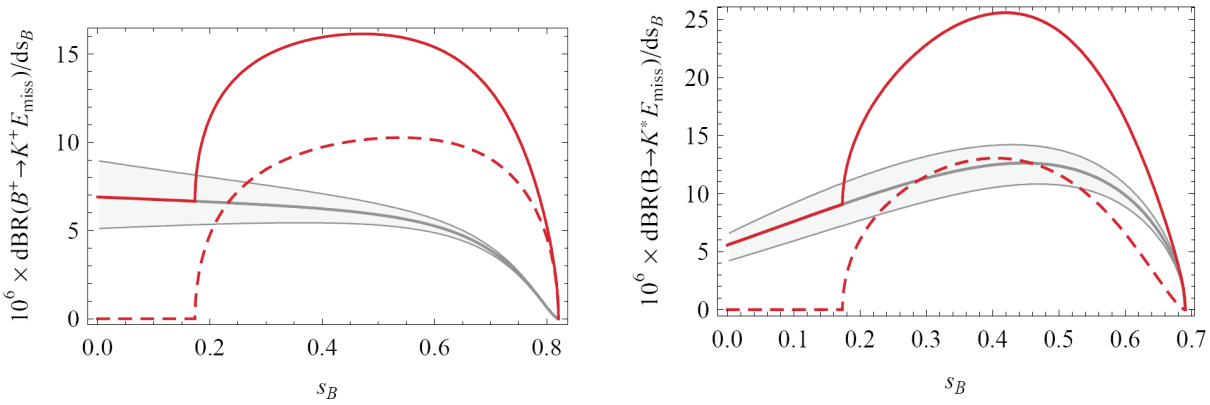

(a) $B^+ \to K^+ \nu\bar{\nu}$ (b) $B \to K^* \nu\bar{\nu}$

Figure 2.9.: Dependence of the $B^+ \to K^+ \nu\bar{\nu}$ and $B \to K^* \nu\bar{\nu}$ branching fractions on the normalised neutrino invariant mass squared s_B in a scenario in which SM-like $b \to s\nu\bar{\nu}$ overlap with $b \to sSS$ decays. The chosen parameters are $m_s = 1.1$ GeV, $C_L^S = 0$, $C_R^S = 2.8 \times 10^{-8}$ GeV^{-2}. The grey curves show the theoretical uncertainties, the red dashed curves the pure $b \to sSS$ contribution and the red solid curve the resulting combination. (Taken from [10]).

Such considerations also find application in the models of dark matter. The decay $B \to K + E_{\mathrm{miss}}$ can directly be an efficient probe of dark matter models in the mass range of $1-2$ GeV, as it is explained in [9]. Dedicated underground experiments have little sensitivity to dark matter in the GeV and sub-GeV range. Following results were obtained:

$$\mathcal{B}(B^+ \to K^+ SS) = 2.8 \times 10^{-4} \kappa^2 F(m_S) \quad ,$$
$$\mathcal{B}(B^+ \to K^{*+} SS) = 4.3 \times 10^{-4} \kappa^2 F(m_S) \quad .$$

For light scalars $m_S \sim 100$ MeV and $\kappa \sim \mathcal{O}(1)$ the decay rate rates with emission of dark matter particles are ~ 50 times larger than the decays with neutrinos in the final state. The predicted branching ratio together with the experimental limits is shown in fig. 2.10.

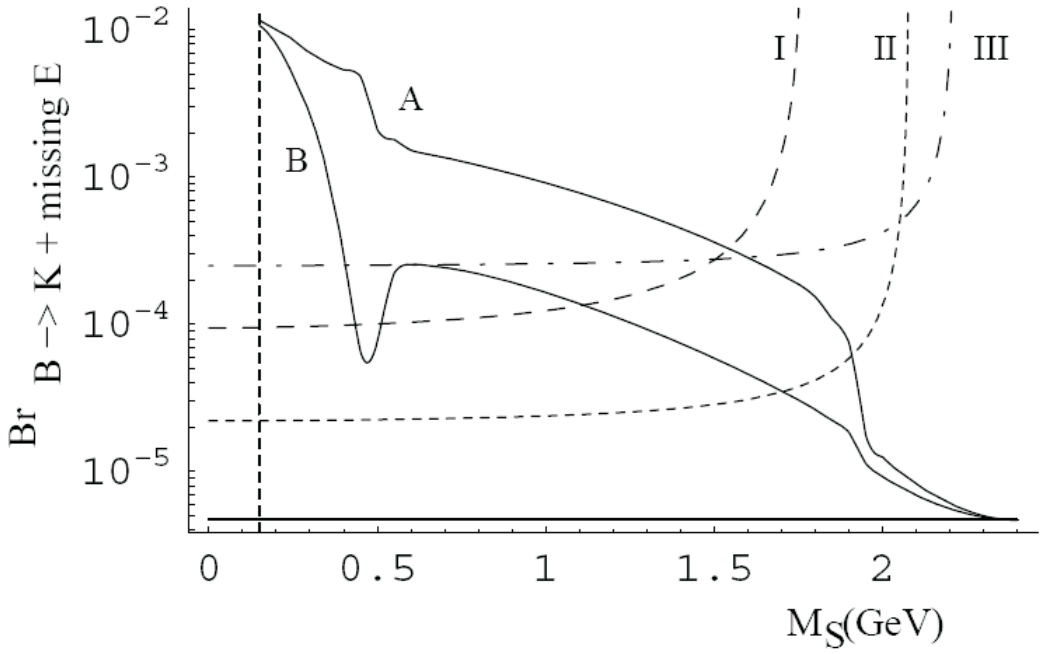

Figure 2.10.: Predicted branching ratios for the decay $B \to K + E_{\text{miss}}$, with limits from BaBar(I) [15], CLEO(II) [16] and expected results from BaBar (III). Parameter space above curves I and II is excluded. The solid horizontal line shows the SM $B^+ \to K^+\nu\bar{\nu}$ signal. Parameter space to the left of the vertical dashed line is also excluded by $K^+ \to \pi^+ + E_{\text{miss}}$. A and B show the upper and lower bounds of the allowed parameter space. (Taken from [9]).

2.2.4. Non-standard Z couplings

In many models beyond SM, NP effects in Wilson coefficients $C^{\nu}_{L,R}$ are dominated by Z penguins. This can be analysed in a generic scenario with decays $B \to K^{(*)}l^+l^-$, $B \to K^{(*)}\nu\bar{\nu}$ and $B_s \to \mu^+\mu^-$, as it was done in [8]. The $\bar{s}bZ$ vertex is particularly receptive to non-standard dynamics and the $\bar{s}bZ$ coupling is also not strongly constraint by the present data. In the generic extension of the SM with new particles $M_X > M_z$, due to the spontaneous breaking of $SU(2)_L \times U(1)_Y$ it is allowed, in the case of the Z boson, to build an effective FCNC coupling of dimension four, without any explicit M_X suppression. So the $\Delta F = 1$ FCNC couplings do not necessarily decouple by dimensional argument in the limit $M_X/M_Z >> 1$, leading to an independent behaviour of these couplings with respect to the other FCNC amplitudes. The resulting couplings are summarised in table 2.2. Significantly larger couplings can be observed within this extended model.

SM	Extension
$\lvert Z^L_{sb}\rvert \sim 0.04$	$\lvert Z^L_{sb}\rvert \sim 0.3$
$\lvert Z^L_{db}\rvert \sim 0.01$	$\lvert Z^L_{db}\rvert \sim 0.06$

Table 2.2.: Theoretical predictions for $b \to s\nu\bar{\nu}$ and $b \to d\nu\bar{\nu}$ couplings in the SM and in a model extended with non-standard Z coupling [8].

2.2.5. Further models

There are many other different NP models which could contribute to the observables of the decays in question. A fourth generation of quarks and leptons could lead to a contribution of a similar order of magnitude as the SM process [13, 17]. There are also exotic scenarios with FCNC couplings of the Z generated already at the tree level. This can be achieved with non-sequential generations of quarks [18] (different number of up- and down-type quarks) or with an extra $U(1)$ symmetry [19]. Further possibility is the topcolor assisted technicolor [20]. Within this model new strong dynamics and extra Z' bosons, which distinguish the third generation from the remaining two, would lead to an enhancement of transitions such as $b \to s\nu_\tau\bar{\nu_\tau}$. Other models, like littlest Higgst with T-Parity [21] or Randall-Sundrum model with custodial protection of left-handed Z couplings to down quarks [22], lead only to very small deviations from SM.

2.2.6. Experimental status

The search for $B \to h^{(*)}\nu\bar{\nu}$ decays was already performed by the CLEO, Belle and BaBar collaborations. No signal evidence was observed. The experimental upper limits for these branching fractions are summarised in table 2.3. For most channels the limits are two orders, for some channels one order, of magnitude larger than the Standard Model predictions. Higher statistics and better efficiency is necessary to observe a possible deviation from the Standard Model.

Decay	Branching ratio	Experiment	Source
$B^+ \to K^+\nu\bar{\nu}$	$< 1.3 \cdot 10^{-5}$	BaBar	[23]
	$< 1.4 \cdot 10^{-5}$	Belle	[1]
	$< 2.4 \cdot 10^{-4}$	Cleo	[16]
$B^0 \to K^0\nu\bar{\nu}$	$< 5.6 \cdot 10^{-5}$	BaBar	[23]
	$< 1.6 \cdot 10^{-4}$	Belle	[1]
$B^+ \to K^{*+}\nu\bar{\nu}$	$< 8 \cdot 10^{-5}$	BaBar	[24]
	$< 1.4 \cdot 10^{-4}$	Belle	[1]
$B^0 \to K^{*0}\nu\bar{\nu}$	$< 1.2 \cdot 10^{-4}$	BaBar	[24]
	$< 3.4 \cdot 10^{-4}$	Belle	[1]
$B^+ \to \pi^+\nu\bar{\nu}$	$< 1.0 \cdot 10^{-4}$	BaBar	[15]
	$< 1.7 \cdot 10^{-4}$	Belle	[1]
$B^0 \to \pi^0\nu\bar{\nu}$	$< 2.2 \cdot 10^{-4}$	Belle	[1]
$B^+ \to \rho^+\nu\bar{\nu}$	$< 1.5 \cdot 10^{-4}$	Belle	[1]
$B^0 \to \rho^0\nu\bar{\nu}$	$< 4.4 \cdot 10^{-4}$	Belle	[1]
$B^0 \to \phi\nu\bar{\nu}$	$< 5.8 \cdot 10^{-4}$	Belle	[1]

Table 2.3.: Current experimental limits at 90% CL on the $B \to h^{(*)}\nu\bar{\nu}$ branching fraction.

3. Belle and BelleII experiments

The KEKB accelerator, which stands at the High Energy Accelerator Research Organization (KEK) in Tsukuba (Japan) is a particle collider specialised in producing B-mesons, a so called B-factory. Belle is a multi-purpose detector at the sole interaction point of the KEKB accelerator. The full description of the detector can be found in [25]. Although the large data sample, over 1 ab^{-1} in total, obtained during 10 years of data taking, allowed a large number of precision studies and observations, and several analyses are still ongoing, a step toward higher luminosity is necessary to solve various open questions.

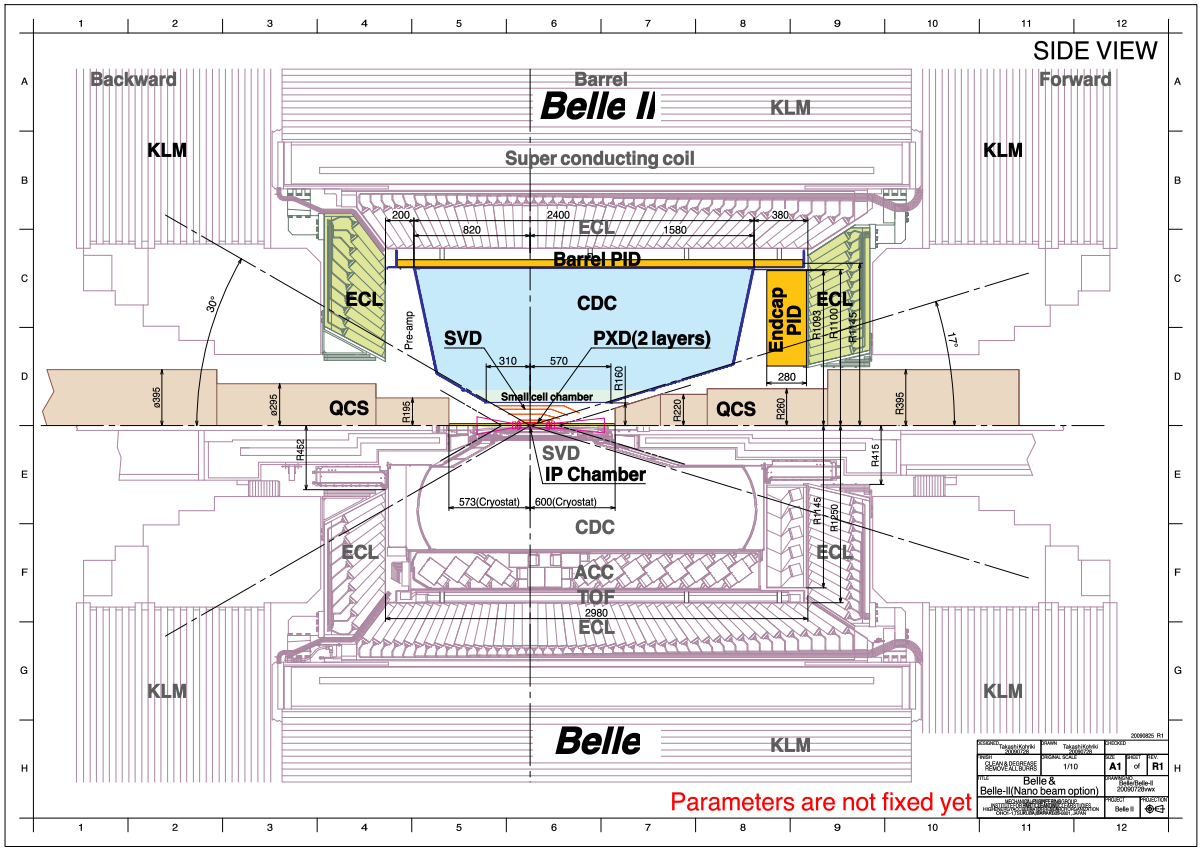

Figure 3.1.: Cross sections of the Belle and Belle II detectors in comparison. (Taken from [26]).

In the coming years the KEKB accelerator will be upgraded to the SuperKEKB accelerator. The target luminosity of the new machine is $8 \times 10^{35}\text{cm}^{-2}\text{s}^{-1}$, which will increase the luminosity achieved by the KEKB accelerator by a factor of 40. An extensive motivation with description of new physics processes which might be observed with the new luminosity is given in [27]. The description of the new Belle II detector can be found in the Belle II Technical Design Report [26]. It is important to mention, that the detector design is not yet finalised and optimisation studies are ongoing. A comparison of Belle and Belle II detectors can be seen in fig. 3.1.

In the following sections the functionality and main characteristics of the KEKB accelerator and the Belle detector and their planned upgrades, SuperKEKB and Belle II, are described.

3.1. The KEKB accelerator

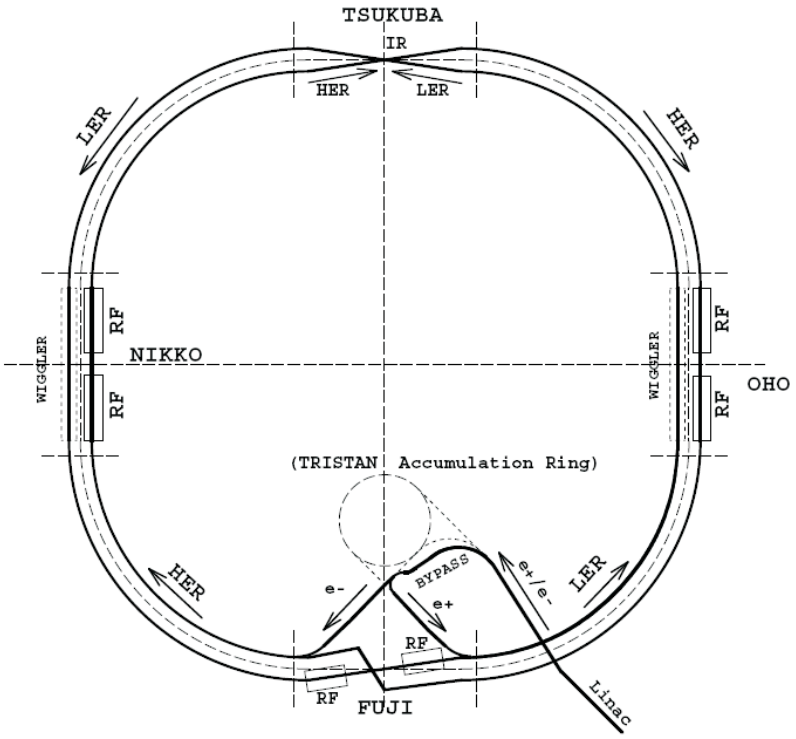

Figure 3.2.: Schematic layout of the KEKB accelerator system. (Taken from [28]).

The KEKB is a two ring asymmetric e^+e^- accelerator (see fig 3.2). The circumference of both rings is 3016 m. The electrons are filled in the high energy ring (HER) with an

energy of 8 GeV, the positrons circulate in the low energy ring (LER) with an energy of 3.5 GeV. This leads to a centre-of-mass energy of $\sqrt{s} = 2\sqrt{E_{e^+}E_{e^+}} = 10.58$ GeV. The asymmetry and the value of the centre-of-mass energy are two main features of the accelerator.

The energy of 10.58 GeV corresponds to the $\Upsilon(4S)$ resonance, which is a bound $b\bar{b}$ state with a mass directly above the production threshold for a B meson pair (~ 10.56 GeV), as shown in fig. 3.3 . Thus this resonance decays to a $B^0\bar{B}^0$ or B^+B^- pair with a probability of $\approx 96\%$, which is the reason why such accelerators are also called B-factories. As apart from the $B\bar{B}$ pair nothing else is produced, the events create only 9 charged tracks in average.

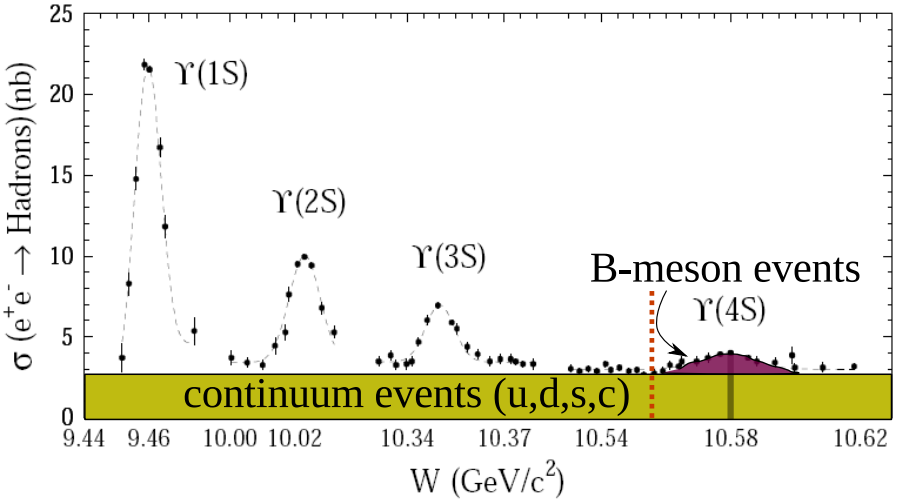

Figure 3.3.: The cross section of e^+e^- to hadrons. The red dashed line marks the threshold for production of a $B\bar{B}$ pair which is just below the $\Upsilon(4S)$ resonance. (Taken from [29, 30]).

circumference	3016 m
e^- energy (HER)	8 GeV
e^+ energy (LER)	3.5 GeV
crossing angle	22 mrad
number of bunches	1584
bunch crossing frequency	509 MHz

Table 3.1.: Technical specifications of the KEKB accelerator [31].

The different energies of e^+ and e^- give the $\Upsilon(4S)$ a Lorentz boost of 0.425. Therefore the created B mesons are also boosted, which leads to a measurable flight length in the order of 100μm. This allows the study of B mesons decay time.

Further technical specifications of the KEKB accelerator are given in table 3.1 and more information can be found in [28]. In 2009 the accelerator achieved a world record in luminosity of $2.11 \times 10^{34}\text{cm}^{-2}\text{s}^{-1}$.

3.2. The SuperKEKB accelerator

The same tunnel will be used for the upgraded SuperKEKB accelerator. One of the major changes compared to its predecessor will be the so called Nano-Beam scheme. In this scheme the longitudinal size of the overlap region of the two beams at the interaction point is minimised, as it is shown in fig. 3.4.

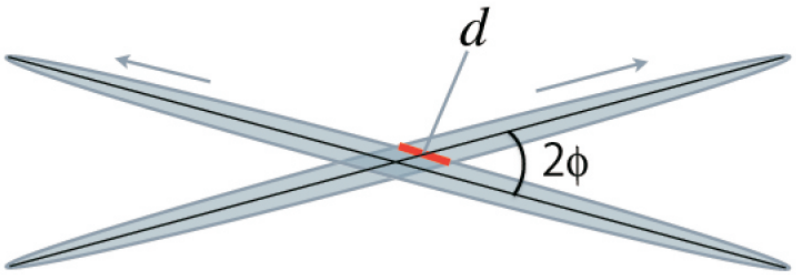

Figure 3.4.: Schematic view of beam collision in the Nano-Beam scheme. d illustrates the overlap region between two beams, while ϕ is the half crossing angle of 41.5 mrad. (Taken from [26]).

To realise this scheme a larger horizontal crossing angle and extremely small horizontal emmitances and horizontal beta functions for both beams are required. The crossing angle of the SuperKEKB will be roughly four times as large as the angle of the present

KEKB and will contribute to reducing the beam overlap region. The beam energies will be less asymmetric after the upgrade, leading to a smaller Lorentz boost of 0.28.

The luminosity is mainly determined by the following three parameters: the beam current I, the vertical beam-beam parameter ξ_y and the vertical beta function β_y^* at the IP. To achieve the target luminosity the current will be increased by a factor of 2 while the beta function will be decreased by a factor of 20 according to the Nano-Beam scheme. The essential parameters of the KEKB and the SuperKEKB accelerators are summarised and compared in table 3.2.

	KEKB achieved	SuperKEKB
Energy (GeV) (LER/HER)	3.5/8.0	4.0/7.0
Crossing angle	22 mrad	83 mrad
ξ_y	0.129/0.090	0.090/0.088
β_y^* (mm)	5.9/5.9	0.27/0.41
I (A)	1.64/1.19	2.60/2.62
Luminosity $10^{34}\mathrm{cm}^{-2}\mathrm{s}^{-1}$	2.11	80

Table 3.2.: Main parameters of the SuperKEKB and the present KEKB accelerator [26].

3.3. The Belle detector

The Belle detector is a multi-purpose particle detector around the sole interaction point of the KEKB accelerator. It was designed to perform CP violation and rare B decay measurements with high precision. It is a large solid-angle magnetic spectrometer and its task is to detect the visible final state particles produced in the e^+e^- collisions at the interaction point. These particles are:

Charged particles: $K^\pm$, $\pi^\pm$, $e^\pm$, $p^\pm$, $\mu^\pm$

Neutral particles: γ, K_0^L

It is important to detect and identify these particles with high efficiency, since a B meson will usually decay to some combination of these final state particles. The detector consists of several subdetectors, the combination of the information obtained from them allows the reconstruction of the whole collision event. A schematic view of the detector is shown in fig. 3.5 and fig. 3.6. The detector components are described in more details in the following.

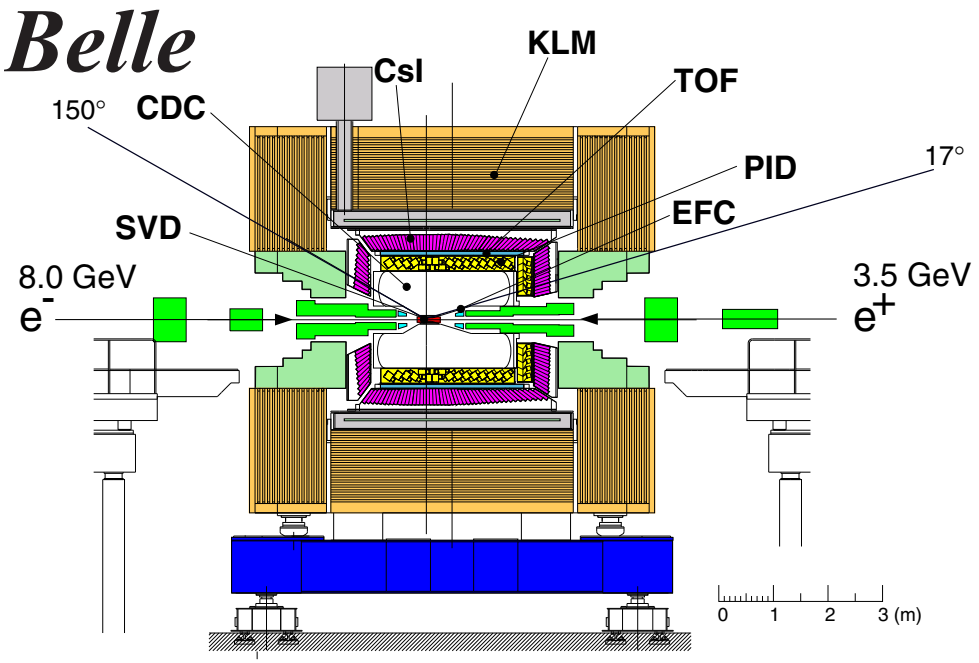

Figure 3.5.: Overview of the Belle detector and its components. (Taken from [25]).

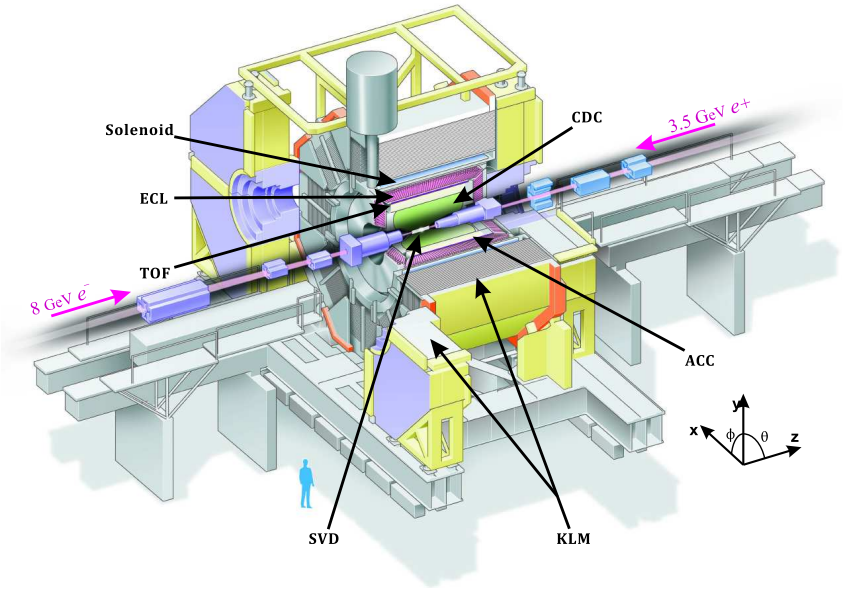

Figure 3.6.: Overview of the Belle detector and its components in a three dimensional perspective. (Taken from [25]).

3.3.1. Beam pipe

A cylindrical dual layer beryllium beam pipe encloses the interaction region. It is the first amount of material through which particles must go before reaching the detector. To reduce Coulomb scattering which affects the particle trajectory, it is important to choose a thin material with low atomic number. To prevent overheating induced by the beam, Helium flows through the gap between the cylinders and acts as coolant. The total thickness of the beam pipe corresponds to 0.9% of a radiation length. A schematic view of the beam pipe is shown in fig. 3.7.

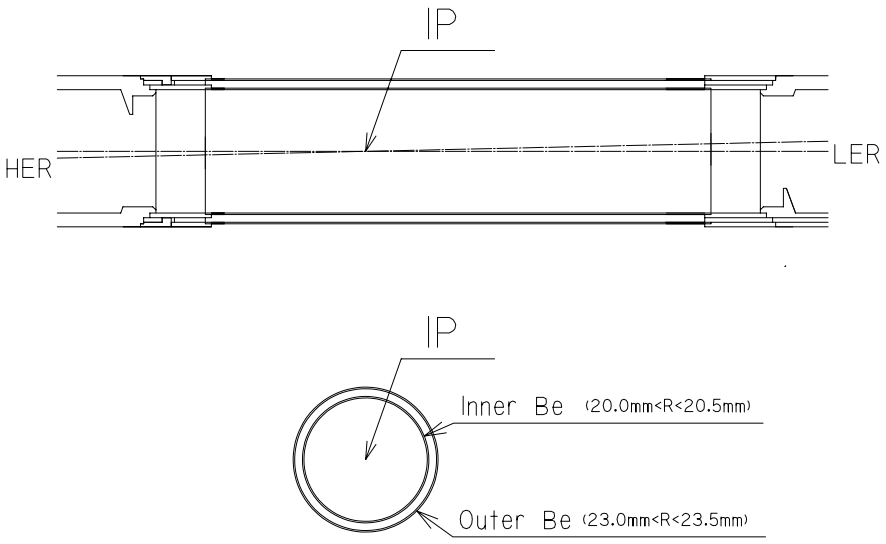

Figure 3.7.: Side view and the cross-section of the Belle beam pipe. (Taken from [25]).

3.3.2. Silicon Vertex Detector (SVD)

The Silicon Vertex Detector is the innermost detector in Belle and responsible for precise measurements of B meson decay vertex position. This is crucial for observation of time-dependent CP violation, which was one of the main objectives of the Belle experiment. The SVD consists of three concentric layers of silicon sensors and covers a polar angle of $23° < \theta < 139°$. The geometrical configuration is illustrated in fig. 3.8. On each layer ladders consisting of double sided silicon strip detectors (DSSD) are mounted. Each ladder is made of two half-ladders that are joined by a support structure, but are electrically independent of each other. The DSDS's are 300μm thick and provide depleted pn-junctions. When a charged particle passes the junction, it creates electron-hole pairs. The produced

electrons and holes drift to the corresponding n^+ or p^+ strips on the surface of the DSSD. The p^+-stripes are aligned along the beam axis and allow the measurement of the z position. The n^+-stripes are aligned perpendicular to the beam axis, thus measuring the $r\phi$ position.

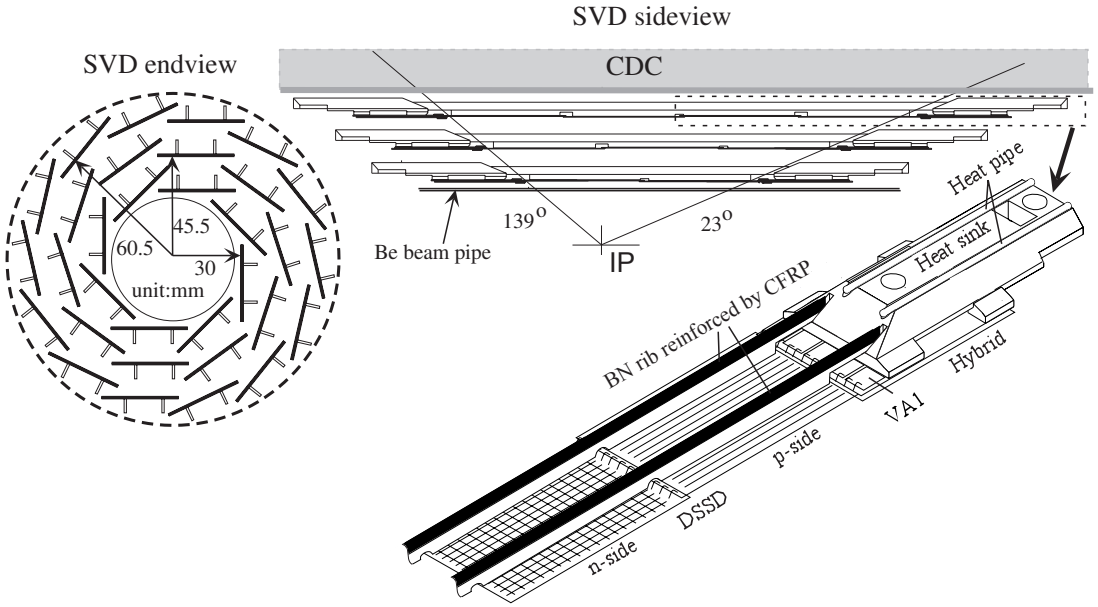

Figure 3.8.: Geometrical configuration of the SVD1. (Taken from [25]).

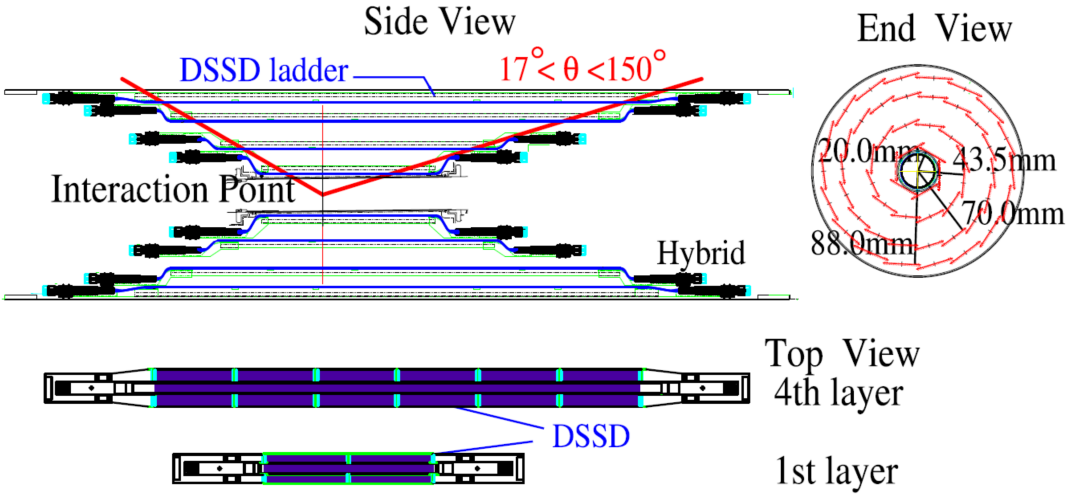

Figure 3.9.: Geometrical configuration of the SVD2. (Taken from [32]).

The initial SVD, SVD1, operated from 1999 to 2003. After 152×10^6 $B\bar{B}$ pairs were accumulated, a redesigned improved SVD was installed: SVD2. During this upgrade the innermost layer was moved 1.0 cm closer to the IP, a fourth layer was added and the geometry acceptance was increased to $17° < \theta < 150°$. A schematic view of SVD2 is shown in fig. 3.9.

The performance of the SVD can be estimated through impact parameter resolution. The impact parameter is the distance of closest approach to the IP. Usually two impact parameters are quoted: one in the $r\phi$ plane ($\sigma_{r\phi}$) and one in z direction (σ_z). The resolution of the impact parameters depends on track momentum (p) and polar angle (θ) and can be expressed as:

$$\text{SVD1: } \sigma_{r\phi} = 19.2 \oplus \frac{54}{p\beta \sin^{3/2}\theta}\ \mu\text{m}, \quad \sigma_z = 42.2 \oplus \frac{44.3}{p\beta \sin^{5/2}\theta}\ \mu\text{m} \quad ,$$
$$\text{SVD2: } \sigma_{r\phi} = 21.9 \oplus \frac{35.5}{p\beta \sin^{3/2}\theta}\ \mu\text{m}, \quad \sigma_z = 27.8 \oplus \frac{31.9}{p\beta \sin^{5/2}\theta}\ \mu\text{m} \quad .$$

The term in the denominator is also denoted as pseudomomentum and $\oplus$ indicates a quadratic sum. Fig. 3.10 shows the dependence of the impact parameters on pseudomomentum.

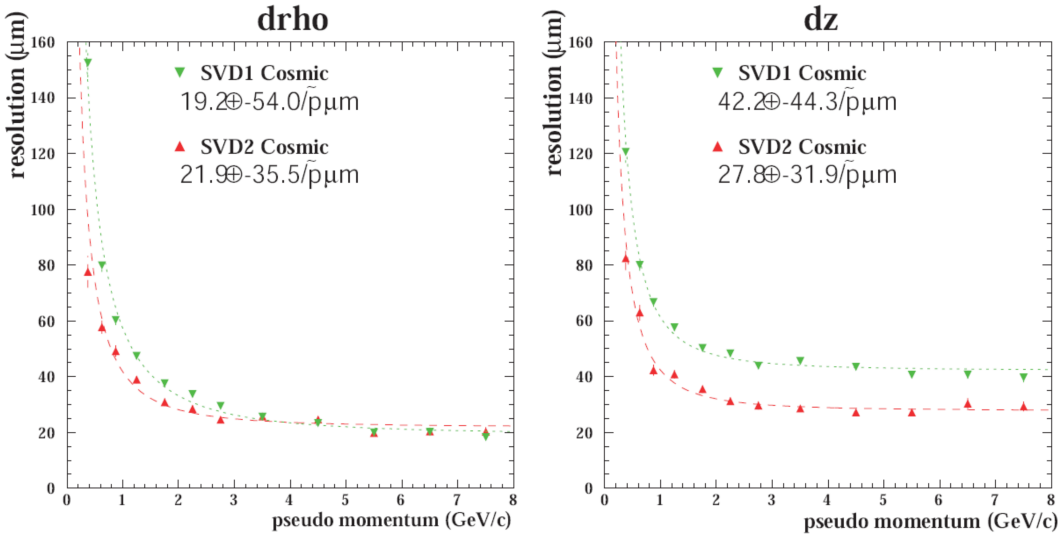

Figure 3.10.: Impact parameter resolution of charged tracks with associated SVD hits from cosmic ray data for SVD1 and SVD2. In the left plot the $\sigma_{r\phi}$ parameter is shown and in the right plot the σ_z parameter. (Taken from [32].)

3.3.3. Central Drift Chamber (CDC)

The Belle Central Drift Chamber provides measurements of the trajectories of charged particles. The track momenta are measured from their curvatures in the magnetic field induced by the superconducting solenoid magnet around the drift chamber. The CDC also measures dE/dx, specific energy loss by ionisation, of charged tracks, to provide particle identification information. In a constant magnetic field the path of the charged particle can be described by a helix which is defined by five parameters. This will be described in more detail in section 7.5.

- **Working principle**

  A charged particle travelling through matter interacts with electrons and nuclei of the material. The fundamental effect for the function of a drift chamber is the energy loss of charged particles in matter. During its passage the particle ionises the atoms of the material and creates electron-ion pairs. In a static electric field the electrons will drift to the positively charged anode, while the positive ions will move to the negatively charged cathode. Because of different masses, electrons and ions have a different drift velocity: electrons are lighter and thus faster than ions. The value of the drift velocity depends on the field strength, the property of the matter molecules, density and temperature. In a presence of a high electric field, the electrons can be accelerated to have enough energy to cause a secondary ionisation which can lead to a cascade of charge.

  This ionisation effect is used to detect charged particles. The original principle of a proportional counter consists of a wire under high voltage enclosed in a tube filled with a certain gas mixture. The charged particle will ionise gas atoms while passing through the tube. The created electrons and ions are accelerated by the electric field around the wire, leading to an ionisation cascade which is collected on the wire. The resulting current, which can be measured on the wire, is proportional to the energy of the ionising particle.

  By placing a number of anode wires between two cathode planes one can realise a multi-wire proportional chamber, where each anode wire is acting as a proportional counter described above. The spatial resolution of particle trajectories is determined by the spacing of the anode wires. To increase the accuracy of the track reconstruction one can measure the drift time of the electrons in the gas. To determine the exact time at which the charged particle passes through, an external timing signal from another subdetector is required. A schematic display of a track trajectory and drift length circles is shown in fig. 3.11. A detailed explanation about

working principles of drift chambers can be found in [33].

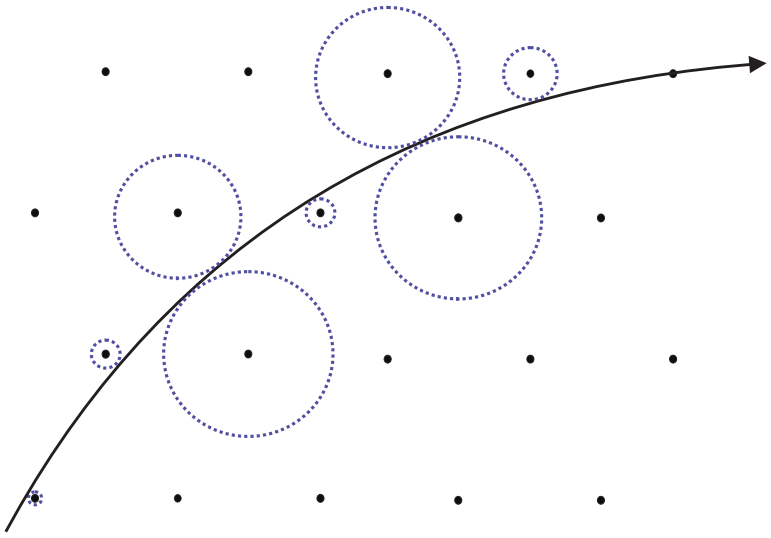

Figure 3.11.: A schematic view of a particle passing through a drift chamber. The dashed lines show the drift length circles around the wires.

The Belle CDC consists of 50 layers of anode wires and 3 cathode strip layers, resulting in 8400 drift cells. The CDC geometry is illustrated in fig. 3.12.

The gas mixture which is filling the CDC consists of 50% helium and 50% ethane. The low-Z gas mixture was chosen to minimise multiple Coulomb scattering in order to ensure a good momentum resolution, especially for low momentum tracks.

The p_T resolution of the Belle CDC is given by:

$$\sigma(p_T) = \left(0.28 p_T \oplus \frac{0.35}{\beta}\right)\% \quad .$$

If information of the SVD and the CDC is combined the p_T resolution improves to:

$$\sigma(p_T) = \left(0.19 p_T \oplus \frac{0.30}{\beta}\right)\% \quad .$$

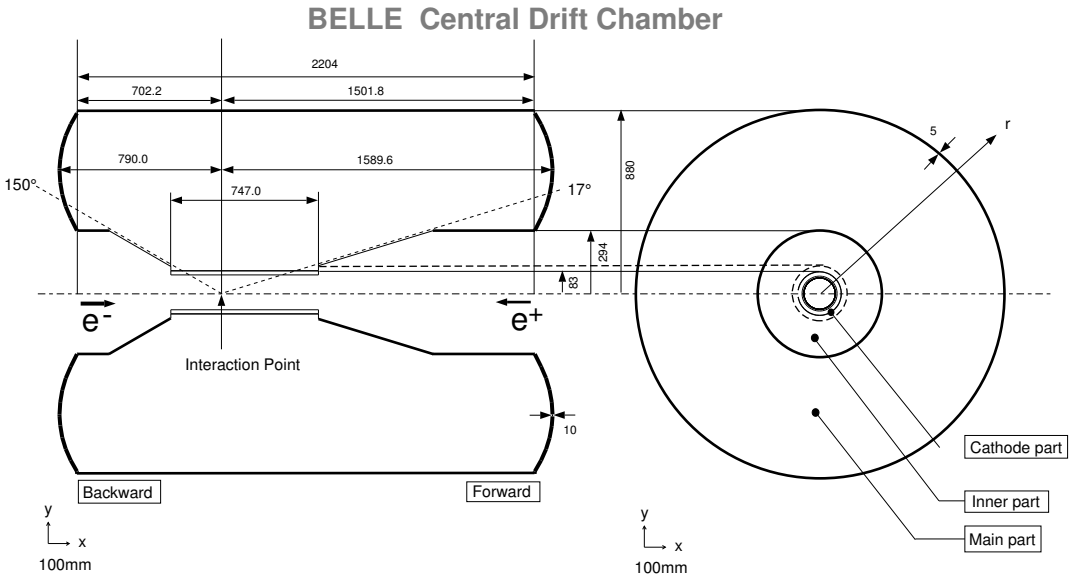

Figure 3.12.: Geometrical configuration of Belle CDC. (Taken from [25]).

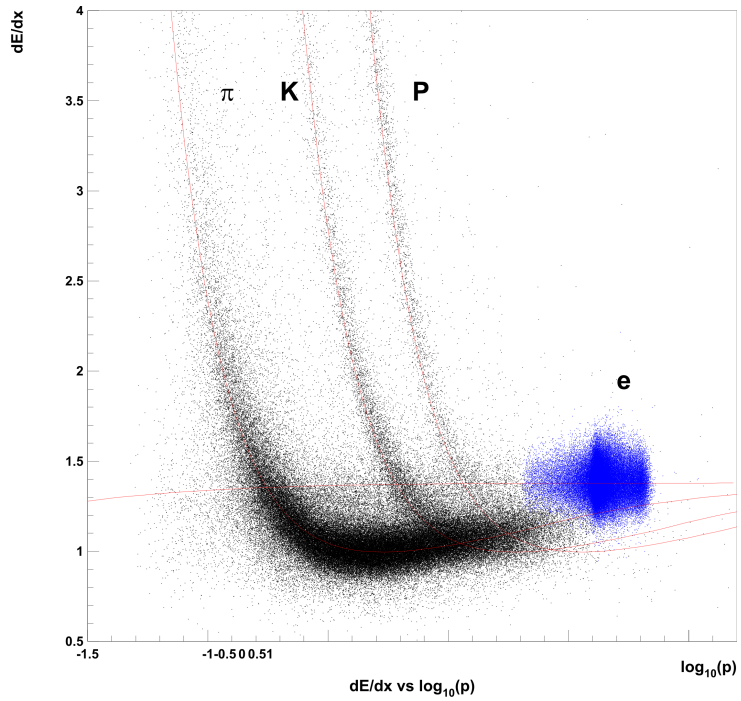

Figure 3.13.: Truncated mean of dE/dx over particle momentum obtained from collision data. (Taken from [25]).

CDC signals are also used to determine the specific energy loss dE/dx of charged particles. A plot of measured dE/dx values as a function of particle momentum is shown in fig. 3.13. To estimate the most probable energy loss the truncated-mean method was used: the largest 20% of measured dE/dx values for each track were discarded and the remaining data was averaged. As the energy loss is dependent on the mass of the particles, the characteristics of the dE/dx curve can be used to perform particle identification.

3.3.4. Aerogel Čerenkov Counter system (ACC)

The purpose of the Aerogel Čerenkov Counter is to provide particle identification information in order to distinguish between $K^{\pm}$ and $\pi^{\pm}$ in the high momentum range of 1.0 to 4.0 GeV/c. In this way the particle identification is extended beyond the momentum coverage of dE/dx measurements by CDC and time-of-flight measurements by the Time-Of-Flight detector (TOF).

When the velocity of a charged particle in a medium exceeds speed of light, Čerenkov radiation is emitted. To emit Čerenkov radiation the refractive index of the material has to satisfy the following condition:

$$n > \frac{1}{\beta} = \sqrt{1 + \left(\frac{m}{p}\right)^2} \quad , \tag{3.1}$$

where m and p are the mass and momentum of the particle, respectively. By selecting an appropriate material in which pions will emit Čerenkov light, but heavier kaons will not, one can distinguish between them. The ACC is a threshold counter and cannot image the Čerenkov angle.

The Belle ACC is divided into a barrel region and a forward endcap. A geometrical overview is shown in fig. 3.14. The barrel consists of 960 counter modules separated into sets of 60 in the ϕ direction. 228 modules arranged in 5 concentric layers build the forward endcap. Each counter is arranged in such a way that it points towards the interaction region. A counter module consists of silica aerogel encased in an aluminium box of $12 \times 12 \times 12$ cm^3 in size. The refractive indices of the silica aerogel blocks, which ensure a good $K^{\pm}/\pi^{\pm}$ separation, depend on the polar angle ($1.010 < n < 1.030$). The emitted pulses of Čerenkov light are detected with photomultiplier tubes.

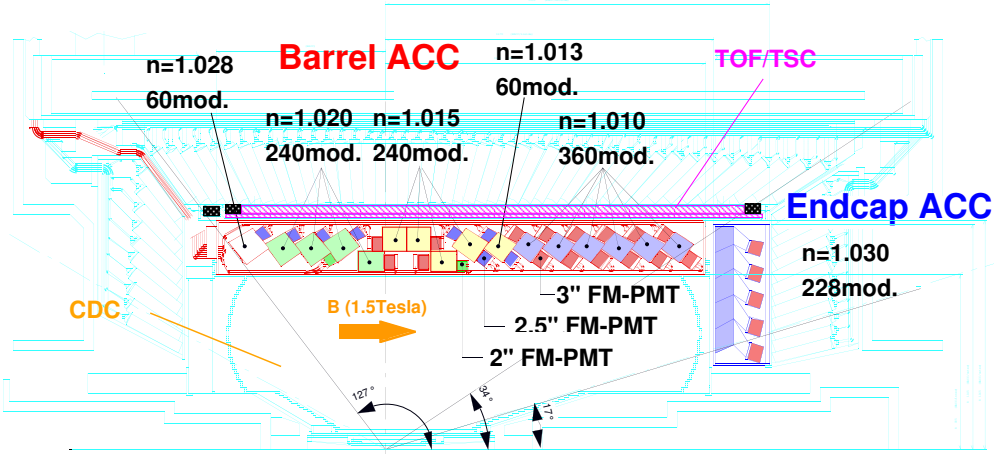

Figure 3.14.: The Belle ACC configuration. (Taken from [25]).

3.3.5. Time-Of-Flight counter (TOF)

The purpose of the Time of Flight Counter is to provide particle identification, especially to distinguish between $K^{\pm}$ and $\pi^{\pm}$ in the low momentum region below 1.2 GeV/c. The detector measures the time the particle travelled from the collision at the interaction point. Using the track momentum p and the flight length L, the particle mass m can be determined from the measured time-of-flight T:

$$m = \frac{p}{c}\sqrt{\left(\frac{cT}{L}\right)^2 - 1} \quad . \tag{3.2}$$

A TOF module consists of two TOF counters and one trigger scintillation counter (TSC) counter, a schematic view is shown in fig. 3.15. 64 TOF modules are located in the barrel region covering a polar angle of $34° < \theta < 120°$. The separation between kaons, pions and protons in the momentum region below 1.2 GeV/c provided by TOF is shown in fig. 3.16. Assuming a time resolution of 100 ps the data points are consistent with the simulation.

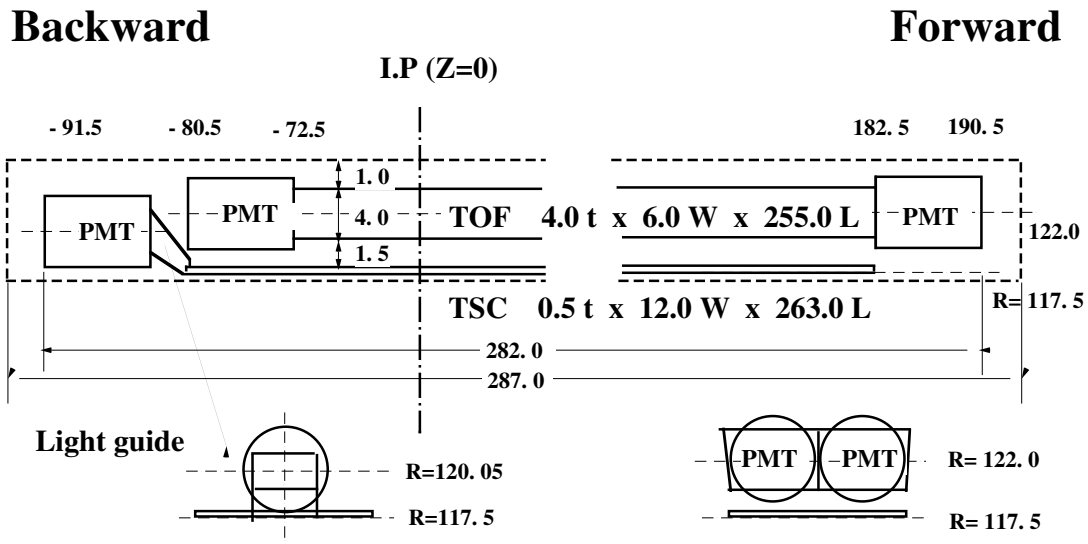

Figure 3.15.: The Configuration of a TOF module. (Taken from [25]).

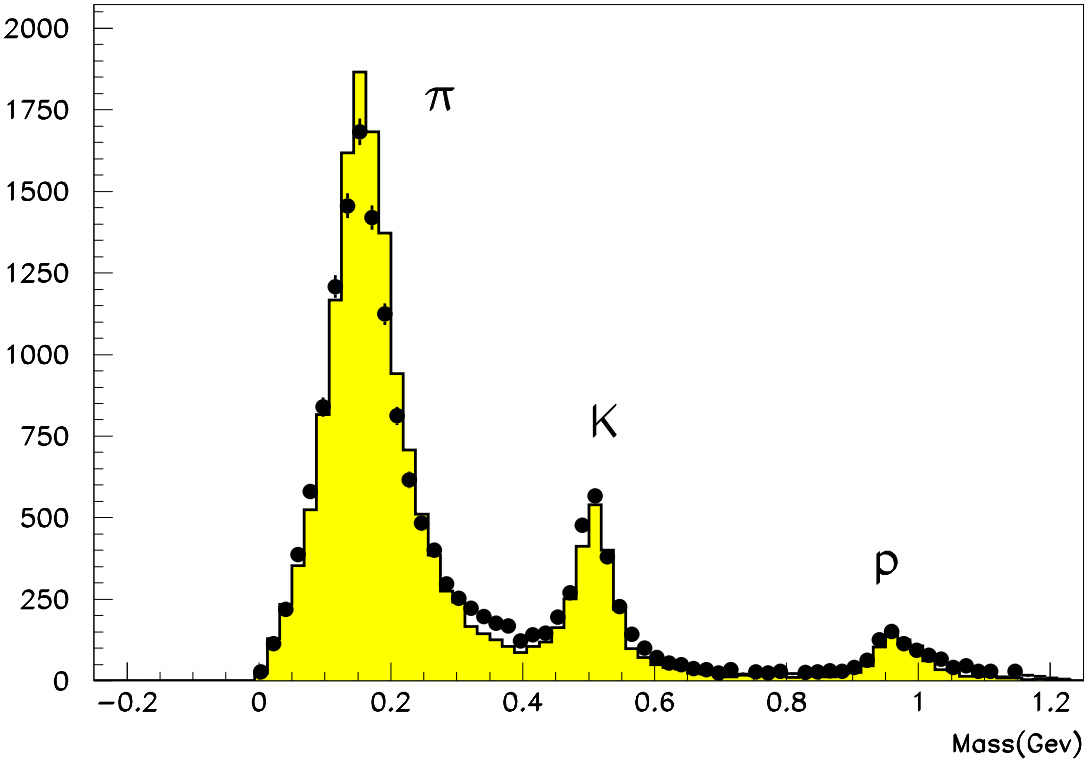

Figure 3.16.: Mass distribution obtained from TOF measurements (data points) in comparison with Monte Carlo simulation (yellow filled histogram). (Taken from [25]).

3.3.6. Electromagnetic Calorimeter (ECL)

The Electromagnetic Calorimeter measures electromagnetic showers caused by electrons and photons. The ECL consists of 8736 thallium-doped (Tl) CsI crystal counters. Each CsI(Tl) crystal is arranged so that it points towards the IP. The barrel component has 6624 crystals divided into 46 sections in θ and 144 sections in ϕ. The forward (backward) endcap has 1152 (960) crystals divided into 13 (10) sections in θ and $48-144$ $(64-144)$ sections in ϕ depending on θ. The ECL covers a polar angle of $12° < \theta < 155°$. The geometry of the ECL is illustrated in fig. 3.17.

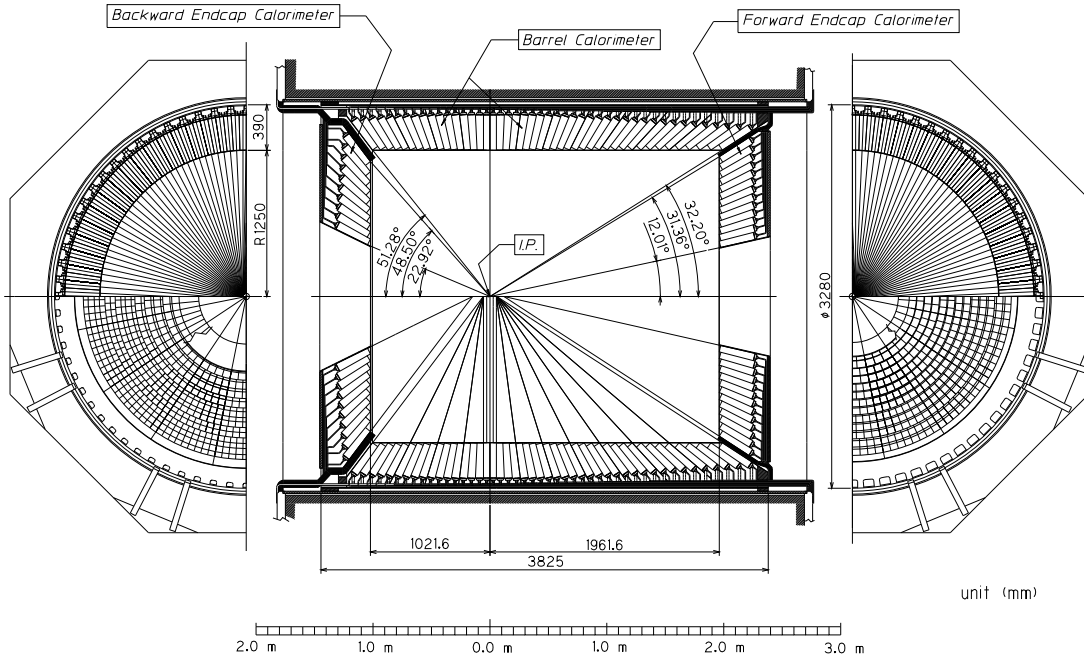

Figure 3.17.: The geometry of the Belle ECL. (Taken from [25]).

The energy resolution can be parametrised as:

$$\frac{\sigma_E}{E} = \left(1.34 \oplus \frac{0.066}{E} \oplus \frac{0.81}{E^{1/4}}\right)\% \quad ,$$

and the position resolution as

$$\sigma_{\mathrm{Pos}} = \left(0.27 + \frac{3.4}{E^{1/2}} + \frac{1.8}{E^{1/4}}\right) \mathrm{mm} \quad ,$$

where E is in units of GeV.

ECL can also perform electron identification. An electron deposits energy in ECL through bremsstrahlung and pair production. Other charged particles, like $K^{\pm}$ or $\pi^{\pm}$, deposit a much smaller amount of energy by ionisation.

3.3.7. Extreme Forward Calorimeter (EFC)

To extend the polar coverage of the energy measurement, additional crystal calorimeters are installed in the angular range of $6.4° < \theta < 11.5°$ and $163.3° < \theta < 171.2°$ to cover the forward and backward regions, respectively. As in this region the radiation is higher, another radiation hard crystal type, Bismuth Germanate ($Bi_4Ge_3O_{12}$) was chosen. Forward and backward part of the EFC are composed of 32 segments in the ϕ- and 5 segments in the θ-direction.

3.3.8. Detector solenoid

The superconducting solenoid provides a magnetic field of 1.5 T. It covers all detector components except the KLM and bends the trajectories of charged particles, thus allowing the track momentum measurement in the CDC. The superconducting coil consists of a single layer niobium-titanium-copper alloy embedded in a high purity aluminium stabiliser. The coil is wound around the inner surface of an aluminium support cylinder of 3.4 m diameter and 4.4 m in length. Cooling is provided by circulating liquid helium through a tube on the inner surface of the aluminium cylinder. Fig. 3.18 illustrates the layout of the superconducting solenoid.

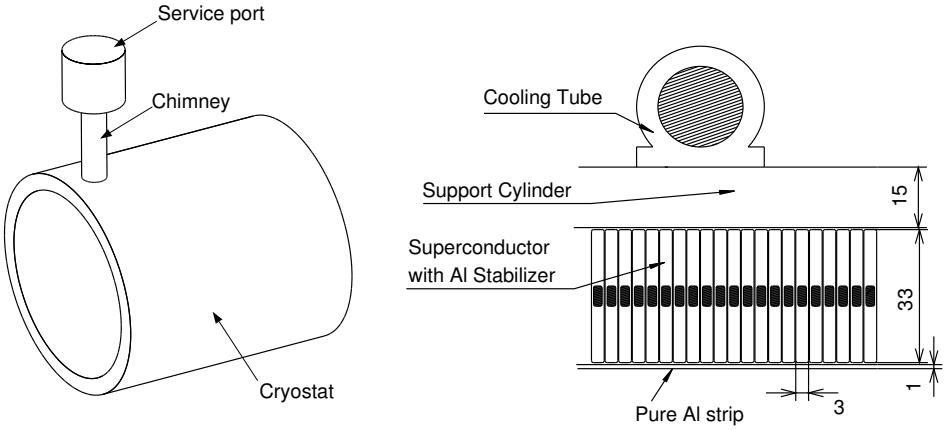

(a) Outlook of the magnet

(b) Cross sectional view of the coil

Figure 3.18.: The geometry of the superconducting solenoid. (Taken from [25]).

3.3.9. K_L and Muon detector system (KLM)

The K_L^0 and Muon Detector provides identification of long-living, highly penetrative particles, such as $\mu^{\pm}$ and K_L^0.

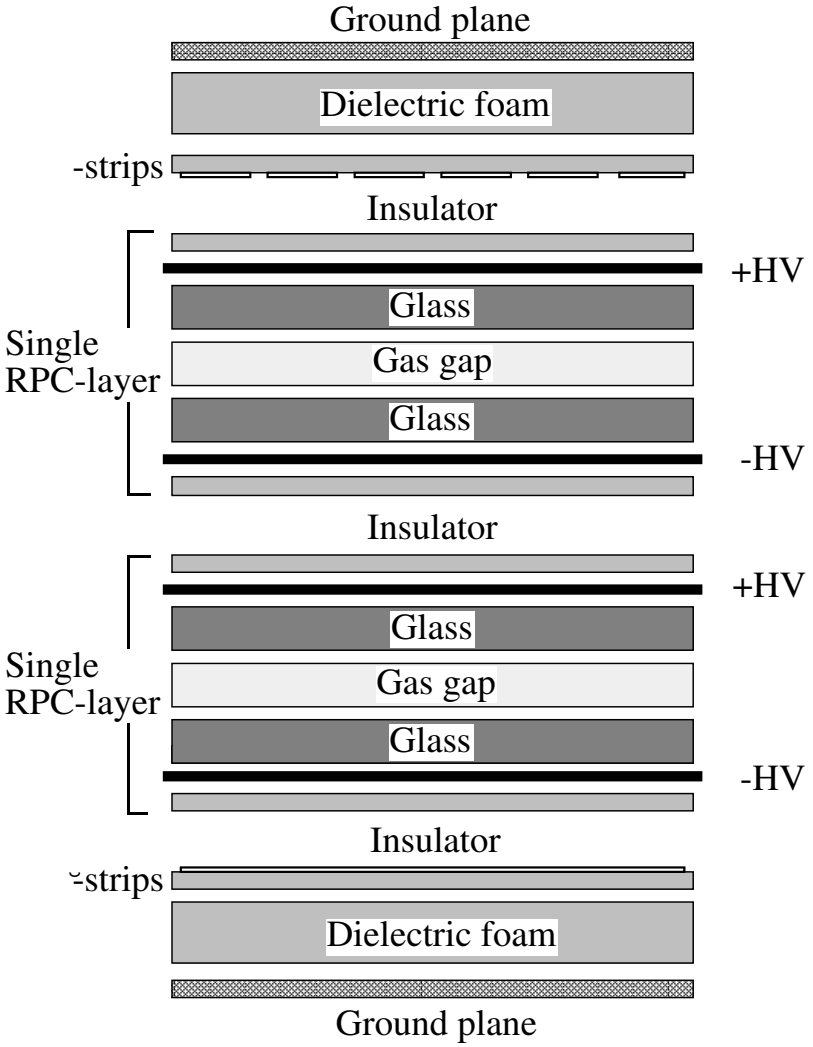

Figure 3.19.: The cross section of a RPC superlayer. (Taken from [25]).

The KLM is build of alternating layers of charged particle detectors and 4.7 cm thick iron plates. The polar region of $20° < \theta < 155°$ is covered with 15 resistive plate counter

(RPC) superlayers and 14 iron layers in the barrel region, and 14 RPC superlayers in each endcap. The iron layers also serve as a return yoke for the magnetic flux provided by the superconducting solenoid. The structure of a RPC superlayer is shown in fig. 3.19.

When hadrons interact with the iron plates, they produce a shower of ionising particles, that can be detected by the RPC layers. A K_L^0 candidate can be identified through a KLM cluster without an associated track in the CDC. Muons can be identified through the absence of strong interaction. Hadrons are rapidly absorbed by the iron layers, while muons produce only thin clusters in the KLM and have a greater penetration depth.

3.4. The Belle II detector

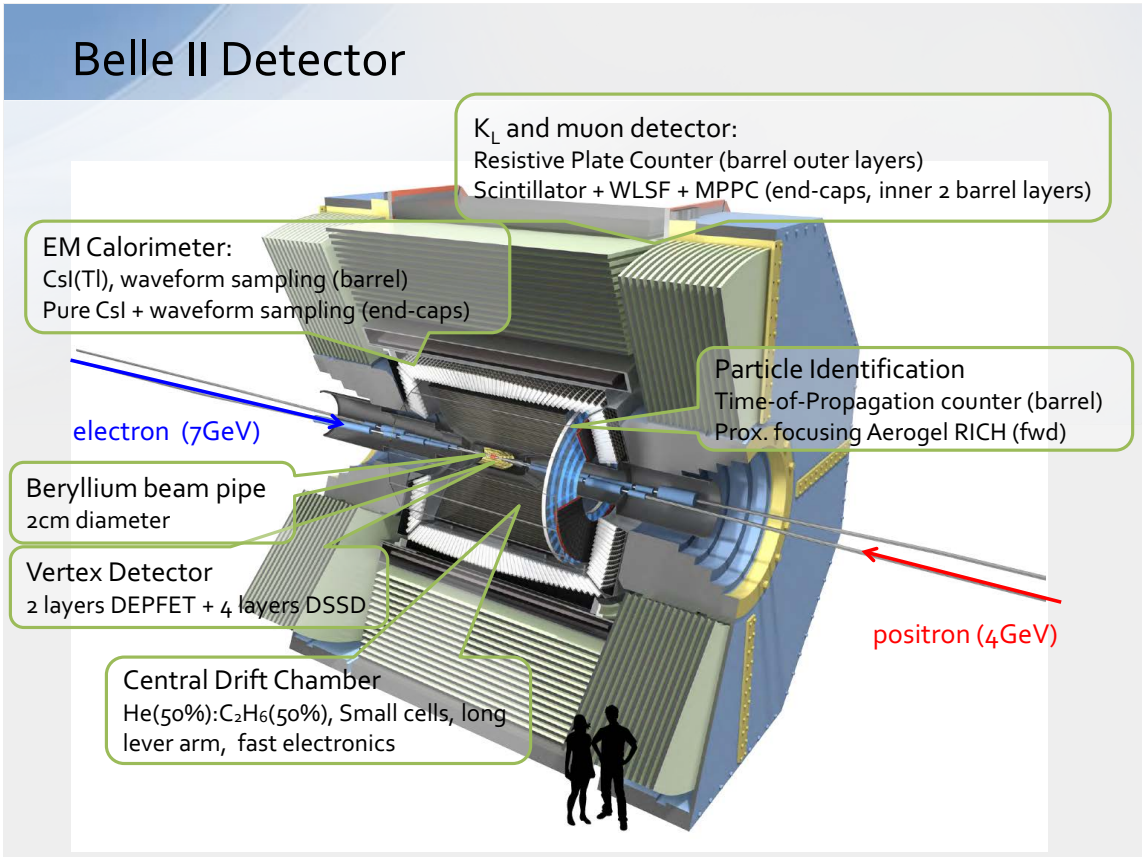

Figure 3.20.: A three dimensional layout of the BelleII detector with the description of the main features of the subdetectors [34] .

During the transition from the Belle to the Belle II detector, new detector components will be added and several subdetectors will be upgraded. An overview of the Belle II detector is shown in fig. 3.20, the changes of the particular subdetectors compared to the Belle experiment are described in the following sections.

3.4.1. Beam pipe

The Belle II beam pipe will be of a very similar design as the Belle beam pipe, but with a smaller outer radius of about 10 mm. Due to increased beam-induced background the cooling of the beam pipe gains on importance. A paraffin liquid $C_{10}H_{22}$ will be used as coolant between the cylinders to keep the temperature below 10°C.

3.4.2. Pixel Detector (PXD)

The pixel detector was not present in the Belle experiment, but will be an important component of the Belle II detector. Due to a smaller beam pipe radius the vertex reconstruction can be improved by moving the innermost detector closer to the interaction point. To operate a detector so close to the interaction point is however very challenging, as the background increases strongly with smaller radius. The occupancy of a silicon strip detector would be too high under these conditions. Pixel sensors have a larger number of channels, and therefore a much smaller occupancy. To keep the material budget low the innermost sensor layers should also be very thin.

The Belle II PXD will consist of two layers of DEPFET pixel sensors. A schematic view is shown in fig. 3.21. The DEPFET (Depleted Field Effect Transistor) is a semiconductor based detector that combines detection and amplification within one device. The working principle is illustrated in the sensor cross section shown in fig. 3.22. Incident particles create electron-hole pairs in the fully depleted silicon bulk, and the resulting electrons are accumulated at the internal gate. The current through the p-channel MOSFET integrated onto the silicon is modulated through the collected electrons. Due to this monolithic structure the amplification of the charge occurs very close to its generation without transfer losses. Another important feature of DEPFETs is a very low noise performance even at room temperature due to the very small capacitance of the internal gate.

No support structure or cooling material within the active region of the detector will be necessary for the operation of the PXD. The sensors will be only 75μm thick, while retaining a high signal to noise ratio. The small pixel size should limit the background occupancy to $1 - 2\%$. The resulting high data volume is addressed via several data reduction methods which are currently being studied.

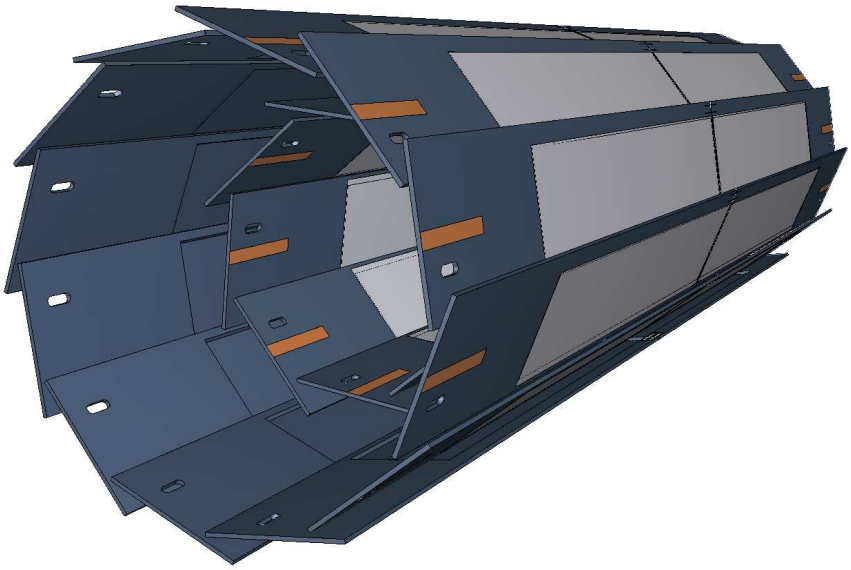

Figure 3.21.: Schematic view of the geometrical arrangement of the sensors for the PXD. The light grey surfaces are the sensitive DEPFET pixels, which are thinned to 75 microns and cover the entire acceptance of the tracker system. (Taken from [26]).

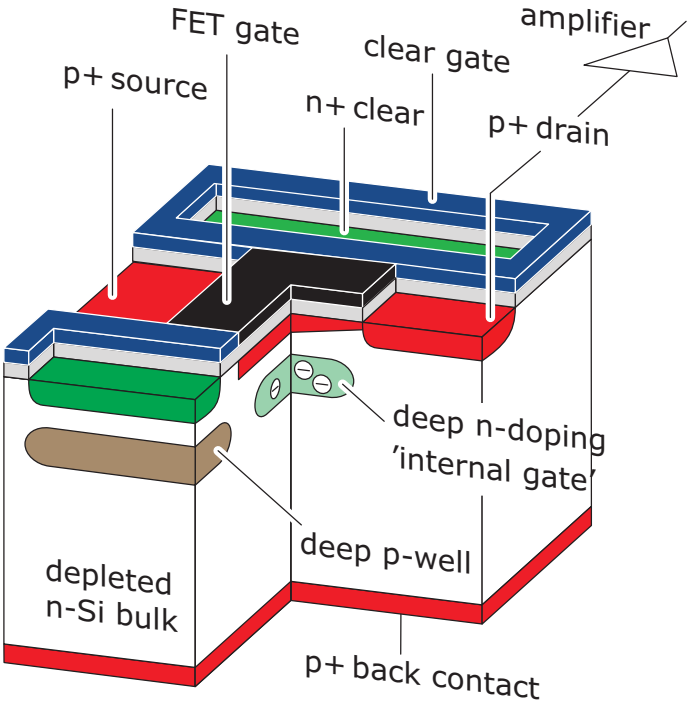

Figure 3.22.: Operating principle of a DEPFET. (Taken from [26]).

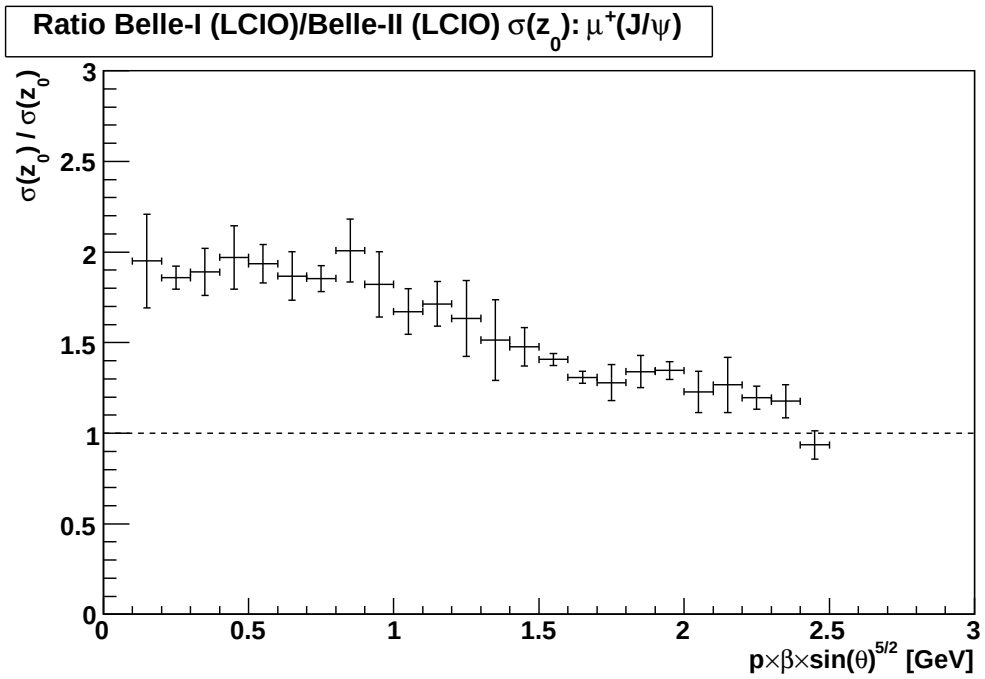

Figure 3.23.: Belle over Belle II ratio of the z_0 track impact parameter resolutions as function of the pseudo-momentum, $p\beta \sin^{5/2}\theta$. At low momenta, the impact parameter resolution of Belle II is about twice as good as that of Belle. (Taken from [26]).

Simulation studies to evaluate the performance showed a resolution improvement of factor 2 compared to the Belle performance for low momentum tracks. Belle over Belle II ratio of the z_0 track impact parameter resolution is shown in fig. 3.23.

3.4.3. Silicon Vertex Detector (SVD)

Due to the pixel detector, the Belle II silicon strip detector will be moved further outside, providing better reconstruction for particles with short flight length (K_s^0, low momentum tracks). Otherwise the design of the Belle II SVD follows in generally its predecessor, the SVD2 of the Belle experiment.

The Belle II SVD consists of 4 layers, with the inner radius of 38 mm and the outer radius of 140 mm. The polar angular acceptance ranges from 17° to 150°. To increase the radial coverage without significantly increasing the number of sensors, slanted sensors are used in the forward region. The SVD layout is shown in fig. 3.24.

Similar technology as in the Belle detector is used for the double sided silicon strip sensors building the detector layers. The mechanical structure and the cooling circuit are optimised in order to reduce the material budget. The readout will have a much shorter

shaping time compared to the Belle SVD due to APV25 chips, making the detector less prone to the increasing background.

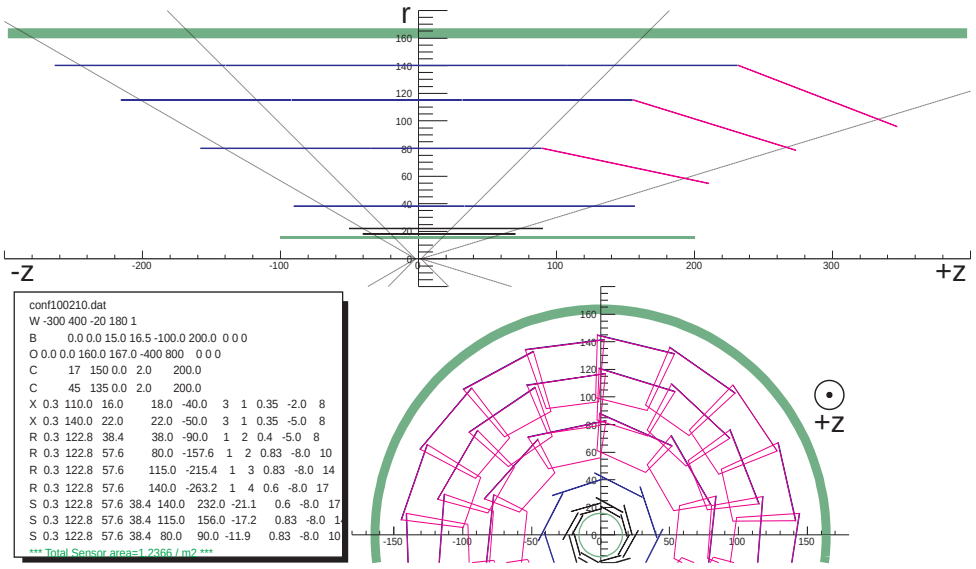

Figure 3.24.: Configuration of the four SVD layers, with slanted sensors in the forward region, and the two PXD layers. All dimensions are in mm. (Taken from [26]).

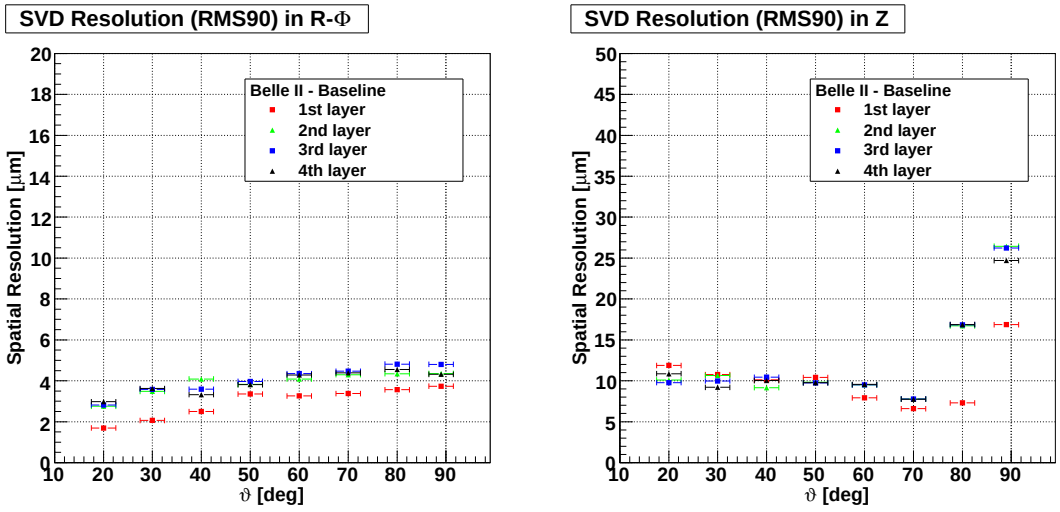

(a) $r\phi$ direction

(b) z direction

Figure 3.25.: Expected intrinsic resolution in $r\phi$ and z direction for 0.5 GeV single muons. (Taken from [26]).

The expected performance was studied in simulations and the expected intrinsic SVD resolutions in $r\phi$ and z directions are shown in fig. 3.25.

3.4.4. Central Drift Chamber (CDC)

As the Belle CDC has fulfilled all the expectations during the ten years of data taking, the Belle II CDC will keep the same main structure.

	Belle	Belle II
Radius of inner cylinder (mm)	77	160
Radius of outer cylinder (mm)	880	1130
Radius of innermost sense wire (mm)	88	168
Radius of outermost sense wire (mm)	863	1111.4
Number of layers	50	56
Number of sense wires	8,400	14,336
Gas	He–C_2H_6	He–C_2H_6
Diameter of sense wire (μm)	30	30

Table 3.3.: Main parameters of the Belle CDC and the CDC upgrade for Belle II [26].

A new readout electronics system with new ASIC chips will be updated to handle higher trigger rates with less dead time. Due to increased number of layers in the inner detectors the inner cylinder of the CDC is moved outwards. As the outer detectors will be more compact than in the Belle experiment, the outer radius of the CDC will increase, thus allowing a longer ladder arm for tracking. The drift chamber is build of 14336 wires which are arranged in 56 layers. The same gas mixture as in the Belle detector (50% helium and 50% ethane) is used. A summary of main parameters can be found in table 3.3 and the layout of the CDC structure is shown in fig. 3.26.

Each six layers with the same orientation are grouped into superlayers. The innermost superlayer has two additional layers to cope with high occupancy from beam induced backgrounds. The layers which are parallel to the z axis are denoted as axial (A) layers, while the layers arranged under a small angle to the z axis are referred to as stereo layers (U or V). So in total the 56 layers are grouped into 9 superlayers with a configuration AUAVAUAVA. The wire configurations and the stereo angles are summarised in table 3.4. The comparison of the wire spacing and cell size between the Belle and Belle II drift chambers can be seen in fig. 3.27.

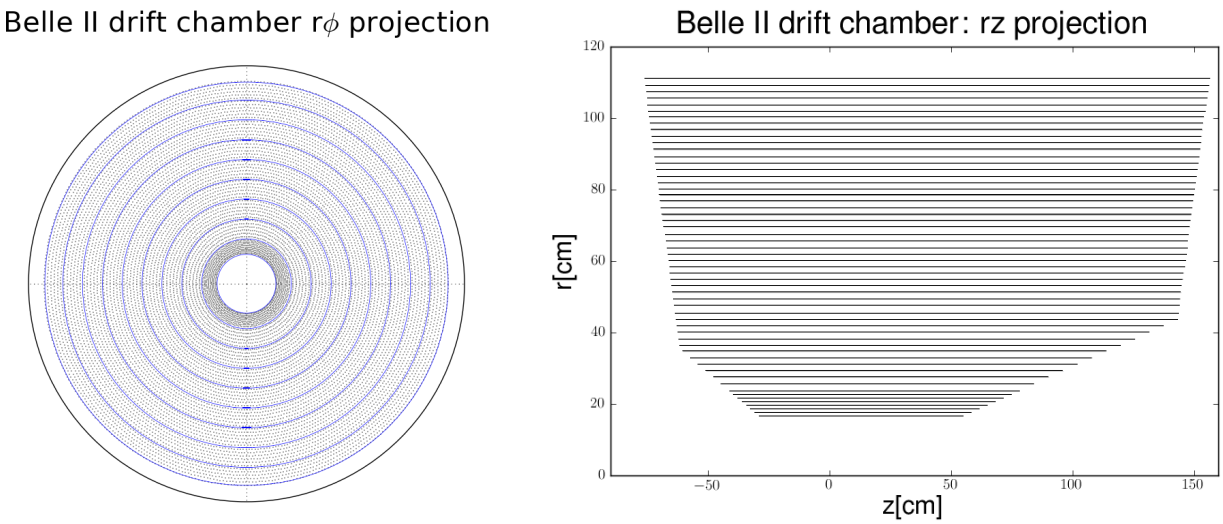

(a) $r\phi$ view (b) rz view

Figure 3.26.: Layout of the Belle II drift chamber.

superlayer type and No.	No. of layers	Signal cells per layer	radius (mm)	Stereo angle (mrad)
Axial 1	8	160	168.0 – 238.0	0.
Stereo U 2	6	160	257.0 – 348.0	45.4 – 45.8
Axial 3	6	192	365.2 – 455.7	0.
Stereo V 4	6	224	476.9 – 566.9	-55.3 – -64.3
Axial 5	6	256	584.1 – 674.1	0.
Stereo U 6	6	288	695.3 – 785.3	63.1 – 70.0
Axial 7	6	320	802.5 – 892.5	0.
Stereo V 8	6	352	913.7 – 1003.7	-68.5 – -74.0
Axial 9	6	384	1020.9 – 1111.4	0.

Table 3.4.: Configuration of the Belle II CDC sense wires [26].

The expected performance without background was studied in beam tests, the obtained position and energy loss resolutions are similar to or better than those achieved with the Belle CDC. As the larger beam background in Belle II might degrade the CDC tracking performance, the simulations including background are necessary and are ongoing.

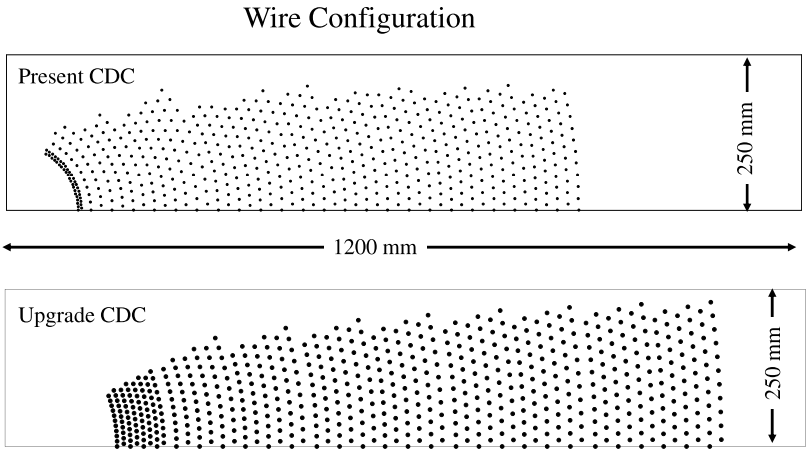

Figure 3.27.: Wire configuration of the Belle II CDC compared to the Belle CDC. (Taken from [26]).

3.4.5. Time-Of-Propagation counter (TOP)

The particle identification in the barrel region of the Belle II detector will be provided by a Time-Of-Propagation (TOP) counter, which will replace the TOF and the ACC subdetectors of the Belle experiment. TOP measures the time of propagation of the Čerenkov photons reflected inside a quartz radiator. Two coordinates (x, y) and a precise timing allow the reconstruction of the Čerenkov image. A schematic overview is shown in fig. 3.28.

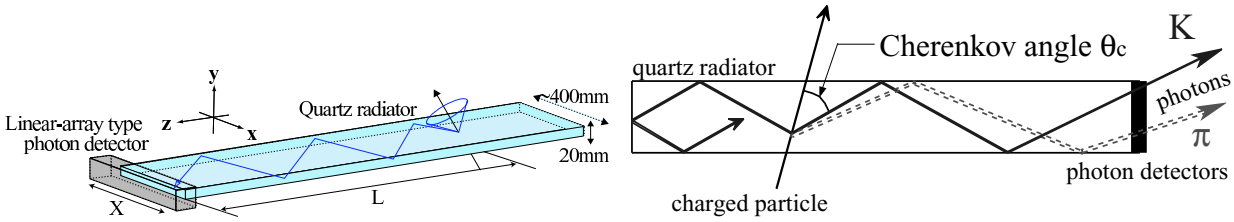

Figure 3.28.: Conceptual overview and schematic side-view of TOP counter and internal reflecting Čerenkov photons. (Taken from [26]).

The array of quartz bars will surround the outer wall of the CDC. As the existing Belle barrel ECL structure will be kept, the outer envelope of the TOP counter is fixed by the existing barrel ECL. A conceptual design is shown in fig 3.29. The TOP counter will have very fast readout electronics and will extend the range of a very good $K^{\pm}/\pi^{\pm}$ separation to the kinematical limits of the experiment. Several simulation studies using different setups were performed and lead to consistent results. An example of the $K/^{\pm}\pi^{\pm}$ separation is shown in fig. 3.30.

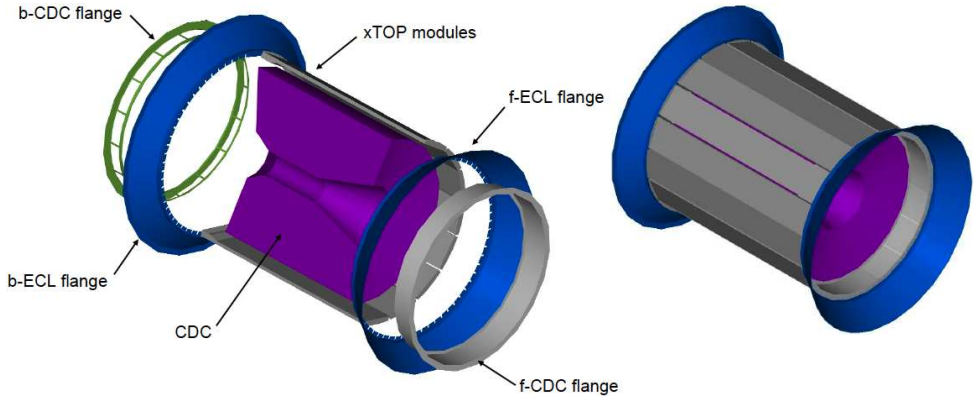

Figure 3.29.: A 3D conceptual rendering of the TOP detector integrated together with the CDC. f-ECL/b-ECL flange shows the structure of ECL conical part. f-CDC/b-CDC flange is the support of CDC from ECL flanges. (Taken from [26]).

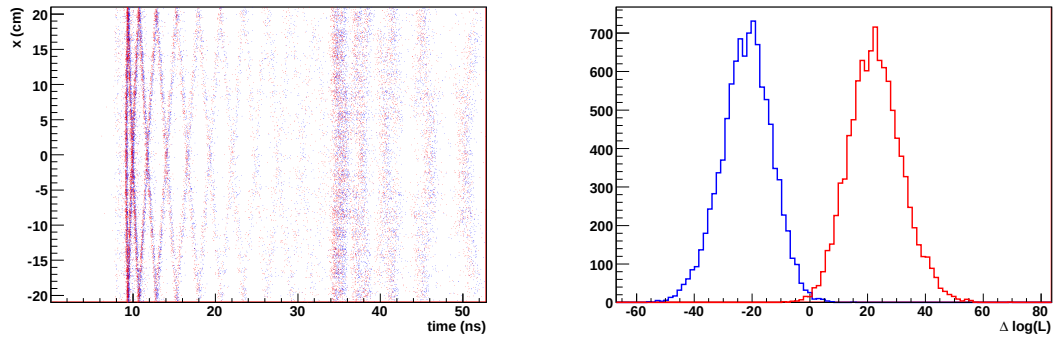

Figure 3.30.: (Left) Sample distributions for an ensemble of 500 tracks of detected photon positions, x, and times, t, for a 2-bar counter with 3 GeV/c pions (red) and kaons (blue) at normal incidence on the quartz bar. (Right) Distributions of $\Delta log(\mathcal{L})$ for pions (red) and kaons (blue), corresponding to the distributions on the left. (Taken from [26]).

3.4.6. Aerogel Ring-Imaging Čerenkov detector (ARICH)

The proximity-focusing Aerogel Ring-Imaging Čerenkov detector (ARICH) will provide particle identification in the forward endcap of the Belle II detector. It has been designed to separate kaons from pions over most of their momentum spectrum and to provide the discrimination between pions, muons and electrons below 1 GeV/c. The detector consist of an aerogel radiator, where Čerenkov photons are produced by charged particles and an array of sensitive photon detectors capable of detecting single photons with good resolution in two dimensions. The ARICH principle is schematically illustrated in fig. 3.31. The ARICH container consists of two cylinders, the tentative mechanical structure is shown in fig. 3.32.

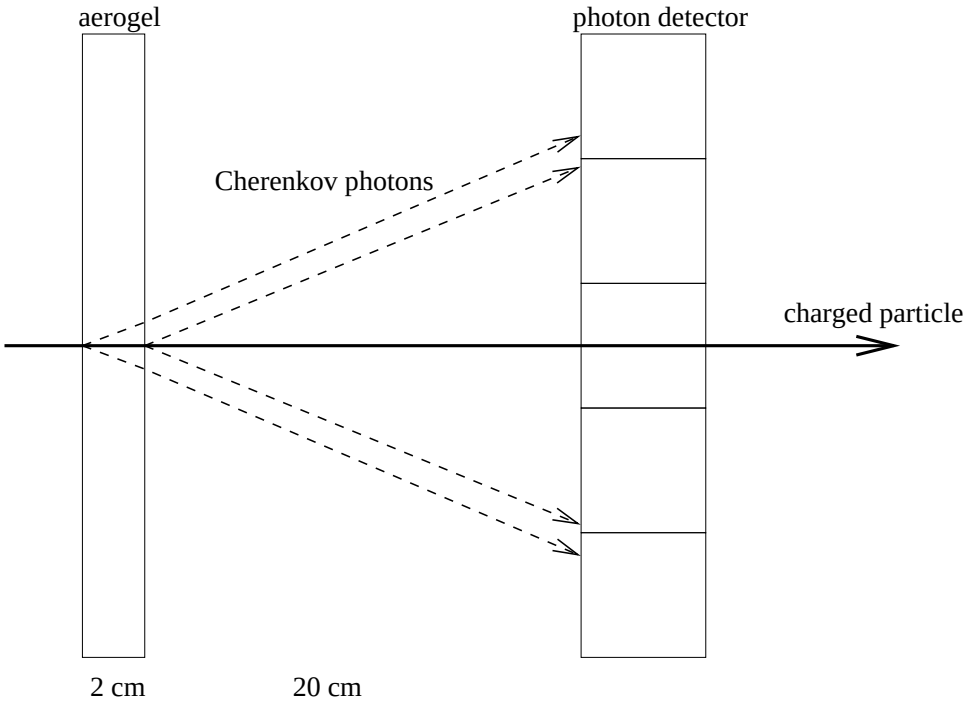

Figure 3.31.: Proximity focusing ARICH-principle [26].

The expected average number of detected Čerenkov photons is 20 and the resolution of the Čerenkov angle was found to be 3.1 mrad. This would lead to a better than 5σ $\pi^{\pm}/K^{\pm}$ separation at the kinematic limit of 4 GeV/c and a 4σ $\pi^{\pm}/e^{\pm}$ separation up to 1 GeV.

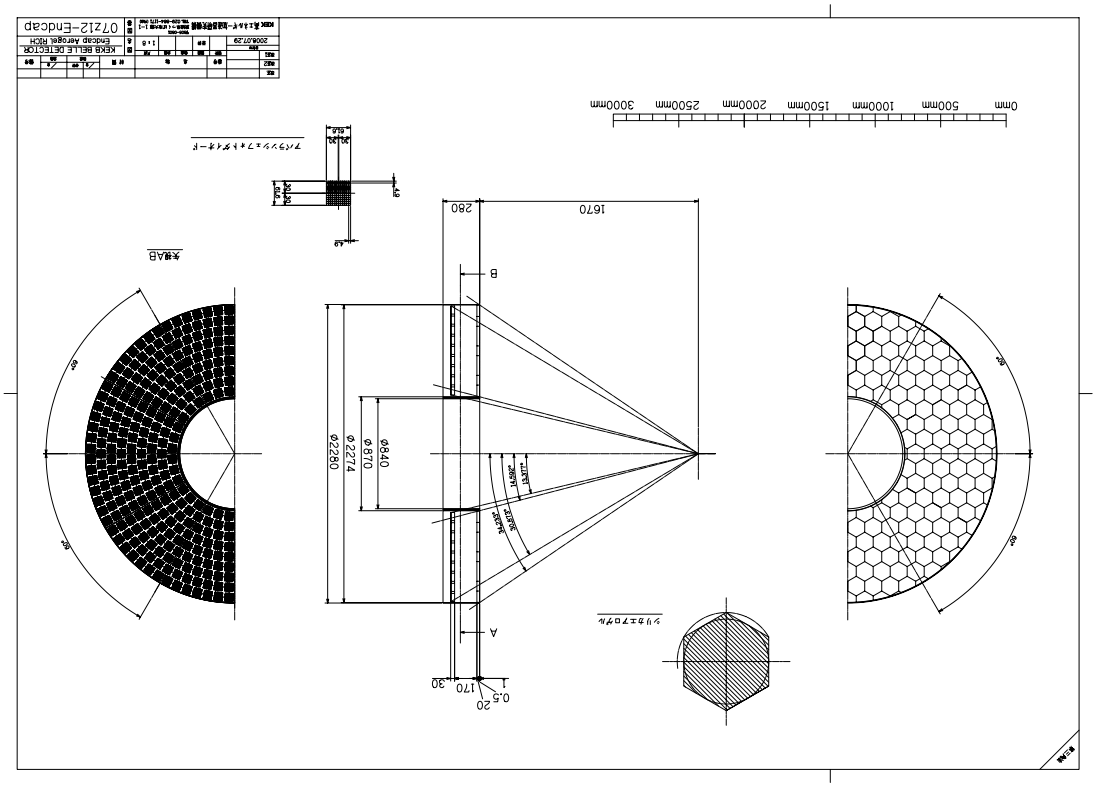

Figure 3.32.: Schematic drawing of the ARICH mechanical structure. (Taken from [26]).

3.4.7. Electromagnetic Calorimeter (ECL)

The Belle ECL has demonstrated high resolution and good performance, therefore the same crystals and mechanical structure will be reused in the Belle II experiment. To cope with the higher background rate and the pile-up noise, the calorimeter electronics will be modified. The shaping time will be reduced and a pipelined readout with waveform processing will be used. Applying an energy-dependent in-time cut can suppress the number of fake photons by a factor of 7, while keeping the efficiency for true photons at more than 93% for photons with an energy above 30 MeV.

3.4.8. Detector solenoid

The superconducting solenoid providing a magnetic field of 1.5 T for the Belle experiment will be reused for the Belle II detector.

3.4.9. K_L and Muon detector system (KLM)

The barrel part of the KLM from the Belle detector will be kept in the Belle II experiment, as the barrel RPCs can be operated successfully even with the higher beam background. Due to the limited shielding in the endcap regions the background rate in the KLM endcaps might degrade the RPC efficiency below 50%. Therefore the endcap RPCs will be replaced with scintillators.

The scintillator strips have a cross section of $(7-10) \times 40$ mm and a length of up to $\sim$ 2.8 m. 16 800 scintillator strips are arranged in two orthogonal planes to form a superlayer within each gap in the magnet yoke. A scintillation light is trapped in embedded wavelength-shifting fibers and delivered to photodetectors. Due to limited space and strong magnetic field in Belle II, photomultipiers cannot be used, so multiplex silicon photodiodes operating in the Geiger mode will serve as photodetectors. The layer layout and the light detection principle are shown in fig. 3.33.

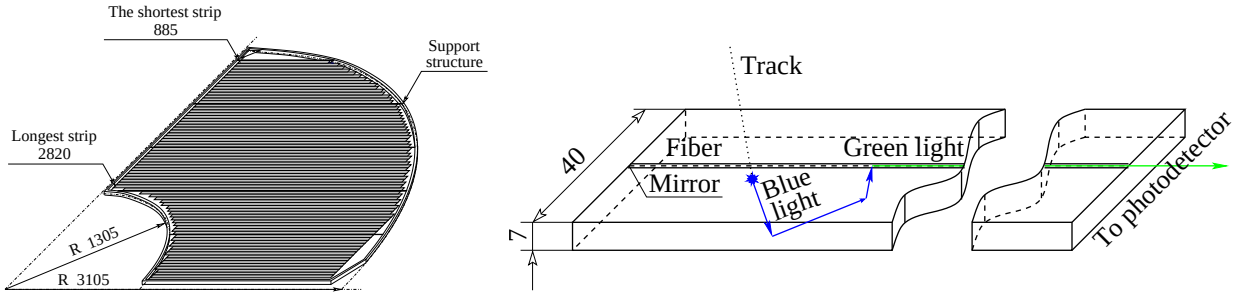

Figure 3.33.: (Left) One layer formed by scintillator strips. (Right) Scintillator light detection in the strip. (Taken from [26]).

4. Full reconstruction

4.1. Introduction

As already mentioned in chapter 3, the e^+e^- centre-of-mass energy at the KEKB accelerator corresponds to the $\Upsilon(4S)$ resonance (10.58 GeV). This resonance lies just above the threshold of producing a $B\bar{B}$ pair (10.56 GeV). The e^+e^- spectrum of this region was shown in fig. 3.3. In over 96% of the cases $\Upsilon(4S)$ decays into a $B\bar{B}$ pair and nothing else. This very specific feature of B-factories allows usage of new reconstruction techniques, not common at hadron colliders.

The knowledge, that all signals observed in the detector originate from the two B mesons, makes it possible to setup a unique constraint on the reconstruction of the events. As the initial state is known, not all final state particles have to be detected in order to get reconstructed. The most prominent examples for decays which become accessible using this constraint are decays which include neutrinos in the final state. By fully reconstructing one B meson, we can conclude that everything else left in the detector must originate from the other B meson. This is illustrated in fig. 4.1 with an exemplary signal decay of $B \to \tau\nu$. We refer to the fully reconstructed B meson as B_{tag} and the remaining B meson as B_{sig}.

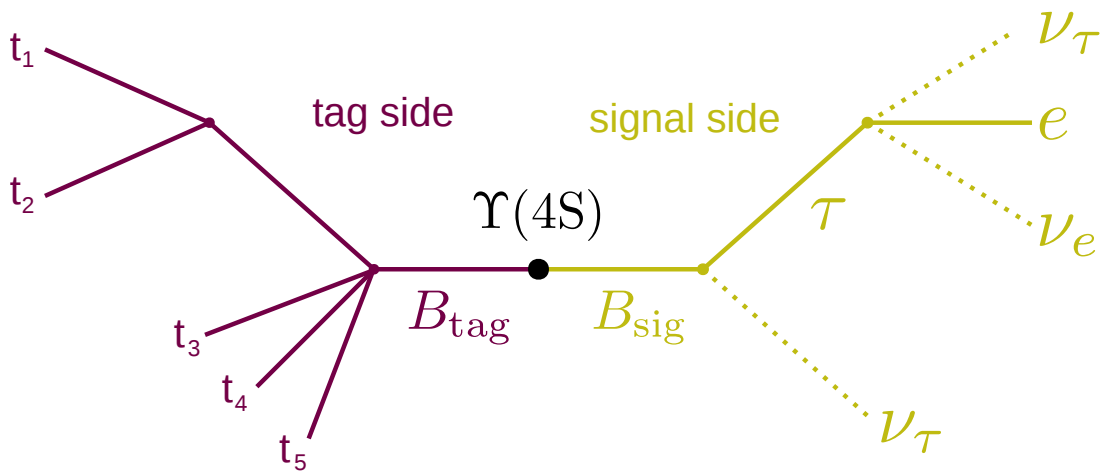

Figure 4.1.: An example of a fully reconstructed B_{tag} (left side) and signal B_{sig} containing neutrinos in the final state (right side). (Taken from [30]).

4.2. NeuroBayes-based full reconstruction

For the analysis performed in this thesis the new probabilistic full reconstruction algorithm was used. A detailed description of this method can be found in [30] and [35]. In the following a short explanation of the main principles will be given.

The main goal of the full reconstruction is to reconstruct the B_{tag} meson in one of many different decay channels with highest possible efficiency and purity. To reconstruct as many B_{tag} mesons as possible, the reconstruction efficiency ϵ_{tot} has to be maximised:

$$\epsilon_{\text{tot}} = \sum_{i}^{N} \epsilon_i \mathcal{B}_i \quad , \tag{4.1}$$

where ϵ_i and $\mathcal{B}_i$ are the efficiency and the branching fraction of the decay channel i, respectively, and N is the total number of the decay channels. As the branching fractions are fixed by nature, we can maximise ϵ_{tot} by increasing the individual efficiencies ϵ_i or the number or reconstructed decay channels N.

There are several aspects to be considered in the implementation of this idea. There are many hundreds of known B decay channels and most of these channels include D and D^* mesons, which also decay in a large spectrum of decay channels that have to be reconstructed. Most of the channels have small branching fractions of an order of $10^{-3} - 10^{-5}$. In addition, only decay channels where all final state particles are detectable (e.g. no neutrinos) can be used for the full reconstruction of the B_{tag}. There are also a lot of possible wrong combinations of the final state particles, which have to be rejected by the reconstruction framework. By just doing naively each possible combination, the event processing will take an unacceptably long time.

The purity of the found B_{tag} candidates is very important for many analyses. In other analyses however to achieve the highest possible efficiency is more important. This full reconstruction framework allows user to choose the efficiency and purity appropriate for his analysis.

4.2.1. Multivariate approach

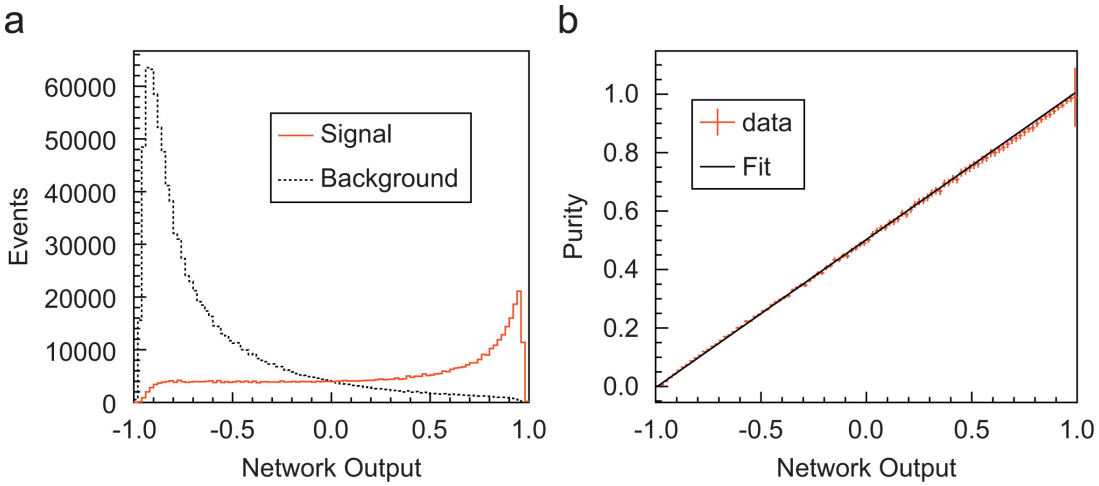

Figure 4.2.: Left side a: the distribution of the NeuroBayes output for signal (red) and background (black) for an exemplary classification task. Right side b: purity as a function of the NeuroBayes output. (Taken from [35]).

Multivariate approach means combining all significant variables into one single scalar variable. For the new probabilistic full reconstruction the package NeuroBayes [36] was used. The idea of this package is to pass all of the relevant variables, through a sophisticated preprocessing algorithm, to a neural network. The task of the network is to classify each event as signal or background, an example of a resulting classification is shown in fig. 4.2*a*. To achieve this the network maps all the input variables to a signal output variable while taking into account the correlations between the variables. The output variable of NeuroBayes, in the following referred to as NeuroBayes output, can be interpreted as a Bayesian probability for signal. In fig. 4.2*b* the purity is plotted a function of the NeuroBayes output. A linear dependence can be observed, which indicates that the output is a good measure of probability for the candidate to be signal. If a NeuroBayes training is performed with the same signal to background ratio as found in data, the output can be directly interpreted as the signal probability. In other cases a correction has to be calculated.

4.2.2. Hierarchical reconstruction

As already mentioned before, the calculation of all possible combinations for high multiplicity channels will consume too much time and computing power. To achieve a high reconstruction efficiency nevertheless, a hierarchical approach was chosen. The reconstruction is divided in four stages, as shown in table 4.1 and illustrated in fig. 4.3. At each

stage the signal probabilities are calculated. Cuts on these probabilities are dependent on the channel which is reconstructed and are applied only in the next stage.

The channels were added to the framework according to their expected gain in efficiency. In total 1104 exclusive decay channels were used.

Stage	Reconstructed particles
1	Charged tracks, K_s, γ, π^0
2	$D^{\pm}_{(s)}$. D^0, J/Ψ
3	$D^{*\pm}_{(s)}$, D^{*0}
4	$B^{\pm}$,B^0

Table 4.1.: Particles reconstructed during the 4 stages of the full reconstruction [35].

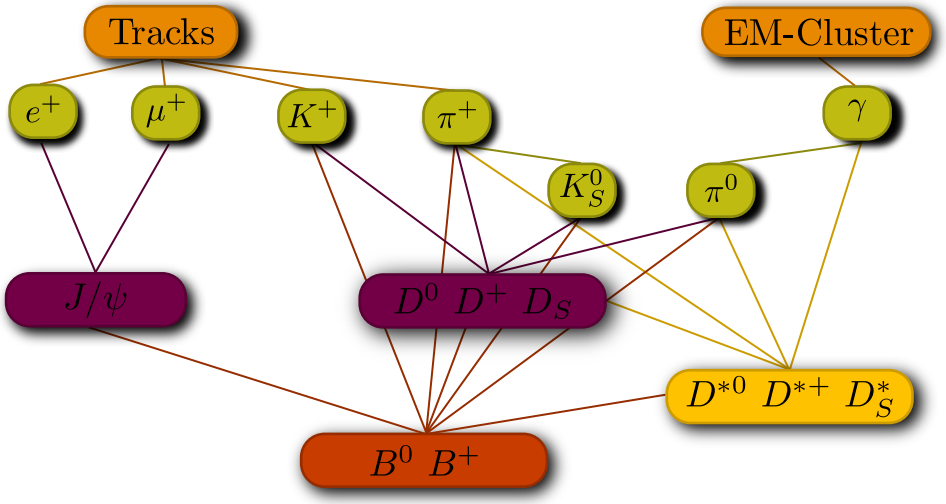

Figure 4.3.: The 4 stages of the full reconstruction. (Taken from [30]).

4.2.3. Continuum suppression

Apart from the combinatorial background there is also the background from non-$B\bar{B}$ events. These events are originating from $e^+e^- \to q\bar{q}$ events and have a jet-like structure. The different event shape allows a separation between $q\bar{q}$ events and the spherical $B\bar{B}$ events. Usage of the shape event variables might introduce a bias in certain analyses, so

the continuum suppression is outsourced in an optional module which can be used after the execution of the full reconstruction.

4.2.4. Performance

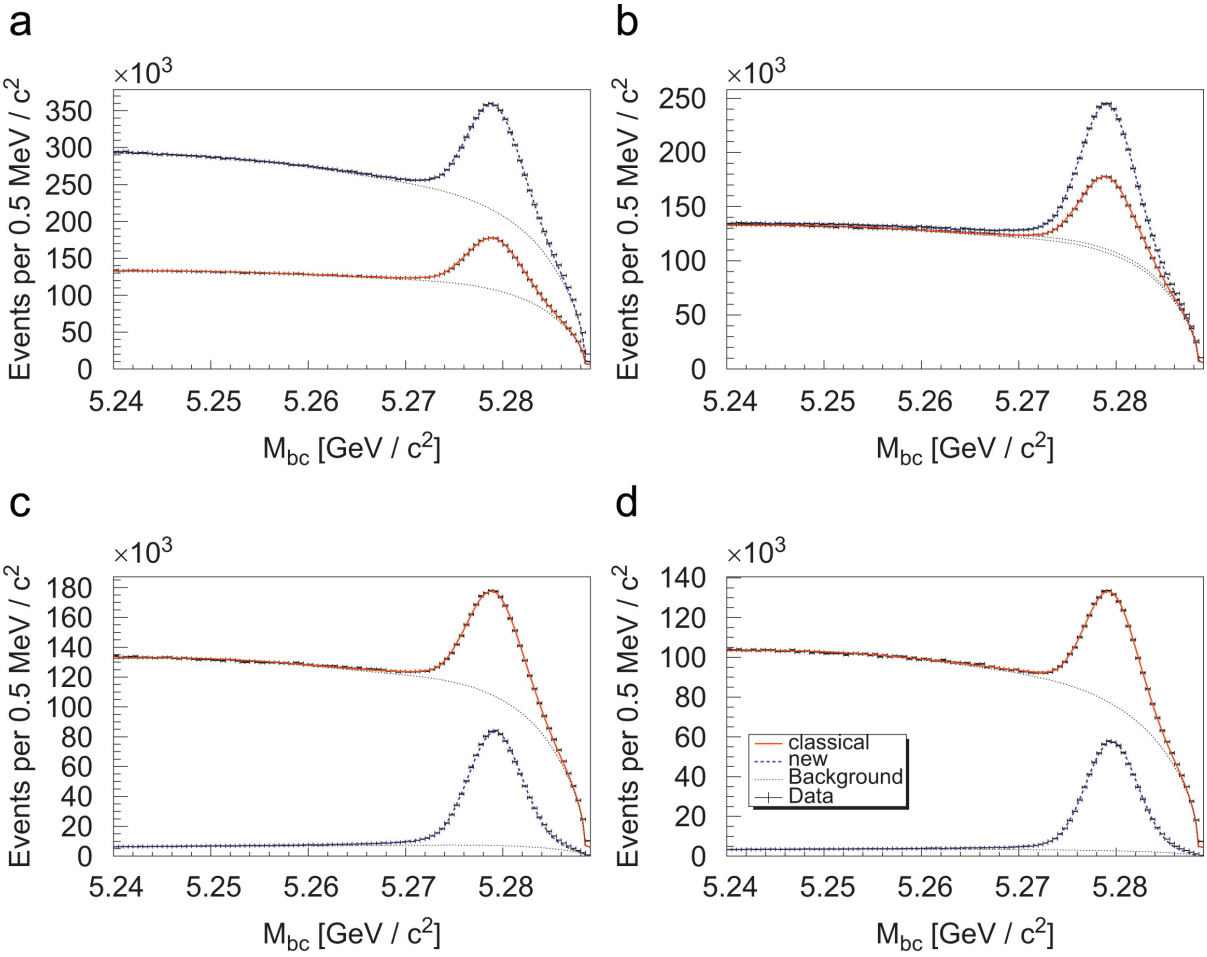

Figure 4.4.: M_{bc} plots for different selections: The dashed blue line is a fit to the new full reconstruction distribution, the solid red line to the classical one. The network cuts are chosen to have (a) roughly equal purity (B^+), (b) roughly equal background level (B^+), (c) roughly equal efficiency (B^+), (d) roughly equal efficiency (B^0) compared to the classical reconstruction. (Taken from [35]).

To evaluate the performance of the new full reconstruction we compare its performance with the classical, cut-based reconstruction method previously used in the Belle collaboration (e.g. [1]). Performance can be compared by estimating the numbers of correctly

reconstructed B_{tag} candidates with both methods. These numbers are estimated using the distribution of the beam-constraint mass M_{bc}, which is defined as follows:

$$M_{\text{bc}} = \sqrt{E_{\text{beam}}^2 - p_B^2} \quad , \tag{4.2}$$

where E_{beam} is the beam energy and p_B is the momentum of the reconstructed B_{tag}.

To compare the results between the two methods we select a NeuroBayes output cuts which lead to a similar efficiency or purity as the previous method had. The resulting fits to the M_{bc} distributions are shown in fig. 4.4. Over 2 million neutral B mesons and over 3 million charged B mesons could be reconstructed, which is considerably above the numbers achieved by the previous method. We compare purity and efficiency for different NeuroBayes output cuts with the purity and efficiency point of the cut-based reconstruction for B^+ mesons in fig. 4.5. We can observe twice as higher efficiency for the same purity. For the same efficiency the purity rises from 25% to over 80%.

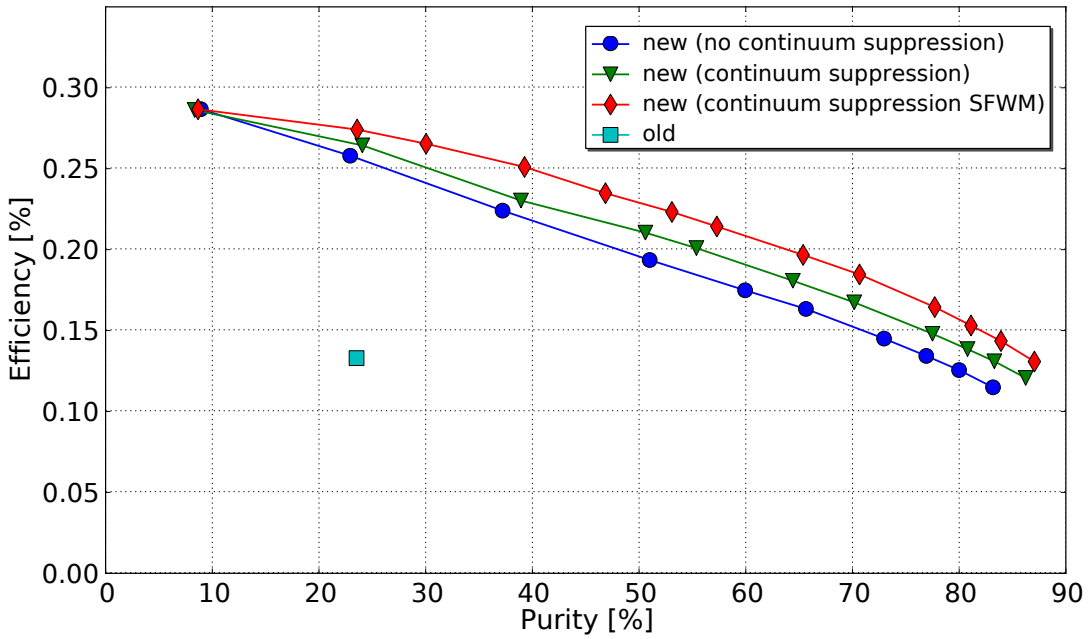

Figure 4.5.: Purity-efficiency points for different NeuroBayes output cuts compared to the point of the cut-based method. (Taken from [30]).

5. Analysis

5.1. Overview of the analysis strategy

First the B_{tag} candidate is reconstructed using the new full reconstruction method (see chapter 4). The signal side is then reconstructed in the following modes:

- $B^+ \to K^+ \nu\bar{\nu}$
- $B^+ \to K^{*+} \nu\bar{\nu}$
  $K^{*+} \to K^+ \pi^0$
  $K^{*+} \to K^0_s \pi^+$
- $B^+ \to \pi^+ \nu\bar{\nu}$
- $B^+ \to \rho^+ \nu\bar{\nu}$
- $B^0 \to K^0_s \nu\bar{\nu}$
- $B^0 \to K^{*0} \nu\bar{\nu}$
  $K^{*0} \to K^+ \pi^-$
- $B^0 \to \pi^0 \nu\bar{\nu}$
- $B^0 \to \rho^0 \nu\bar{\nu}$
- $B^0 \to \phi \nu\bar{\nu}$

To reduce the background several selection criteria are applied. Simulated experiments based on Monte Carlo are used to estimate the signal efficiency of the selection and the expected background.

The remaining energy in the electromagnetic calorimeter, E_{ECL}, is used to estimate the number of signal events. As in a signal event everything apart from two neutrinos is reconstructed, no activity should be left in the detector and thus we expect the signal events to peak at low E_{ECL} values. The signal yield is extracted by a binned fit to the E_{ECL}. The procedure to estimate the significance of observed signal as well as to set up a limit on the branching fraction are prepared. The analysis is performed 'blind': the data sample in the signal region was opened after the whole analysis procedure was fixed.

These channels were already analysed within the Belle collaboration using a data sample of 492fb^{-1} in [1]. After the implementation of the new full reconstruction, the analysis of the $K^{(*)}$ channels was performed using the full Belle data sample in [30]. Compared to this former analysis, the study within this thesis was again extended by including the decays to the lighter mesons. Furthermore, the cuts applied in the selection were studied and a new continuum suppression cut was introduced, leading to a higher signal sensitiv-

ity. Moreover, the counting procedure used for the signal yield estimation was replaced by a fit, ensuring the consideration of the signal shape.

5.2. Used data samples

The complete Belle data sample of 711 fb^{-1} ($\approx 771 \times 10^6$ $B\bar{B}$ pairs) collected on the $\Upsilon(4S)$ resonance was analysed within this thesis. To study and validate the analysis procedure official Belle Monte Carlo samples with simulated experiments were used. These samples are organised according to the simulated physics processes. As not every e^+e^- collision leads to a creation of the $\Upsilon(4S)$ resonance, non-resonant events $e^+e^- \to q\bar{q}$, denoted as continuum events, compose an important background. Generic decays of the $\Upsilon(4S)$ resonance via the dominating $b \to c$ transition are simulated in the charged Monte Carlo samples for $B^\pm$ and mixed Monte Carlo samples for $B^0/\bar{B}^0$. The branching fractions of the decays are fixed to their world averaged values [2]. These samples are combined to the generic Monte Carlo, which is supposed to reproduce the realistic mixture of events recorded by Belle. The composition of the combined sample is shown in table 5.1. To study the background generic Monte Carlo corresponding to 5 times the data luminosity was used. The rare decays occurring via $b \to s$ and $b \to d$ transitions, are simulated in the rare Monte Carlo. Despite the low branching fractions this component might be an important background for this analysis. A sample corresponding to 50 times the data luminosity was used to study it.

Generic Monte Carlo component	Description	Relative amount
charged	$\Upsilon(4S)$ decays into generically decaying charged B mesons	12%
mixed	$\Upsilon(4S)$ decays into generically decaying neutral B mesons	12%
charm	continuum $e^+e^- \to c\bar{c}$ decays	30%
uds	continuum $e^+e^- \to u\bar{u}, d\bar{d}, s\bar{s}$ decays	46%

Table 5.1.: Composition of the generic Monte Carlo.

For each of the 9 considered modes a signal Monte Carlo sample was produced. The used EvtGen model includes form factors calculated by [37], [38] and [39]. This model was implemented and tested by Kai-Feng Chen [1] and was also used in the predecessor analysis [30].

5.3. Candidate selection

Important measure to estimate the quality of the reconstructed tracks are impact parameters, which denote the distance from the point of closest approach to the interaction point. Tracks have to fulfil the following quality criteria to be used in the further reconstruction:

- The impact parameter in the $r\phi$ plane should pass the cut: $|dr| < 2$.
- The impact parameter in the z/beam direction should pass the cut: $|dz| < 2$.
- The transverse momentum p_t should be above 0.1 GeV .

Following reconstruction criteria were used for each type of light meson candidates:

- $\boldsymbol{K^{\pm}}$
  Candidates have to pass the cut on the particle identification likelihood ratio: $\frac{\mathcal{L}_K}{(\mathcal{L}_K+\mathcal{L}_\pi)} > 0.6$.
- $\boldsymbol{\pi^{\pm}}$
  Candidates have to pass the cut on the particle identification likelihood ratio: $\frac{\mathcal{L}_K}{(\mathcal{L}_K+\mathcal{L}_\pi)} < 0.4$.
- $\boldsymbol{\pi^0}$
  Candidates are formed from two photon candidates with an energy of at least 50 MeV. The invariant mass of the π^0 candidate, obtained from the energy of the two photons, has to satisfy 117.8 MeV/c^2 $< m_{\pi^0} <$ 150.2 MeV/c^2. The energy asymmetry between the two photos $a_\gamma = \frac{|E_{\gamma 1}-E_{\gamma 2}|}{|E_{\gamma 1}+E_{\gamma 2}|}$ should be smaller then 0.9.
- $\boldsymbol{K_s^0}$
  The *GoodKS* selection criteria, developed and validated within the Belle collaboration, are required. The invariant mass of the candidate has to be within $\pm$15 MeV/c^2 of the nominal K^0 mass.
- $\boldsymbol{K^{*0}}$
  One charged pion and one charged kaon with opposite charge are combined to form K^{*0} candidates. The invariant mass has to be within $\pm$75 MeV/c^2 of the nominal K^{*0} mass.
- $\boldsymbol{K^{*+}}$
  Candidates are reconstructed in two different decay modes: $K^{*+} \to K^+\pi^0$ and $K^{*+} \to K_s^0\pi^+$. The invariant mass has to within $\pm$75 MeV/c^2 of the nominal K^{*+} mass.

- $\boldsymbol{\rho^+}$
  One charged and one neutral pion are combined to form ρ^+ candidates. The invariant mass has to within ± 150 MeV/c^2 of the nominal ρ^+ mass.

- $\boldsymbol{\rho^0}$
  Two charged pions with opposite charge are combined to form ρ^0 candidates. The invariant mass has to within ± 150 MeV/c^2 of the nominal ρ^0 mass.

- $\boldsymbol{\phi}$
  Two charged kaons with opposite charge are combined to form ϕ candidates. The invariant mass has to within ± 10 MeV/c^2 of the nominal ϕ mass.

5.4. Signal selection

The variable used for the final signal extraction is the extra energy in the calorimeter E_{ECL}, which is not assigned to any of the reconstructed particles. The clusters are required to exceed the following energy thresholds:

- Forward endcap: 100 MeV
- Barrel: 50 MeV
- Backward Endcap: 150 MeV

An upper cut of 1.2 GeV on the summed extra energy is applied.

To be sensitive to a signal contribution, the number of candidates has to be considerably reduced. We apply several selection criteria to remove as much background as possible while avoiding to loose too much signal. The variables and the cut values used for the signal selection are summarised in the following. Only a few exemplary distributions of the variables are shown, distributions for all channels can be found in the appendix A.1.

- $\mathbf{B}_{tag}$
  During the full reconstruction the best B_{tag} candidate is selected. We use the calculated NB$_{out}$ as well as the mass and the energy of the B_{tag} to reduce the background. Following criteria are applied:
  - **Correct charge combination with the signal-side candidate**
  - **Beam constraint mass**
    Beam constraint mass M_{bc} is defined as follows:

$$M_{\mathrm{bc}} = \sqrt{E^2_{\mathrm{beam}} - p^2_B} \quad ,$$

where E_{beam} is the half of the total beam energy and p_B is the momentum of the reconstructed B_{tag}. The nominal value for M_{bc} is 5.2795 GeV. The following cut is applied:

$$M_{\text{bc}} > 5.27\text{GeV} \quad .$$

The M_{bc} distributions for two exemplary channels, with all other cuts applied, are shown in fig. 5.1.

· **Energy difference**
ΔE is the difference between the nominal and the measured energy of the B meson:

$$\Delta E = E_B - E_{\text{beam}} \quad ,$$

where E_{beam} is the half of the total beam energy and E_B is the reconstructed energy of the B meson. The nominal value for ΔE is 0 GeV. We apply the following cut:

$$-0.08\text{GeV} < \Delta E < 0.06\text{GeV} \quad .$$

The ΔE distribution for two exemplary channels, with all other cuts applied, is shown in fig. 5.2.

· **NeuroBayes output of the $\mathbf{B}_{tag}$**
To further enhance the signal content a cut on the NeuroBayes output of the B_{tag} is applied

$$NB_{\text{out}} > 0.02 \quad .$$

The distribution of NB_{out}, with all other cuts applied, is shown in fig. 5.3.

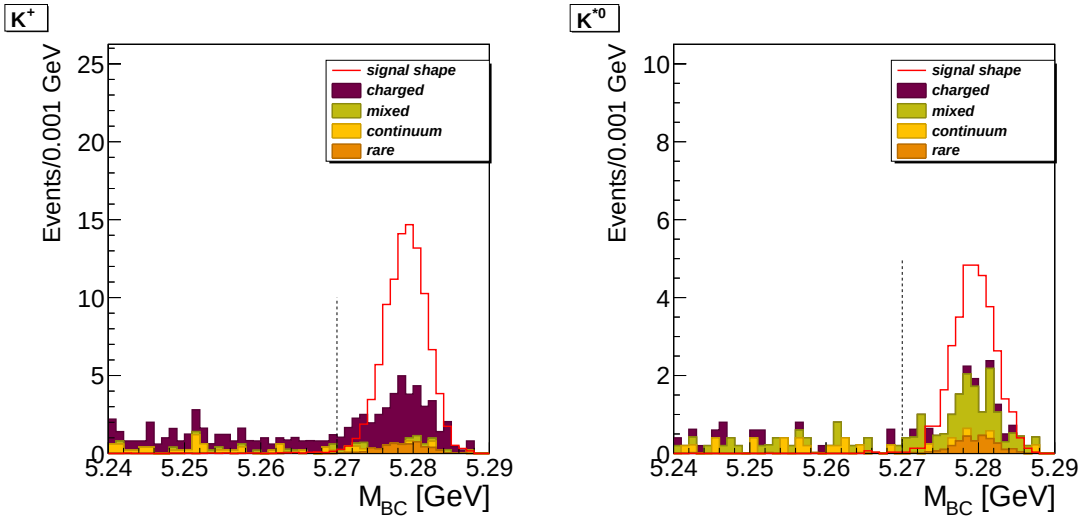

(a) $B^+ \to K^+\nu\bar{\nu}$ (b) $B^0 \to K^{*0}\nu\bar{\nu}$

Figure 5.1.: The M_{bc} distribution for background (filled histogram) and signal (red line) Monte Carlo, with all other cuts applied. The signal distribution is normalised to an arbitrary value to illustrate the shape. The dashed line marks the cut value.

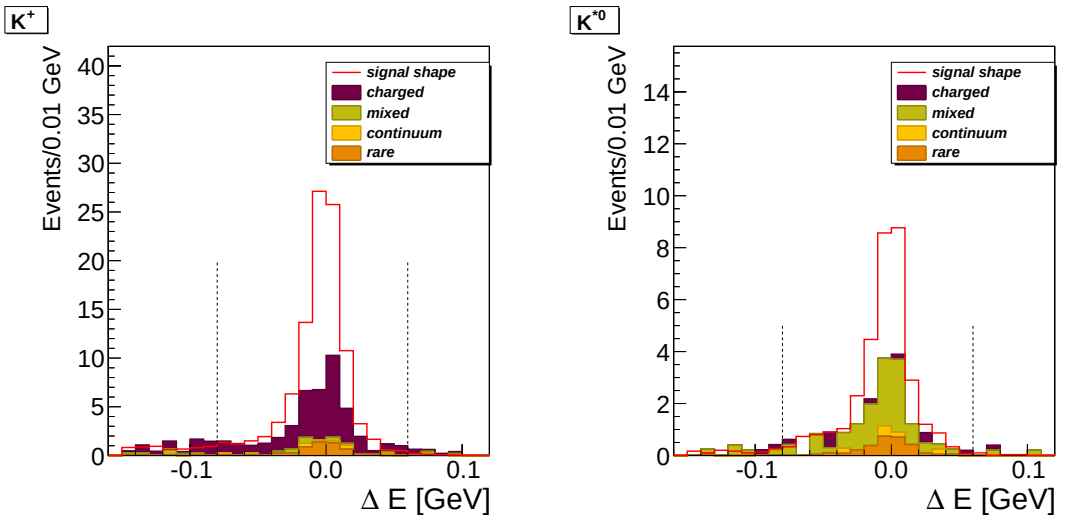

(a) $B^+ \to K^+\nu\bar{\nu}$ (b) $B^0 \to K^{*0}\nu\bar{\nu}$

Figure 5.2.: The ΔE distribution for background (filled histogram) and signal (red line) Monte Carlo, with all other cuts applied. The signal distribution is normalised to an arbitrary value to illustrate the shape. The dashed lines mark the cut values.

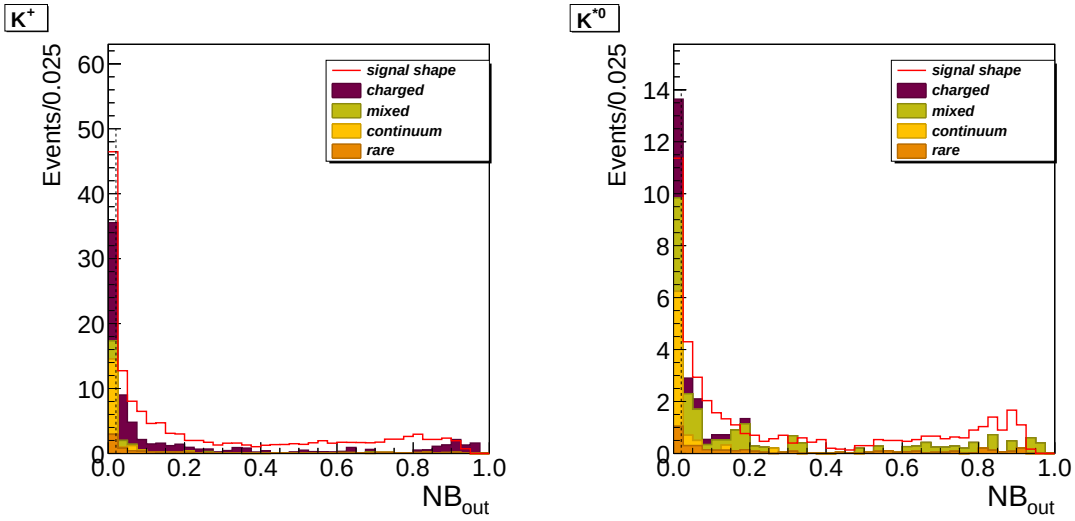

(a) $B^+ \to K^+\nu\bar{\nu}$ (b) $B^0 \to K^{*0}\nu\bar{\nu}$

Figure 5.3.: The NB_{out} distribution for background (filled histogram) and signal (red line) Monte Carlo, with all other cuts applied. The signal distribution is normalised to an arbitrary value to illustrate the shape. The dashed line marks the cut value.

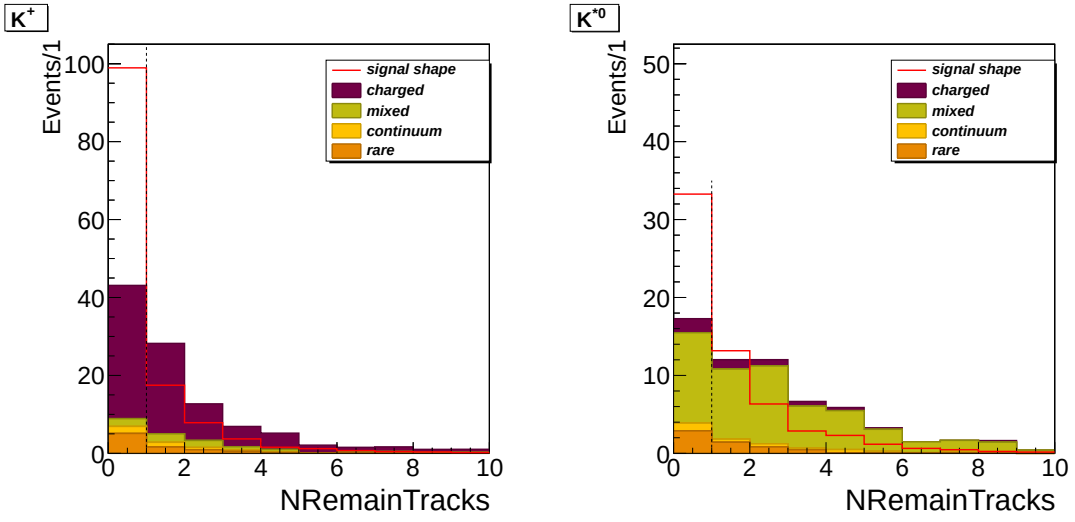

(a) $B^+ \to K^+\nu\bar{\nu}$ (b) $B^0 \to K^{*0}\nu\bar{\nu}$

Figure 5.4.: The distribution of number of remaining tracks in the events for background (filled histogram) and signal (red line) Monte Carlo, with all other cuts applied. The signal distribution is normalised to an arbitrary value to illustrate the shape. The dashed line marks the cut value.

- **No remaining π^0 candidates or charged tracks**
  No additional π^0 or track candidates should be left in the event. All detected tracks are vetoed, without any quality cuts. The distributions are shown in fig 5.4 and fig. 5.5.

- **Missing momentum**
  To avoid events with particles escaping through the beam pipe, a following requirement of the angle between the missing momentum and the beam pipe is applied:

$$-0.86 < \cos\theta_{miss} < 0.95 \quad .$$

  The distribution of the cosine is shown in fig 5.6.

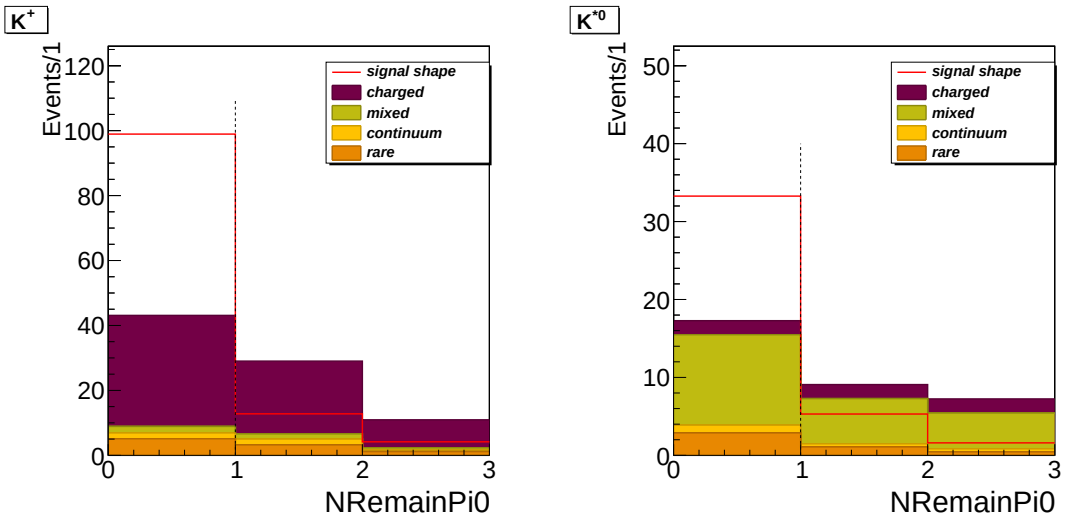

(a) $B^+ \to K^+\nu\bar{\nu}$ (b) $B^0 \to K^{*0}\nu\bar{\nu}$

Figure 5.5.: The distribution of number of remaining π^0 in the events for background (filled histogram) and signal (red line) Monte Carlo, with all other cuts applied. The signal distribution is normalised to an arbitrary value to illustrate the shape. The dashed line marks the cut value.

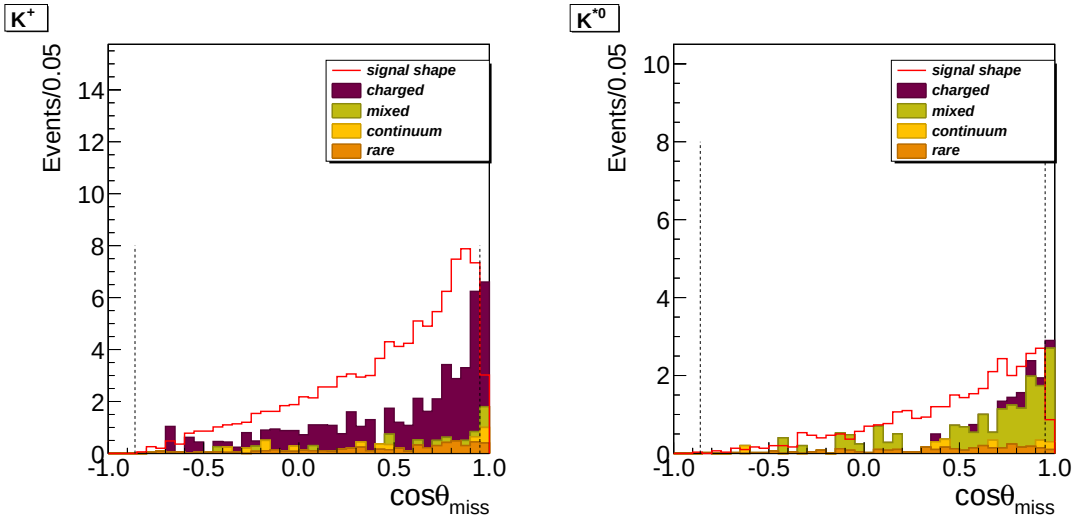

(a) $B^+ \to K^+\nu\bar{\nu}$ (b) $B^0 \to K^{*0}\nu\bar{\nu}$

Figure 5.6.: The distribution of the angle between the missing momentum and the beam pipe for background (filled histogram) and signal (red line) Monte Carlo, with all other cuts applied. The signal distribution is normalised to an arbitrary value to illustrate the shape. The dashed lines mark the cut values.

- **Continuum suppression**
  In this analysis the continuum is already suppressed during the full reconstruction. The *ekpcontsuppress* module [30] is executed after the full reconstruction. Using event shape variables (super-Fox Wolfram moments [40]), which can separate continuum from $B\bar{B}$ events, the NBout and NBRank are recalculated and used during the further analysis.

  However, a considerable amount of continuum background is still in the signal box after all other selection cuts are applied. The relative amount of different background components is shown in fig. 5.7. The fraction of continuum varies between 15% and 30% depending on the channel. To suppress this component further discriminating variables were investigated. A good discriminator was found in the angle between the thrust axis of the B_{sig} and the rest of the charged tracks, evaluated in the $\Upsilon(4S)$ rest frame ($\cos_{\text{TOB}}$). Since jet-like continuum events are strongly directional, the cosine of this angle is close to $-1/1$, whether for spherical $B\bar{B}$ events this angle is uniformly distributed. In general we would expect a symmetric distribution. However, as the Fox Wolfram moments are correlated to the $\cos_{\text{TOB}}$, the distribution can look differently after the use of *ekpcontsuppress*. This is illustrated in fig. 5.8 on example of two of the considered channels.

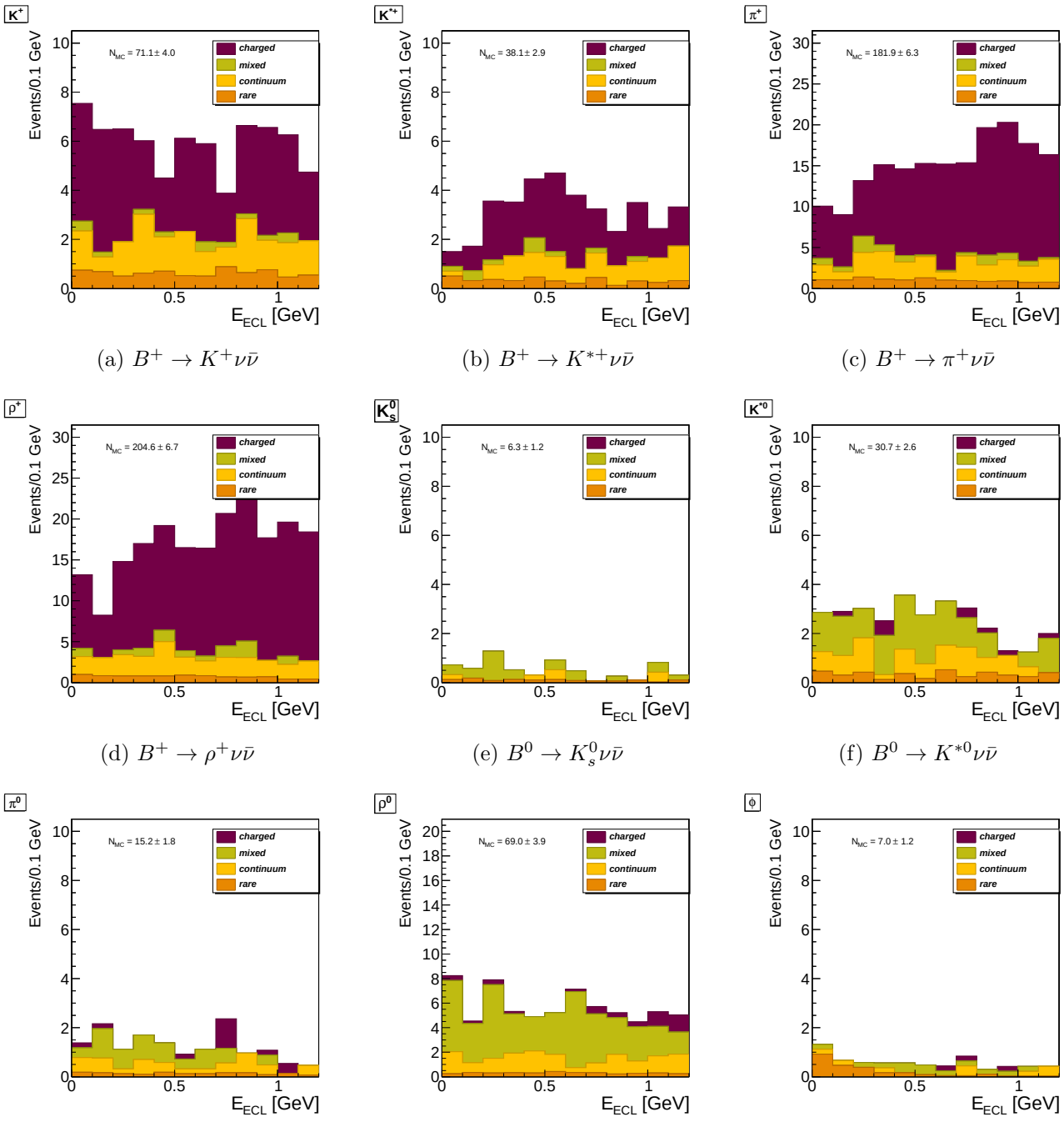

(a) $B^+ \to K^+\nu\bar{\nu}$ (b) $B^+ \to K^{*+}\nu\bar{\nu}$ (c) $B^+ \to \pi^+\nu\bar{\nu}$

(d) $B^+ \to \rho^+\nu\bar{\nu}$ (e) $B^0 \to K^0_s\nu\bar{\nu}$ (f) $B^0 \to K^{*0}\nu\bar{\nu}$

(g) $B^0 \to \pi^0\nu\bar{\nu}$ (h) $B^0 \to \rho^0\nu\bar{\nu}$ (i) $B^0 \to \phi\nu\bar{\nu}$

Figure 5.7.: The E_{ECL} distributions of the different types of Monte Carlo generated events. All other selection criteria except the discussed continuum suppression are applied. The continuum background component (second from below) is marked yellow.

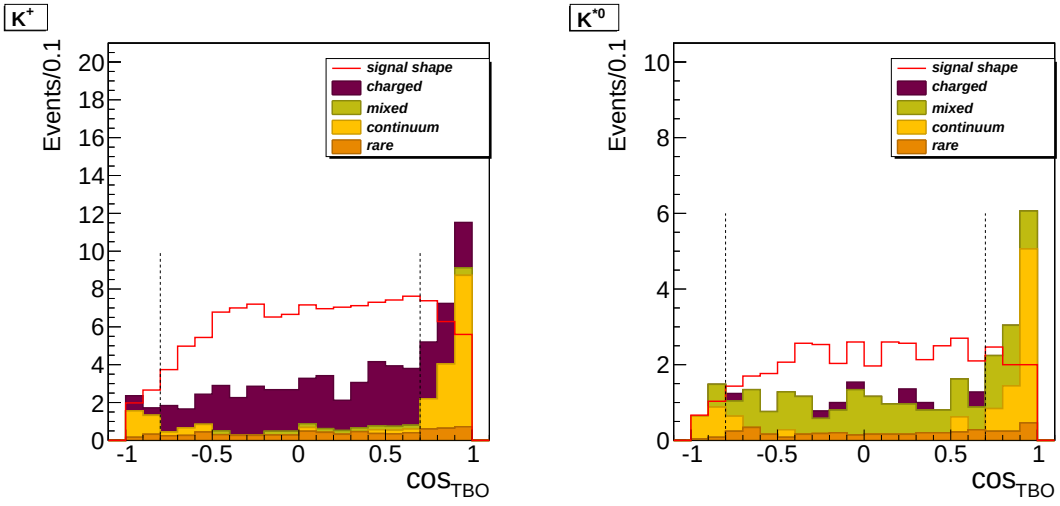

(a) $B^+ \to K^+\nu\bar{\nu}$ (b) $B^0 \to K^{*0}\nu\bar{\nu}$

Figure 5.8.: The distribution of the cosine between the thrust axis of the B_{sig} and the rest of the charged tracks. All other selection criteria except the discussed continuum suppression are applied. The continuum background component is marked yellow. The dashed lines mark the chosen cut values.

Channel	Rejected continuum background [%]	Rejected background [%]	Signal efficiency [%]
$B^+ \to K^+\nu\bar{\nu}$	89.5	39.4	78.1
$B^+ \to K^{*+}\nu\bar{\nu}$ $K^{*+} \to K^+\pi^0$	88.1	41.2	80.9
$B^+ \to K^{*+}\nu\bar{\nu}$ $K^{*+} \to K^0_s\pi^+$	100	41.6	78.0
$B^+ \to \pi^+\nu\bar{\nu}$	89.1	34.4	79.0
$B^+ \to \rho^+\nu\bar{\nu}$	88.7	32.5	77.4
$B^0 \to K^0_s\nu\bar{\nu}$	83.3	32.8	77.4
$B^0 \to K^{*0}\nu\bar{\nu}$ $K^{*0} \to K^+\pi^-$	88.6	43.8	77.8
$B^0 \to \pi^0\nu\bar{\nu}$	87.5	42.6	80.4
$B^0 \to \rho^0\nu\bar{\nu}$	90.9	39.8	76.7
$B^0 \to \phi\nu\bar{\nu}$	100	50	77.3

Table 5.2.: The effect of the cut on the cosine between the thrust axis of the B_{sig} and the rest of the charged tracks: $-0.8 < \cos_{\text{TBO}} < 0.7$.

The following cut is used for the signal selection:

$$-0.8 < \cos_{\mathrm{TBO}} < 0.7 \quad .$$

The impact of this cut on signal efficiency and background suppression is summarised in table 5.2.

- **Momentum of the light meson**
  The distribution of the momentum of the light meson from the signal events is strongly model dependent and therefore not exactly known.
  We apply a generalised cut of

$$1.6 \text{ GeV} < p < 2.5 \text{ GeV}$$

for all channels, except for the ϕ channel, where no momentum cut was applied, as the momentum distribution of the ϕ meson is unknown. At low momenta we expect a high amount of background from $b \rightarrow$c decays, whether the higher cut of 2.5 GeV is introduced to reject the background from two body charmless decays like $B \rightarrow K^*\gamma$ [1].

Nevertheless a study of the meson momentum distribution was performed, as this variable can be used to extract signal in the later analyses. Several peaks can be observed in the remaining p background distribution, as is shown in fig. 5.9. These peaks are corresponding to specific miss-reconstructed two body decays. In the expected K-momentum distribution of $B^+ \rightarrow K^+\nu\bar{\nu}$, with all other selection cuts applied, a broad peak around 1.7 GeV can be observed. These events correspond to miss-reconstructed decays to charmonium like $B^+ \rightarrow J/\Psi K^+$ and $B^+ \rightarrow \eta_c K^+$. The smaller peaks around 2.3 GeV are coming from $B^+ \rightarrow D^{\bar{0}(*)}x$ decays (x stands here for $e^{\pm}\nu$,$\mu^{\pm}\nu$, $K^{\pm}$,$\pi^{\pm}$,$\rho^{\pm}$). For the $B^+ \rightarrow \pi^+\nu\bar{\nu}$ channel this peak is especially dominant, which can be explained with a higher branching fractions for $B^+ \rightarrow D^0\pi^+$ and for $B^+ \rightarrow D^{*0}\pi^+$. Further discussion of the background composition can be found in section 5.7.

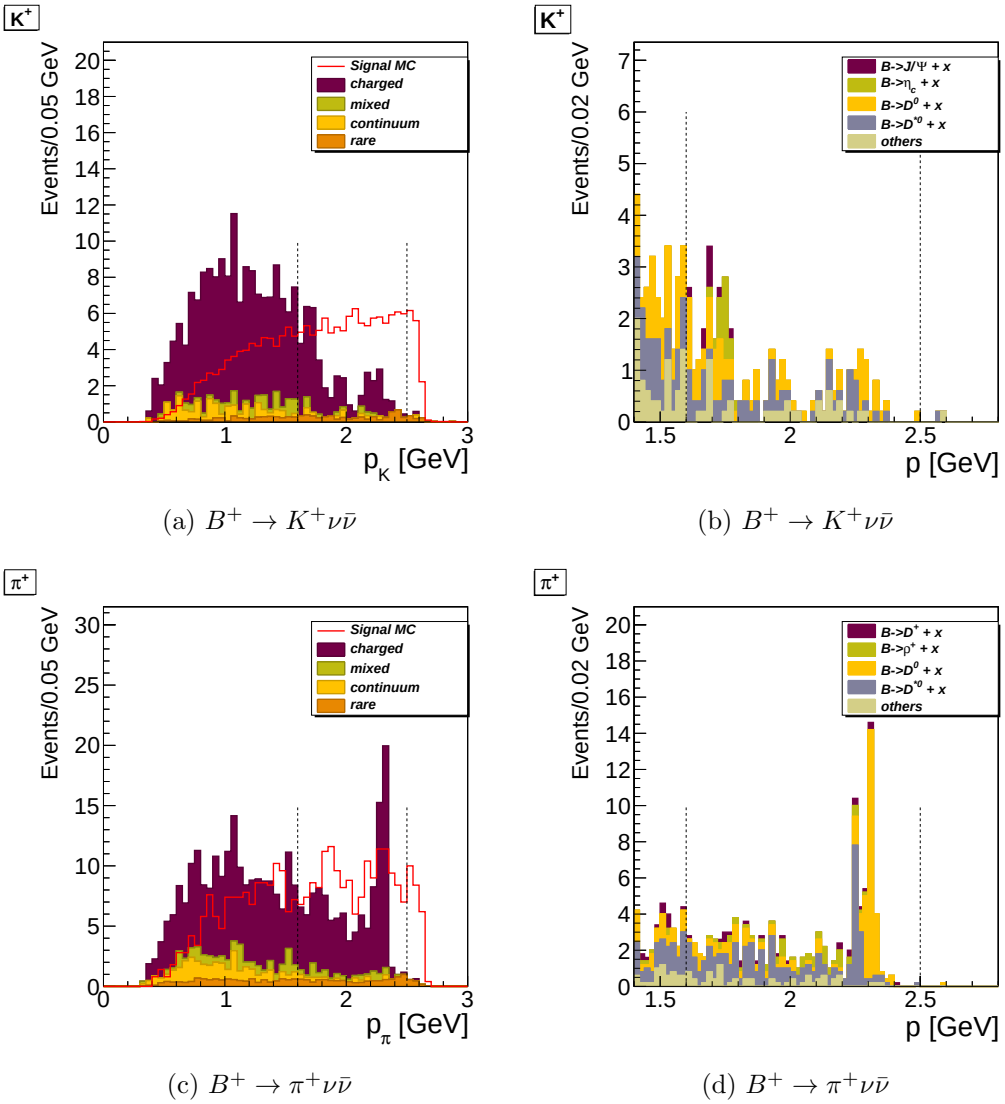

(a) $B^+ \to K^+\nu\bar{\nu}$ (b) $B^+ \to K^+\nu\bar{\nu}$

(c) $B^+ \to \pi^+\nu\bar{\nu}$ (d) $B^+ \to \pi^+\nu\bar{\nu}$

Figure 5.9.: The distribution of the momentum of the light meson. On the left side the whole momentum region is shown, the dashed lines mark the cut values. On the right side a zoom into the relevant momentum region is plotted, with contributions from different decays.

5.5. Correction of B_{tag} efficiency

The efficiency of the new NeuroBayes based full reconstruction shows some differences between Monte Carlo and data. The data/Monte Carlo ratio depending on the tag decay mode was studied in another analysis [41] with various charm semileptonic signal sides.

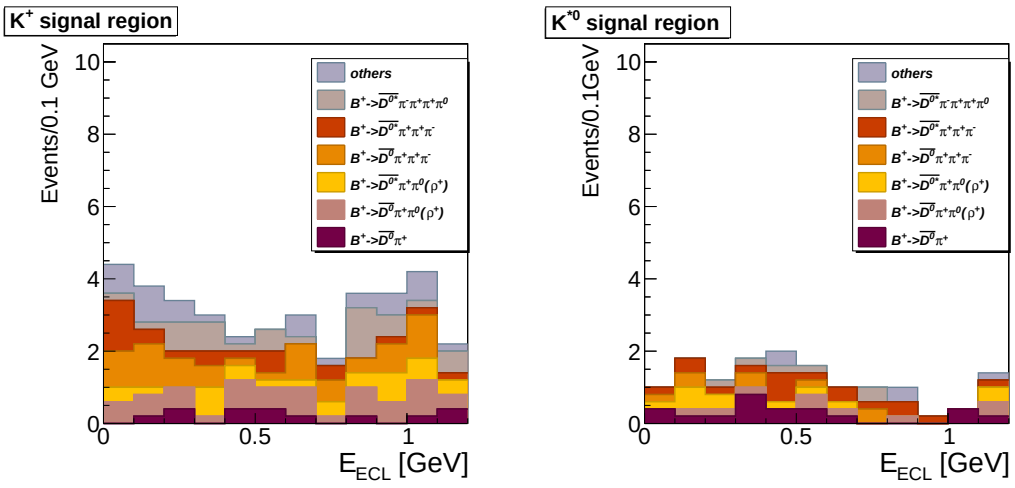

(a) $B^+ \to K^+\nu\bar{\nu}$ (b) $B^0 \to K^{*0}\nu\bar{\nu}$

Figure 5.10.: The distribution of the B_{tag} channels for the remaining background in the signal box for K^+ and K^{*0} channels. One can observe that different B_{tag} candidates contributed to different E_{ECL} regions.

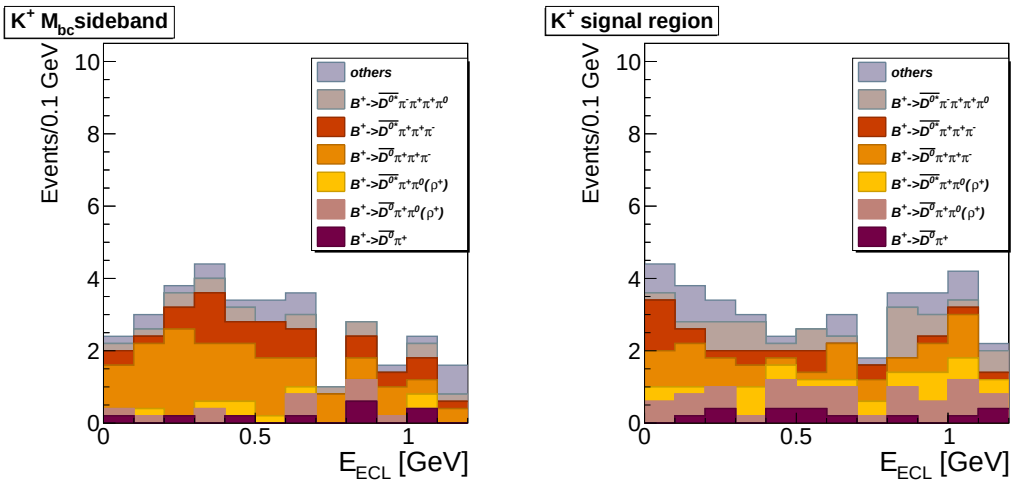

(a) M_{bc}sideband (b) signal region

Figure 5.11.: The distribution of the B_{tag} channels for the remaining background in the M_{bc} sideband and the signal box for the $B^+ \to K^+\nu\bar{\nu}$ channel. One can observe that the composition of B_{tag} candidate reconstruction channels differs in the signal and sideband region.

We apply this correction on all B_{tag} candidates, which were matched to be correct (BTagMCInfo > 0). This is true for in average $\sim 50\%$ of the background events remaining in the signal box after the selection. As shown in fig. 5.10 different B_{tag} channels contribute to different E_{ECL} regions.

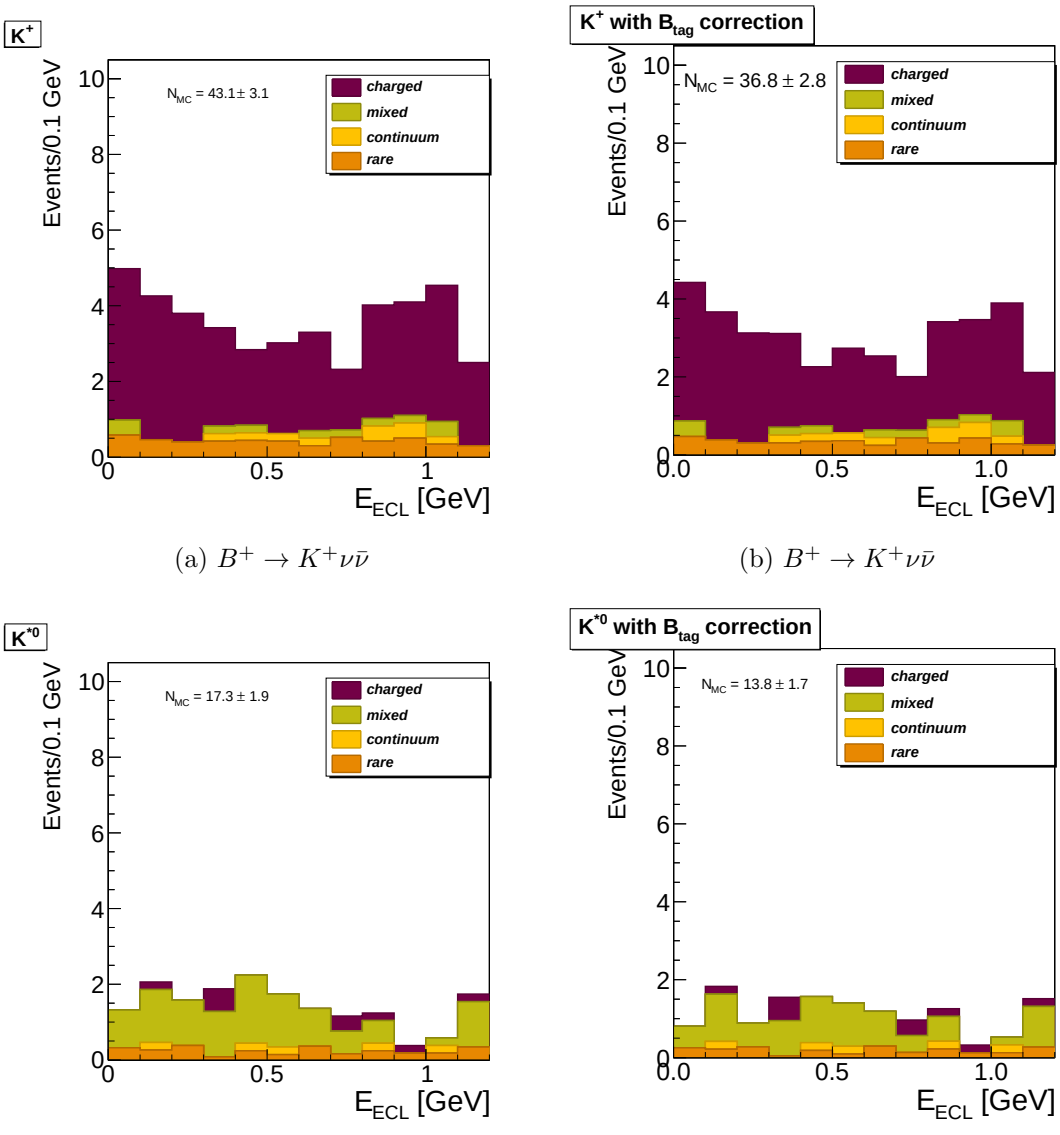

(a) $B^+ \to K^+\nu\bar{\nu}$ (b) $B^+ \to K^+\nu\bar{\nu}$

(c) $B^0 \to K^{*0}\nu\bar{\nu}$ (d) $B^0 \to K^{*0}\nu\bar{\nu}$

Figure 5.12.: The Monte Carlo background distribution in the signal box before and after the reweighting of the correct B_{tag} events.

An alternative possibility to correct for this would be to consider data and Monte Carlo efficiency in the sideband, as it was performed in the predecessor analysis [30]. However, different B_{tag} channels contribute to the signal and sideband regions in this analysis, as is shown in fig. 5.11. In these plots we do not apply the BTagMCInfo > 0 condition, as in the sideband nearly no B_{tag} candidates were matched as correctly reconstructed.

We apply the B_{tag} correction weights on the correctly matched candidates. Thus, this correction not only rescales the expected number of events, but also slightly changes the shape of the expected background. Fig. 5.12 shows the effect of the reweighting on two of the channels, plots for all channels can be found in the appendix A.9.

5.6. Comparison between Monte Carlo simulation and data

We use the events from M_{bc} sideband ($M_{\text{bc}} < 5.27$ GeV), where no signal events are expected, to verify data and Monte Carlo agreement. We also want to mention that no B_{tag} correction is applied on these Monte Carlo samples, as there are no fully matched correct B_{tag} candidates in this samples. The E_{ECL} distributions for the M_{bc} sideband sample, with all other signal selection cuts applied and normalised to the same total number of events, are shown in fig. 5.13. In generally data and Monte Carlo agree well. In fig. 5.14 the same histograms without the normalisation are shown to compare the absolute numbers of expected and observed events.

We calculate the probability values to check if the two histograms are compatible. We perform a Kolmogorov test [42], which compares the shapes of both histograms and is also assumed to give better results for histograms with low statistics then a usual χ^2 test. The obtained probability values are summarised in table 5.3. No significant deviation can be observed. Nevertheless, we want to mention some possible discrepancies. In some channels (K^+, K^{*0}, π^0) a deficiency in data in the upper E_{ECL} region ($E_{\text{ECL}} > 0.7$ GeV) can be observed. Especially for the K^+ channel the shape of data point seems to differ from the shape from Monte Carlo. However, with such high statistical uncertainties it is not possible to conclude if we see a hint for a discrepancy or just statistical fluctuations.

To achieve higher statistics for a better comparison we release some cuts and perform another comparison between data and Monte Carlo. Following two setups were used:

- Release the cut on the light meson momentum: results are shown in table 5.4 and fig. 5.15.
- Release the π^0 veto, remaining tracks veto, angle of missing momentum and ΔE cut: results are shown in table 5.4 and fig. 5.16.

Channel	p-Value Kolmogorov test
$B^+ \to K^+\nu\bar{\nu}$	0.533
$B^+ \to K^{*+}\nu\bar{\nu}$	0.983
combined	
$B^+ \to \pi^+\nu\bar{\nu}$	0.993
$B^+ \to \rho^+\nu\bar{\nu}$	0.781
$B^0 \to K_s^0\nu\bar{\nu}$	0.975
$B^0 \to K^{*0}\nu\bar{\nu}$	0.359
$K^{*0} \to K^+\pi^-$	
$B^0 \to \pi^0\nu\bar{\nu}$	0.871
$B^0 \to \rho^0\nu\bar{\nu}$	0.971
$B^0 \to \phi\nu\bar{\nu}$	0.444

Table 5.3.: Probability values of the compatibility of data and Monte Carlo background in the M_{bc} sideband.

Channel	p-Value Kolmogorov test (a)	p-Value Kolmogorov test (b)
$B^+ \to K^+\nu\bar{\nu}$	0.836	0.661
$B^+ \to K^{*+}\nu\bar{\nu}$	0.328	0.184
combined		
$B^+ \to \pi^+\nu\bar{\nu}$	0.941	0.9996
$B^+ \to \rho^+\nu\bar{\nu}$	0.590	0.998
$B^0 \to K_s^0\nu\bar{\nu}$	0.321	0.830
$B^0 \to K^{*0}\nu\bar{\nu}$	0.810	0.152
$K^{*0} \to K^+\pi^-$		
$B^0 \to \pi^0\nu\bar{\nu}$	0.974	0.9994
$B^0 \to \rho^0\nu\bar{\nu}$	0.999	0.355
$B^0 \to \phi\nu\bar{\nu}$	0.444	0.610

Table 5.4.: Probability values of the compatibility of data and Monte Carlo background in the M_{bc} sideband with (a) no cut on the momentum of the light meson applied and (b) with following cuts released: missing momentum angle, π^0 veto, remaining tracks veto, ΔE.

Although fluctuations in some bins can be observed, in general the shapes of data and Monte Carlo distributions agree. In the plots presented here both distributions are normalised to the same total number of events. The plots where also the absolute numbers of events can be compared can be found in the appendix (fig. A.11 and fig. A.12).

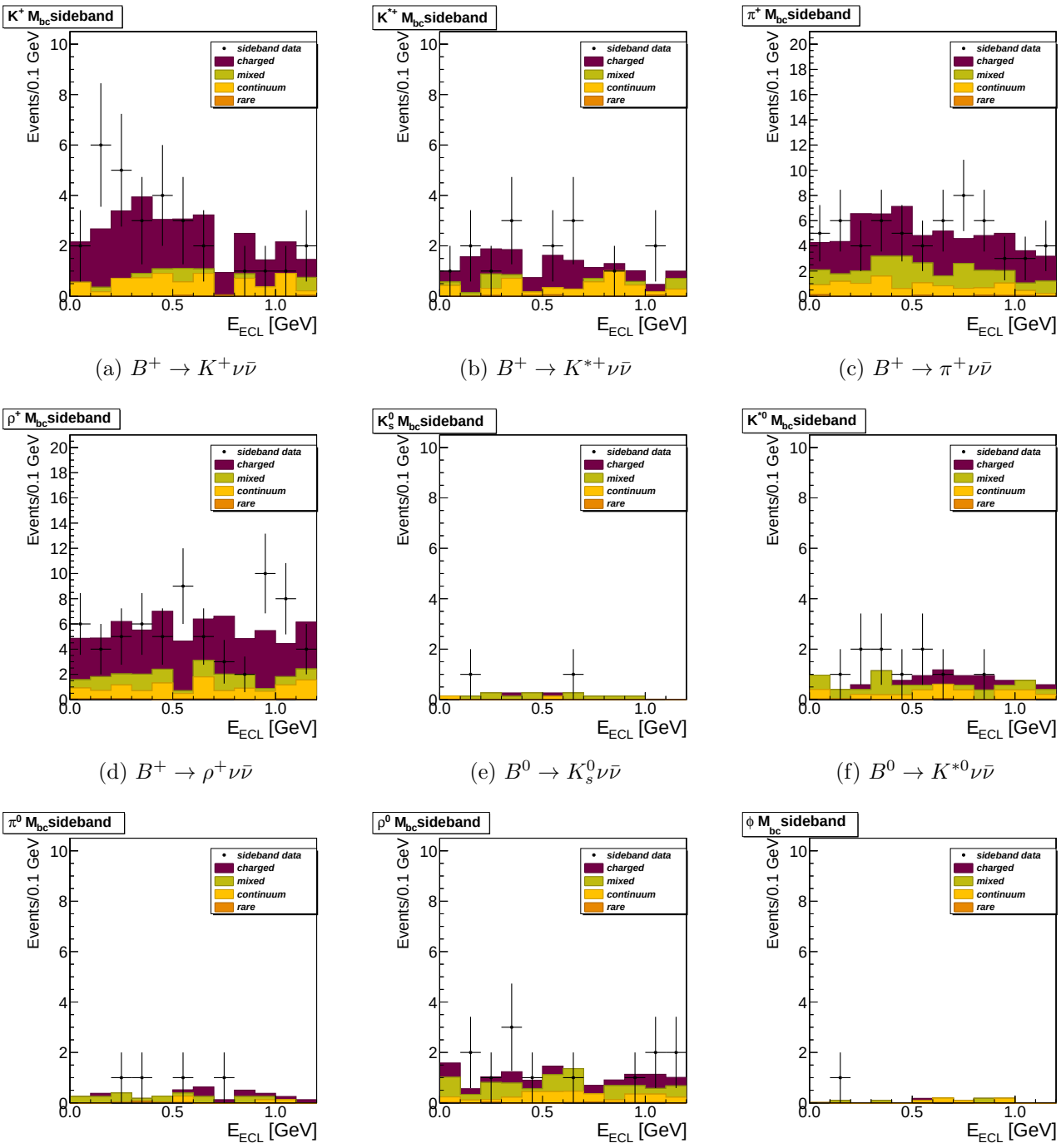

(a) $B^+ \to K^+\nu\bar{\nu}$ (b) $B^+ \to K^{*+}\nu\bar{\nu}$ (c) $B^+ \to \pi^+\nu\bar{\nu}$

(d) $B^+ \to \rho^+\nu\bar{\nu}$ (e) $B^0 \to K^0_s\nu\bar{\nu}$ (f) $B^0 \to K^{*0}\nu\bar{\nu}$

(g) $B^0 \to \pi^0\nu\bar{\nu}$ (h) $B^0 \to \rho^0\nu\bar{\nu}$ (i) $B^0 \to \phi\nu\bar{\nu}$

Figure 5.13.: The E_{ECL} distributions in the M_{bc} sideband. The blacks dots show the data distribution, while the filled histogram shows a stack plot of the background components. Both histograms are normalised to the same total number of events.

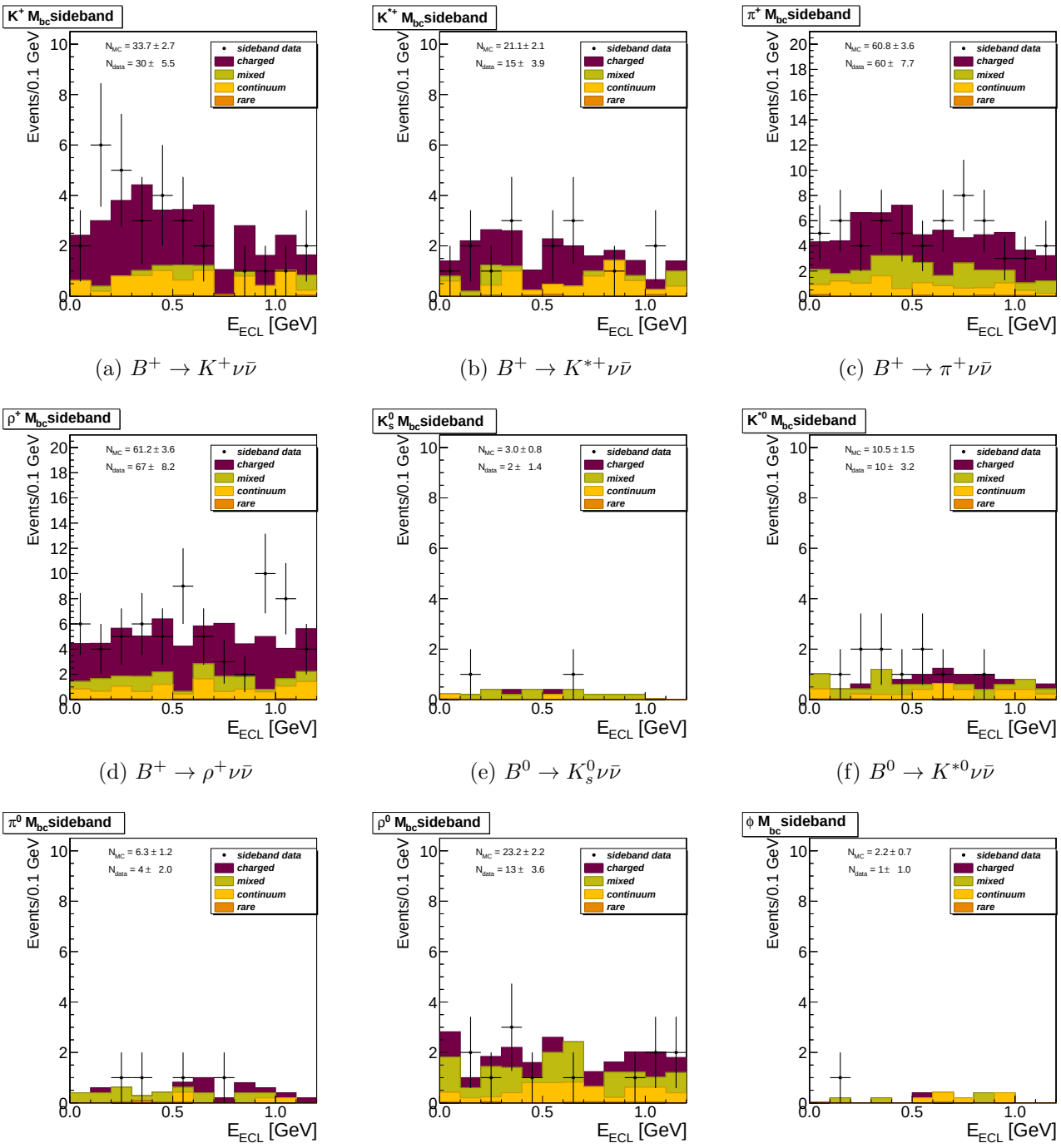

(a) $B^+ \to K^+\nu\bar{\nu}$ (b) $B^+ \to K^{*+}\nu\bar{\nu}$ (c) $B^+ \to \pi^+\nu\bar{\nu}$

(d) $B^+ \to \rho^+\nu\bar{\nu}$ (e) $B^0 \to K^0_s\nu\bar{\nu}$ (f) $B^0 \to K^{*0}\nu\bar{\nu}$

(g) $B^0 \to \pi^0\nu\bar{\nu}$ (h) $B^0 \to \rho^0\nu\bar{\nu}$ (i) $B^0 \to \phi\nu\bar{\nu}$

Figure 5.14.: The $E_{\rm ECL}$ distributions in the $M_{\rm bc}$ sideband. The blacks dots show the data distribution, while the filled histogram shows a stack plot of the background components.

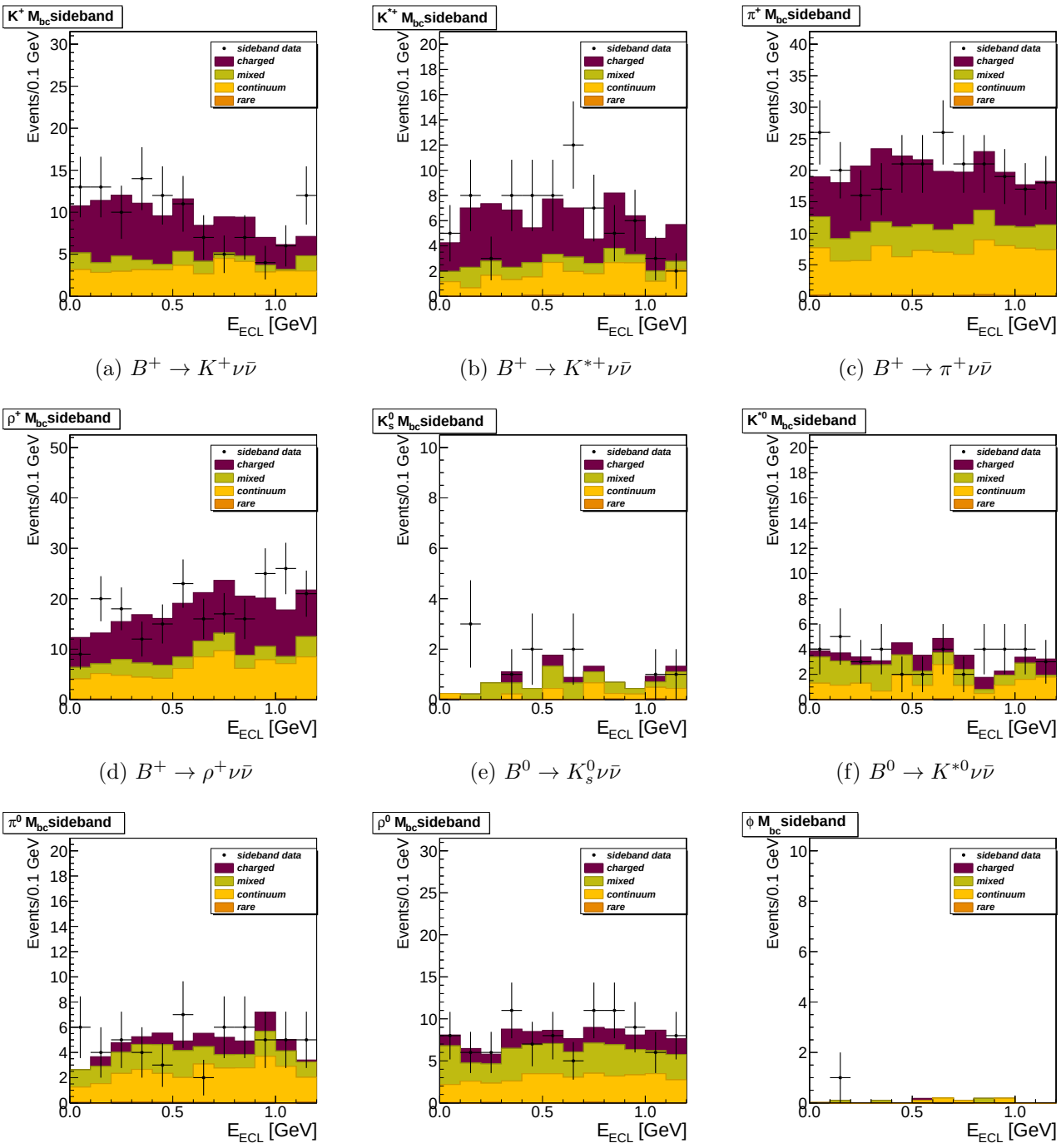

(a) $B^+ \to K^+\nu\bar{\nu}$ (b) $B^+ \to K^{*+}\nu\bar{\nu}$ (c) $B^+ \to \pi^+\nu\bar{\nu}$

(d) $B^+ \to \rho^+\nu\bar{\nu}$ (e) $B^0 \to K^0_s\nu\bar{\nu}$ (f) $B^0 \to K^{*0}\nu\bar{\nu}$

(g) $B^0 \to \pi^0\nu\bar{\nu}$ (h) $B^0 \to \rho^0\nu\bar{\nu}$ (i) $B^0 \to \phi\nu\bar{\nu}$

Figure 5.15.: The E_{ECL} distributions in the M_{bc} sideband with no cut on the momentum of the light meson applied. The blacks dots show the data distribution, while the filled histogram shows a stack plot of the background components. Both histograms are normalised to the same total number of events.

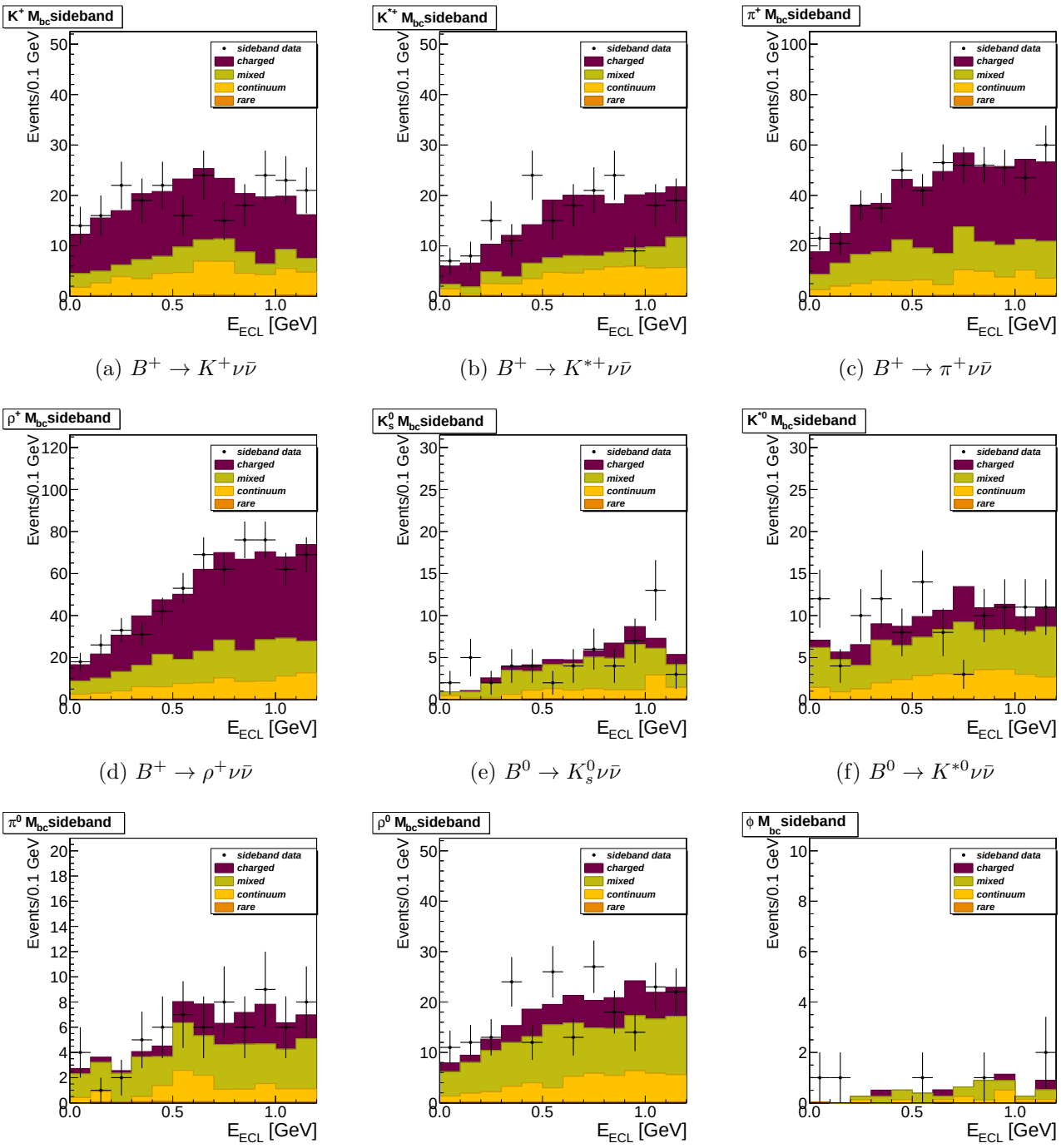

(a) $B^+ \to K^+\nu\bar{\nu}$ (b) $B^+ \to K^{*+}\nu\bar{\nu}$ (c) $B^+ \to \pi^+\nu\bar{\nu}$

(d) $B^+ \to \rho^+\nu\bar{\nu}$ (e) $B^0 \to K^0_s\nu\bar{\nu}$ (f) $B^0 \to K^{*0}\nu\bar{\nu}$

(g) $B^0 \to \pi^0\nu\bar{\nu}$ (h) $B^0 \to \rho^0\nu\bar{\nu}$ (i) $B^0 \to \phi\nu\bar{\nu}$

Figure 5.16.: The E_{ECL} distributions in the M_{bc} sideband with following cuts released: missing momentum angle, π^0 veto, remaining tracks veto, ΔE.. The blacks dots show the data distribution, while the filled histogram shows a stack plot of the background components. Both histograms are normalised to the same total number of events.

5.7. Background estimation and composition

In fig. 5.17 the expected background distributions for all channels are shown. The biggest contribution for the charged modes comes from the generic charged B decays. For the neutral modes the largest contribution arises from the generic neutral B decays. The contributions from continuum and rare decays are relatively small in all channels. The only exception is the ϕ channel, where the rare decays compose most of the background. In table 5.5 the numbers of expected background events in the E_{ECL} signal box ($0 < E_{\mathrm{ECL}} < 1.2$ GeV) are summarised. Although we intend to let the total yield free in the final it, we use these event numbers to study the signal yield extraction procedure and estimate the expected limits in section 7.5. The main background for charged modes are decays $B^+ \to D^{(*)0} + (e^{\pm}\nu, \mu^{\pm}\nu), K^{(*)\pm}, \pi^{\pm}$, for the neutral modes decays $B^0 \to D^{(*)\pm} + (e^{\pm}\nu, \mu^{\pm}\nu, K^{*\pm}, K^{\pm}K^0)$. There are also contributions from decays to J/Ψ or η_c. The relative amount and the distribution of those components is shown in fig. 5.18.

Channel	Number of expected background events
$B^+ \to K^+\nu\bar{\nu}$	36.8 ± 2.8
$B^+ \to K^{*+}\nu\bar{\nu}$	17.2 ± 1.9
$K^{*+} \to K^+\pi^0$	
$B^+ \to K^{*+}\nu\bar{\nu}$	2.4 ± 0.7
$K^{*+} \to K^0_s\pi^+$	
$B^+ \to K^{*+}\nu\bar{\nu}$	19.6 ± 2.1
combined	
$B^+ \to \pi^+\nu\bar{\nu}$	101.4 ± 4.7
$B^+ \to \rho^+\nu\bar{\nu}$	117.0 ± 5.1
$B^0 \to K^0_s\nu\bar{\nu}$	3.4 ± 0.9
$B^0 \to K^{*0}\nu\bar{\nu}$	13.8 ± 1.7
$K^{*0} \to K^+\pi^-$	
$B^0 \to \pi^0\nu\bar{\nu}$	7.3 ± 1.3
$B^0 \to \rho^0\nu\bar{\nu}$	33.7 ± 2.7
$B^0 \to \phi\nu\bar{\nu}$	2.1 ± 0.6

Table 5.5.: Expected numbers of background events.

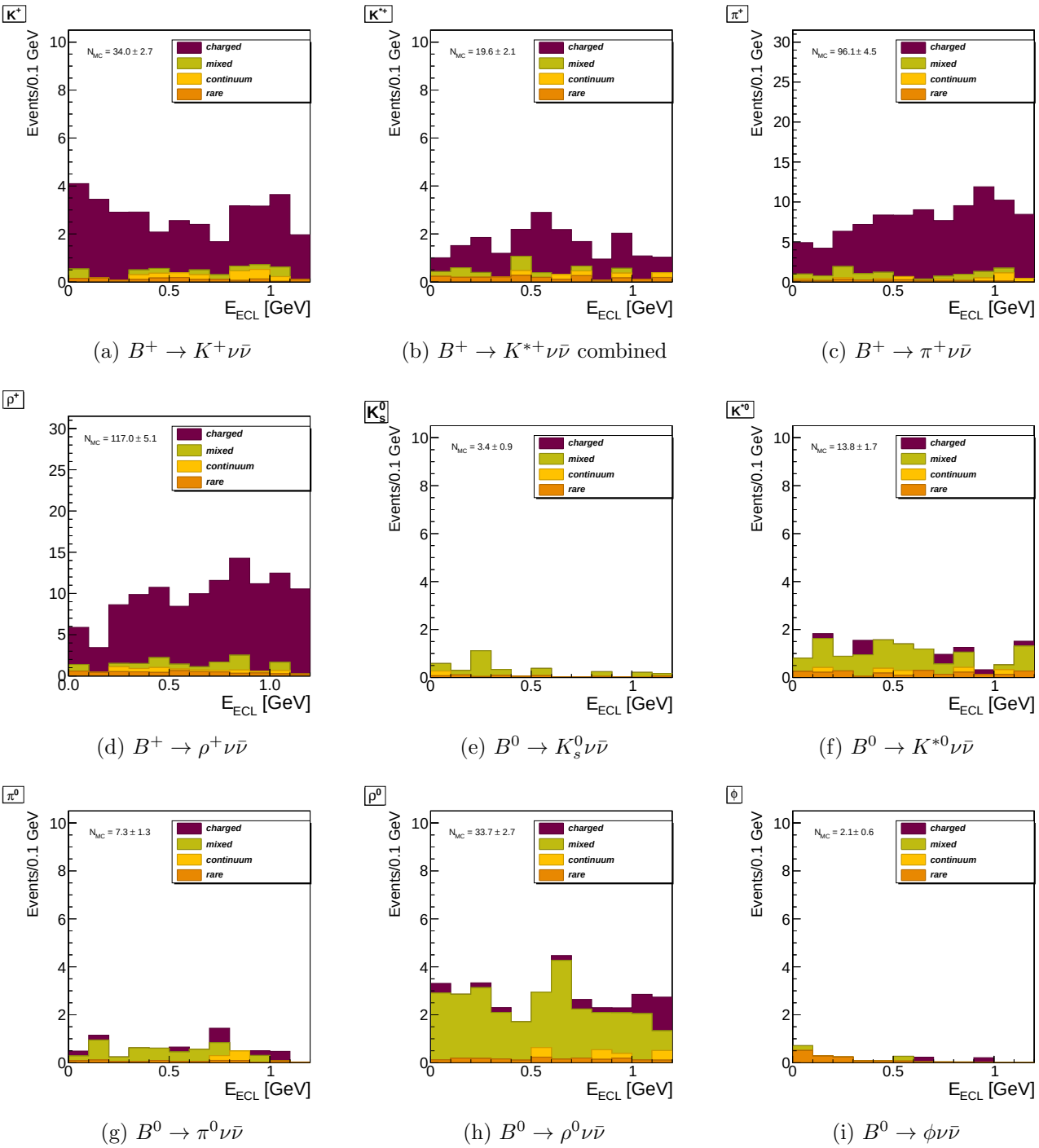

(a) $B^+ \to K^+\nu\bar{\nu}$ (b) $B^+ \to K^{*+}\nu\bar{\nu}$ combined (c) $B^+ \to \pi^+\nu\bar{\nu}$

(d) $B^+ \to \rho^+\nu\bar{\nu}$ (e) $B^0 \to K^0_s\nu\bar{\nu}$ (f) $B^0 \to K^{*0}\nu\bar{\nu}$

(g) $B^0 \to \pi^0\nu\bar{\nu}$ (h) $B^0 \to \rho^0\nu\bar{\nu}$ (i) $B^0 \to \phi\nu\bar{\nu}$

Figure 5.17.: The E_{ECL} distributions of the expected background after the complete signal side selection and B_{tag} correction.

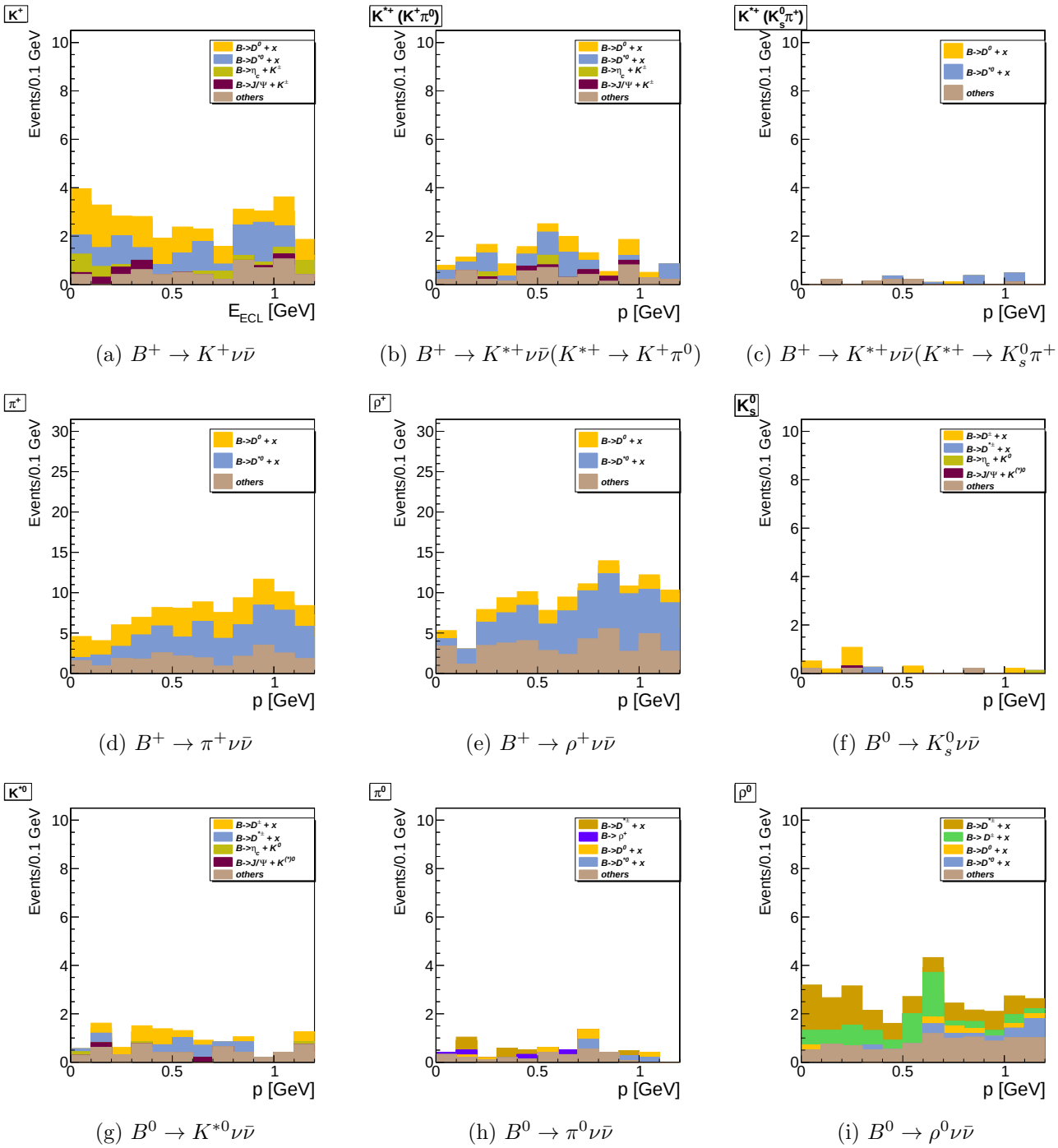

(a) $B^+ \to K^+\nu\bar{\nu}$ (b) $B^+ \to K^{*+}\nu\bar{\nu}(K^{*+} \to K^+\pi^0)$ (c) $B^+ \to K^{*+}\nu\bar{\nu}(K^{*+} \to K^0_s\pi^+)$

(d) $B^+ \to \pi^+\nu\bar{\nu}$ (e) $B^+ \to \rho^+\nu\bar{\nu}$ (f) $B^0 \to K^0_s\nu\bar{\nu}$

(g) $B^0 \to K^{*0}\nu\bar{\nu}$ (h) $B^0 \to \pi^0\nu\bar{\nu}$ (i) $B^0 \to \rho^0\nu\bar{\nu}$

Figure 5.18.: The E_{ECL} distributions of the expected background. Different background components are shown.

5.8. Signal efficiency

Using the signal Monte Carlo we can estimate the signal efficiencies in the signal box ($0 < E_{\mathrm{ECL}} < 1.2\mathrm{GeV}$) after the selection:

$$\epsilon_{sig} = \frac{N_{sig}}{N_{gen}} \quad . \tag{5.1}$$

For each channel a sample with 10 million signal events was generated. We apply the same B_{tag} correction weights on correctly reconstructed B_{tag} candidates as we did for the generic Monte Carlo samples (see section 5.5). One also has to take into account all intermediate branching fractions. The resulting efficiencies and the corrections are summarised in table 5.6. The signal shapes for all channels are shown in fig. 5.19.

Channel	Branching fraction factor	$\epsilon_{sig}[10^{-5}]$ raw	Averaged B_{tag} correction	$\epsilon_{sig}[10^{-5}]$ final
$B^+ \to K^+\nu\bar{\nu}$	-	71.6	0.79	56.76 ± 0.67
$B^+ \to K^{*+}\nu\bar{\nu}$	0.33	22.5	0.80	17.89 ± 0.66
$K^{*+} \to K^+\pi^0$				
$B^+ \to K^{*+}\nu\bar{\nu}$	0.692×0.666	12.9	0.79	10.20 ± 0.60
$K^{*+} \to K^0_s\pi^+$	$\times0.5$			
$B^+ \to K^{*+}\nu\bar{\nu}$				14.73 ± 0.64
combined				
$B^+ \to \pi^+\nu\bar{\nu}$	-	42.3	0.80	33.8 ± 0.52
$B^+ \to \rho^+\nu\bar{\nu}$	-	17.1	0.78	13.47 ± 0.32
$B^0 \to K^0_s\nu\bar{\nu}$	0.692	11.93	0.70	8.36 ± 0.29
$B^0 \to K^{*0}\nu\bar{\nu}$	0.66	18.5	0.74	14.4 ± 0.40
$K^{*0} \to K^+\pi^-$				
$B^0 \to \pi^0\nu\bar{\nu}$	-	23.4	0.71	16.6 ± 0.34
$B^0 \to \rho^0\nu\bar{\nu}$	-	8.8	0.72	6.34 ± 0.21
$B^0 \to \phi\nu\bar{\nu}$	0.492	7.9	0.73	5.77 ± 0.15

Table 5.6.: Signal efficiencies obtained from signal Monte Carlo samples with 10M events each and the corresponding corrections.

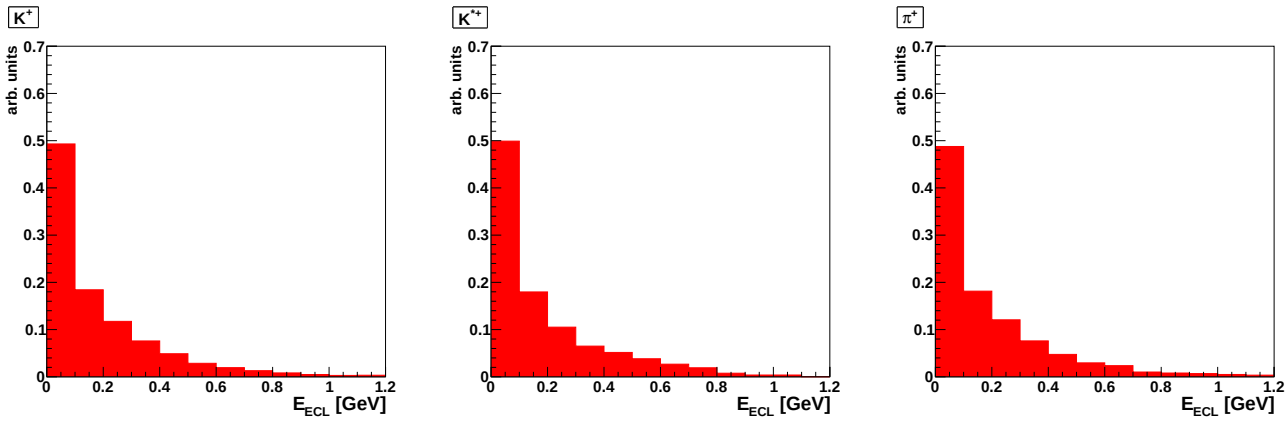

(a) $B^+ \to K^+\nu\bar{\nu}$

(b) $B^+ \to K^{*+}\nu\bar{\nu}$ combined

(c) $B^+ \to \pi^+\nu\bar{\nu}$

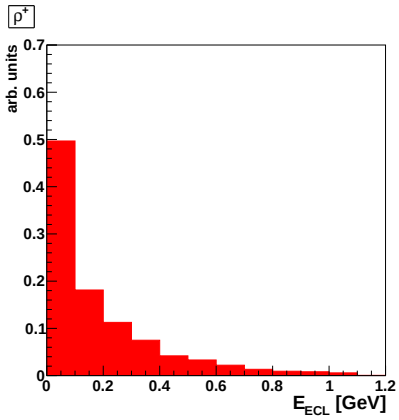

(d) $B^+ \to \rho^+\nu\bar{\nu}$

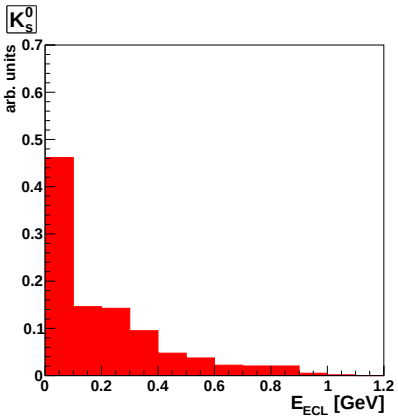

(e) $B^0 \to K^0_s\nu\bar{\nu}$

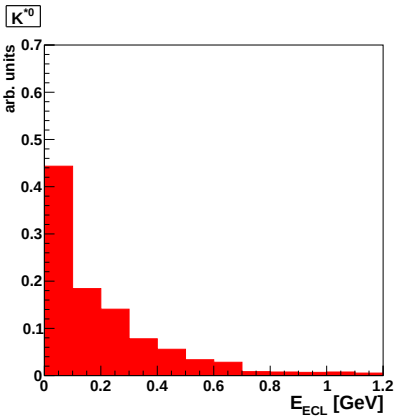

(f) $B^0 \to K^{*0}\nu\bar{\nu}$

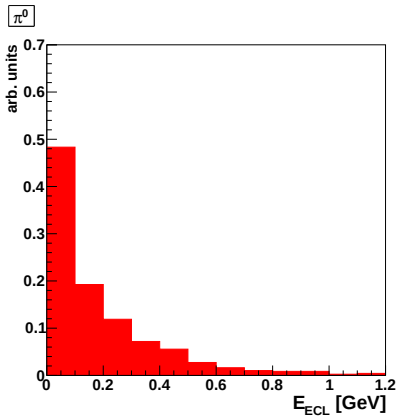

(g) $B^0 \to \pi^0\nu\bar{\nu}$

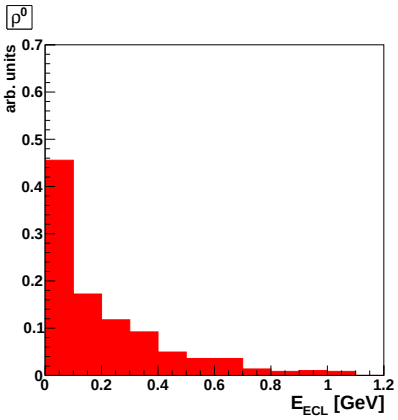

(h) $B^0 \to \rho^0\nu\bar{\nu}$

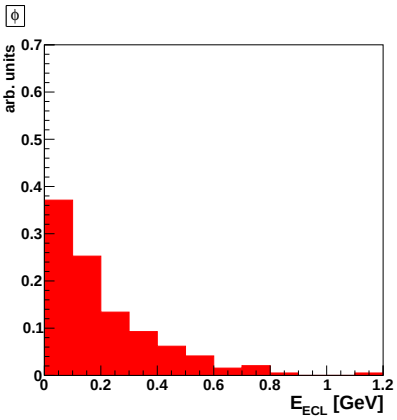

(i) $B^0 \to \phi\nu\bar{\nu}$

Figure 5.19.: The normalised E_{ECL} distributions of the signal Monte Carlo.

5.9. Signal yield extraction

In the previous analysis of these decays within the Belle collaboration [1] [30] the signal yield was extracted by counting. The goal in this analysis is to investigate the option of signal yield estimation through a fit to the E_{ECL} distribution. The signal shape shows a very characteristic shape, especially in the first 3 E_{ECL} bins ($E_{ECL} < 0.3$GeV), which is not taken into account by the counting method. So we expect this approach to lead to better results compared to the counting method. However, we want to use the counting method as a benchmark and compare the expected results between the two approaches.

5.9.1. Counting procedure

For the counting procedure we define new signal and sideband windows for the E_{ECL}. The signal box is between 0 and 0.3 GeV, while the sideband box is between 0.5 and 1.2 GeV. This is illustrated in fig. 5.20 along with an exemplary signal distribution. We use the E_{ECL} sideband to normalise the Monte Carlo expectation to the signal region. In this way we obtain a modified background expectation in the signal window:

$$N^{corrected}_{MC,signalbox} = N_{MC,signalbox} \frac{N_{data,sideband}}{N_{MC,sideband}}$$

The number of observed signal events can then be obtained:

$$N_{signal} = N_{data,signalbox} - N^{corrected}_{MC,signalbox}$$

The statistical error of this procedure is determined from the uncertainties of the expected and observed event numbers. The errors on the background numbers are taken from table 5.5 and the errors on the observed data events are assumed to be Poisson errors.

A study using simulated Monte Carlo experiments was performed to validate this procedure. 10000 Monte Carlo samples with 0 signal and the expected number of background events were simulated and the resulting signal yield calculated. The results are shown in appendix fig. A.13. We can observe small biases in some channels, but in general the input number of events is well reproduced. The strongest bias can be observed in the ϕ and K^0_s channels, which are the channels with the lowest statistics in the background sample. We summarise the results, bias on the mean values and the RMS of the distribution, in table 5.7.

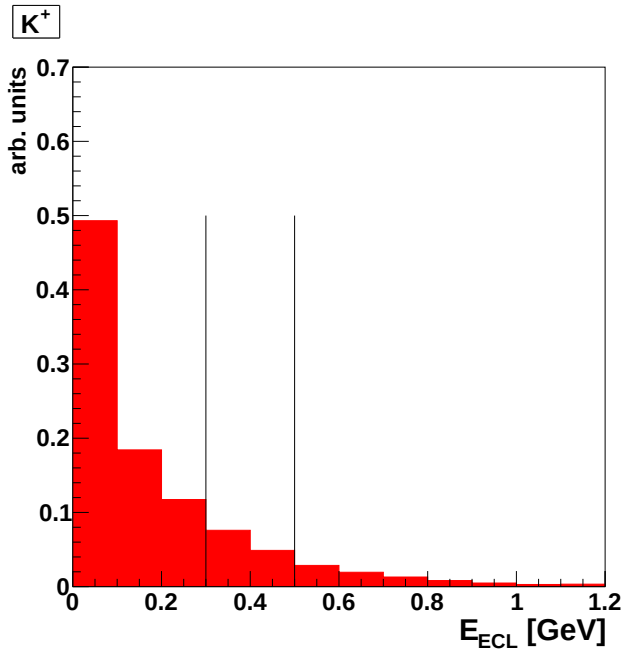

Figure 5.20.: The definitions of the signal and sideband regions for the counting procedure. The signal region is between 0 and 0.3 GeV and the sideband region is between 0.5 and 1.2 GeV.

Now we want to test the procedure for the case, that we observe a signal contribution. We generate the same numbers for background events as before and add 15 signal events to the simulated experiments. The results are shown in appendix fig. A.14. We observe a significant bias in the signal yield distribution, in all channels the reconstructed signal yield is underestimated and below the input value of 15. The results are summarised in table 5.8.

We can conclude that the counting procedure works well in case of 0 signal events and thus can be used to setup a limit on the branching fractions. However, if we would expect a noticeable amount of signal, this procedure would lead to a considerable bias. The reason is, that the signal events are not restricted to the the E_{ECL} region < 0.3GeV, but are also populating the E_{ECL} sideband. In this way the signal events contribute to the excess in the sideband and cause a lower signal excess in the signal region. As we want the procedure to be valid for both cases, signal or no signal observation, the counting method is not an optimal approach.

Channel	Bias of the signal yield	RMS
$B^+ \to K^+\nu\bar{\nu}$	-0.029 ± 0.043	4.24 ± 0.03
$B^+ \to K^{*+}\nu\bar{\nu}$	-0.061 ± 0.025	2.48 ± 0.02
combined		
$B^+ \to \pi^+\nu\bar{\nu}$	-0.175 ± 0.046	4.63 ± 0.03
$B^+ \to \rho^+\nu\bar{\nu}$	0.044 ± 0.047	4.69 ± 0.03
$B^0 \to K^0_s\nu\bar{\nu}$	-0.543 ± 0.021	2.19 ± 0.02
$B^0 \to K^{*0}\nu\bar{\nu}$	0.153 ± 0.023	2.33 ± 0.02
$K^{*0} \to K^+\pi^-$		
$B^0 \to \pi^0\nu\bar{\nu}$	0.045 ± 0.017	1.67 ± 0.01
$B^0 \to \rho^0\nu\bar{\nu}$	0.054 ± 0.038	3.76 ± 0.03
$B^0 \to \phi\nu\bar{\nu}$	-0.624 ± 0.015	1.47 ± 0.01

Table 5.7.: Results of the simulated Monte Carlo experiments counting study with expected background and 0 signal events.

Channel	Bias of the signal yield	RMS
$B^+ \to K^+\nu\bar{\nu}$	-3.76 ± 0.06	5.39 ± 0.04
$B^+ \to K^{*+}\nu\bar{\nu}$	-3.76 ± 0.04	4.32 ± 0.03
combined		
$B^+ \to \pi^+\nu\bar{\nu}$	-3.59 ± 0.06	5.75 ± 0.04
$B^+ \to \rho^+\nu\bar{\nu}$	-3.61 ± 0.006	5.80 ± 0.04
$B^0 \to K^0_s\nu\bar{\nu}$	-6.63 ± 0.05	4.86 ± 0.04
$B^0 \to K^{*0}\nu\bar{\nu}$	-3.97 ± 0.04	4.16 ± 0.03
$K^{*0} \to K^+\pi^-$		
$B^0 \to \pi^0\nu\bar{\nu}$	-3.65 ± 0.04	3.90 ± 0.03
$B^0 \to \rho^0\nu\bar{\nu}$	-4.52 ± 0.05	5.09 ± 0.04
$B^0 \to \phi\nu\bar{\nu}$	-5.67 ± 0.04	4.16 ± 0.03

Table 5.8.: Results of the simulated Monte Carlo experiments counting study with expected background and 15 signal events.

5.9.2. Fitting procedure

To estimate the signal yield an extended binned maximum likelihood fit is performed to the E_{ECL} distribution. We model the PDF shapes for signal and background components with histograms obtained from Monte Carlo and already shown in 5.7 and 5.8. Although

the statistical uncertainty of the background shape is quite high, we consider the continuos histogram PDF obtained from Monte Carlo as the most adequate background model. The uncertainty on this model is however expected to be the largest source of the systematic uncertainty. The way of include this error in the calculation of the systematic error in described in section 6.2. The fit has two free parameters: signal and background yields. The total likelihood is then:

$$\mathcal{L} = \frac{(\sum_j N_j)^N \quad e^{-\sum_j N_j}}{N!} \quad \prod_{i=1}^{N} \sum_j N_j \mathcal{P}_j \quad , \tag{5.2}$$

with N: total number of observed events, j: iterator over fit components (signal and background), N_j: yields (free parameters), i: iterator over events and $\mathcal{P}_j$: PDF of fit components.

One difficulty of this approach is the low statistics in the relevant background Monte Carlo samples. Another related issue is that in some channels we expect only a small number of events, which might lead to instabilities during the fit.

To validate the fitting procedure four different Monte Carlo studies were performed. In the first study we simulated 10000 experiments with 150 background + 50 signal events for each channel. We consider the distributions for the fitted signal yield, error and the pull. The mean value of the signal distribution should reproduce the input value and the pull distribution should have a mean at 0 and a width of 1. The results of this study for three channels are shown in fig. 5.21, the plots for other channels can be found in the appendix fig. A.15. The input values are reproduced correctly and the pulls are normally distributed.

In the next step we want to check the fit performance for 0 signal yield, as this is also our expectation in data. We expect an asymmetrical distribution around 0 for the signal yield, thus we compute asymmetric errors with Minos and we fit the resulting distribution with a bifurcated Gaussian for a better visualisation. The results of the simulated experiments study with 150 background events and 0 signal events are shown in fig. A.16 in the appendix. In general the distributions look as expected.

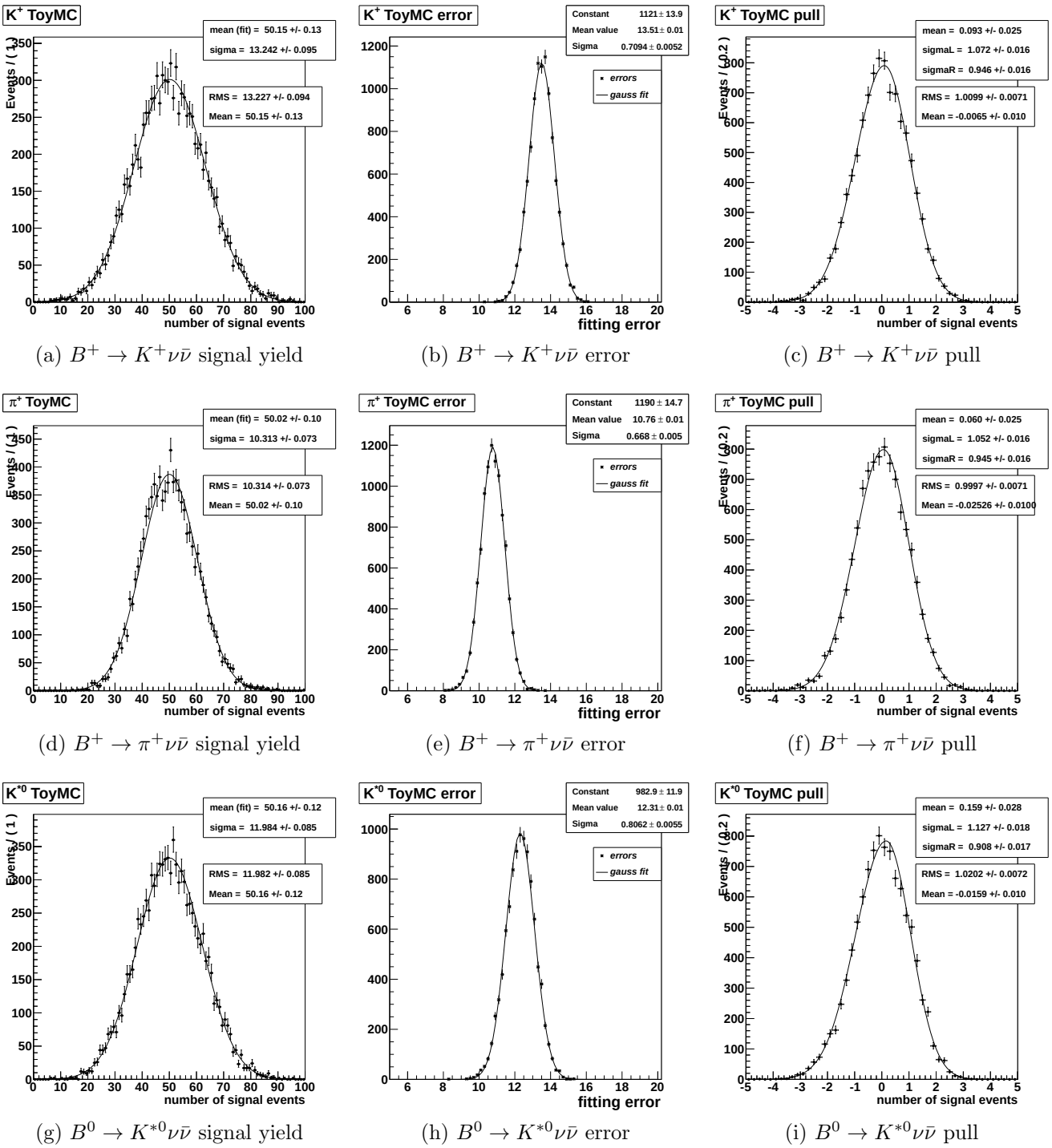

(a) $B^+ \to K^+\nu\bar{\nu}$ signal yield (b) $B^+ \to K^+\nu\bar{\nu}$ error (c) $B^+ \to K^+\nu\bar{\nu}$ pull

(d) $B^+ \to \pi^+\nu\bar{\nu}$ signal yield (e) $B^+ \to \pi^+\nu\bar{\nu}$ error (f) $B^+ \to \pi^+\nu\bar{\nu}$ pull

(g) $B^0 \to K^{*0}\nu\bar{\nu}$ signal yield (h) $B^0 \to K^{*0}\nu\bar{\nu}$ error (i) $B^0 \to K^{*0}\nu\bar{\nu}$ pull

Figure 5.21.: The mean, fitting error and pull distributions of the simulated Monte Carlo experiments study with 150 background and 50 signal events. Here the results for the channels (from up to down) $B^+ \to K^+\nu\bar{\nu}$, $B^+ \to \pi^+\nu\bar{\nu}$ and $B^0 \to K^{*0}\nu\bar{\nu}$ are shown.

In the next step we want to check the fit performance for 0 signal yield and the expected number of background events (see table 5.5). The expected numbers of events is quite low, so we have to check the effect of the low statistics on the fit. At first we consider the results for the channels with number of events larger than 30 (K^+, π^+, ρ^+, ρ^0). The results of these fits are shown in fig. 5.22. The distributions are similar to ones from the previous simulation study, we observe asymmetric Gaussian distributions and no large bias.

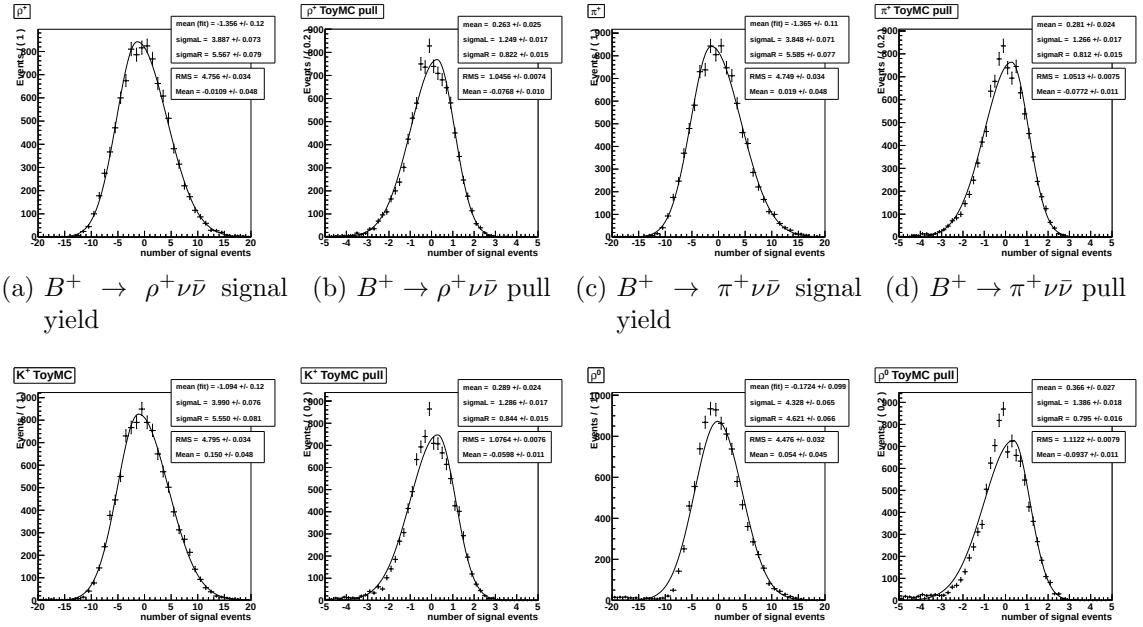

(a) $B^+ \to \rho^+\nu\bar{\nu}$ signal yield (b) $B^+ \to \rho^+\nu\bar{\nu}$ pull (c) $B^+ \to \pi^+\nu\bar{\nu}$ signal yield (d) $B^+ \to \pi^+\nu\bar{\nu}$ pull

(e) $B^+ \to K^+\nu\bar{\nu}$ signal yield (f) $B^+ \to K^+\nu\bar{\nu}$ pull (g) $B^0 \to \rho^0\nu\bar{\nu}$ signal yield (h) $B^0 \to \rho^0\nu\bar{\nu}$ pull

Figure 5.22.: The mean and pull distributions of the simulated Monte Carlo experiments study with expected background and 0 signal events. Here the results for the channels (from left to right, from up to down) with simulated number of background events : $B^+ \to \rho^+\nu\bar{\nu}$ (117), $B^+ \to \pi^+\nu\bar{\nu}$ (102), $B^+ \to K^+\nu\bar{\nu}$ (37) and $B^0 \to \rho^0\nu\bar{\nu}$ (34) are shown.

The expected event numbers for the other 5 channels (K^{*+}, K^{*0}, K^0_s, π^0 and ϕ) are small ($2 < n < 20$), thus fitting the realistic experiments for these channels is more problematic. However, also for these channels more than 95% of the fits converge successfully and we obtain mostly reasonable results. The distributions for these channels are shown in fig. 5.23.

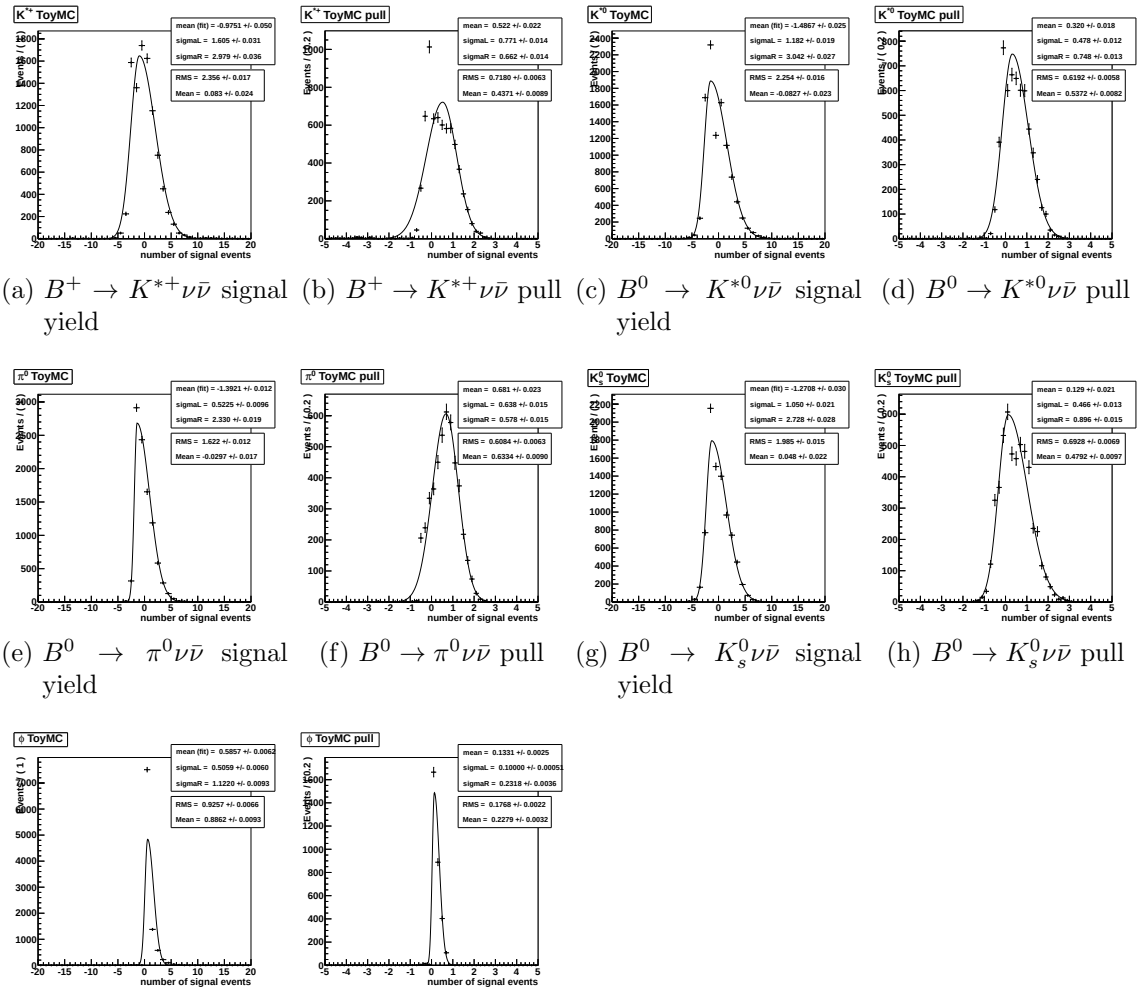

(a) $B^+ \to K^{*+}\nu\bar{\nu}$ signal yield (b) $B^+ \to K^{*+}\nu\bar{\nu}$ pull (c) $B^0 \to K^{*0}\nu\bar{\nu}$ signal yield (d) $B^0 \to K^{*0}\nu\bar{\nu}$ pull

(e) $B^0 \to \pi^0\nu\bar{\nu}$ signal yield (f) $B^0 \to \pi^0\nu\bar{\nu}$ pull (g) $B^0 \to K^0_s\nu\bar{\nu}$ signal yield (h) $B^0 \to K^0_s\nu\bar{\nu}$ pull

(i) $B^0 \to \phi\nu\bar{\nu}$ signal yield (j) $B^0 \to \phi\nu\bar{\nu}$ pull

Figure 5.23.: The mean and pull distributions of the simulated Monte Carlo experiments study with expected background and 0 signal events. Here the results for the channels (from left to right, from up to down) with simulated number of background events :$B^+ \to K^{*+}\nu\bar{\nu}$ (20), $B^0 \to K^{*0}\nu\bar{\nu}$ (14), $B^0 \to \pi^0\nu\bar{\nu}$ (7), $B^0 \to K^{0_s}\nu\bar{\nu}$ (4) and $B^0 \to \phi\nu\bar{\nu}$ (2) are shown.

There are cases where a valid minimum is found, but the error cannot be properly calculated. In these cases we want to use the width of the mean value distribution from the simulated experiments as the error. If the fit procedure should fail, we will perform a likelihood scan to get the minimum manually (the error will be taken from the mean distribution of the simulated experiments as well). The description of this procedure together with examples to validate it are shown in section 5.9.3.

The results for the expected number of background events and no signal contribution are summarised in table 5.9.

Channel	Bias of the signal yield	RMS	Lower error from Gaussian	Upper error from Gaussian
$B^+ \to K^+\nu\bar{\nu}$	0.150 ± 0.048	4.80 ± 0.04	3.99 ± 0.08	5.55 ± 0.08
$B^+ \to K^{*+}\nu\bar{\nu}$ combined	0.083 ± 0.024	2.36 ± 0.02	1.61 ± 0.03	2.98 ± 0.04
$B^+ \to \pi^+\nu\bar{\nu}$	0.019 ± 0.048	4.75 ± 0.03	3.85 ± 0.07	5.59 ± 0.08
$B^+ \to \rho^+\nu\bar{\nu}$	-0.011 ± 0.048	4.76 ± 0.04	3.89 ± 0.07	5.57 ± 0.08
$B^0 \to K^0_s\nu\bar{\nu}$	0.048 ± 0.022	1.99 ± 0.02	1.05 ± 0.02	2.73 ± 0.03
$B^0 \to K^{*0}\nu\bar{\nu}$ $K^{*0} \to K^+\pi^-$	-0.083 ± 0.023	2.26 ± 0.02	1.18 ± 0.02	3.04 ± 0.03
$B^0 \to \pi^0\nu\bar{\nu}$	-0.030 ± 0.017	1.62 ± 0.01	0.53 ± 0.01	2.33 ± 0.02
$B^0 \to \rho^0\nu\bar{\nu}$	0.054 ± 0.045	4.48 ± 0.03	4.33 ± 0.07	4.62 ± 0.07
$B^0 \to \phi\nu\bar{\nu}$	0.886 ± 0.009	0.93 ± 0.01	0.51 ± 0.01	1.11 ± 0.01

Table 5.9.: Results of the simulated Monte Carlo experiments fitting study with expected background and 0 signal events.

Channel	Bias of the signal yield	RMS	Lower error from Gaussian	Upper error from Gaussian
$B^+ \to K^+\nu\bar{\nu}$	0.04 ± 0.07	6.78 ± 0.05	6.21 ± 0.11	7.36 ± 0.12
$B^+ \to K^{*+}\nu\bar{\nu}$ combined	0.05 ± 0.05	5.34 ± 0.04	4.66 ± 0.09	5.99 ± 0.09
$B^+ \to \pi^+\nu\bar{\nu}$	0.05 ± 0.07	6.82 ± 0.05	5.99 ± 0.11	7.64 ± 0.12
$B^+ \to \rho^+\nu\bar{\nu}$	-0.11 ± 0.07	6.73 ± 0.05	6.12 ± 0.11	7.33 ± 0.12
$B^0 \to K^0_s\nu\bar{\nu}$	-0.57 ± 0.07	6.12 ± 0.05	6.24 ± 0.09	6.00 ± 0.09
$B^0 \to K^{*0}\nu\bar{\nu}$ $K^{*0} \to K^+\pi^-$	-0.09 ± 0.06	5.48 ± 0.04	4.74 ± 0.09	6.18 ± 0.09
$B^0 \to \pi^0\nu\bar{\nu}$	-0.15 ± 0.05	5.02 ± 0.04	4.79 ± 0.08	5.25 ± 0.08
$B^0 \to \rho^0\nu\bar{\nu}$	-0.13 ± 0.07	6.60 ± 0.05	5.97 ± 0.11	7.22 ± 0.11
$B^0 \to \phi\nu\bar{\nu}$	-0.15 ± 0.06	5.30 ± 0.04	4.92 ± 0.09	5.66 ± 0.09

Table 5.10.: Results of the simulated Monte Carlo experiments fitting study with expected background and 15 signal events.

We also want to know if the fit will give us a correct result in case of signal observation. We generate the same numbers for background events as before and add 15 signal events to the simulated experiments. The distributions are shown in fig. A.17 and the results are summarised in table 5.10.

5.9.3. Recovery of a failed fit

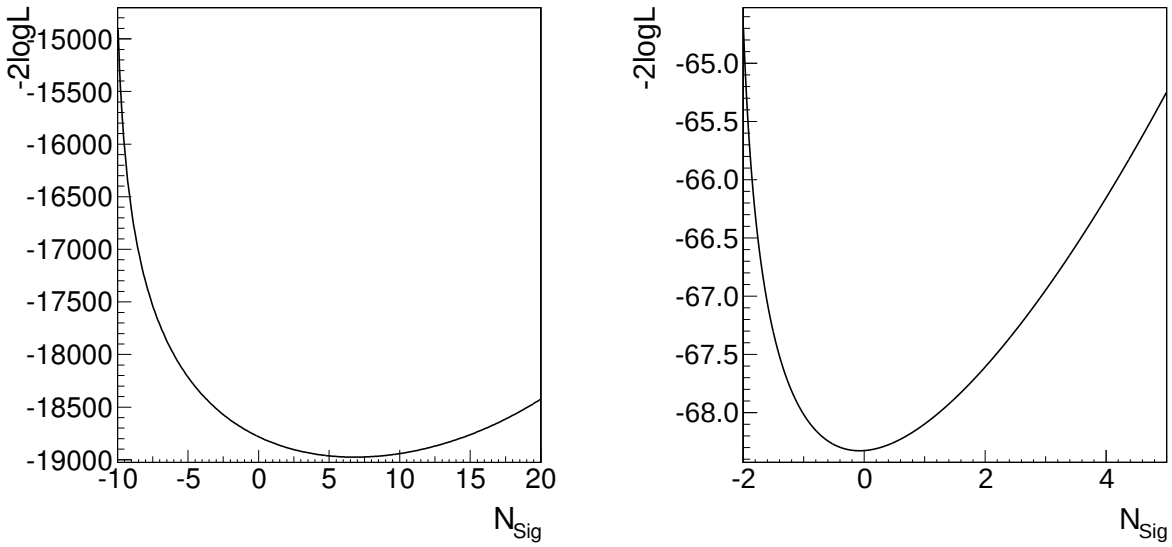

(a) $B^0 \to \rho^0 \nu\bar{\nu}$ (b) $B^+ \to K^{*+} \nu\bar{\nu}$

Figure 5.24.: Likelihood scans for two simulated experiments to illustrate how the minimum can be found manually.

Example	Fit result	Minimum of the scan	RMS from the toy MC
$B^0 \to \rho^0 \nu\bar{\nu}$	$6.82^{+5.89}_{-5.06}$	6.85	± 5.40
$B^+ \to K^{*+} \nu\bar{\nu}$	$-0.08^{+2.58}_{-1.48}$	-0.08	± 2.13

Table 5.11.: Comparison of direct fit results and the results from manual recovery procedure.

For the case of a failed fit or failed error calculation during the fit, an alternative procedure to obtain a valid result was studied. Simulated experiments to compare the results of

both approaches were used: the result obtained directly from the fit and the result of the likelihood scan. The errors can be obtained from a simulated Monte Carlo experiments with the observed number of signal and background events. We quote here the RMS of the distribution, but the asymmetric error determination would be possible too. However, for the calculation of the limit and of the significance we will use the likelihood scan and thus the quoted errors on the signal yield wont be used directly. The results of two examples are shown in fig. 5.24 and table 5.11. The procedure can reproduce the fit results within a satisfactory precision.

5.9.4. Comparison of counting and fitting

The results already presented in the previous subsection are now again summarised in tables 5.12 and 5.13 for a better comparison. The statistical errors and thus the sensitivity of both approaches, counting and fitting, are in average quite similar. However, with the counting method we observed a large bias in case of a noticeable signal amount. The bias is much smaller in case of the fitting. As we want the procedure to be valid for both cases, signal or no signal observation, the fitting method is preferable. We also have to consider, that the lowe efficiency in the counting case will lead to a worse limit. It was shown with simulated Monte Carlo experiments that the fitting approach works well, even for low statistic cases, so we will apply this method on the final data.

Channel	Bias of the signal yield (counting)	RMS (counting)	Bias of the signal yield (fitting)	RMS (fitting)
$B^+ \to K^+\nu\bar{\nu}$	-0.029 ± 0.043	4.24 ± 0.03	0.150 ± 0.048	4.80 ± 0.04
$B^+ \to K^{*+}\nu\bar{\nu}$ combined	-0.061 ± 0.025	2.48 ± 0.02	0.083 ± 0.024	2.36 ± 0.02
$B^+ \to \pi^+\nu\bar{\nu}$	-0.175 ± 0.046	4.63 ± 0.03	0.019 ± 0.048	4.75 ± 0.03
$B^+ \to \rho^+\nu\bar{\nu}$	0.044 ± 0.047	4.69 ± 0.03	-0.011 ± 0.048	4.76 ± 0.04
$B^0 \to K_s^0\nu\bar{\nu}$	-0.543 ± 0.021	2.19 ± 0.02	0.048 ± 0.022	1.99 ± 0.02
$B^0 \to K^{*0}\nu\bar{\nu}$ $K^{*0} \to K^+\pi^-$	0.153 ± 0.023	2.33 ± 0.02	-0.083 ± 0.023	2.26 ± 0.02
$B^0 \to \pi^0\nu\bar{\nu}$	0.045 ± 0.017	1.67 ± 0.01	-0.030 ± 0.017	1.62 ± 0.01
$B^0 \to \rho^0\nu\bar{\nu}$	0.054 ± 0.038	3.76 ± 0.03	0.054 ± 0.045	4.48 ± 0.03
$B^0 \to \phi\nu\bar{\nu}$	-0.624 ± 0.015	1.47 ± 0.01	0.886 ± 0.009	0.93 ± 0.01

Table 5.12.: Results of the simulated Monte Carlo experiments study with expected background and 0 signal events with counting and fitting approach in comparison.

Channel	Bias of the signal yield (counting)	RMS (counting)	Bias of the signal yield (fitting)	RMS (fitting)
$B^+ \to K^+\nu\bar{\nu}$	-3.76 ± 0.06	5.39 ± 0.04	0.04 ± 0.07	6.78 ± 0.05
$B^+ \to K^{*+}\nu\bar{\nu}$	-3.76 ± 0.04	4.32 ± 0.03	0.05 ± 0.05	5.34 ± 0.04
combined				
$B^+ \to \pi^+\nu\bar{\nu}$	-3.59 ± 0.06	5.75 ± 0.04	0.05 ± 0.07	6.82 ± 0.05
$B^+ \to \rho^+\nu\bar{\nu}$	-3.61 ± 0.006	5.80 ± 0.04	-0.11 ± 0.07	6.73 ± 0.05
$B^0 \to K_s^0\nu\bar{\nu}$	-6.63 ± 0.05	4.86 ± 0.04	-0.57 ± 0.07	6.12 ± 0.05
$B^0 \to K^{*0}\nu\bar{\nu}$	-3.97 ± 0.04	4.16 ± 0.03	-0.09 ± 0.06	5.48 ± 0.04
$K^{*0} \to K^+\pi^-$				
$B^0 \to \pi^0\nu\bar{\nu}$	-3.65 ± 0.04	3.90 ± 0.03	-0.15 ± 0.05	5.02 ± 0.04
$B^0 \to \rho^0\nu\bar{\nu}$	-4.52 ± 0.05	5.09 ± 0.04	-0.13 ± 0.07	6.60 ± 0.05
$B^0 \to \phi\nu\bar{\nu}$	-5.67 ± 0.04	4.16 ± 0.03	-0.15 ± 0.06	5.30 ± 0.04

Table 5.13.: Results of the simulated Monte Carlo experiments study with expected background and 15 signal events with counting and fitting approach in comparison.

5.10. Limit and significance estimation

5.10.1. Expected limits

As we expect no significant signal, we prepare the procedure to set up an upper limit on each branching fraction. This upper limit for number of signal events at 90% confidence limit will be obtained by integrating the likelihood function $\mathcal{L}(n)$:

$$\int_0^N \mathcal{L}(n)dn = 0.9 \int_0^\infty \mathcal{L}(n)dn \quad . \tag{5.3}$$

With N_{sig} = upper limit for number of signal events, $N_{B\bar{B}}$ = number of $B\bar{B}$ pairs and ϵ_{sig} = signal efficiency, we can obtain the limit on the branching fraction:

$$\mathcal{B} = \frac{N_{sig}}{N_{B\bar{B}} \times \epsilon_{sig}} \tag{5.4}$$

Using simulated experiments we can estimate the expected branching fraction limit. We use the simulated sample with expected numbers of background events and no signal events and calculate the branching fraction limit for each experiment. In fig. 5.25 the distributions of the limits for 1000 experiments for each channel are shown. We summarise the best obtained limits as well as the mean values of the distributions in table 5.14. The systematics are not included in this calculation. We also cite the expected limits of the

previous analysis [1] for comparison. The limits in the previous analysis were determined in a different way: it was a counting experiment and the expected limit was determined in case exactly the expected number of background events was observed in the signal box.

The limit depends very strongly on the total number of background events. For some channels the expected event numbers are similar compared to the previous analysis, thus we get similar expected limits. For other channels the expected event numbers could be reduced significantly, thus leading to much better expected limits.

Channel	Best expected branching ratio limit at 90% CL	Average expected branching ratio limit at 90% CL	Expected branching ratio limit at 90% CL previous Belle analysis (492fb^{-1})
$B^+ \to K^+\nu\bar{\nu}$	1.0×10^{-5}	2.2×10^{-5}	10×10^{-5}
$B^+ \to K^{*+}\nu\bar{\nu}$ combined	2.8×10^{-5}	5.3×10^{-5}	22×10^{-5}
$B^+ \to \pi^+\nu\bar{\nu}$	1.9×10^{-5}	3.9×10^{-5}	10×10^{-5}
$B^+ \to \rho^+\nu\bar{\nu}$	4.2×10^{-5}	9.7×10^{-5}	19×10^{-5}
$B^0 \to K_s^0\nu\bar{\nu}$	4.0×10^{-5}	7.3×10^{-5}	16×10^{-5}
$B^0 \to K^{*0}\nu\bar{\nu}$ $K^{*0} \to K^+\pi^-$	2.3×10^{-5}	4.9×10^{-5}	20×10^{-5}
$B^0 \to \pi^0\nu\bar{\nu}$	2.1×10^{-5}	3.6×10^{-5}	10×10^{-5}
$B^0 \to \rho^0\nu\bar{\nu}$	8.5×10^{-5}	16.5×10^{-5}	16×10^{-5}
$B^0 \to \phi\nu\bar{\nu}$	5.4×10^{-5}	9.1×10^{-5}	13×10^{-5}

Table 5.14.: Expected limits on branching fractions obtained from simulated experiments.

5.10.2. Significance

For the case of a signal contribution we prepare the procedure to estimate the significance of this observation. The significance is calculated by comparing the likelihood values at maximum and at 0:

$$S = \sqrt{2\log\left(\frac{\mathcal{L}_{max}}{\mathcal{L}_0}\right)} \quad . \tag{5.5}$$

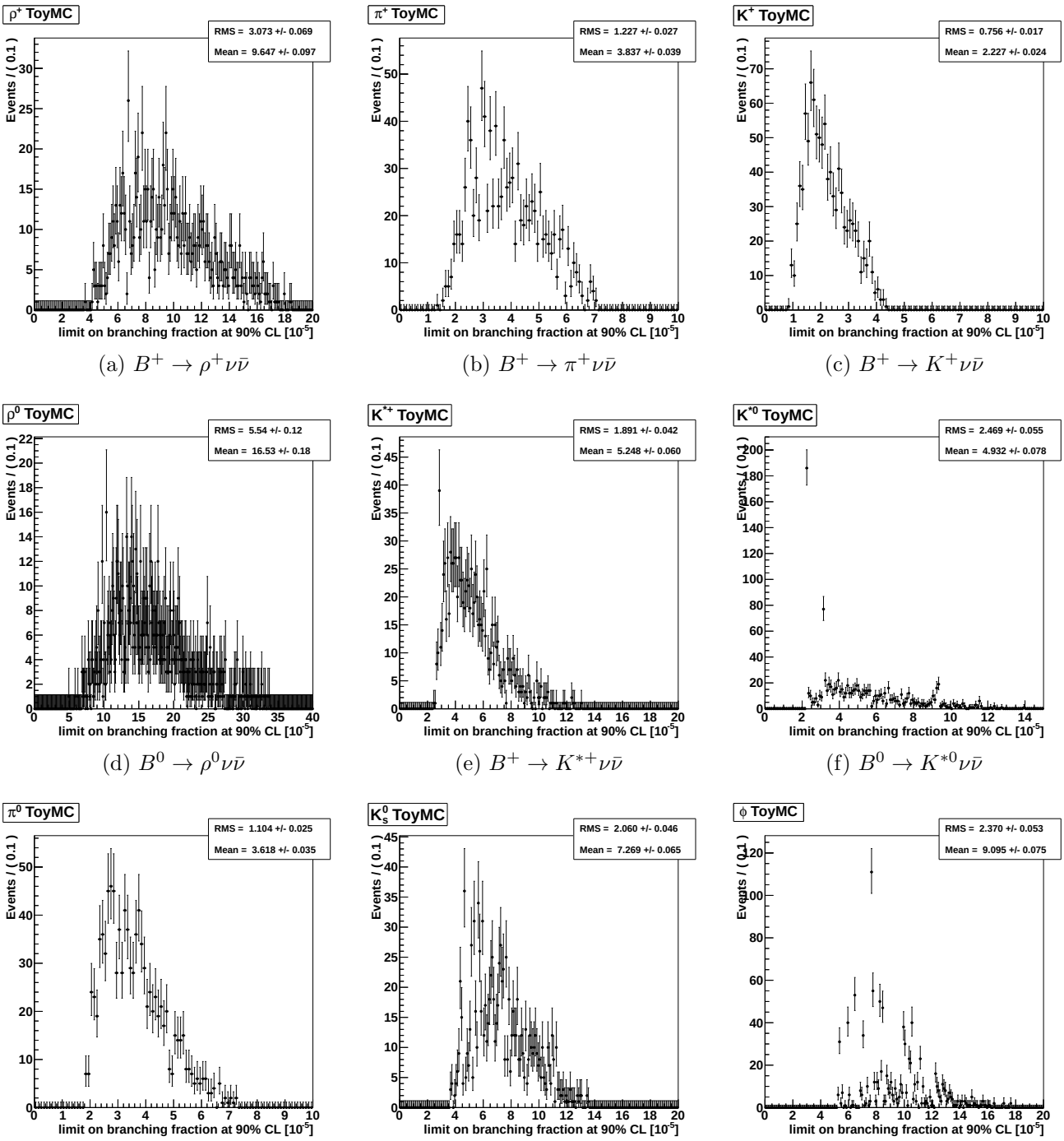

(a) $B^+ \to \rho^+ \nu\bar{\nu}$ (b) $B^+ \to \pi^+ \nu\bar{\nu}$ (c) $B^+ \to K^+ \nu\bar{\nu}$

(d) $B^0 \to \rho^0 \nu\bar{\nu}$ (e) $B^+ \to K^{*+} \nu\bar{\nu}$ (f) $B^0 \to K^{*0} \nu\bar{\nu}$

(g) $B^0 \to \pi^0 \nu\bar{\nu}$ (h) $B^0 \to K^0_s \nu\bar{\nu}$ (i) $B^0 \to \phi \nu\bar{\nu}$

Figure 5.25.: Branching fraction limits obtained from 1000 simulated Monte Carlo experiments.

5.11. Systematic errors

There are several sources of systematic uncertainties, those of them which can be determined before looking into data are listed below:

- **The number of $B\bar{B}$ pairs**
  The number of $B\bar{B}$ pairs used in this analysis is 771×10^6 with an error of 1.4%.
- **Track reconstruction efficiency**
  The systematic uncertainty on each single charged track is 0.35% [43].
- K_s^0 **reconstruction efficiency** The systematic uncertainty on the reconstruction efficiency is 2.23% [44].
- π^0 **reconstruction efficiency**
  The systematic error on the π^0 reconstruction efficiency is estimated to be 4% [45].
- K/π **particle identification**
  As this error will be negligible compared to the dominant errors, we renounce the exact determination of this error for each channel and assume a tolerant 2% error for each K or π track.
- B_{tag} **efficiency**
  As described in section 5.5, we apply a B_{tag} correction to compensate for the difference in the B_{tag} efficiency between data and Monte Carlo. The errors of these correction factors were determined in [41] to be 4.2% for charged B and 4.5% for neutral B.
- **Veto efficiency**
  The difference in the charged track an π^0 veto efficiency was studied in [30] using a $D^{(*)}l\nu$ sample. We include the obtained 8.3% as a systematic error on the signal efficiency.

Following two errors will be determined after obtaining the fit results on data:

- **Fit bias**
  Simulated Monte Carlo experiments with observed event numbers will be performed and if there is a bias, it will be included as systematic error.
- **Background model**
  We will replace the nominal background model (histogram obtained from MC) with other models. We will fit each default background model with two different appropriate functions (Chebyshev polynomials), and use the resulting model to repeat the main fit. The largest deviation from the nominal fit will be assigned as systematic uncertainty.

6. Results

At first we compare the total numbers of observed events in the signal box $E_{\mathrm{ECL}} < 1.2$ GeV with our expectations from simulated Monte Carlo experiments. The results are shown in table 6.1. Except for the ρ^+ channel and the $K^{*+}(K_s^0\pi^+)$ subchannel, where we observe less events than expected, the observed event numbers are in good agreement with the expectations.

Channel	MC expectation	Data
$B^+ \to K^+\nu\bar{\nu}$	36.8 ± 2.8	43 ± 6.6
$B^+ \to K^{*+}\nu\bar{\nu}$	17.2 ± 1.9	21 ± 4.6
$K^{*+} \to K^+\pi^0$		
$B^+ \to K^{*+}\nu\bar{\nu}$	2.4 ± 0.7	0
$K^{*+} \to K_s^0\pi^+$		
$B^+ \to K^{*+}\nu\bar{\nu}$	19.6 ± 2.1	21 ± 4.6
combined		
$B^+ \to \pi^+\nu\bar{\nu}$	101.4 ± 4.7	107 ± 10.4
$B^+ \to \rho^+\nu\bar{\nu}$	117.0 ± 5.1	90 ± 9.5
$B^0 \to K_s^0\nu\bar{\nu}$	3.4 ± 0.9	4 ± 2
$B^0 \to K^{*0}\nu\bar{\nu}$	13.8 ± 1.7	10 ± 3.2
$K^{*0} \to K^+\pi^-$		
$B^0 \to \pi^0\nu\bar{\nu}$	7.3 ± 1.3	6 ± 2.5
$B^0 \to \rho^0\nu\bar{\nu}$	33.7 ± 2.7	31 ± 5.6
$B^0 \to \phi\nu\bar{\nu}$	2.1 ± 0.6	3 ± 1.7

Table 6.1.: Comparison of the event numbers observed in data with the expected numbers from simulated Monte Carlo experiments.

6.1. Fit results

In fig. 6.1 the final fit results are shown. In table 6.2 the resulting signal yields are summarised.

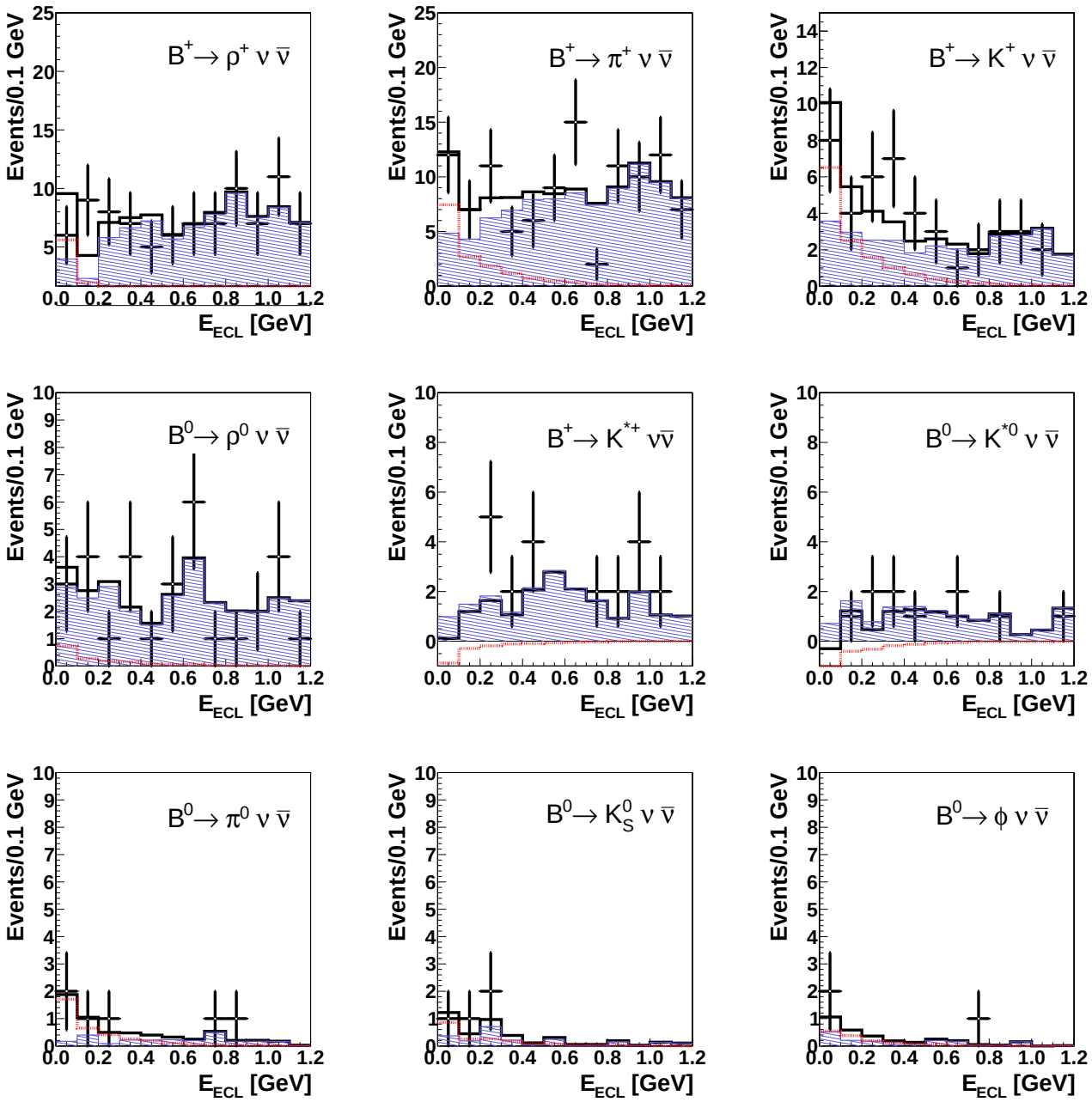

Figure 6.1.: Fit results to the E_{ECL} distributions. Points with error bars are data and the black solid line is the total result. The blue cross-hatched region is the background component and the red dashed line shows the signal contribution.

Channel	Signal yield
$B^+ \to K^+\nu\bar{\nu}$	$13.3^{+7.4}_{-6.6}$
$B^+ \to K^{*+}\nu\bar{\nu}$ combined	$-1.7^{+1.7}_{-1.1}$
$B^+ \to \pi^+\nu\bar{\nu}$	$15.2^{+7.1}_{-6.2}$
$B^+ \to \rho^+\nu\bar{\nu}$	$11.3^{+6.3}_{-5.4}$
$B^0 \to K^0_s\nu\bar{\nu}$	$1.8^{+3.3}_{-2.4}$
$B^0 \to K^{*0}\nu\bar{\nu}$ $K^{*0} \to K^+\pi^-$	$-2.3^{+10.2}_{-3.5}$
$B^0 \to \pi^0\nu\bar{\nu}$	$3.5^{+2.6}_{-1.9}$
$B^0 \to \rho^0\nu\bar{\nu}$	$1.6^{+5.0}_{-4.1}$
$B^0 \to \phi\nu\bar{\nu}$	$1.4^{+2.9}_{-0.9}$

Table 6.2.: Signal yields and statistical errors obtained from the fit to data.

6.2. Systematic errors

Apart from the systematics determined in section 5.11, we determine the two remaining errors.

Fit bias
To determine the fit bias we perform simulated Monte Carlo experiments using the event numbers observed in data as input. Then we perform the fit procedure and check if the signal yield is correctly reproduced. In case the deviation between the central value of the number of signal events and the input value is larger than the error on that value, we include the deviation as systematic error. The results are shown in table 6.3.

Background shape
To evaluate uncertainty on the background shape, we fit our nominal background model, a histogram PDF, with two functions. We select two functions which describe the background shape in the most adequate way. The main fit is repeated using the

new background model and the deviation from the nominal fit is calculated. The results are summarised in table 6.4. We include the largest deviation as a systematic error.

To get the total error all individual errors are added in quadrature. All systematic errors are summarised in table 6.5.

Channel	Fit bias [number of events]
$B^+ \to K^+\nu\bar{\nu}$	-
$B^+ \to K^{*+}\nu\bar{\nu}$ combined	0.14
$B^+ \to \pi^+\nu\bar{\nu}$	-
$B^+ \to \rho^+\nu\bar{\nu}$	-
$B^0 \to K^0_s\nu\bar{\nu}$	-
$B^0 \to K^{*0}\nu\bar{\nu}$ $K^{*0} \to K^+\pi^-$	0.64
$B^0 \to \pi^0\nu\bar{\nu}$	0.41
$B^0 \to \rho^0\nu\bar{\nu}$	0.12
$B^0 \to \phi\nu\bar{\nu}$	0.63

Table 6.3.: Fit bias from the simulated experiments.

Channel	0 order Chebyshev polynomial	1st order Chebyshev polynomial	2nd order Chebyshev polynomial
$B^+ \to K^+\nu\bar{\nu}$	15.7%	3%	-
$B^+ \to K^{*+}\nu\bar{\nu}$ combined	74%	89%	-
$B^+ \to \pi^+\nu\bar{\nu}$	-	6.0%	6.1%
$B^+ \to \rho^+\nu\bar{\nu}$	-	35.4%	26.7%
$B^0 \to K^0_s\nu\bar{\nu}$	53%	53%	-
$B^0 \to K^{*0}\nu\bar{\nu}$ $K^{*0} \to K^+\pi^-$	10%	23.8%	-
$B^0 \to \pi^0\nu\bar{\nu}$	1.2%	10.6%	-
$B^0 \to \rho^0\nu\bar{\nu}$	-	22.7%	18.6%
$B^0 \to \phi\nu\bar{\nu}$	32.8%	5.6%	-

Table 6.4.: Deviations from the nominal fit for alternative background models.

Channel	$N_{B\bar{B}}$	Track/π^0/K_s^0 reconstruction efficiency	PID	Signal reconstruction efficiency	B_{tag} correction	Vetoes	Fit bias	Background model	total
$B^+ \to K^+\nu\bar{\nu}$	1.4	0.25	2	1.2	4.2	8.3	-	15.7	18.5
$B^+ \to K^{*+}\nu\bar{\nu}$	1.4	4.1	4	3.7	4.2	8.3	7.9	89	90.2
combined									
$B^+ \to \pi^+\nu\bar{\nu}$	1.4	0.35	2	1.5	4.2	8.3	-	6.1	11.5
$B^+ \to \rho^+\nu\bar{\nu}$	1.4	4.2	2	2.3	4.2	8.3	-	35.4	37.2
$B^0 \to K_s^0\nu\bar{\nu}$	1.4	2.33	2	3.5	4.5	8.3	-	53	54.0
$B^0 \to K^{*0}\nu\bar{\nu}$	1.4	0.35	4	2.8	4.5	8.3	28	24	38.4
$K^{*0} \to K^+\pi^-$									
$B^0 \to \pi^0\nu\bar{\nu}$	1.4	4.0	-	2.1	4.5	8.3	11.7	10.6	19.0
$B^0 \to \rho^0\nu\bar{\nu}$	1.4	0.7	4	3.3	4.5	8.3	7.3	22.7	26.2
$B^0 \to \phi\nu\bar{\nu}$	1.4	1.4	4	2.6	4.5	8.3	44.0	32.8	55.9

Table 6.5.: Summary of all systematic errors in %.

6.3. Final results

We perform a likelihood scan to determine the significance of the result according to 5.5 and the branching fraction limit, as expained in 5.10.1. To include the systematics we convolute the likelihood curve numerically with a Gaussian, where the systematic error is taken as the width of the Gaussian. The scans are shown in fig. 6.2.

The final signal yields with corresponding statistical and systematical errors are shown together with the significance of the observed signal contribution in table 6.6. The systematical errors are in general smaller than statistical errors. We observe no significant signal, although we obtain values larger then 2σ for two channels (K^+ and π^+).

In table 6.7 we summarise the final limits obtained from the scans shown in fig. 6.2 and compare them to the results from the previous Belle analysis as well as with the current world best limits collected by the Particle Data Group (PDG). Most of the limits could be improved compared to the previous Belle analysis. The limits which are better compared to current PDG values are marked in bold.

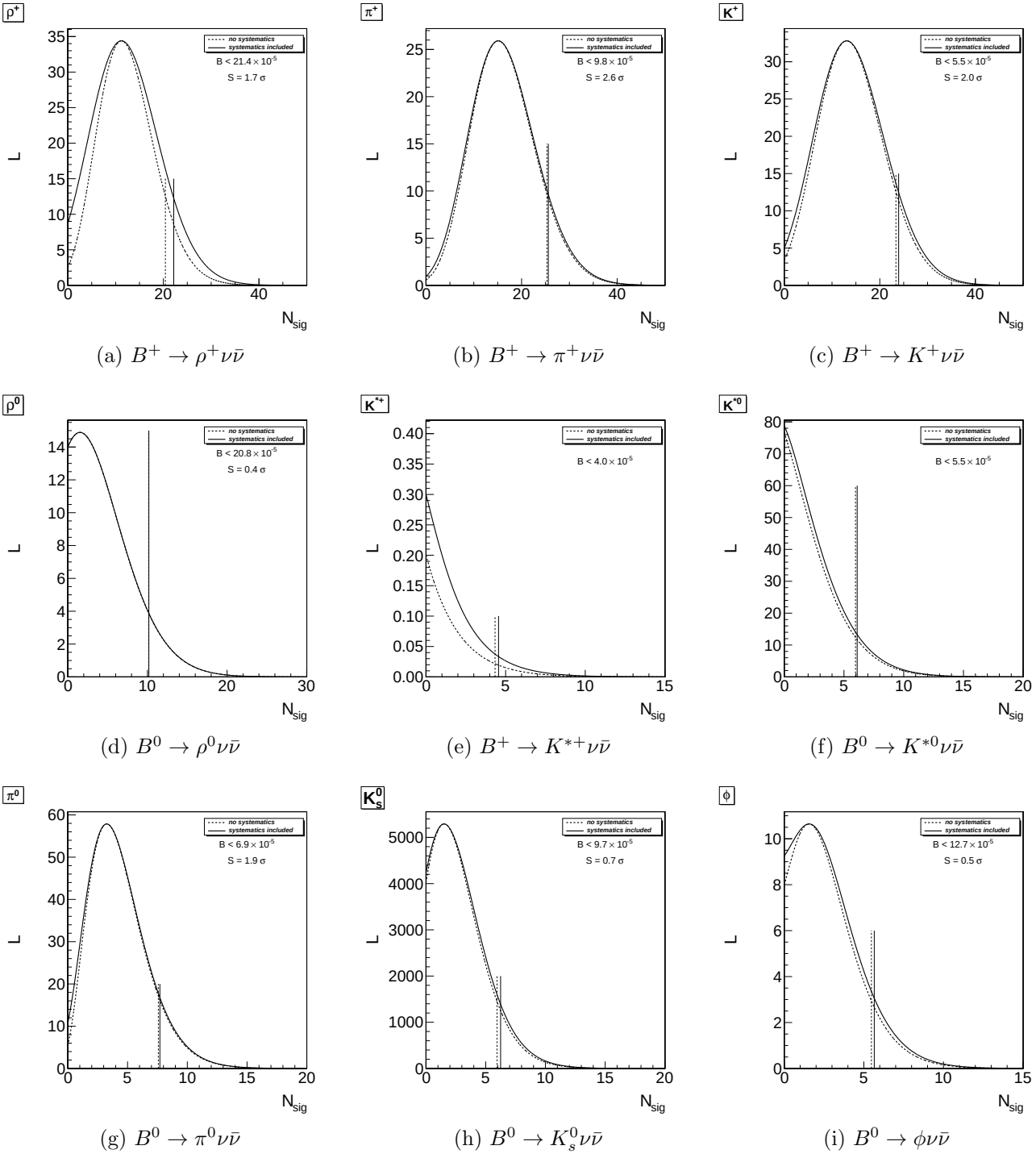

(a) $B^+ \to \rho^+ \nu\bar{\nu}$ (b) $B^+ \to \pi^+ \nu\bar{\nu}$ (c) $B^+ \to K^+ \nu\bar{\nu}$

(d) $B^0 \to \rho^0 \nu\bar{\nu}$ (e) $B^+ \to K^{*+} \nu\bar{\nu}$ (f) $B^0 \to K^{*0} \nu\bar{\nu}$

(g) $B^0 \to \pi^0 \nu\bar{\nu}$ (h) $B^0 \to K_s^0 \nu\bar{\nu}$ (i) $B^0 \to \phi \nu\bar{\nu}$

Figure 6.2.: Likelihood distributions and the according significance and branching fraction limit at 90% CL. The dotted lines show the distribution and the limit without the systematics, while the solid lines show the total result.

Channel	Signal yield	Significance
$B^+ \to K^+\nu\bar{\nu}$	$13.3^{+7.4}_{-6.6}(stat) \pm 2.5(syst)$	2.0σ
$B^+ \to K^{*+}\nu\bar{\nu}$ combined	$-1.7^{+1.7}_{-1.1}(stat) \pm 1.5(syst)$	-
$B^+ \to \pi^+\nu\bar{\nu}$	$15.2^{+7.1}_{-6.2}(stat) \pm 1.8(syst)$	2.6σ
$B^+ \to \rho^+\nu\bar{\nu}$	$11.3^{+6.3}_{-5.4}(stat) \pm 4.2(syst)$	1.7σ
$B^0 \to K^0_s\nu\bar{\nu}$	$1.8^{+3.3}_{-2.4}(stat) \pm 1.0(syst)$	0.7σ
$B^0 \to K^{*0}\nu\bar{\nu}$ $K^{*0} \to K^+\pi^-$	$-2.3^{+10.2}_{-3.5}(stat) \pm 0.9(syst)$	-
$B^0 \to \pi^0\nu\bar{\nu}$	$3.5^{+2.6}_{-1.9}(stat) \pm 0.7(syst)$	1.9σ
$B^0 \to \rho^0\nu\bar{\nu}$	$1.6^{+5.0}_{-4.1}(stat) \pm 0.4(syst)$	0.4σ
$B^0 \to \phi\nu\bar{\nu}$	$1.4^{+2.9}_{-0.9}(stat) \pm 0.8(syst)$	0.5σ

Table 6.6.: Signal yields obtained from the fit to data with statistical and systematic errors and the significance of the signal contribution.

Channel	Branching ratio limit at 90% CL	Branching ratio limit at 90% CL previous Belle analysis [1]	PDG limit at 90% CL [2]
$B^+ \to K^+\nu\bar{\nu}$	5.5×10^{-5}	1.4×10^{-5}	1.3×10^{-5}
$B^+ \to K^{*+}\nu\bar{\nu}$ combined	$\mathbf{4.0 \times 10^{-5}}$	14×10^{-5}	8×10^{-5}
$B^+ \to \pi^+\nu\bar{\nu}$	$\mathbf{9.8 \times 10^{-5}}$	17×10^{-5}	10×10^{-5}
$B^+ \to \rho^+\nu\bar{\nu}$	21.4×10^{-5}	15×10^{-5}	15×10^{-5}
$B^0 \to K^0_s\nu\bar{\nu}$	9.7×10^{-5}	16×10^{-5}	5.6×10^{-5}
$B^0 \to K^{*0}\nu\bar{\nu}$ $K^{*0} \to K^+\pi^-$	5.5×10^{-5}	34×10^{-5}	1.2×10^{-5}
$B^0 \to \pi^0\nu\bar{\nu}$	$\mathbf{6.9 \times 10^{-5}}$	22×22^{-5}	22×10^{-5}
$B^0 \to \rho^0\nu\bar{\nu}$	$\mathbf{20.8 \times 10^{-5}}$	44×10^{-5}	44×10^{-5}
$B^0 \to \phi\nu\bar{\nu}$	12.7×10^{-5}	5.8×10^{-5}	5.8×10^{-5}

Table 6.7.: Branching fraction limits at 90% CL.

6.3.1. Investigation of the signal contribution

Although we do not observe significant signal contributions, we do observe a considerable amount of signal events with a significance of around 2σ in two channels, K^+ and π^+. We want to investigate these events by looking at the missing mass and the missing momentum direction distributions for these two channels. We compare the prediction from Monte Carlo and data to check for inconsistencies.

- **Missing mass**

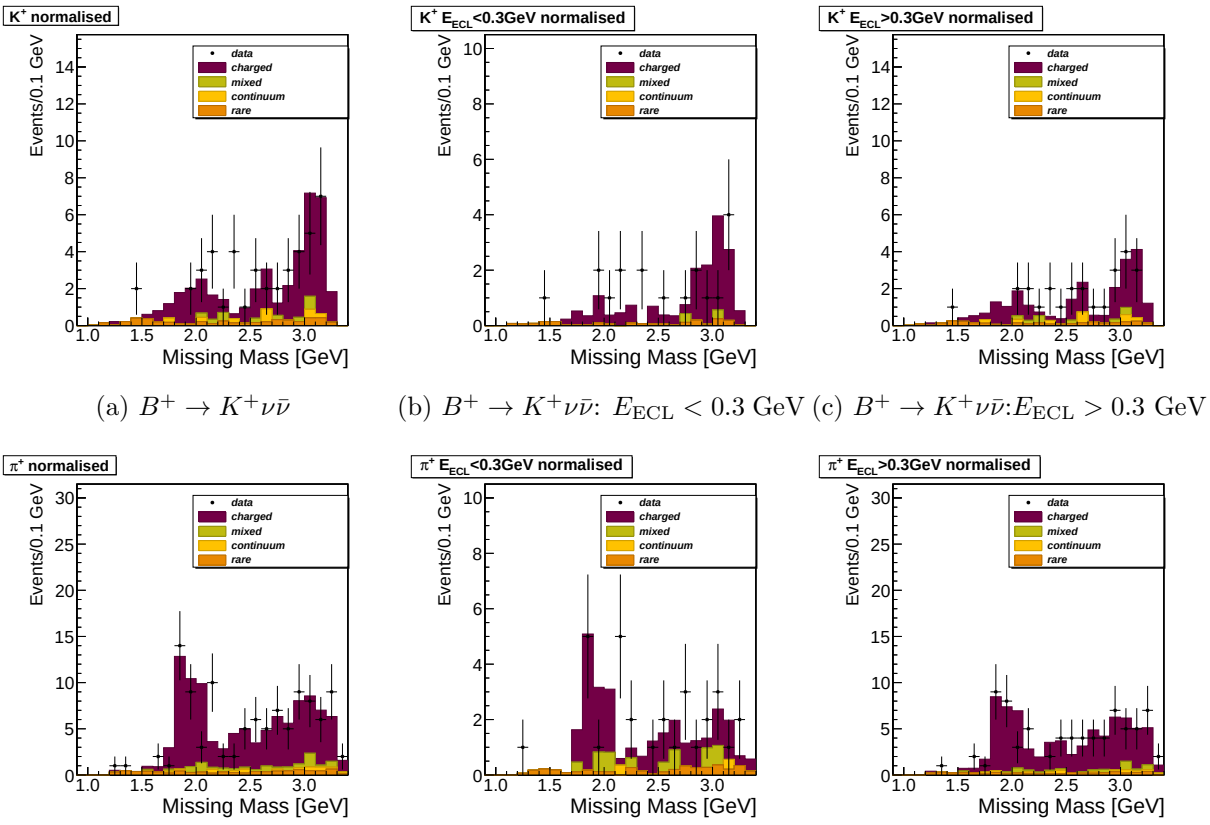

(a) $B^+ \to K^+\nu\bar{\nu}$ (b) $B^+ \to K^+\nu\bar{\nu}$: $E_{\mathrm{ECL}} < 0.3$ GeV (c) $B^+ \to K^+\nu\bar{\nu}$:$E_{\mathrm{ECL}} > 0.3$ GeV

(d) $B^+ \to \pi^+\nu\bar{\nu}$ (e) $B^+ \to \pi^+\nu\bar{\nu}$: $E_{\mathrm{ECL}} < 0.3$ GeV (f) $B^+ \to \pi^+\nu\bar{\nu}$: $E_{\mathrm{ECL}} > 0.3$ GeV

Figure 6.3.: Missing mass distributions for K^+ and π^+ channels with data and Monte Carlo normalised to the same number of entries. From left to right the whole E_{ECL} region, $E_{\mathrm{ECL}} < 0.3$ GeV, and $E_{\mathrm{ECL}} > 0.3$ GeV are shown.

In fig. 6.3 the missing mass distributions for the whole E_{ECL} region, for $E_{\mathrm{ECL}} < 0.3$ GeV ,and $E_{\mathrm{ECL}} > 0.3$ GeV are shown. These histograms are normalised to the same number of entries. Not normalised histograms can be found in appendix fig. A.18.

We can see, that we have have more events in data than expected from Monte Carlo in the signal region $E_{\mathrm{ECL}} < 0.3$ GeV. However, we cannot observe any significant deviation from the expected shape or any specific structure that would explain the excess.

- **Angle between missing momentum and beam**

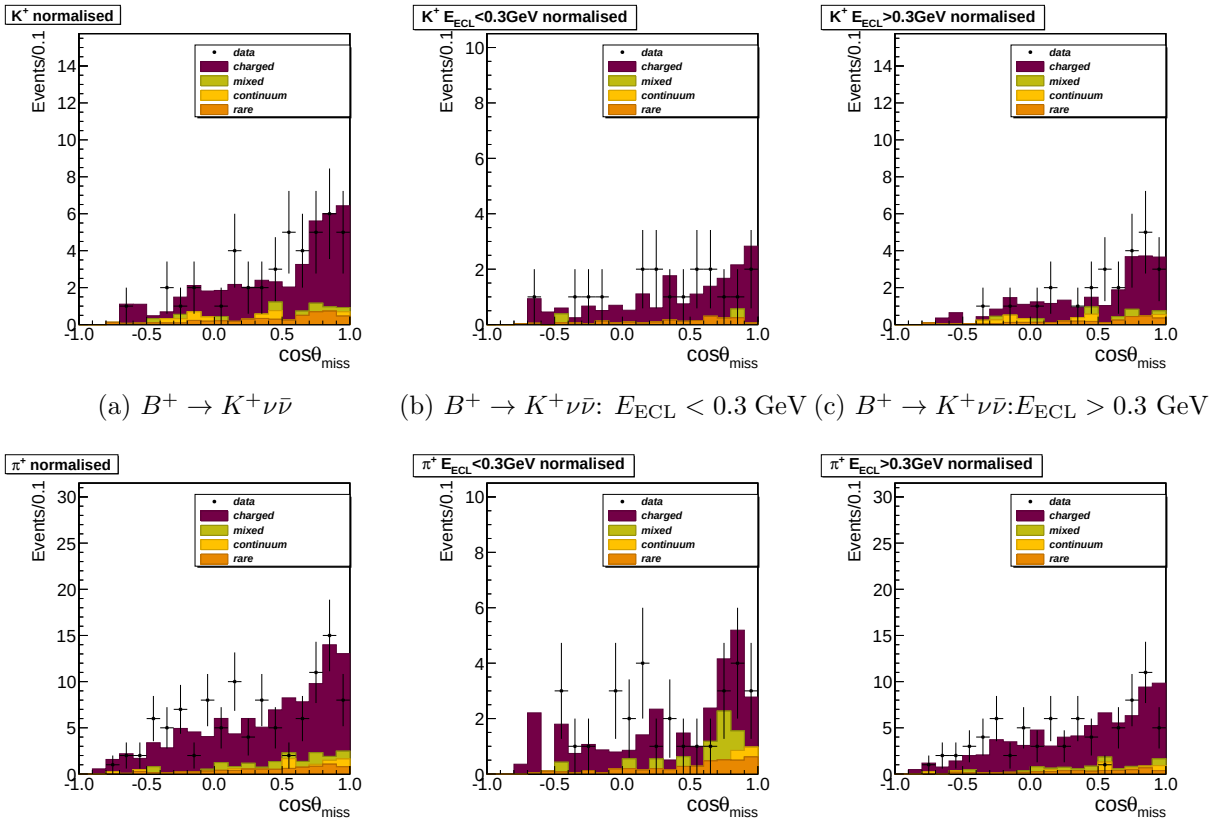

(a) $B^+ \to K^+\nu\bar{\nu}$ (b) $B^+ \to K^+\nu\bar{\nu}$: $E_{\mathrm{ECL}} < 0.3$ GeV (c) $B^+ \to K^+\nu\bar{\nu}$:$E_{\mathrm{ECL}} > 0.3$ GeV

(d) $B^+ \to \pi^+\nu\bar{\nu}$ (e) $B^+ \to \pi^+\nu\bar{\nu}$: $E_{\mathrm{ECL}} < 0.3$ GeV (f) $B^+ \to \pi^+\nu\bar{\nu}$: $E_{\mathrm{ECL}} > 0.3$ GeV

Figure 6.4.: Missing momentum to beam angle distributions for K^+ and π^+ channels with data and Monte Carlo normalised to the same number of entries. From left to right the whole E_{ECL} region, $E_{\mathrm{ECL}} < 0.3$ GeV, and $E_{\mathrm{ECL}} > 0.3$ GeV are shown.

In fig. 6.4 the missing momentum to beam angle distributions for the whole E_{ECL} region, for $E_{\mathrm{ECL}} < 0.3$ GeV, and $E_{\mathrm{ECL}} > 0.3$ GeV are shown. These histograms are normalised to the same number of entries. Not normalised histograms can be found in appendix fig. A.19.

We can see, that in π^+ case the excess events originate mostly from the central region. Otherwise we cannot observe any significant deviation from the expected shape. It can be concluded, that we could not gain additional information concerning the 2σ signal excess through the investigation of these additional variables.

6.4. Conclusion and outlook

A search for nine rare decays with $b \to s$ and $b \to d$ transitions was performed. The full Belle data set of 711 fb^{-1}, the new NeuroBayes based full reconstruction, an additional continuum suppression and a new signal extraction procedure via a binned fit were used to improve the sensitivity of the measurement compared to the previous Belle analysis. No significant signal was observed in any of the channels, although a 2.0σ and 2.6σ hints were found in K^+ and π^+ channels, respectively. Branching fraction limits at 90% CL were evaluated (see table 6.7), most of the limits could be notably improved compared to the previous Belle analysis and for four channels the worlds most stringent limit could be obtained.

We cannot draw evident conclusions concerning the NP models presented in chapter 2, as no significant signal was observed. The obtained limits however can be used to restrict the parameter space of these models. To achieve a more stringent statement, a higher experimental sensitivity is required.

The main key to a higher statistical sensitivity is a larger data sample containing more $B\bar{B}$ pairs. If the observed excess in the signal region for the $\pi^+(K^+)$ channel is indeed coming from the signal contribution, we can very roughly estimate how much luminosity would be necessary to make a signal observation. Assuming the same detector performance and reconstruction method and the scaling of the measurement error of $1/\sqrt{x}$ with x as luminosity scaling factor, we should be able to make a 5σ signal observation already with ~ 3.3 ab^{-1} (5.1 ab^{-1}).

The improvement of the detector performance and the reconstruction efficiency will also contribute to a better sensitivity. The usage of the semileptonic tagging, instead of the hadronic tagging used in this analysis, could lead to a $4-5$ times better efficiency, while worsening the signal to background ratio by a factor of 2 [46].

The upcoming Belle II experiment, with the expected data sample of 50 ab^{-1} and an improved reconstruction should allow us to measure branching fractions of $B \to h^{(*)}\nu\bar{\nu}$ in the same order of magnitude as the SM predictions and thus enable a potential NP observation.

7. Tracking for Belle II

This chapter describes the tracking studies performed within this thesis. First a basic introduction to tracking is given, followed by an explanation of pattern recognition principles. In section 7.3 the track finding algorithm developed within this thesis is described. The performance evaluation is summarised in the subsequent section. The results of the track finding algorithm are used in the track fitting for the precise determination of the track parameters, as is explained in section 7.5. In the conecutive section the results of the track fitting are presented and finally a summary of this chapter is given.

7.1. Introduction

To reconstruct a collision event from various signals provided by different detector components an elaborate reconstruction software is necessary. Tracking denotes the procedure of retrieving the trajectories of charged particles.

In a homogeneous magnetic field a moving charged particle is deflected by the Lorentz force and its trajectory follows a helix. In a plane orthogonal to the $\vec{B}$ field, the track trajectory can be described by a circle.The momentum component in this plane, denoted as transverse momentum p_t in the following, can be obtained from the circle radius r:

$$p_t[\mathrm{GeV/c}] = 0.3 \cdot B[\mathrm{T}] \cdot r[\mathrm{m}]$$

The longitudinal momentum component is not affected by the $\vec{B}$ field, so the 3 dimensional trajectory follows a helix, as is illustrated in fig. 7.1.

A precise determination of direction and magnitude of particle momentum is essential for further event reconstruction. Found trajectories are extrapolated to other detector components, for example calorimeters or imaging Čerenkov devices. The signals found at the extrapolated positions in these detectors provide the information required for particle identification. Extrapolation of particle trajectories to a common vertex allows the reconstruction of decaying mother particles, which do not reach the detector (e. g. B mesons).

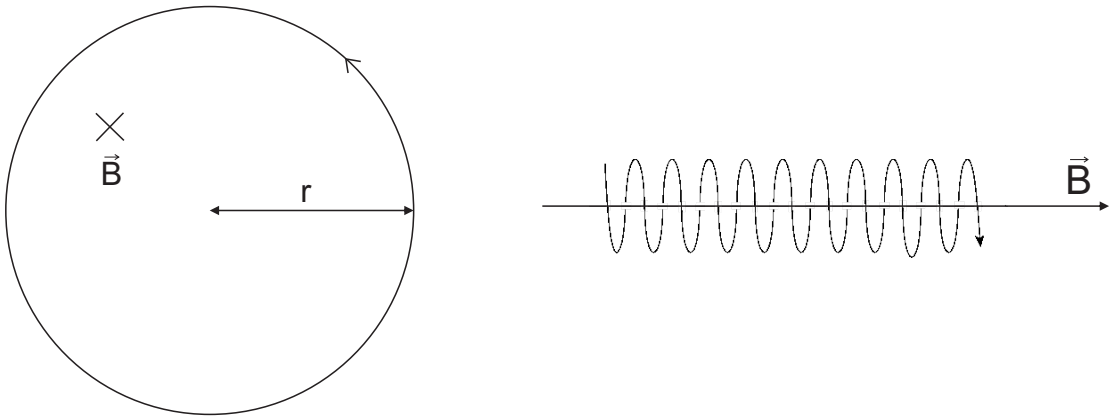

(a) (b)

Figure 7.1.: Charged particle trajectory orthogonal (a) and parallel (b) to the magnetic field.

Due to energy loss while passing through material, the momentum of the particle and thus the curvature of its trajectory decreases, so a helix description is only an approximation for a realistic trajectory.

The p_t resolution is dominated by the measurement error and multiple scattering contributions. The measurement error depends on the intrinsic detector resolution, while the multiple scattering depends on the amount of material the particle is traversing.

The determination of track parameters can be divided into two steps: track finding or pattern recognition and track parameter fitting. The main goal of the pattern recognition is to find hits which belong to the same track. The created track candidates contain the hit collection, as well as the preliminary track parameters estimated from these hits. Track parameters are used to fully describe the particle trajectory and are described in detail in section 7.5. Different approaches can be used in track finding, more details will be given in the following section. The task of the track fitting is to obtain the best estimate of track parameters and their covariance matrix using the information provided by the track candidates. The correct estimation of multiple scattering and other physical effects during track extrapolation through the material is one of the challenging tasks of track fitting.

An average Belle II event will contain 9 charged tracks on average, which is a moderate amount compared to other high energy physics experiments at hadron colliders. However, the beam induced background at Belle II will strongly increase compared to the Belle case. Depending on the amount and spectrum of the background particles, they might contaminate the signals from $B\bar{B}$ events and deteriorate the tracking performance.

7.2. Pattern recognition

Pattern recognition is an assignment or association of one specific object, for example a detector hit, to one of several classes of objects, for example track candidates. In high energy physics there are two major approaches for pattern recognition: global and local methods.

Global methods treat all detector hits simultaneously and in a similar way. One advantage of this approach is therefore the absence of any seeding bias. The main disadvantage is high computing time which slows down the track finding. A widely used example of this method is the Hough transformation [47].

Local methods use a seed, a minimal set of hits as a starting point, and follow the track trajectory through the detector, connecting the found hits. Such track following methods are more efficient in terms of speed than global methods. The main problem of this approach shows itself in a high occupancy environment, where several continuations are possible for a track candidate. In that case a sophisticated selection between the possible paths is needed.

Although a large number of already existing particle physics experiments did accomplish the task of track finding and event reconstruction, no generally accepted optimal method exist. Different experimental setups lead to the development of diverse pattern recognition methods. The best track finding strategy for a certain setup depends on various condition (involved subdetector technology and material budget, momentum spectrum of the particles, expected backgrounds etc.) and is not easy to predict beforehand. Tracking studies including the detector simulation are required to find the optimal method. An overview of different pattern recognition and event reconstruction strategies can be found in [48].

The Central Drift Chamber (CDC) is the main tracking device of the Belle II detector. The 56 CDC layers provide nearly continuous measurements to determine the track trajectory. The spatial resolution of the drift chamber is however not good enough not measure the vertices with the precision required for physics analyses. The silicon detectors SVD and PXD provide better resolutions and will be used for tracking and vertexing close to the interaction point.

The following multi-stage track finding procedure is planned for the Belle II experiment [26]. First pattern recognition is performed in the CDC to find all tracks with transverse momentum high enough to cross most of the CDC. These tracks are then extrapolated to the SVD/PXD, the corresponding hits are assigned to the tracks and removed from the hit collections. In the next step a challenging silicon stand-alone track

finding is performed to find low momentum tracks. In the last step these tracks are extrapolated back to the CDC to collect the corresponding hits possibly produced there and missed during the first step.

7.3. `ConformalFinder`

An algorithm to perform the first pattern recognition step, denoted as the `ConformalFinder` in the following, was developed in the scope of this thesis. We expect the algorithm to find all relatively clean non-curling tracks which are crossing the majority of the CDC layers. The performance should be efficient and stable against the assumed background. The preliminary occupancy estimation for the CDC is 10% in the worst case. The algorithm is based on the local track following approach.

Furthermore, as it was the first tracking algorithm implemented in the new Belle II software framework, its implementation contributed to the development of the simulation and reconstruction chain. The simulated geometry, hit dataobjects and physics processes were tested, several flaws were identified and corrected. The necessary data objects and tools to perform track finding and fitting within the framework were implemented and tested using the `ConformalFinder`.

7.3.1. Main principle

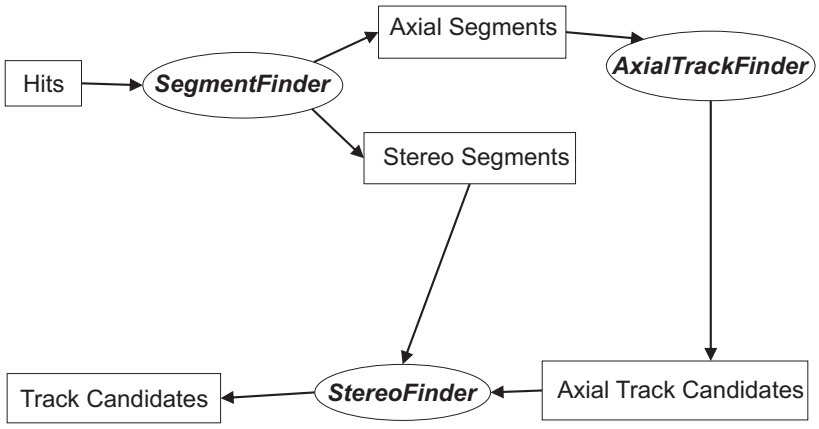

Figure 7.2.: Schematic view of the principle of the `ConformalFinder`

The ConformalFinder consists of several steps executed consecutively. The general procedure is similar to one already used at Belle (trasan).
In the first step hits from the same superlayer are combined to small track sections, denotes as segments in the following. These segments are used for the track following in the further reconstruction. Track candidates are created by a combination of axial segments in two dimensions. In the last step stereo segments are assigned to already created track candidates, thus adding a z coordinate measurement. The general procedure is illustrated in fig. 7.2.

7.3.2. SegmentFinder

The function of the SegmentFinder is to find the track sections within one superlayer. Except the innermost superlayer, which has 8 layers, all superlayers consist of 6 layers. As the algorithm is meant to find tracks with a momentum high enough to cross the whole drift chamber, we are looking for tracklets crossing the superlayer from the innermost to the outermost layer, as illustrated in fig. 7.3. For this purpose a cellular automaton is used.

Cellular Automaton
A cellular automaton is a dynamical system with discrete space and time evolution. Discrete space means that the system consists of concrete cells. A discrete state is assigned to each cell and these states are evaluated during the execution of the algorithm. The states are evaluated on the basis of certain rules and conditions in discrete time steps. Thus the rules are applied and all cell states are updated simultaneously. This continues until the states do not change anymore during the update step.

In the SegmentFinder all hits are considered as such cells. The original states of all hits are set to 0. The only rule is the check if two hits from consecutive layers can be neighbours. This is achieved by comparing the wire Ids of the two hits, only hits with directly adjacent wire Ids are considered neighbours. The search is performed in the $r\phi$ plane.

Starting with the outermost layer it is checked if this hit has a neighbour in the subsequent layer. If this is true the state of the hit is set to the state of the neighbour + 1. The procedure is repeated for all layers and at the end all states are updated simultaneously. This process is repeated until the cells have reached their final states.

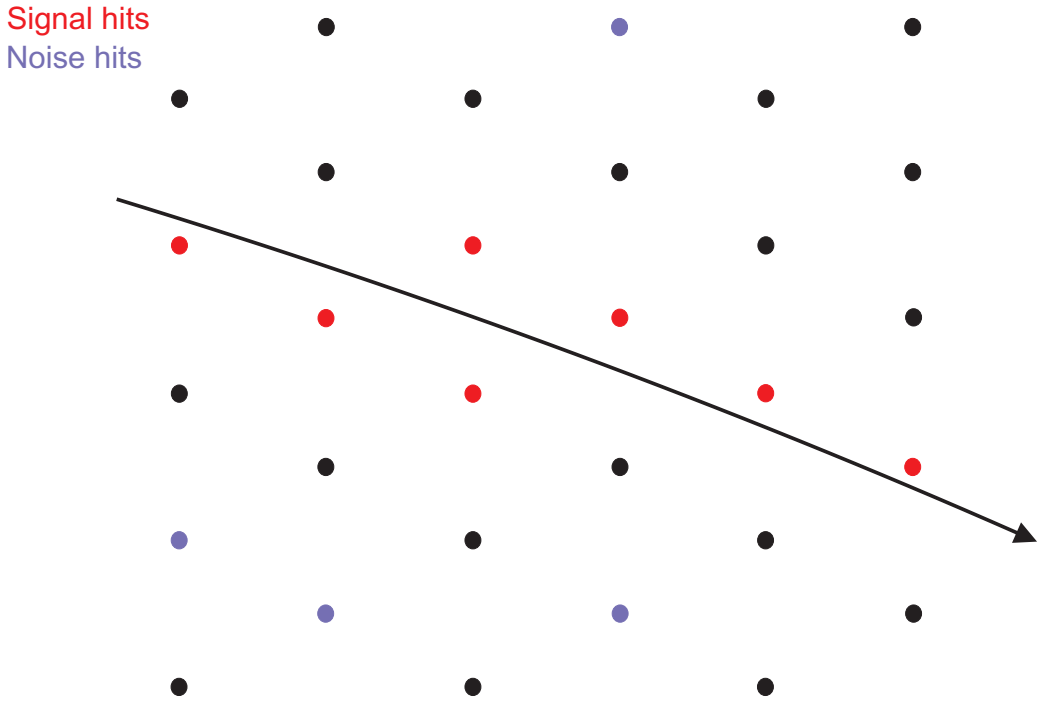

Figure 7.3.: Schematic view of one superlayer to illustrate the function of the `SegmentFinder`

In the next step the segments are created using the state information of the hits. An ideal segment starts in the outermost layer with a hit at state 5, continues in the adjacent layer with a hit at state 4 and finishes in the innermost layer at state 0. After such segments are found, shorter segments with missing hits at either end of the segment are created. After such single hit chains are found, a check for possible neighbours in each layer is performed, as a track might pass between two wires and create a signal in both of them (see fig. 3.11). If there is another hit in the neighbouring wire, it is checked if their drift times are compatible with the hypothesis of a track passing between them. This is accomplished by comparing the sum of the drift lengths to the distance between the wires. If these two numbers are close, it is likely that both hits were created by the same particle passing between them. In this case the second hit is assigned to the given segment.

The advantage of this method is its efficiency in finding approximately straight segments with 1-2 hits per layer. Such segments are created by high momentum tracks coming from the interaction point, which are constituting a large part of the tracks we are interested in. The algorithm is also able to resolve track crossings.

The SegmentFinder is however not able to find segments from low momentum curling tracks, which may create more than two hits per layer.

7.3.3. AxialTrackFinder

After all segments are found, the segments from the five axial superlayers are combined to track candidates by the AxialTrackFinder. The search is performed in two dimensions, as axial wires do not contain any z information.

Conformal Transformation
To simplify this step, the x and y hit coordinates are transformed by a conformal transformation. The following equations are used to transform the coordinates:

$$X = \frac{2x}{x^2 + y^2} \qquad Y = \frac{2y}{x^2 + y^2} \quad . \tag{7.1}$$

In the $r\phi$ projection the track trajectory in the CDC is a circle starting from the origin. The conformal transformation maps these circles to straight lines. All information is preserved, the curvature or the transverse momentum of the track can be retrieved from the point of closest approach of the track line to the origin. The transformation is illustrated in fig. 7.4. The outermost hits are transformed to points close to the origin of the conformal plane, while the innermost hits are on the outside.

To find the track candidates we now search for segments which lie on the same straight line in the conformal plane. The segments in the outermost layer are used as seeds, each of them starts a potential track candidate. In the following step it is checked if there is a compatible segment in the adjacent axial layer. The variables used to decide if the two segments belong to one track are as follows:

- Distance between the two segments in the $r\phi$ plane
- Angle between the lines constructed with the inner- and outermost hits of the segments in the conformal plane
- Shortest distance between the centre of one segment to the line of the other segment in the conformal plane

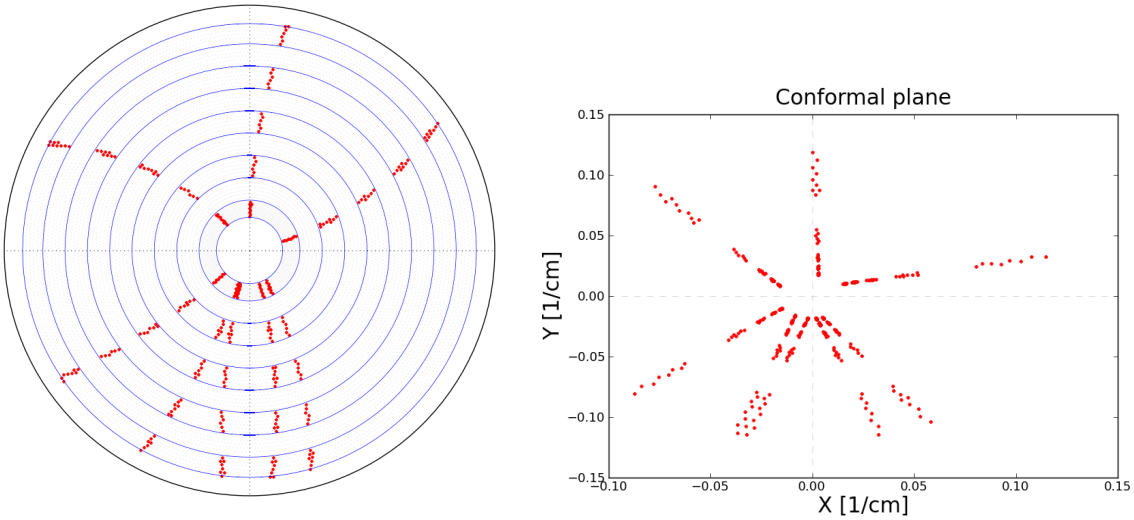

(a) $r\phi$ projection

(b) Conformal plane

Figure 7.4.: Schematic view of the conformal transformation. On the left side the $r\phi$ projection of track trajectories is shown. On the right side these trajectories are transformed onto the conformal plane.

These criteria are illustrated in fig. 7.5. When a compatible segment is found, it is assigned to the track candidate and the search continues in the next superlayer. When two or more compatible segments are found, the track candidate is split and each possible candidate is propagated on its own.

To account for tracks which do no cross the whole drift chamber, the same procedure is repeated using the segments from the other axial superlayers, except the innermost one, as seeds. After all track candidates are found, a linear fit to all the hits in the conformal plane is performed. Track candidates which are not mapped to a line in the conformal plane, and thus have a bad χ^2 after the fit, are discarded.

During the last step of axial track finding the redundant tracks are removed. Only track candidates which share less than 60% of hits with any of the other track candidates are allowed. Out of track candidates sharing more than 60% of hits, the candidate with the largest number of segments and the lowest χ^2 value is selected, the others are discarded. In an additional extension it is checked if some of the short track candidates (two or three axial segments) can be combined to one track. An example of what the output of the `AxialTrackFinder` looks like can be seen in fig. 7.6. The algorithm has a good performance for tracks which are well separable in the $r\phi$ plane.

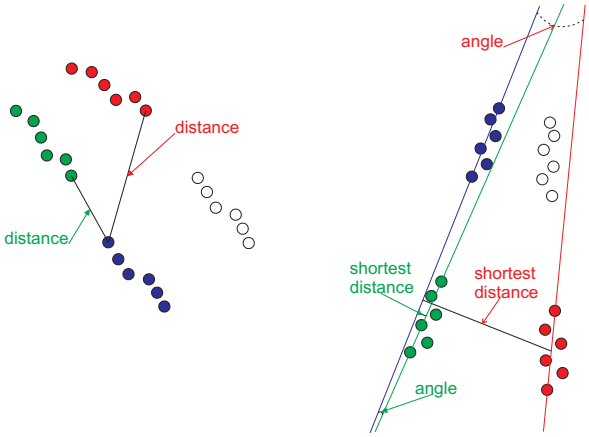

Figure 7.5.: Illustration of the variables used in the `AxialTrackFinder`. For the blue segment we are searching for the matching adjacent segment from the next layer. On the left side it is shown how the distance between the two segments in the $r\phi$ plane is calculated. On the right side the variables used in the conformal plane are shown: the angle between the lines through the segments and the shortest distance between the segment lines.

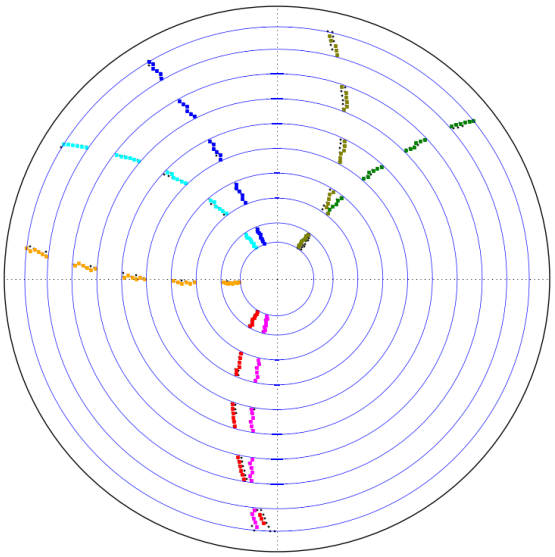

Figure 7.6.: Illustration of an event with 7 tracks after the execution of the `AxialTrackFinder`. Black points mark the centres of the hit wires and different colours show the found track candidates. The criteria two hits from the same layer have to fulfil to get assigned to the same track are quite strict, so sometimes only one hit per layer is assigned. The missed hits are visible as black dots.

7.3.4. StereoFinder

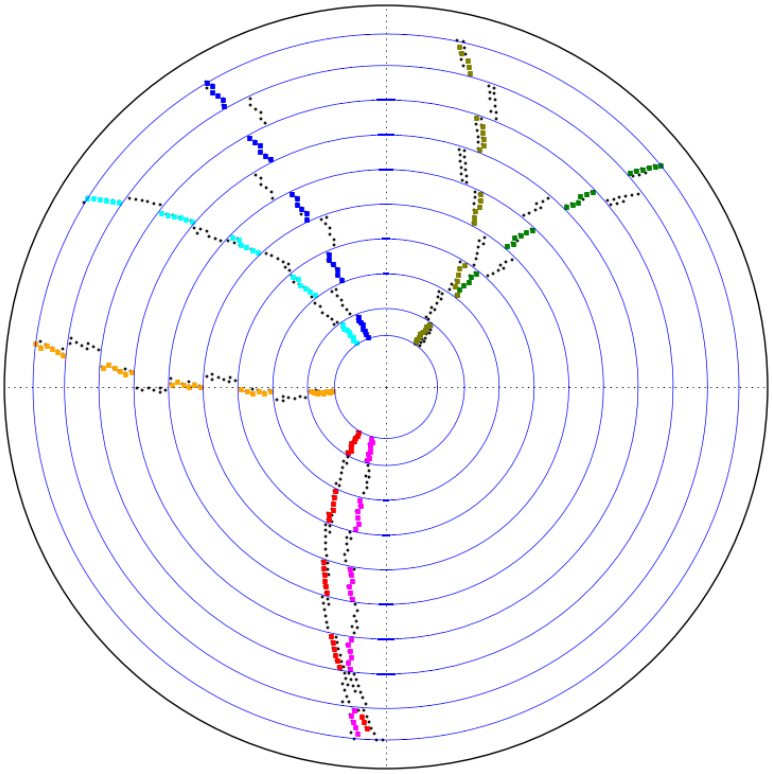

Figure 7.7.: Illustration of an event with 7 tracks after the execution of `AxialTrackFinder` and before the execution of `StereoFinder`. Black points mark the centres of the hit wires, the stereo angle is visible in a shift compared to the trajectory following the axial wires.

In the last step of the `ConformalFinder` the segments from stereo superlayers are assigned to track candidates consisting of axial segments. The stereo wires are installed with a small angle to the z axis and are not parallel to the axial wires. After the correct hits are found this information can be used to reconstruct the z component of the track trajectory. In this stage of the track finding this component is however still unknown. So the search for suitable stereo segments also starts in the $r\phi$ plane, similar to axial segments. If we project the middle point of stereo wires on the $r\phi$ plane, their stereo angle manifests itself in a shift compared to a trajectory following the axial wires, as shown in fig. 7.7. The shift is small for tracks passing the wire close to the wire centre and large for tracks passing the wire near one of its ends. For each axial track candidate we search for compatible segments using two of the criteria already used in the `AxialTrackFinder`:

- Distance between the two segments in the $r\phi$ plane
- Distance between the centre of one segment to the line of the other segment in the conformal plane

The applied cuts are however much looser cuts to take into account the already mentioned shift. After this first selection, the stereo segment is moved in the $r\phi$ plane along the z coordinates of the wires to find the best matching z coordinate, which would align with the axial track candidate in the conformal plane. An illustration is given in fig. 7.8. When the best matching coordinate is found, the following criteria with strict cuts are used:

- Angle between the lines constructed with the inner- and outermost hits of the segments in the conformal plane
- Distance between the centre of one segment to the line of the other segment in the conformal plane

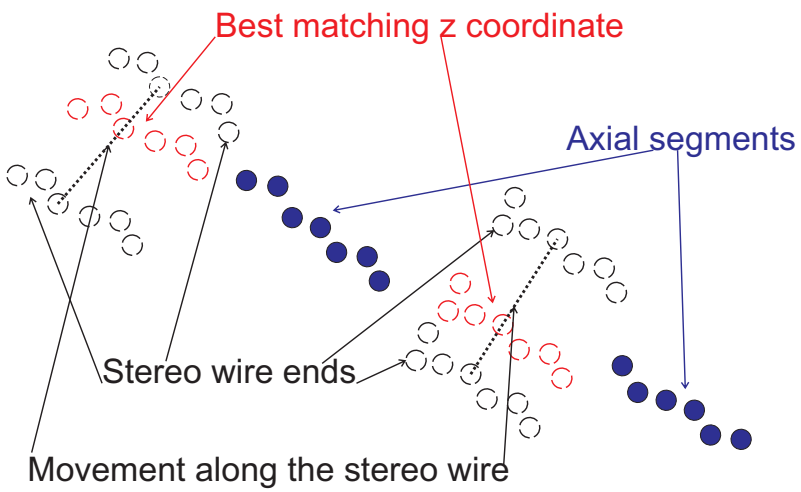

Figure 7.8.: $r\phi$ projection of stereo wires. Stereo segments are moved in the $r\phi$ plane along the z coordinates of the wires to find the best matching z coordinates, which would align them with the axial track candidate.

Only stereo segments fulfilling these strict cuts are kept, others are discarded. However, for tracks close to each other a track candidate still might have several matching stereo segments from the same superlayer. We create stereo track candidates, composed only of stereo segments which were assigned to the same track candidate, and check if the

determined z coordinates of these segments are indeed compatible with each other. This is performed through a linear fit in the rz plane, where a correct track candidate should form a straight line. The superfluous segments are removed and the fit is repeated, until the best matching combination with no more than one segment per superlayer is found. At the end the stereo candidate is merged with the axial track candidate and we obtain the final track candidates. An exemplary result is shown in fig. 7.9.

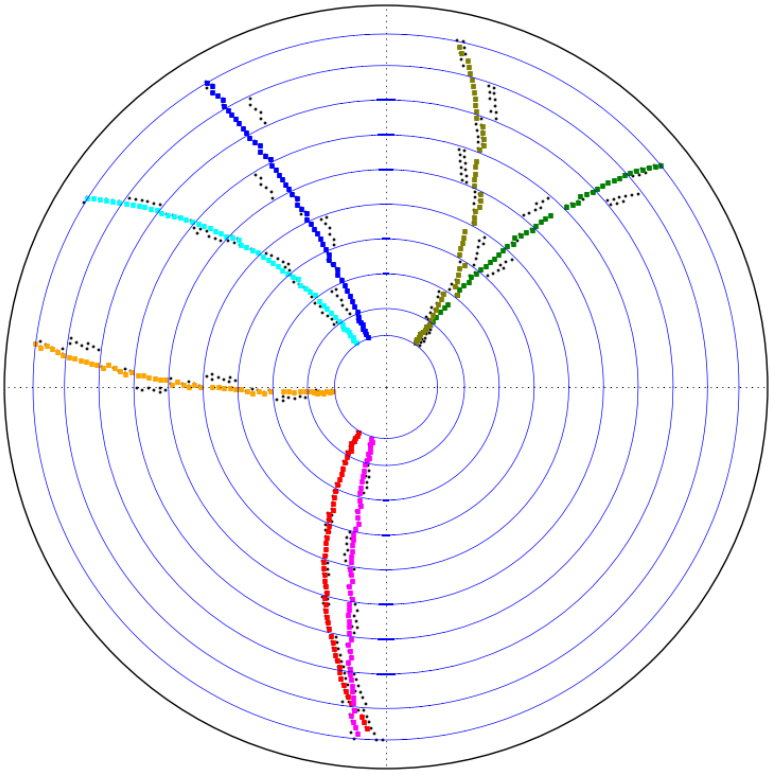

Figure 7.9.: Illustration of an 7 tracks event after the execution of all steps of `ConformalFinder`. Black points mark the centres of the hit wires and different colours show the found track candidates. The projection of the stereo wires assigned to track candidates is shifted compared to the wire centre to match the track trajectory.

7.4. Track finding results

To evaluate the results of the track finding we use two different simulation setups. In the first case we use a particle gun to shoot a certain amount of particles with fixed properties into the detector. In the second case we use a realistic physics case, with one B decaying

to $D^0(K^+\pi^-)\pi^+$ and the other B decaying generically.

7.4.1. Particle gun

To evaluate the performance we define N_{norm}, the maximum number of tracks we could reconstruct, which we use for normalisation of the results. This number differs slightly from the number of simulated tracks, as we cannot reconstruct certain tracks which left the acceptance of the detector or produced too few hits in the drift chamber. Following quantities are used:

- **Efficiency**: number of found tracks relatively to N_{norm}. We define a track as 'found' when we have a track candidate with the majority of its hits originating from the correct track. This was the main figure of merit which was maximised during the development of the algorithm.
- **Good tracks**: number of found tracks fulfilling the following criteria: purity of the candidate $> 60\%$, estimated p_t within 15% of truth, estimated ϕ within 5.7° of truth and estimated θ within 34° of truth. The track parameter estimation is relatively rough and is used as a starting point for the following track fitting step. A fitting study showed that tracks fulfilling these criteria will be fitted with a good resolution. For tracks with lower purity, and thus falsified starting values, we might obtain biased track parameters, so more care during the fitting procedure might be necessary.
- **Ghost tracks**: number of additional track candidates, relatively to the total number of found tracks. One track candidate per simulated track is allowed, all other candidates are counted as ghost tracks.

To simulate only particles which are intended to be found by the `ConformalFinder`, we fix the particle properties for this benchmark study as follows:

particle type: π^+, π^-
momentum: 0.4 GeV $< p <$ 1.6 GeV
polar angle: $50^\circ < \theta < 120^\circ$
azimuthal angle: $0^\circ < \phi < 360^\phi$

The resulting performance of the `ConformalFinder`, depending on the number of tracks per event, is shown in fig. 7.10. We can observe a good track finding efficiency, even for high track multiplicities. For the expected average of 9 tracks per event 96% of all tracks are found.

We can also see how the higher track multiplicity affects the ghost track rate, which increases significantly. This can be explained by looking at an exemplary event with 9 tracks in fig. 7.11. When two tracks are close to each other in the $r\phi$ plane, there are several possible candidates created from neighbouring segments. To distinguish between these candidates and to reject the ghost tracks is the task of the track fitting (see next section 7.5). It is however important to have only a moderate amount of ghost tracks after the track finding to reduce the computing time for the track fitting step. Such tracks, which are lying adjacent to each other in the $r\phi$ plane, also have a major probability of having wrong hit or segment assignments. These tracks then do not fulfil the 'good tracks' criteria, thus this number decreases with increasing ghost track rate.

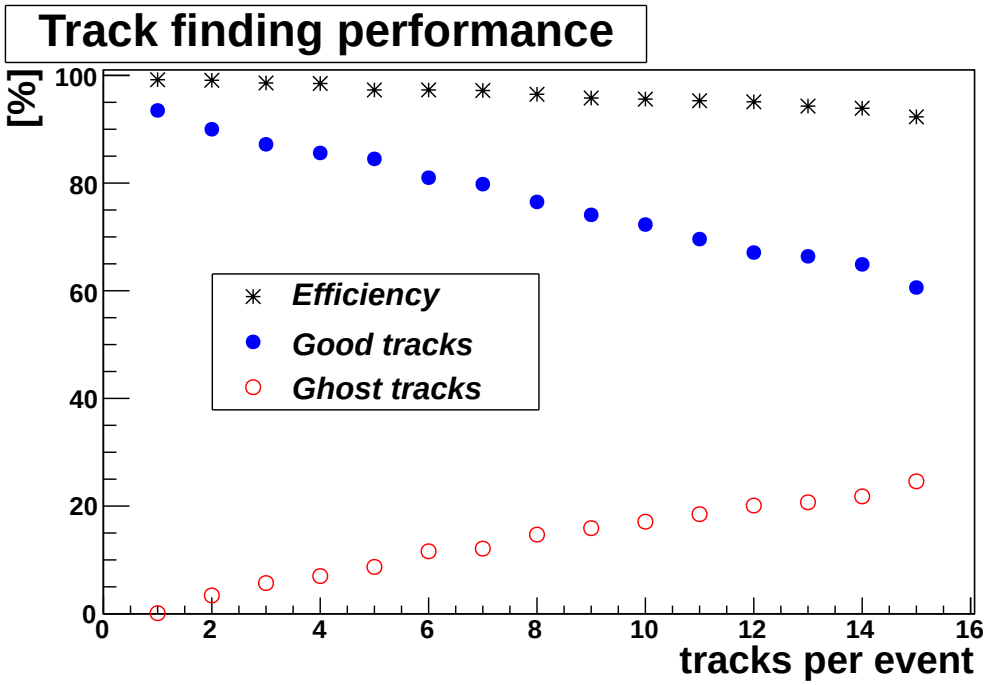

Figure 7.10.: Performance of the `ConformalFinder` depending on the number of tracks per event. The percentages of found tracks (efficiency), of tracks with good parameter estimation (good tracks) and of additional candidates (ghost tracks) are shown.

In a realistic environment we expect beam induced background which might complicate the track finding. The exact amount and properties of the particles reaching the drift chamber are the subject of ongoing studies. The rough worst case estimation states that 10% of all wires will be hit by background particles. As no realistic background simulation was available, a simplified simulation was used. The additional background wire hits are distributed following a $1/r$ distribution over the whole CDC. To illustrate the distribution of the background as well as the algorithm performance, the same event as already shown in fig. 7.11 is shown in fig. 7.12 with 10% background occupancy. The results for events

with 9 tracks depending on the background occupancy are shown in fig. 7.13. We observe the tracking efficiency to be nearly independent of the background level and the amount of ghost tracks to slightly increase with higher background. This encouraging result indicates that the track finding performance is stable against the expected background. More realistic background simulation is however necessary to make final conclusions.

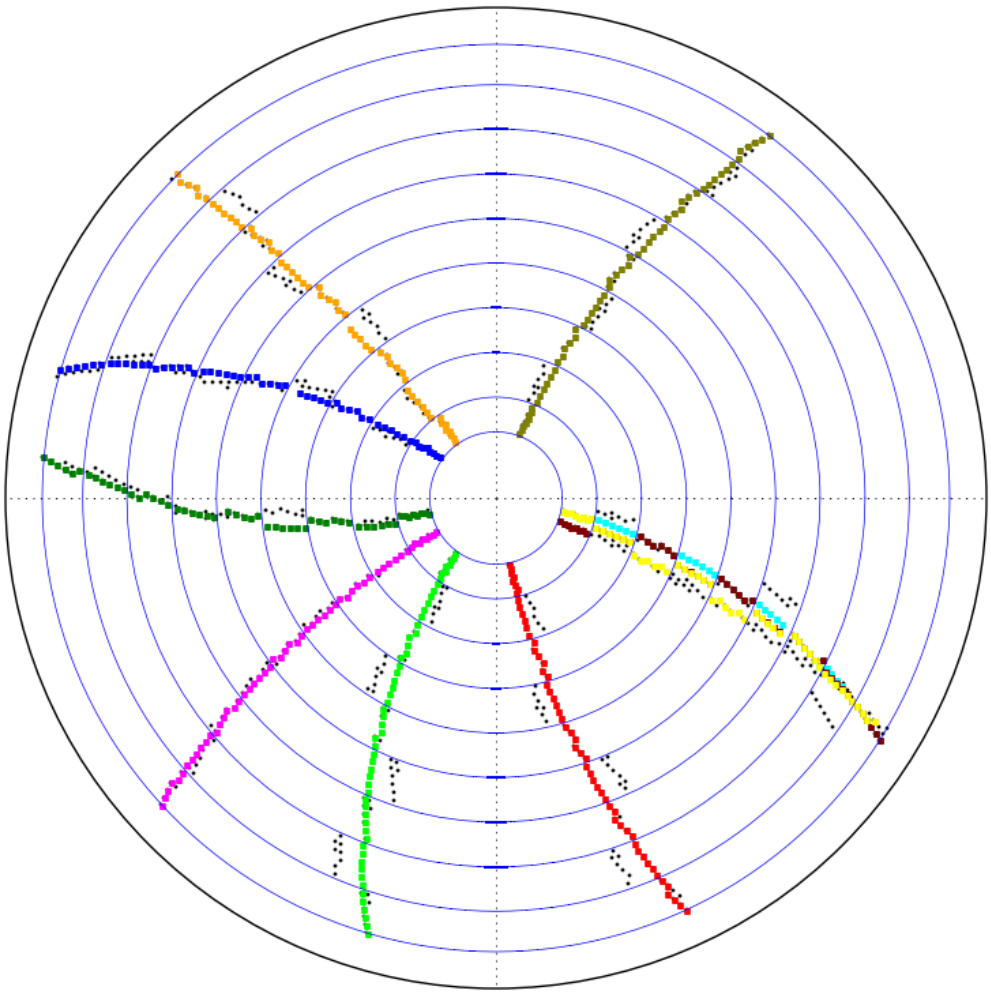

Figure 7.11.: An example of a particle gun event with 9 tracks. Black points mark the centres of the hit wires and different colours illustrate the found track candidates. In the right part of the plot two tracks are lying too close to each other in the $r\phi$ plane to be properly reconstructed. Both tracks are found, but with some wrong segment assignments and an additional ghost track candidate.

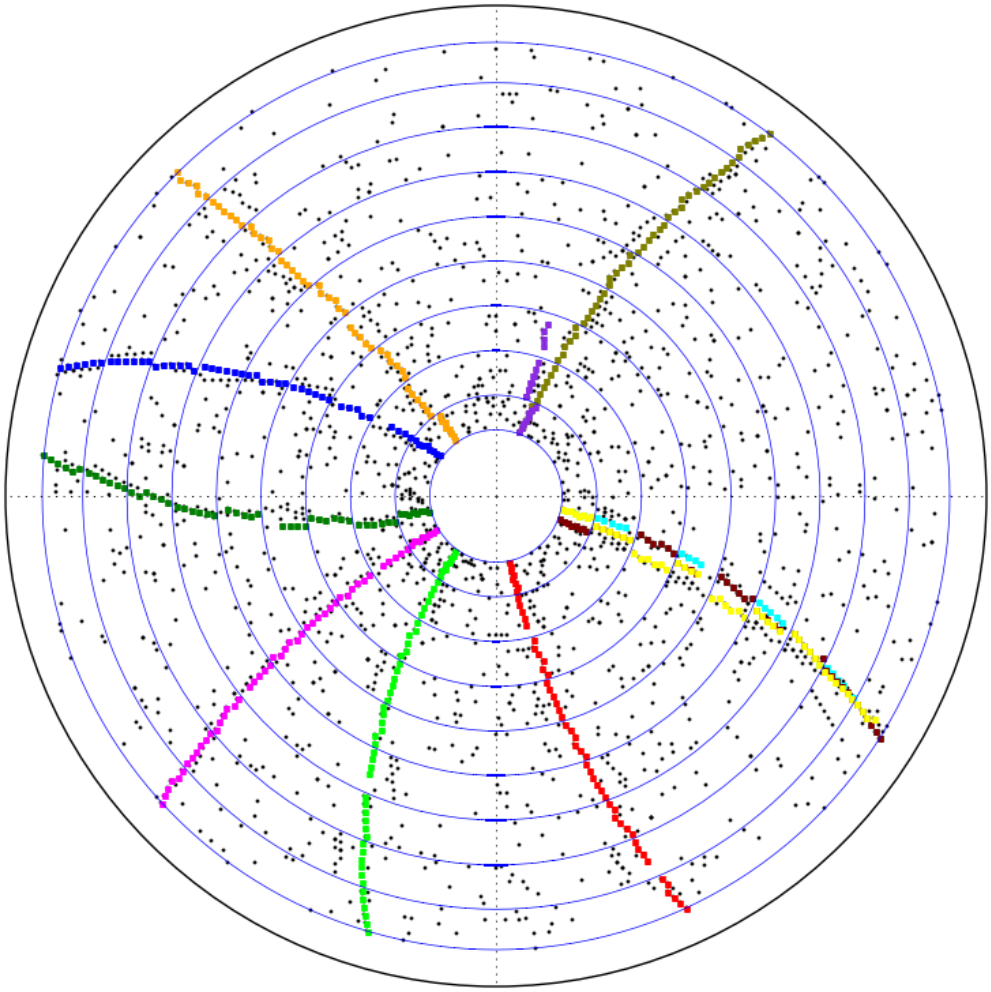

Figure 7.12.: An example of a particle gun event with 9 tracks and 10% background occupancy. Black points mark the centres of the hit wires and different colours illustrate the found track candidates. The results are similar to those without background shown in fig. 7.11.

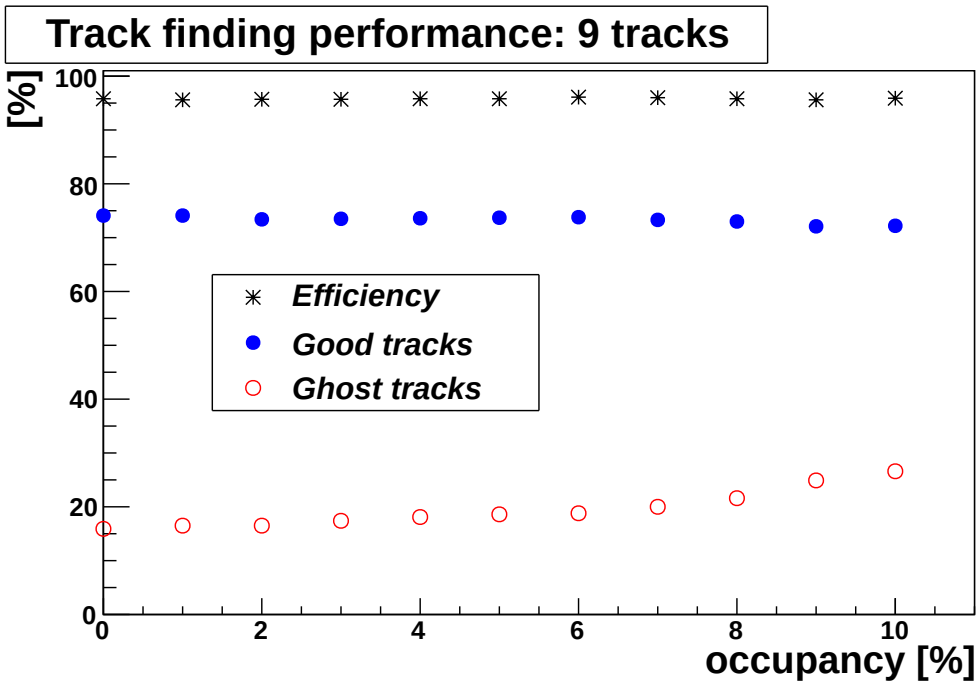

Figure 7.13.: Performance of the `ConformalFinder` for 9 track events depending on background amount. The percentages of found tracks (efficiency), of tracks with good parameter estimation (good tracks) and of additional candidates (ghost tracks) are shown.

7.4.2. $B^0 \to D^0(K^+\pi^-)\pi^+$

In this setup we simulate two neutral B mesons, one of them decays to $D^0(K^+\pi^-)\pi^+$ while the other decays generically corresponding to the current experimental branching fractions. An exemplary decay is shown in fig. 7.14. As is illustrated there, these decays might have low momentum curling tracks, which can be only partially reconstructed with the `ConformalFinder`. So in this setup we are only interested in the reconstruction of our signal decay, $B^0 \to D^0(K^+\pi^-)\pi^+$, and do not evaluate the reconstruction of the other B meson. We use the following quantity to estimate the performance:

- **B_{sig} efficiency**: number of found $B^0_{\text{sig}} \to D^0(K^+\pi^-)\pi^+$ decays compared to the maximum number of $B^0_{\text{sig}} \to D^0(K^+\pi^-)\pi^+$ decays we could reconstruct. The B_{sig} decay is considered as reconstructed if all three final state tracks were found. All simulated B_{sig} decays where all three final state tracks produced hits in the CDC are used as reference.

We obtain a B_{sig} efficiency of 86.4%, which is a encouraging result, as the algorithm was only optimised using particle gun events.

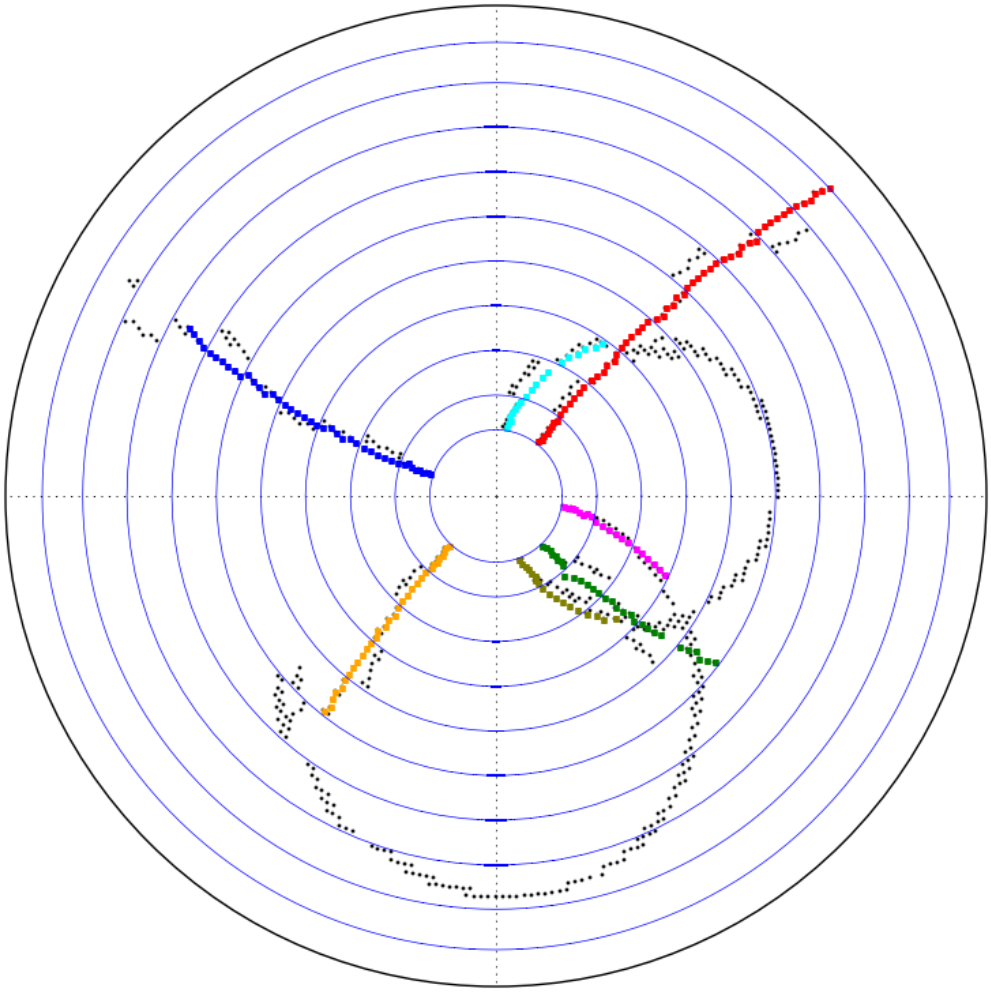

Figure 7.14.: An example of an event with one B meson decaying to $D^0(K^+\pi^-)\pi^+$ while the other decays generically. Black points mark the centres of the hit wires and different colours illustrate the found track candidates. All 6 tracks could be found, although only part of the trajectories of curling tracks could be reconstructed.

7.5. Track fitting

In this section the basic concepts of track fitting with regard to its application in the Belle II experiment are explained.

7.5.1. Track parametrisation

The trajectory of a charged particle in a uniform magnetic field, disregarding the energy loss, can be represented by a helix. The helix can be described by 5 independent parameters, defined at the point of closest approach of the helix to a reference point (origin), called perigee. In Belle II we intend to use the following parametrisation for the trajectory $\vec{\tau}$:

$$\vec{\tau} = (d_0, \phi_0, \omega, z_0, \cot\theta)$$

The parameters are defined as follows:

- d_0 [cm]: signed distance from perigee to the origin in the xy-plane. Negative if the projection of the momentum on this distance points to the origin.
- ϕ_0: track direction angle at the perigee in the xy-plane $[-\pi; \pi]$
- ω [1/cm]: signed curvature q/R, with q: charge of the particle and R: the radius of the track circle in the xy-plane
- z_0 [cm]: z value at the point of closest approach to the beam line
- $\cot\theta$: inverse slope of the track in the rz-plane (dz/ds)

The parameters are visualised in fig 7.15. d_0 and z_0 are also denoted as impact parameters. The particle momentum (in GeV/c) at any point of the trajectory described by its azimuthal angle ϕ can be calculated as follows:

$$\begin{pmatrix} p_x \\ p_y \\ p_z \end{pmatrix} = \frac{1}{|\omega \cdot \alpha|} \begin{pmatrix} -\sin(\phi_0 + \phi) \\ \cos(\phi_0 + \phi) \\ \cot\theta \end{pmatrix} \quad , \tag{7.2}$$

with $\alpha = 1/(1.5 \cdot 0.00299792458)$, obtained from c and the magnetic field strength of 1.5 T.

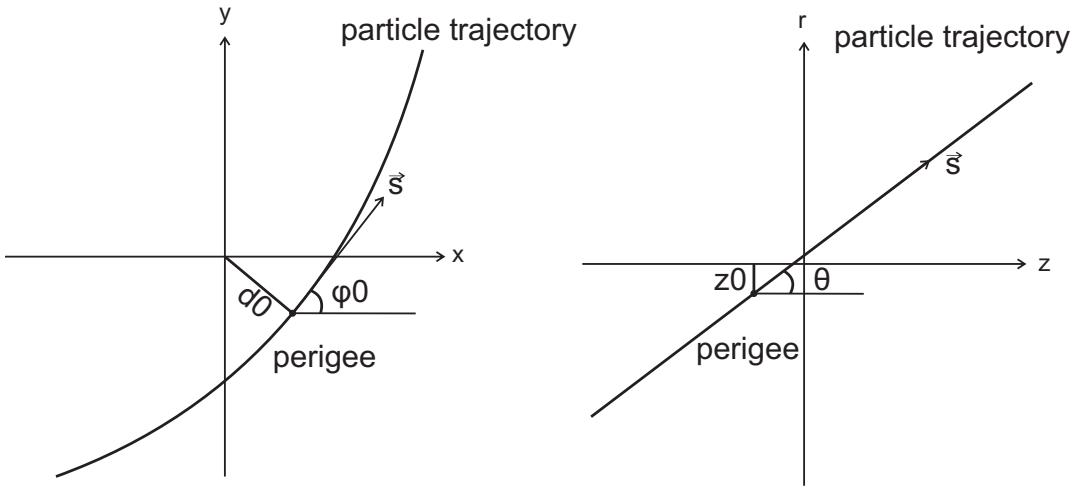

Figure 7.15.: Illustration of the used helix parameters in the xy-plane (left side) and rz-plane (right side).

The coordinates of the perigee can be expressed using the helix parameters:

$$\begin{pmatrix} x_p \\ y_p \\ z_p \end{pmatrix} = \begin{pmatrix} d_0 \cos\phi_0 \\ d_0 \sin\phi_0 \\ z_0 \end{pmatrix} \quad . \tag{7.3}$$

The trajectory of the track close to the origin can be parametrised as a function of ϕ:

$$\begin{pmatrix} x \\ y \\ z \end{pmatrix} \simeq \begin{pmatrix} d_0 \cos\phi_0 \\ d_0 \sin\phi_0 \\ z_0 \end{pmatrix} + \frac{1}{\omega \cdot \alpha} \begin{pmatrix} \cos\phi_0 + \cos(\phi_0 + \phi) \\ \sin\phi_0 + \sin(\phi_0 + \phi) \\ \cot\theta \cdot \phi \end{pmatrix} \quad . \tag{7.4}$$

7.5.2. Kalman filter

The basic principle of most track fitting approaches used in high energy physics is the Kalman filter. It was first described by R.E. Kalman [49] to provide a signal filtering method in electrical engineering and later its application was introduced to particle physics [50].

The main idea is the use of measurements containing noise and other inaccuracies and obtaining values closer to the true values of the measurements. The Kalman filter assumes a linear projection between the measurements. For curved trajectories the transformation of the local parameters of one measurement at radius r_1 to the parameters of the next measurement at radius r_2 is non-linear. To linearise the transformation Taylor series expansions are used, this approach is denoted as extended Kalman filter.

An extended Kalman filter used in particle physics is an recursive iterative algorithm, which collects and directly combines the information from the measurements and their errors. As we have five track parameters with considerable correlations, the measurement errors are describes by a five dimensional covariance matrix. The first step is the prediction of the state vector and the covariance matrix of the next measurement through the extrapolation using the preceding measurements. In the next step the measurement itself is taken into account, a weighted average of the predicted and measured value is calculated and the state vector is updated. This workflow is illustrated in fig. 7.16. The Kalman filter and its variations are widely used for tracking applications in particle physics experiments.

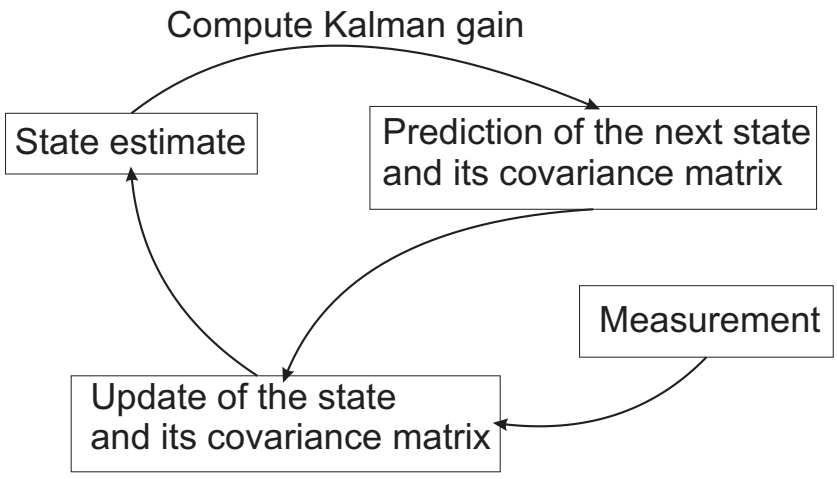

Figure 7.16.: Workflow of the Kalman filter.

7.5.3. Deterministic Annealing Filter (DAF)

In the presence of ambiguous measurements and noise the Kalman filter might not be the optimal solution to determine the correct track parameters. The application of the

Kalman filter requires the hit assignment problem to be resolved by the preceding track finding, wrongly assigned noise hits would lead to biased fit results. One of the algorithms suggested to improve the track fitting is the Deterministic Annealing Filter (DAF) [51]. This algorithm is based on a Kalman filter with an additional reweighting of the observed measurements. DAF determines assignment probabilities for all competing hits, in this way the outlier hits, which are not well compatible with the track parameters, are down-weighted. The filter is run in several iterations, if the hit probability falls below a certain threshold, it is suppressed during the next iteration. The threshold is decreased from iteration to iteration, following a specific annealing scheme. The number of iterations and the annealing scheme can be optimised depending on the noise level and the quality of the starting values.

7.5.4. GENFIT

To perform track fitting within the Belle II framework, we intend to use GENFIT, a generic track fitting framework described in [52]. The concept of GENFIT divides the track fitting problem into three main parts, which are separated from each other: reconstruction hits, track representations and track fitting algorithms.

- **Reconstruction hit** is an object which represents a position measurement from a detector. The raw hit information as well as the coordinate system where it is defined differ between the different subdetector technologies. Different kinds of reconstruction hits can be accessed via a common interface and can be fitted at once.

- **Track representation** is a combination of the track parametrisation and the track extrapolation functionality. A track representation holds the information about the state vector and the covariance matrix. It provides extrapolation functions to extrapolate the track parameters to different places in the detector. Currently the track representation RKTrackRep is used within the Belle II framework, but other track representations with possibly better performances are currently under investigation.

- **Track fitting algorithm**: the task of the fitting algorithm was already explained in previous subsections. Two algorithms are currently implemented within GENFIT: extended Kalman filter and DAF.

The GENFIT framework is currently included in the Belle II framework. In the scope of this thesis the modules necessary to use GENFIT to fit the tracks produced by the Belle II simulation were implemented. The GENFIT performance itself was examined and the detector simulation was tested. Several improvements to the simulation and reconstruction chain were introduced and the implementation of further analysis modules was enabled.

7.6. Track fitting results

To have a reference for the evaluation of the results of the `ConformalFinder` after track fitting, we establish a Monte Carlo based track finding. Monte Carlo track candidates are created using the truth information: all hits created by a particle are collected and the simulated parameters assigned to the candidate, thus creating a 'perfect' track candidate. These track candidates are then fitted with `GENFIT` to obtain Monte Carlo tracks. The parameter resolution depends on the resolution of the single CDC wires and the proper propagation of the tracks through the detector volume during the simulation and the track fitting. We test the Monte Carlo based fitting by looking at the relative resolution of the transverse momentum, which we define as follows:

$$\frac{\sigma_{p_t}}{p_t} = \frac{p_{tREC} - p_{tMC}}{p_{tMC}} \quad , \tag{7.5}$$

with p_{tMC} being the true transverse momentum from the MC simulation and p_{tREC} the transverse momentum resulting from the fit. We use the sample with 9 pion tracks as already presented in section 7.4.1 for this study. The transverse momentum resolution is shown in fig. 7.17.

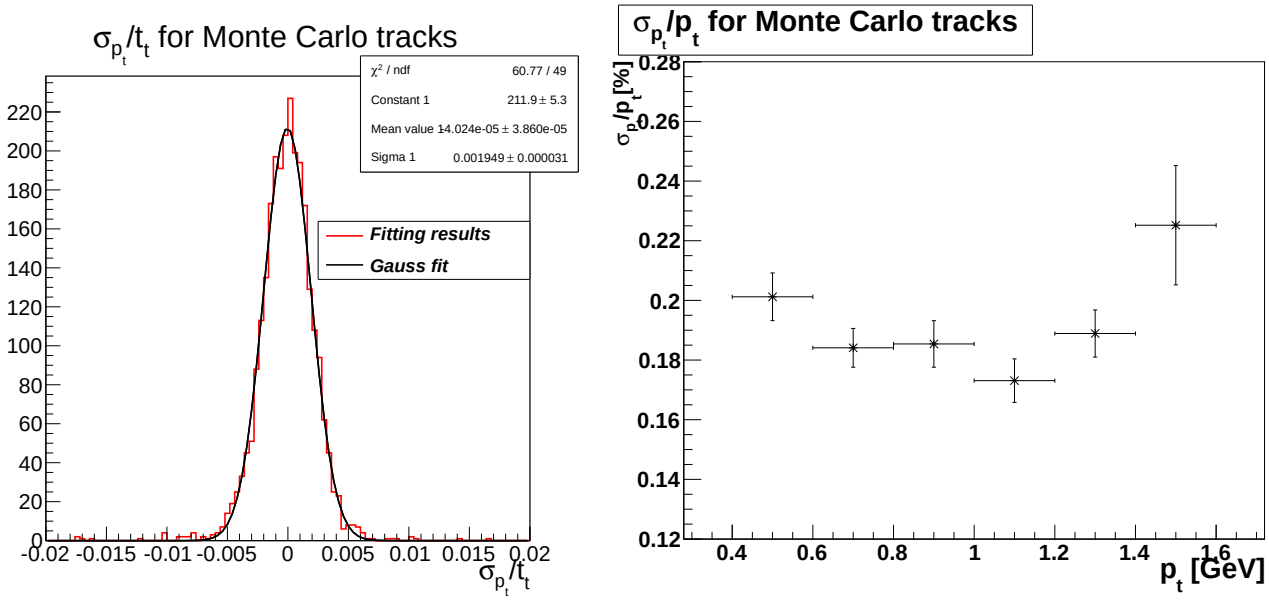

(a) p_t resolution

(b) p_t resolution over p_t

Figure 7.17.: The transverse momentum resolution for Monte Carlo tracks.

We obtain a Gaussian resolution curve with a width of $(0.195 \pm 0.003)\%$, which is compatible with the expectations derived from the performance of Belle CDC. We can also

observe the dependency of the resolution over p_t: the resolution becomes worse for higher p_t due to the smaller curvature. Tracks with $p_t > 1.5$ GeV are nearly straight within the drift chamber dimensions. The resolution also increases slightly for low momentum tracks because of the growing material interactions, where the track extrapolation looses accuracy.

As we now have an established benchmark reference using Monte Carlo tracks, we can evaluate the fitting of the tracks found by the `ConformalFinder`. We use the DAF fitting algorithm with the default annealing scheme. We look at the resolutions of three parameters:

- Transverse momentum: $\frac{\sigma_{p_t}}{p_t} = \frac{p_{tREC} - p_{tMC}}{p_{tMC}}$
- Azimuthal angle: $\sigma_\phi = \phi_{REC} - \phi_{MC}$
- Polar angle: $\sigma_\theta = \theta_{REC} - \theta_{MC}$

The resolutions of these parameters, compared to resolutions of Monte Carlo tracks, are shown in fig. 7.18. We can observe, that the resolution for reconstructed tracks is nearly as good as for Monte Carlo tracks, the differences are below $\sim 10\%$. Furthermore, it can be noted that the deterioration of the p_t resolution arises mostly from tracks with low $p_t < 0.6$ GeV.

Nearly 75% of all reconstructed tracks lie within the central peak. The parameters of the remaining track candidates lie further away from the true values, another fitting step might be necessary to obtain more precise parameters.

We evaluate the performance with additional 10% occupancy background in the same manner and compare them with the results without background. The comparison s shown in fig. 7.19. We observe only a slight deterioration $< 5\%$ of parameter resolution, which shows that the background hits can be successfully down-weighted by the DAF algorithm.

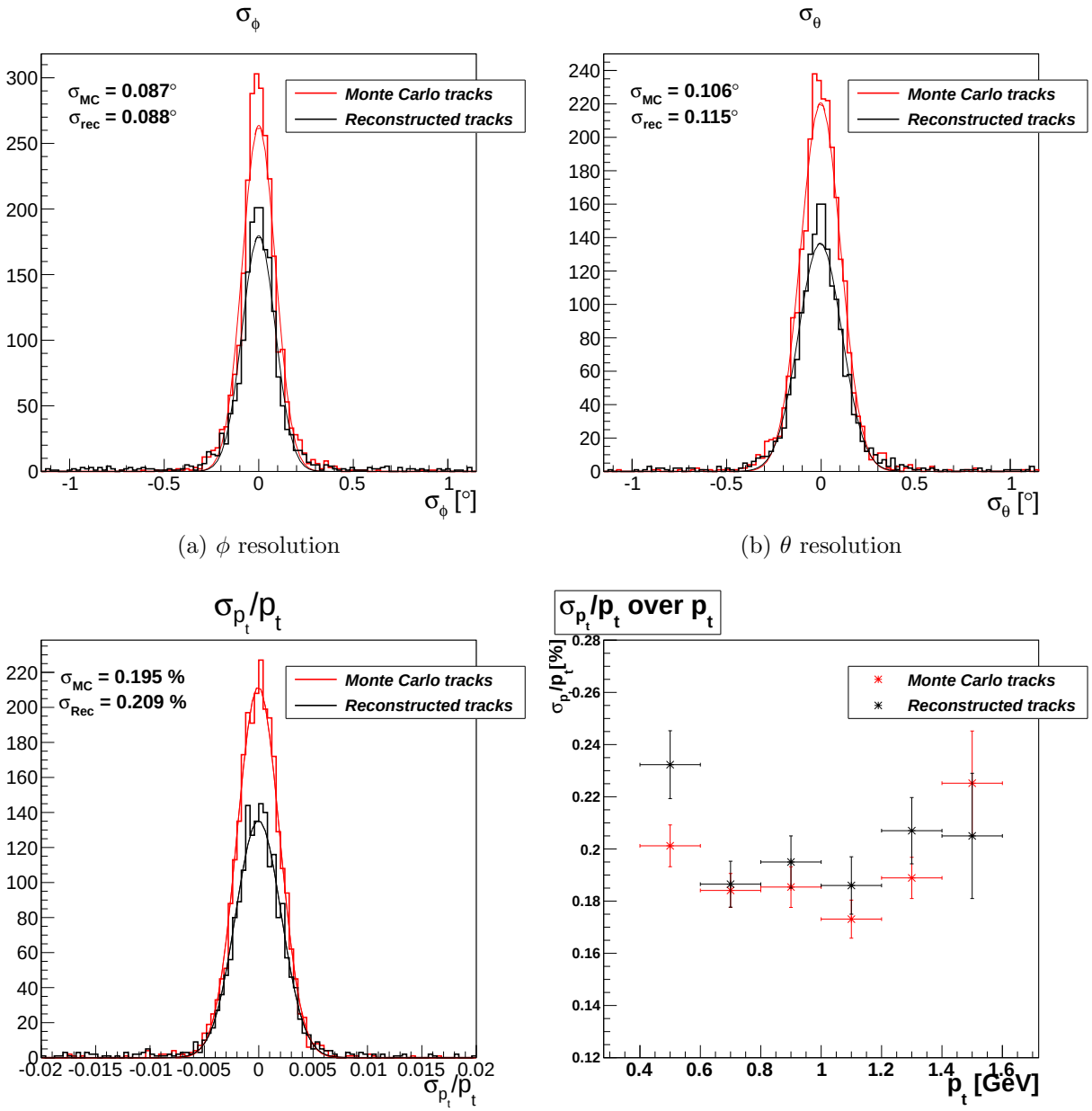

(a) ϕ resolution

(b) θ resolution

(c) p_t resolution

(d) p_t resolution

Figure 7.18.: Parameter resolution of reconstructed tracks compared to the Monte Carlo tracks after fitting. Resolutions of transverse momentum, azimuthal and polar angles are shown.

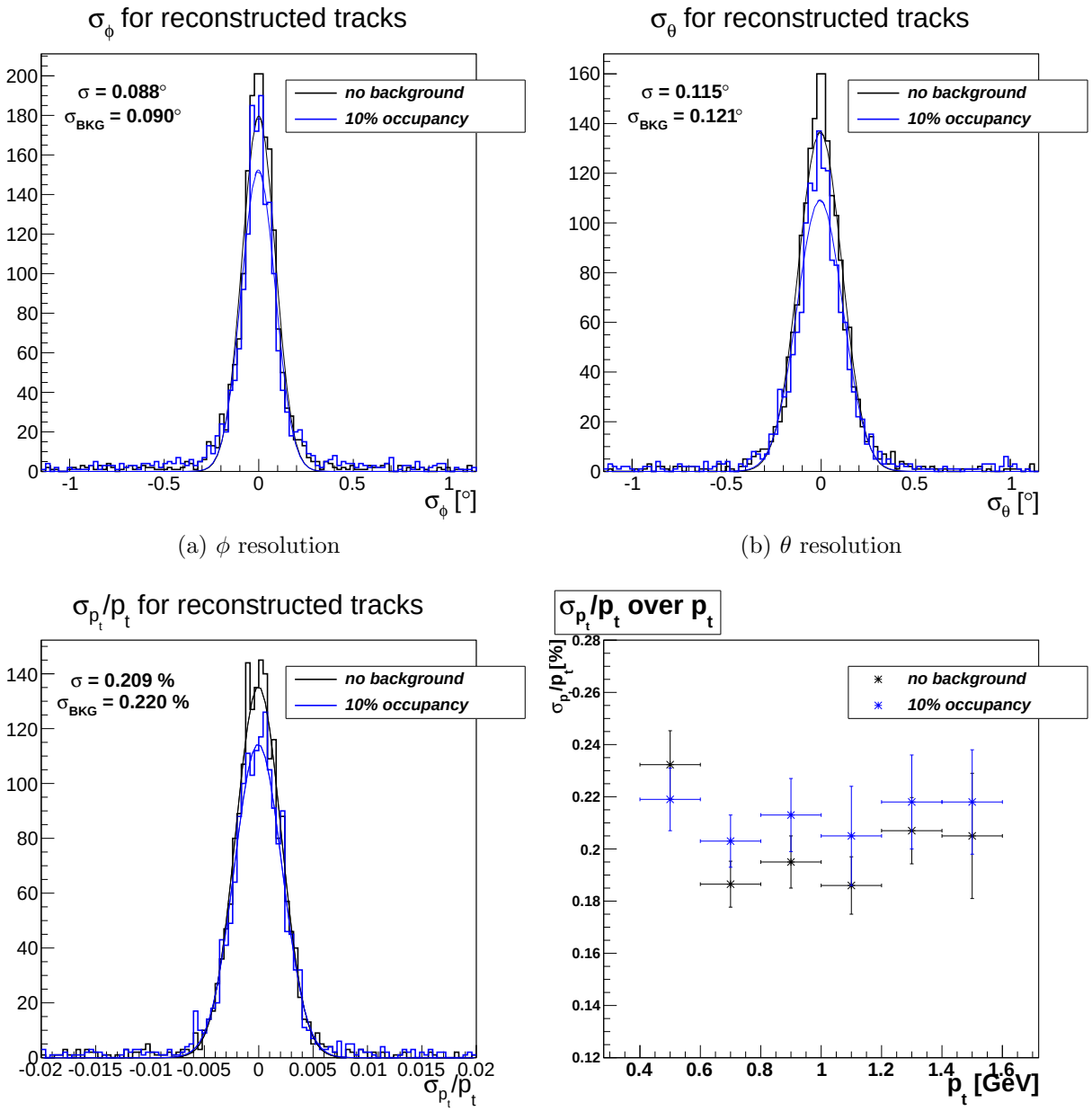

(a) ϕ resolution

(b) θ resolution

(c) p_t resolution

(d) p_t resolution

Figure 7.19.: Parameter resolution of reconstructed tracks after fitting with and without background. Resolutions of transverse momentum, azimuthal and polar angles are shown.

7.7. Conclusion

An algorithm to find high momentum tracks in the central drift chamber, denoted as `ConformalFinder`, was developed and implemented in the Belle II software framework. The algorithm is based on local track following consisting of several steps and combines several techniques like cellular automaton and conformal transformation. Along with the algorithm itself several tools necessary for the execution of the simulation and reconstruction chain were implemented in the Belle II software framework. Track fitting using the external generic framework `GENFIT` was enabled and tested within the framework using Monte Carlo based track finding and the `ConformalFinder`.

Using particle gun events and the $B^0 \to D^0(K^+\pi^-)\pi^+$ decay it was shown that `ConformalFinder` is efficient in finding tracks with $p > 0.4$ GeV in the simulated Belle II drift chamber. Moreover, the track finding performance is stable up to 10% occupancy, which was determined using a simplified background simulation.
The track parameter resolution obtained from the track fitting is, for a majority of the found tracks, only slightly above the Monte Carlo track resolution. Merely a minor deterioration of the resolution is observed in case of 10% occupancy.

The implementation of the `ConformalFinder` as the first track finding alrogithm in the Belle II software framework enabled the development of further steps of the event reconstruction, for example extrapolation of the found tracks to other subdetectors or vertexing. It also laid the foundation for development of improved track finding algorithms and a benchmark for their performance. Currently two different elaborate track finding algorithms, one using a local whereas the other one is using a global approach, which includes the drift time information of the hits, are in development.

8. Summary

A search for decays $B \to h^{(*)}\nu\bar{\nu}$, where $h^{(*)}$ stands for K^+, K_S^0, K^{*+}, K^{*0}, π^+, π^0, ρ^+, ρ^0 and ϕ was performed within this thesis. The full data sample of 711 fb^{-1} ($\approx 771 \times 10^6$ $B\bar{B}$ pairs) collected on the $\Upsilon(4S)$ resonance at Belle and the probabilistic full reconstruction method were used. The signal extraction was optimised to increase the signal sensitivity compared to the previous analysis of these decays. The procedure was studied using simulated experiments and fixed before it was applied on the experimental data.

No significant signal was observed in any of the channels. Signal significances and branching fraction limits at 90% CL were evaluated and are shown in table 8.1. With the data set only 1.5 times larger than the one used in the previous Belle analysis, most of the limits could be considerably improved due to the refined analysis procedure. For four channels the worlds most stringent limit could be obtained.

Channel	Signal significance	Branching ratio limit at 90% CL	Branching ratio limit at 90% CL previous Belle analysis [1]	Current most stringent limit at 90% CL [2]
$B^+ \to K^+\nu\bar{\nu}$	2.0σ	5.5×10^{-5}	1.4×10^{-5}	1.3×10^{-5}
$B^+ \to K^{*+}\nu\bar{\nu}$	-	$\mathbf{4.0 \times 10^{-5}}$	14×10^{-5}	8×10^{-5}
$B^+ \to \pi^+\nu\bar{\nu}$	2.6σ	$\mathbf{9.8 \times 10^{-5}}$	17×10^{-5}	10×10^{-5}
$B^+ \to \rho^+\nu\bar{\nu}$	1.7σ	21.4×10^{-5}	15×10^{-5}	15×10^{-5}
$B^0 \to K_s^0\nu\bar{\nu}$	0.7σ	9.7×10^{-5}	16×10^{-5}	5.6×10^{-5}
$B^0 \to K^{*0}\nu\bar{\nu}$	-	5.5×10^{-5}	34×10^{-5}	1.2×10^{-5}
$B^0 \to \pi^0\nu\bar{\nu}$	1.9σ	$\mathbf{6.9 \times 10^{-5}}$	22×22^{-5}	22×10^{-5}
$B^0 \to \rho^0\nu\bar{\nu}$	0.4σ	$\mathbf{20.8 \times 10^{-5}}$	44×10^{-5}	44×10^{-5}
$B^0 \to \phi\nu\bar{\nu}$	0.5σ	12.7×10^{-5}	5.8×10^{-5}	5.8×10^{-5}

Table 8.1.: Signal significances and branching fraction limits at 90% CL.

As no significant signal was observed, we cannot draw obvious conclusions concerning the NP models presented in chapter 2, although the improved limits can now be used as constraints for these models. As the new limits are still roughly one order of magnitude above the SM predictions, there is a large parameter space left for various NP contributions.

The intriguing hint for NP in a signal significance of over 2σ in K^+ and π^+ channels calls for further investigations in future experiments.

To achieve a higher signal sensitivity a larger data sample containing more $B\bar{B}$ pairs is necessary. In the coming years the KEKB accelerator will be upgraded to SuperKEKB. The target luminosity of the new machine is $8 \times 10^{35}\text{cm}^{-2}\text{s}^{-1}$, which will increase the luminosity achieved by KEKB by a factor of 40. The expected data sample of 50 ab^{-1} and an improved reconstruction should allow the branching fractions measurements of $B \to h^{(*)}\nu\bar{\nu}$ in the same order of magnitude as the SM predictions and thus enable a potential NP observation. The Belle detector will be replaced by the new Belle II detector.

The second part of this thesis contributed to the tracking development for the Belle II experiment. An efficient and precise tracking performance is essential for the correct reconstruction and therefore the physical interpretation of the events. An algorithm to find high momentum tracks in the central drift chamber, denoted as `ConformalFinder`, was developed and implemented in the Belle II software framework in the scope of this thesis. During the integration of the algorithm in the framework the tools necessary for the execution of the simulation and reconstruction chain were established. Furthermore, track fitting using the external generic framework `GENFIT` was included and tested within the framework using track finding based on the truth information and the `ConformalFinder`.

Using different simulation setups it was shown that `ConformalFinder` is efficient in finding tracks with $p > 0.4$ GeV in the simulated Belle II drift chamber (96% of tracks can be found in events with 9 charged tracks) and has a stable performance in a presence of up to 10% background occupancy. The track parameter resolution, obtained from the track fitting, is for the majority of the found tracks only slightly deteriorated ($< 5\%$) compared to the resolution of tracks reconstructed using the truth information.

As the `ConformalFinder` was the first track finding algorithm implemented in the Belle II software framework, its implementation paved the way for the development of improved track finding algorithms and represents a benchmark for their performance. Moreover, the implementation of further steps of the event reconstruction was enabled.

A. Appendix

A.1. N-1 plots

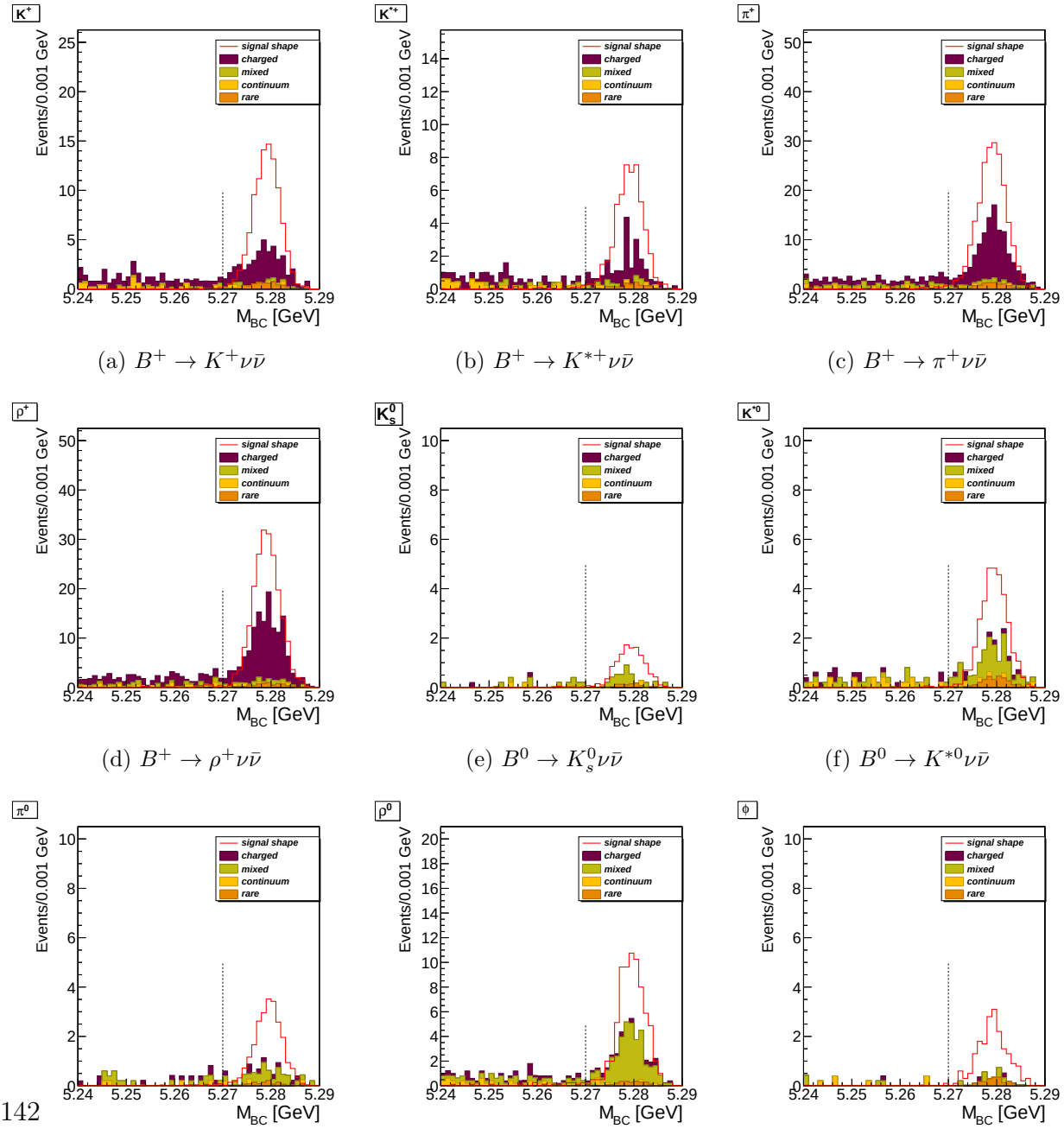

(a) $B^+ \to K^+\nu\bar{\nu}$ (b) $B^+ \to K^{*+}\nu\bar{\nu}$ (c) $B^+ \to \pi^+\nu\bar{\nu}$

(d) $B^+ \to \rho^+\nu\bar{\nu}$ (e) $B^0 \to K^0_s\nu\bar{\nu}$ (f) $B^0 \to K^{*0}\nu\bar{\nu}$

(g) $B^0 \to \pi^0\nu\bar{\nu}$ (h) $B^0 \to \rho^0\nu\bar{\nu}$ (i) $B^0 \to \phi\nu\bar{\nu}$

Figure A.1.: The M_{bc} distribution for background (filled histogram) and signal (red line) Monte Carlo, with all other cuts applied. The signal distribution is normalised to an arbitrary value to illustrate the shape. The dashed line marks the cut value.

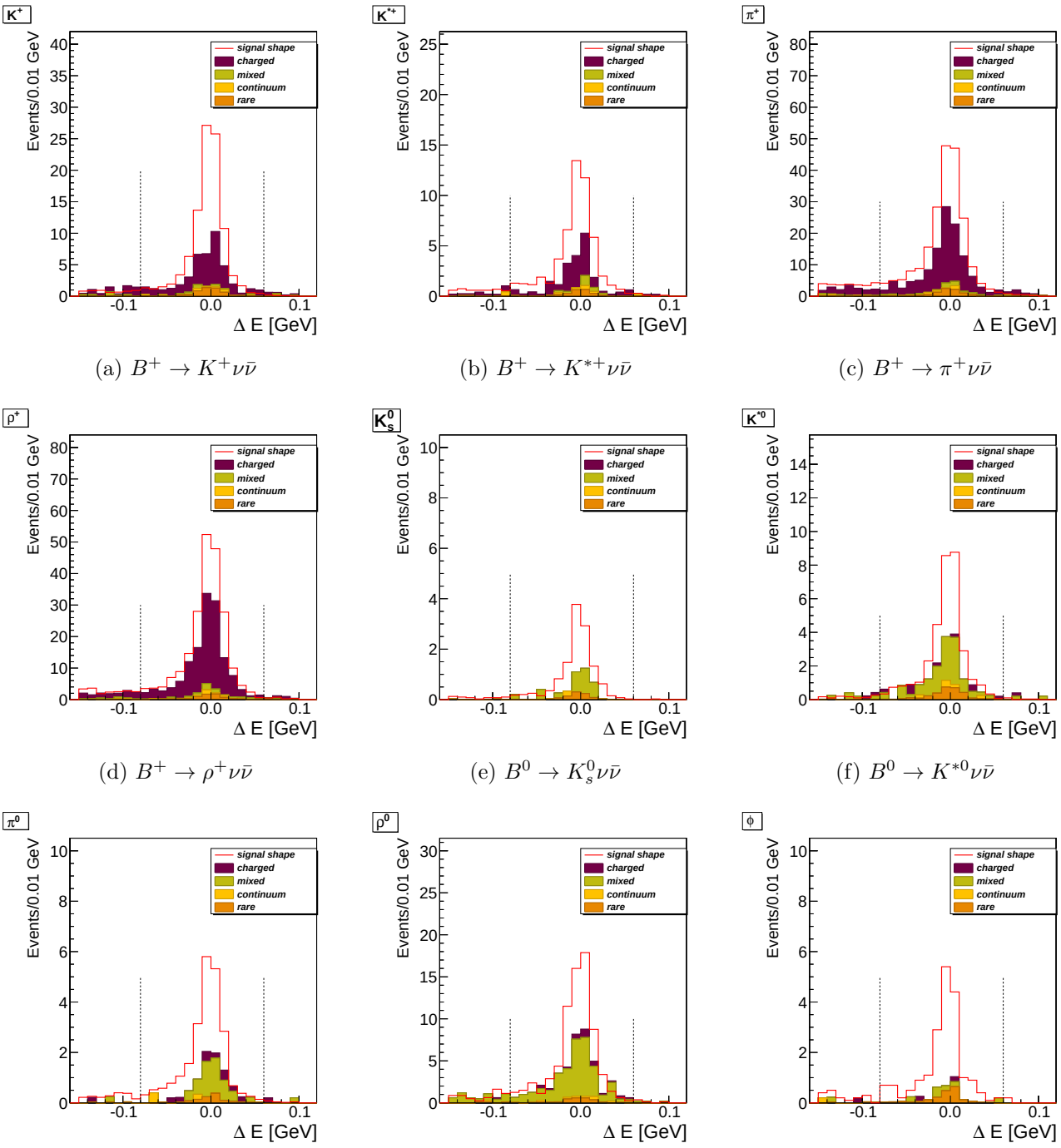

(a) $B^+ \to K^+\nu\bar{\nu}$ (b) $B^+ \to K^{*+}\nu\bar{\nu}$ (c) $B^+ \to \pi^+\nu\bar{\nu}$

(d) $B^+ \to \rho^+\nu\bar{\nu}$ (e) $B^0 \to K^0_s\nu\bar{\nu}$ (f) $B^0 \to K^{*0}\nu\bar{\nu}$

(g) $B^0 \to \pi^0\nu\bar{\nu}$ (h) $B^0 \to \rho^0\nu\bar{\nu}$ (i) $B^0 \to \phi\nu\bar{\nu}$

Figure A.2.: The ΔE distribution for background (filled histogram) and signal (red line) Monte Carlo, with all other cuts applied. The signal distribution is normalised to an arbitrary value to illustrate the shape. The dashed lines mark the cut values.

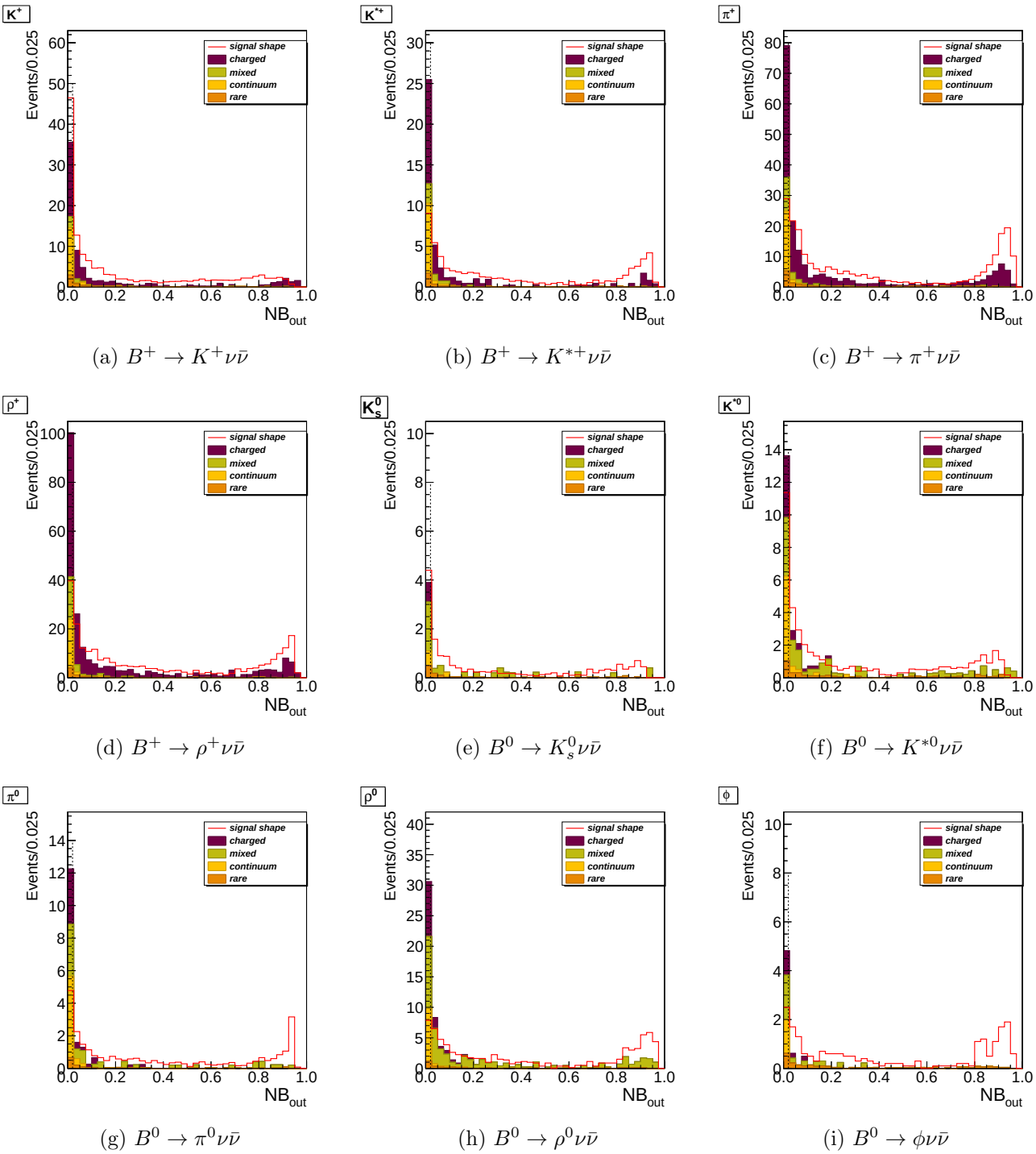

(a) $B^+ \to K^+\nu\bar{\nu}$ (b) $B^+ \to K^{*+}\nu\bar{\nu}$ (c) $B^+ \to \pi^+\nu\bar{\nu}$

(d) $B^+ \to \rho^+\nu\bar{\nu}$ (e) $B^0 \to K^0_s\nu\bar{\nu}$ (f) $B^0 \to K^{*0}\nu\bar{\nu}$

(g) $B^0 \to \pi^0\nu\bar{\nu}$ (h) $B^0 \to \rho^0\nu\bar{\nu}$ (i) $B^0 \to \phi\nu\bar{\nu}$

Figure A.3.: The NB_{out} distribution for background (filled histogram) and signal (red line) Monte Carlo, with all other cuts applied. The signal distribution is normalised to an arbitrary value to illustrate the shape. The dashed line marks the cut value.

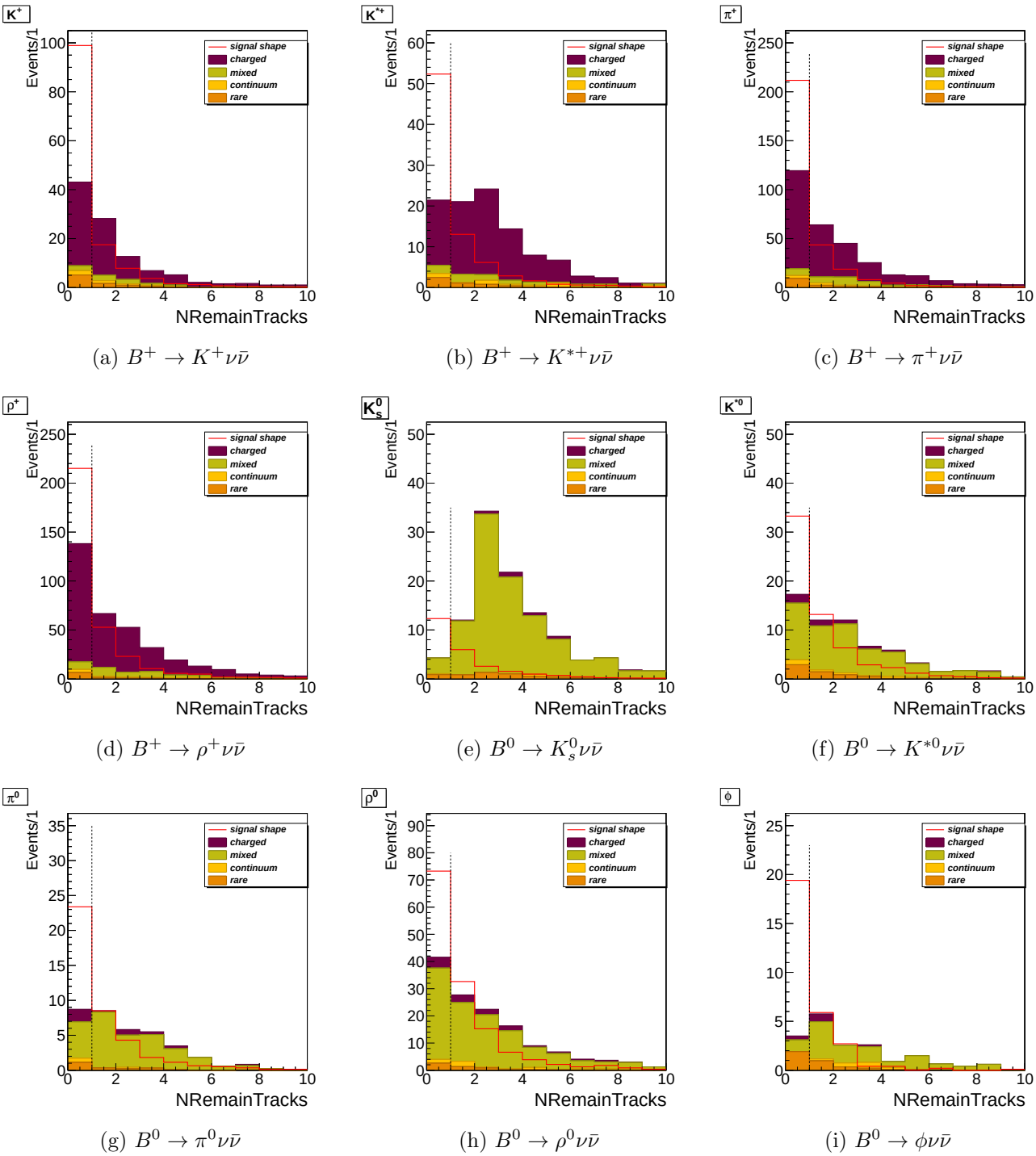

(a) $B^+ \to K^+\nu\bar{\nu}$ (b) $B^+ \to K^{*+}\nu\bar{\nu}$ (c) $B^+ \to \pi^+\nu\bar{\nu}$

(d) $B^+ \to \rho^+\nu\bar{\nu}$ (e) $B^0 \to K^0_s\nu\bar{\nu}$ (f) $B^0 \to K^{*0}\nu\bar{\nu}$

(g) $B^0 \to \pi^0\nu\bar{\nu}$ (h) $B^0 \to \rho^0\nu\bar{\nu}$ (i) $B^0 \to \phi\nu\bar{\nu}$

Figure A.4.: The distribution of number of remaining tracks for background (filled histogram) and signal (red line) Monte Carlo, with all other cuts applied. The signal distribution is normalised to an arbitrary value to illustrate the shape. The dashed line marks the cut value.

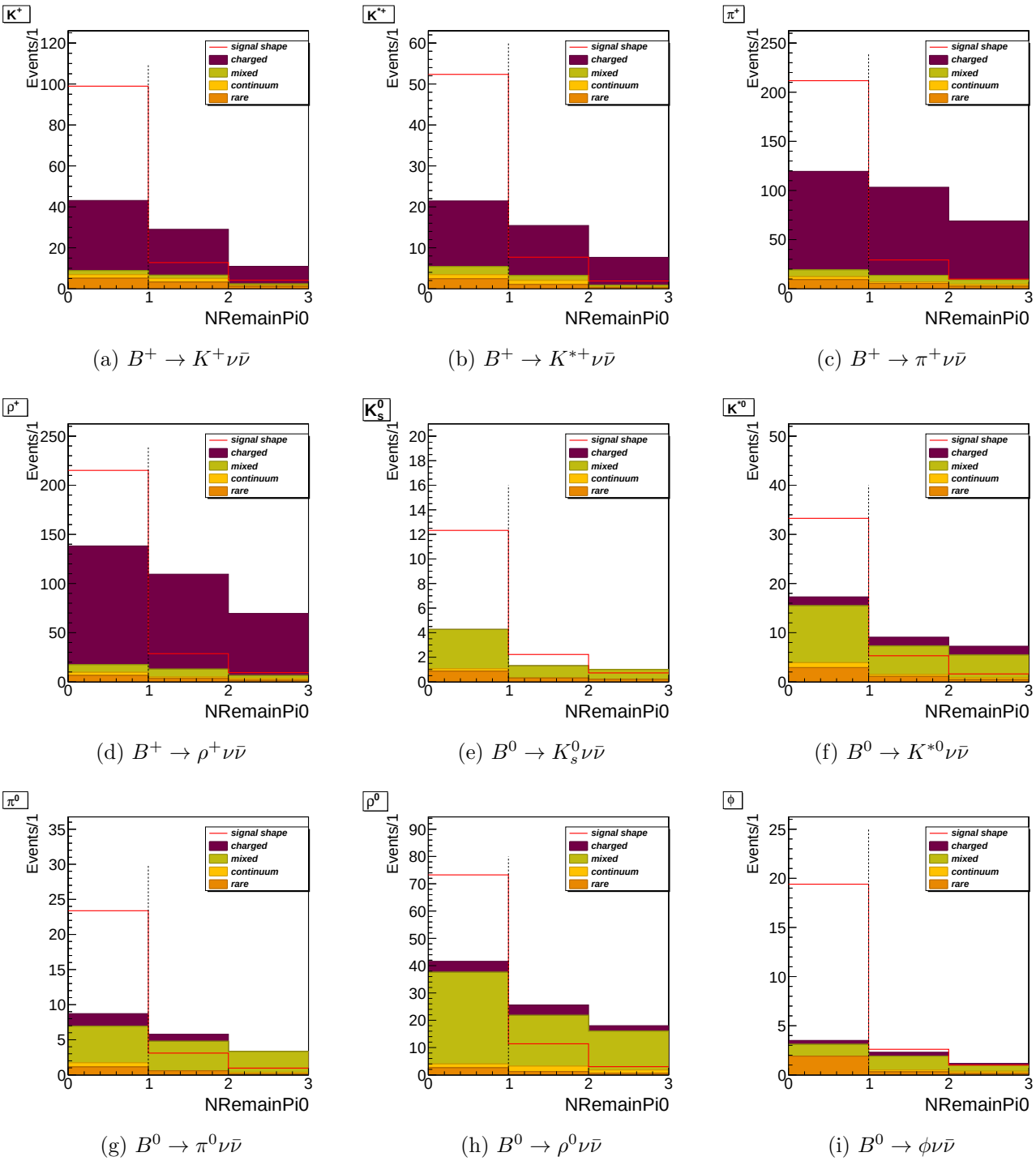

(a) $B^+ \to K^+\nu\bar{\nu}$ (b) $B^+ \to K^{*+}\nu\bar{\nu}$ (c) $B^+ \to \pi^+\nu\bar{\nu}$

(d) $B^+ \to \rho^+\nu\bar{\nu}$ (e) $B^0 \to K^0_s\nu\bar{\nu}$ (f) $B^0 \to K^{*0}\nu\bar{\nu}$

(g) $B^0 \to \pi^0\nu\bar{\nu}$ (h) $B^0 \to \rho^0\nu\bar{\nu}$ (i) $B^0 \to \phi\nu\bar{\nu}$

Figure A.5.: The distribution of number of remaining π^0 for background (filled histogram) and signal (red line) Monte Carlo, with all other cuts applied. The signal distribution is normalised to an arbitrary value to illustrate the shape. The dashed line marks the cut value.

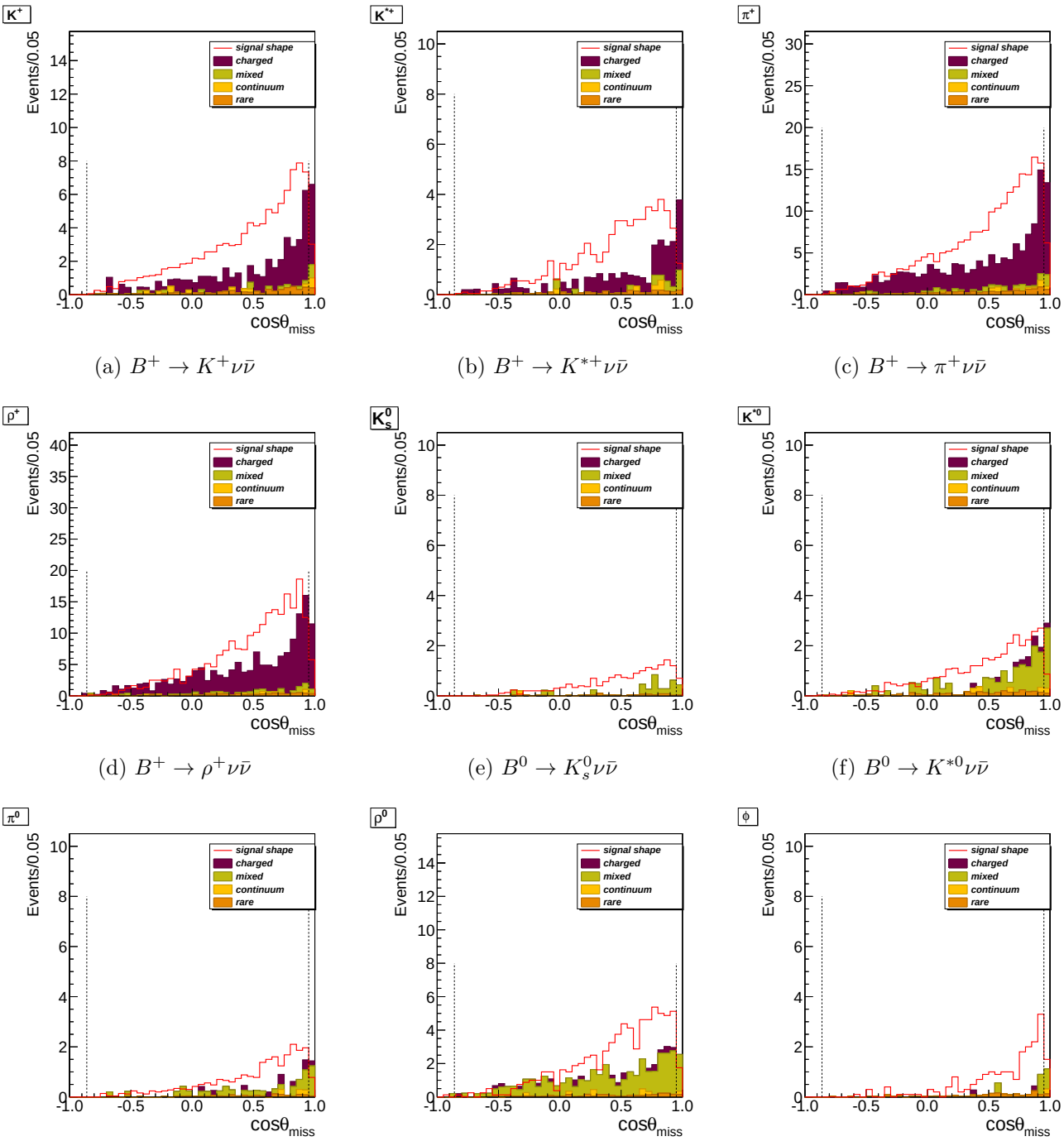

(a) $B^+ \to K^+\nu\bar{\nu}$ (b) $B^+ \to K^{*+}\nu\bar{\nu}$ (c) $B^+ \to \pi^+\nu\bar{\nu}$

(d) $B^+ \to \rho^+\nu\bar{\nu}$ (e) $B^0 \to K^0_s\nu\bar{\nu}$ (f) $B^0 \to K^{*0}\nu\bar{\nu}$

(g) $B^0 \to \pi^0\nu\bar{\nu}$ (h) $B^0 \to \rho^0\nu\bar{\nu}$ (i) $B^0 \to \phi\nu\bar{\nu}$

Figure A.6.: The distribution of the angle between the missing momentum and the beam pipe for background (filled histogram) and signal (red line) Monte Carlo, with all other cuts applied. The signal distribution is normalised to an arbitrary value to illustrate the shape. The dashed lines mark the cut values.

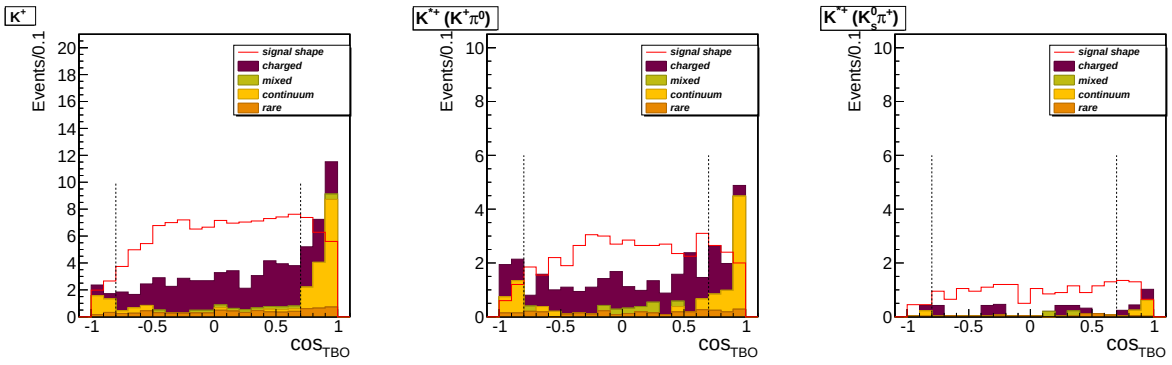

(a) $B^+ \to K^+\nu\bar{\nu}$ (b) $B^+ \to K^{*+}\nu\bar{\nu}(K^{*+} \to K^+\pi^0)$ (c) $B^+ \to K^{*+}\nu\bar{\nu}(K^{*+} \to K^0_s\pi^+)$

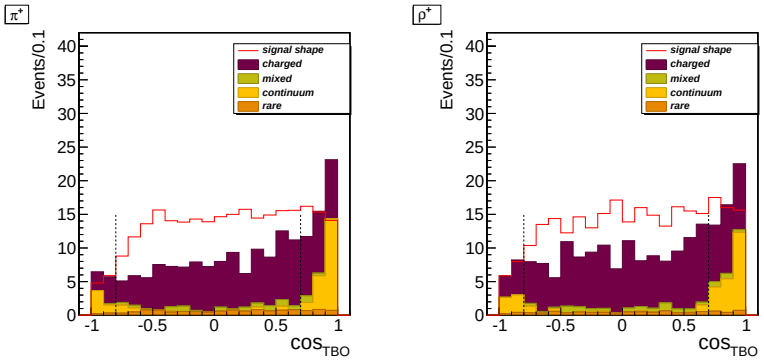

(d) $B^+ \to \pi^+\nu\bar{\nu}$ (e) $B^+ \to \rho^+\nu\bar{\nu}$

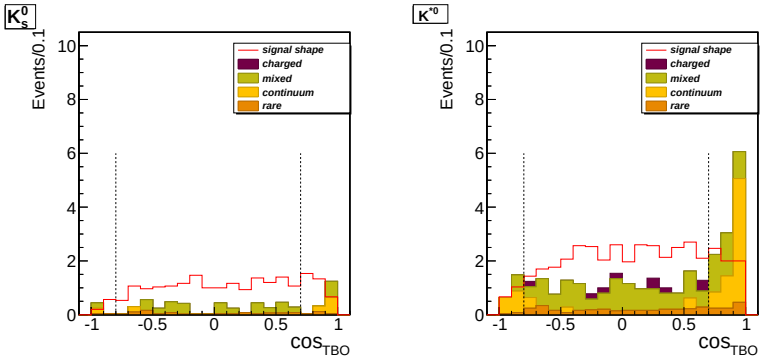

(f) $B^0 \to K^0_s\nu\bar{\nu}$ (g) $B^0 \to K^{*0}\nu\bar{\nu}$

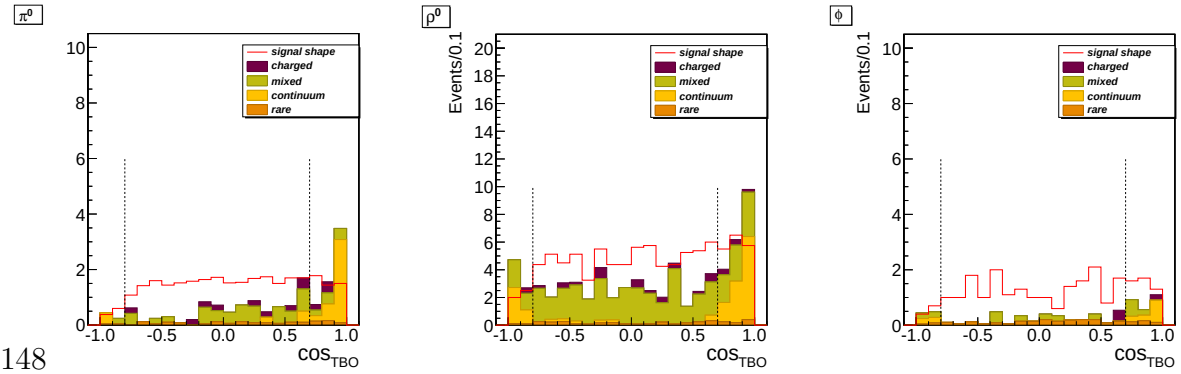

(h) $B^0 \to \pi^0\nu\bar{\nu}$ (i) $B^0 \to \rho^0\nu\bar{\nu}$ (j) $B^0 \to \phi\nu\bar{\nu}$

Figure A.7.: The distribution of the cosine between the thrust axis of the B_{sig} and the rest of the charged tracks. The continuum background component (second from below) is marked yellow. The dashed lines mark the cut values.

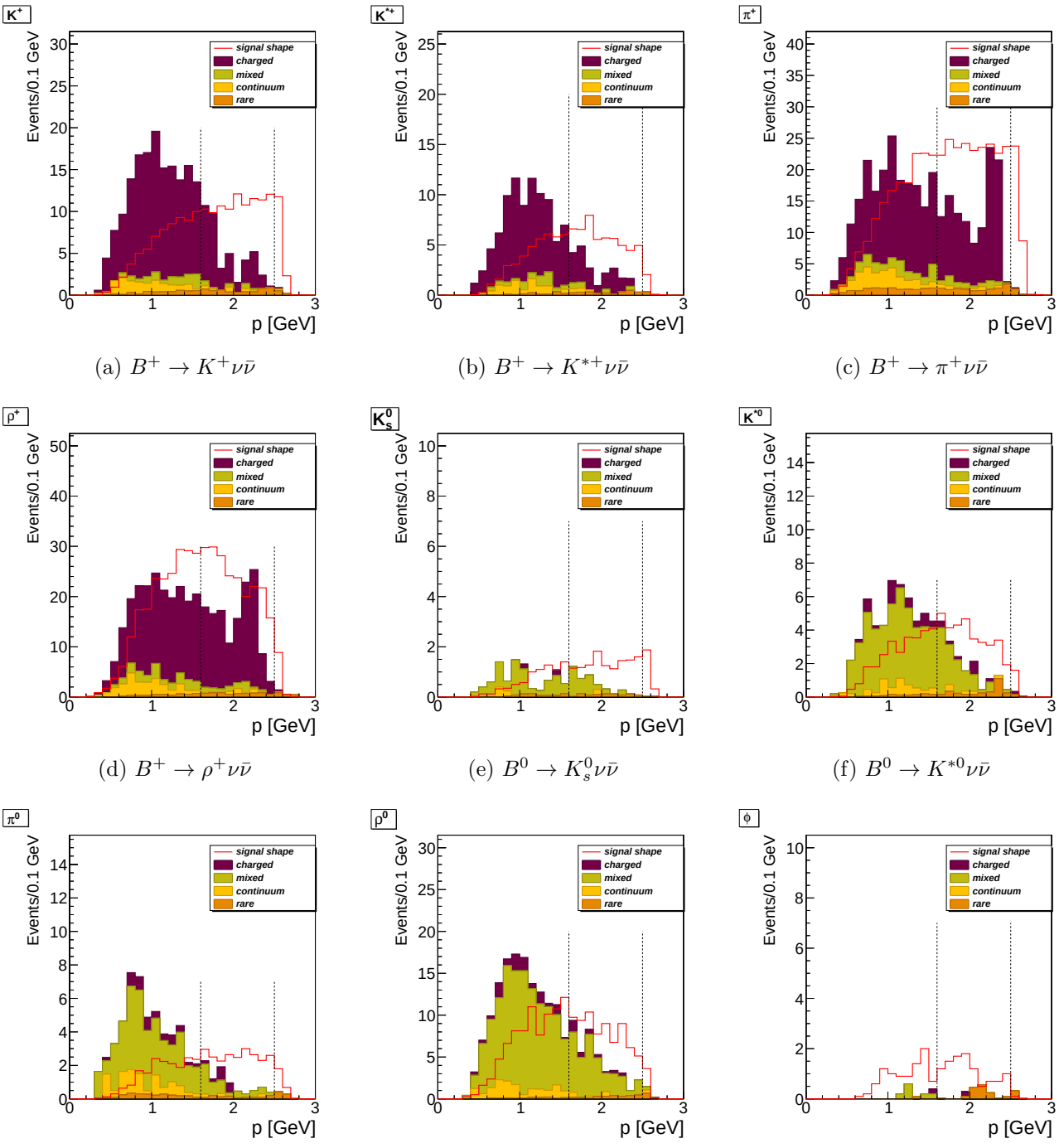

(a) $B^+ \to K^+\nu\bar{\nu}$ (b) $B^+ \to K^{*+}\nu\bar{\nu}$ (c) $B^+ \to \pi^+\nu\bar{\nu}$

(d) $B^+ \to \rho^+\nu\bar{\nu}$ (e) $B^0 \to K^0_s\nu\bar{\nu}$ (f) $B^0 \to K^{*0}\nu\bar{\nu}$

(g) $B^0 \to \pi^0\nu\bar{\nu}$ (h) $B^0 \to \rho^0\nu\bar{\nu}$ (i) $B^0 \to \phi\nu\bar{\nu}$

Figure A.8.: The distribution of the light meson momentum for background (filled histogram) and signal (red line) Monte Carlo, with all other cuts applied. The signal distribution is normalised to an arbitrary value to illustrate the shape. The dashed lines mark the cut values.

A.2. B_{tag} efficiency

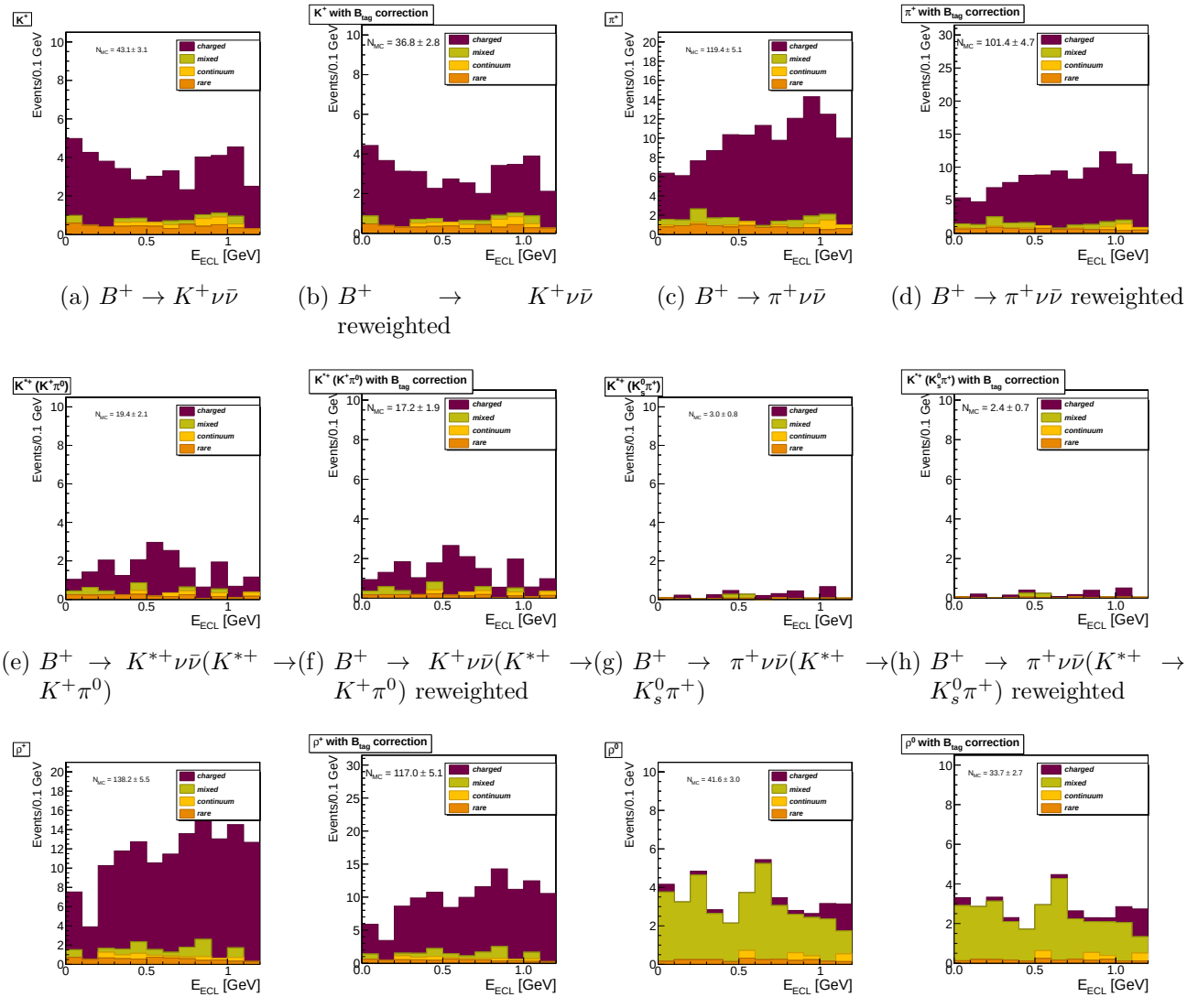

(a) $B^+ \to K^+\nu\bar{\nu}$ (b) $B^+ \to K^+\nu\bar{\nu}$ reweighted (c) $B^+ \to \pi^+\nu\bar{\nu}$ (d) $B^+ \to \pi^+\nu\bar{\nu}$ reweighted

(e) $B^+ \to K^{*+}\nu\bar{\nu}(K^{*+} \to K^+\pi^0)$ (f) $B^+ \to K^+\nu\bar{\nu}(K^{*+} \to K^+\pi^0)$ reweighted (g) $B^+ \to \pi^+\nu\bar{\nu}(K^{*+} \to K^0_s\pi^+)$ (h) $B^+ \to \pi^+\nu\bar{\nu}(K^{*+} \to K^0_s\pi^+)$ reweighted

(i) $B^+ \to \rho^+\nu\bar{\nu}$ (j) $B^+ \to \rho^+\nu\bar{\nu}$ reweighted (k) $B^0 \to \rho^0\nu\bar{\nu}$ (l) $B^0 \to \rho^0\nu\bar{\nu}$ reweighted

Figure A.9.: The Monte Carlo background distribution in the signal box before and after the reweighting of the correct B_{tag} events.

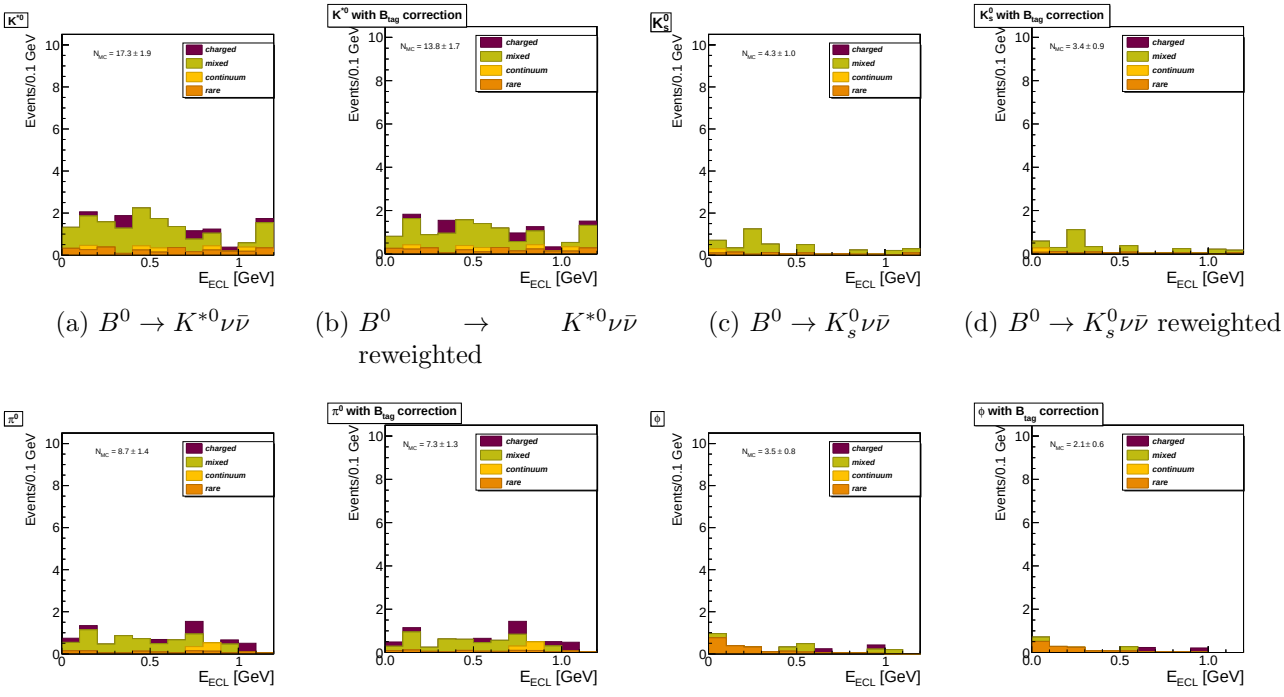

(a) $B^0 \to K^{*0}\nu\bar{\nu}$ (b) $B^0 \to K^{*0}\nu\bar{\nu}$ reweighted (c) $B^0 \to K^0_s\nu\bar{\nu}$ (d) $B^0 \to K^0_s\nu\bar{\nu}$ reweighted

(e) $B^0 \to \pi^0\nu\bar{\nu}$ (f) $B^0 \to \pi^0\nu\bar{\nu}$ reweighted (g) $B^0 \to \phi\nu\bar{\nu}$ (h) $B^0 \to \phi\nu\bar{\nu}$ reweighted

Figure A.10.: The Monte Carlo background distribution in the signal box before and after the reweighting of the correct B_{tag} events.

A.3. Comparison between Monte Carlo and data

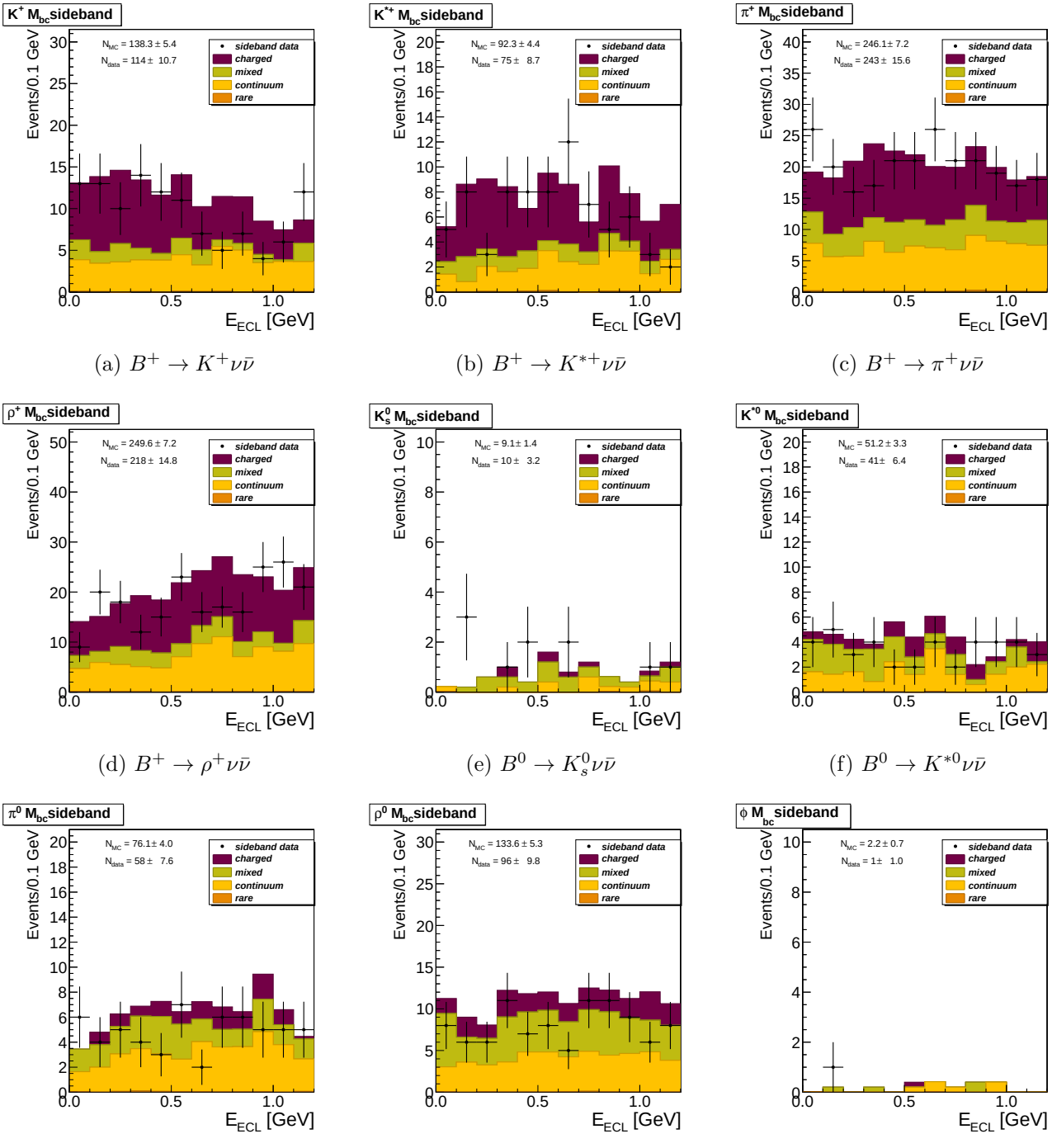

(a) $B^+ \to K^+\nu\bar{\nu}$ (b) $B^+ \to K^{*+}\nu\bar{\nu}$ (c) $B^+ \to \pi^+\nu\bar{\nu}$

(d) $B^+ \to \rho^+\nu\bar{\nu}$ (e) $B^0 \to K^0_s\nu\bar{\nu}$ (f) $B^0 \to K^{*0}\nu\bar{\nu}$

(g) $B^0 \to \pi^0\nu\bar{\nu}$ (h) $B^0 \to \rho^0\nu\bar{\nu}$ (i) $B^0 \to \phi\nu\bar{\nu}$

Figure A.11.: The E_{ECL} distributions in the M_{bc} sideband with no cut on the momentum of the light meson applied. The blacks dots show the data distribution, whether the filled histogram show a stack plot of the background components.

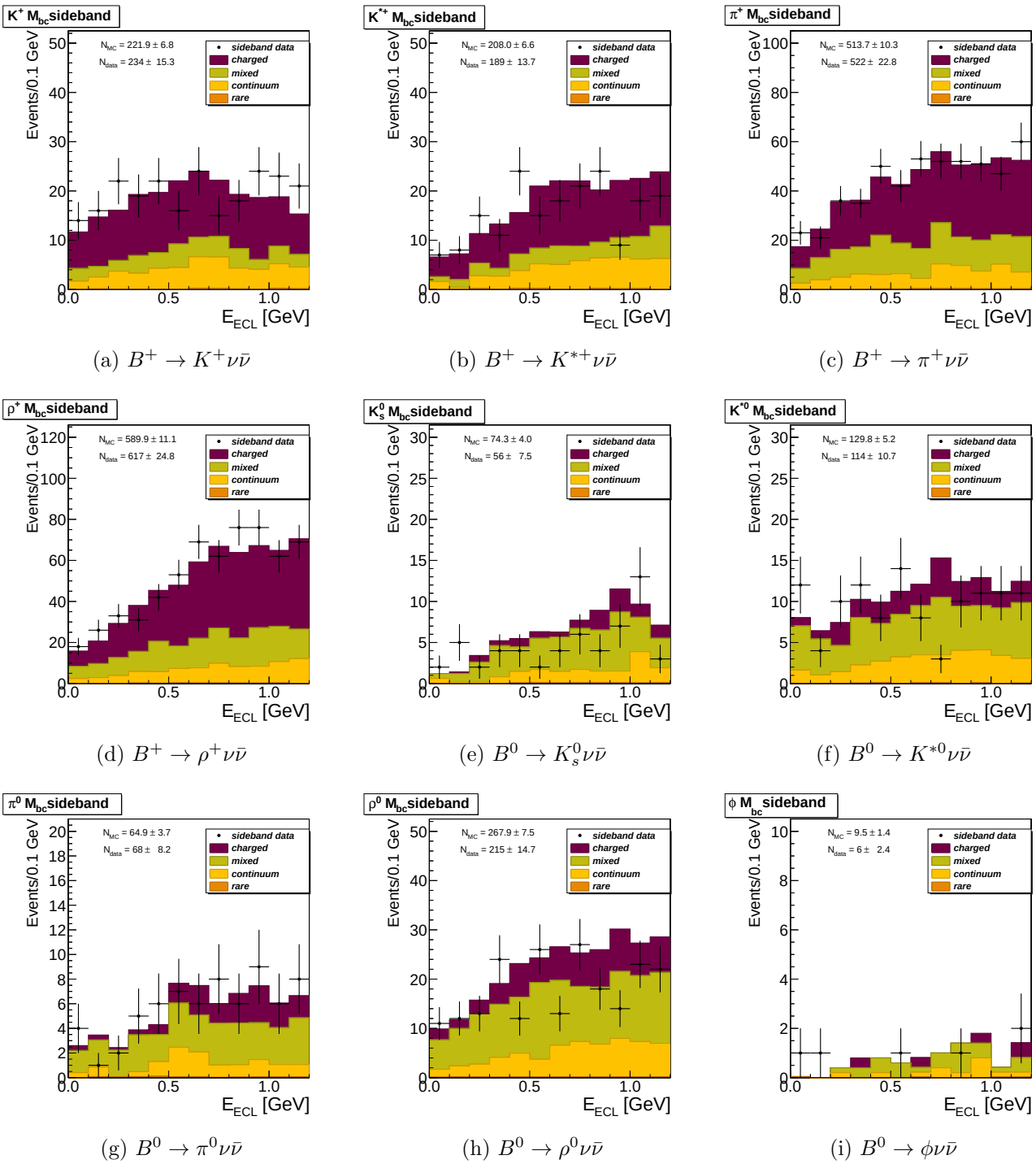

(a) $B^+ \to K^+\nu\bar{\nu}$ (b) $B^+ \to K^{*+}\nu\bar{\nu}$ (c) $B^+ \to \pi^+\nu\bar{\nu}$

(d) $B^+ \to \rho^+\nu\bar{\nu}$ (e) $B^0 \to K^0_s\nu\bar{\nu}$ (f) $B^0 \to K^{*0}\nu\bar{\nu}$

(g) $B^0 \to \pi^0\nu\bar{\nu}$ (h) $B^0 \to \rho^0\nu\bar{\nu}$ (i) $B^0 \to \phi\nu\bar{\nu}$

Figure A.12.: The E_{ECL} distributions in the M_{bc} sideband withfollowing cuts released: missing momentum angle, π^0 veto, remaining tracks veto, ΔE.. The blacks dots show the data distribution, whether the filled histogram show a stack plot of the background components.

A.4. Fitting procedure applied on simulated experiments

A.4.1. Counting

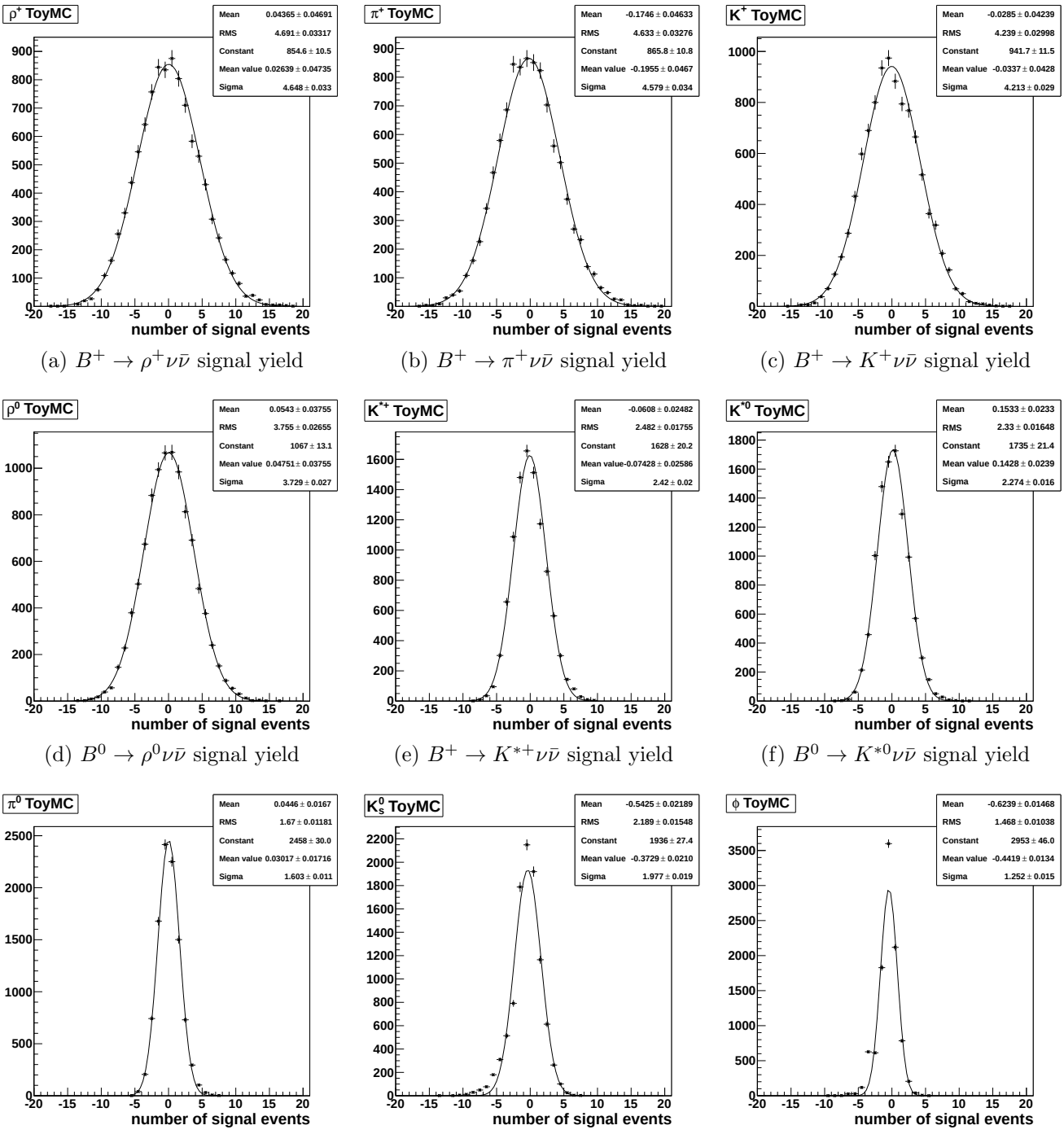

(a) $B^+ \to \rho^+ \nu\bar{\nu}$ signal yield (b) $B^+ \to \pi^+ \nu\bar{\nu}$ signal yield (c) $B^+ \to K^+ \nu\bar{\nu}$ signal yield

(d) $B^0 \to \rho^0 \nu\bar{\nu}$ signal yield (e) $B^+ \to K^{*+} \nu\bar{\nu}$ signal yield (f) $B^0 \to K^{*0} \nu\bar{\nu}$ signal yield

(g) $B^0 \to \pi^0 \nu\bar{\nu}$ signal yield (h) $B^0 \to K^0_s \nu\bar{\nu}$ signal yield (i) $B^0 \to \phi \nu\bar{\nu}$ signal yield

Figure A.13.: The mean of the signal yield of the simulated Monte Carlo experiments counting study with expected background and 0 signal events. Here the results for the channels (from left to right, from up to down) are sorted according to the number of expected background events.

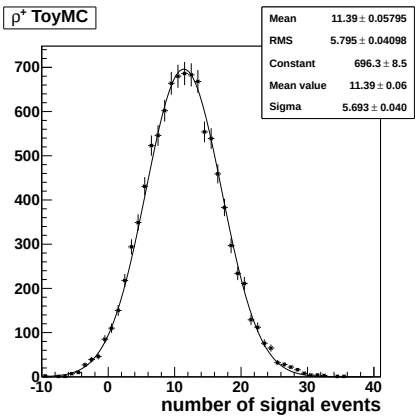

(a) $B^+ \to \rho^+ \nu\bar{\nu}$ signal yield

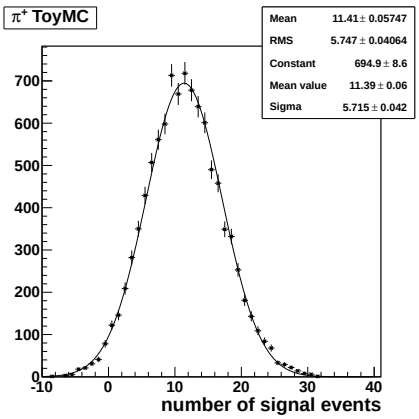

(b) $B^+ \to \pi^+ \nu\bar{\nu}$ signal yield

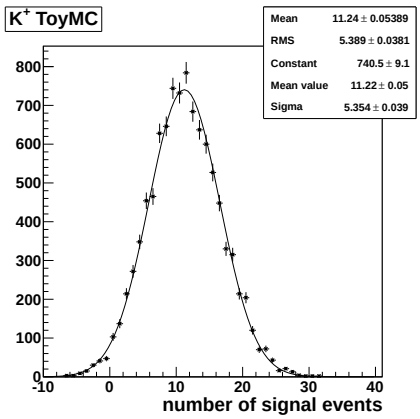

(c) $B^+ \to K^+ \nu\bar{\nu}$ signal yield

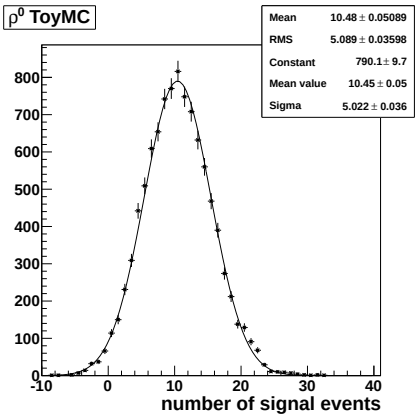

(d) $B^0 \to \rho^0 \nu\bar{\nu}$ signal yield

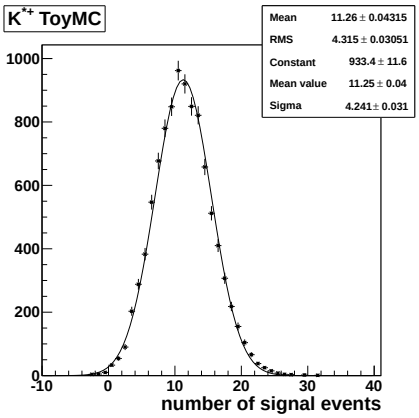

(e) $B^+ \to K^{*+} \nu\bar{\nu}$ signal yield

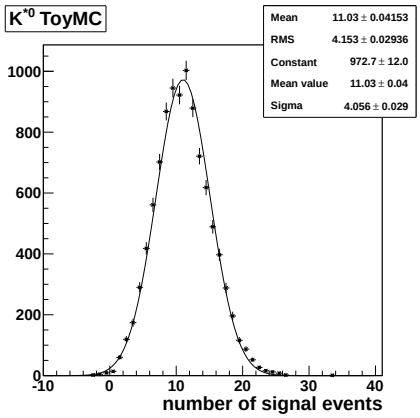

(f) $B^0 \to K^{*0} \nu\bar{\nu}$ signal yield

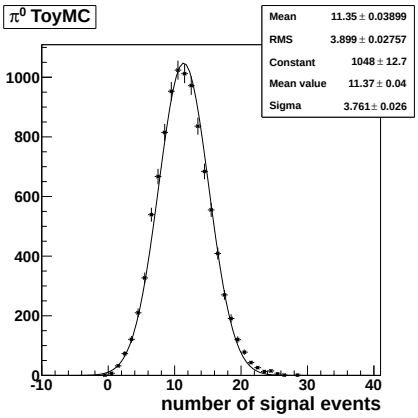

(g) $B^0 \to \pi^0 \nu\bar{\nu}$ signal yield

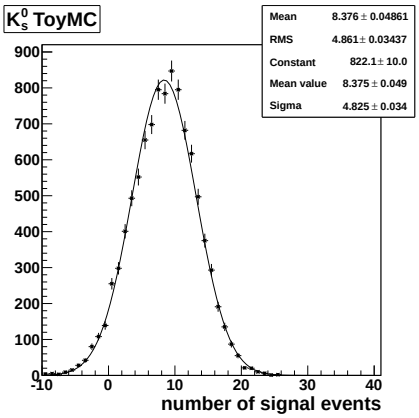

(h) $B^0 \to K_s^0 \nu\bar{\nu}$ signal yield

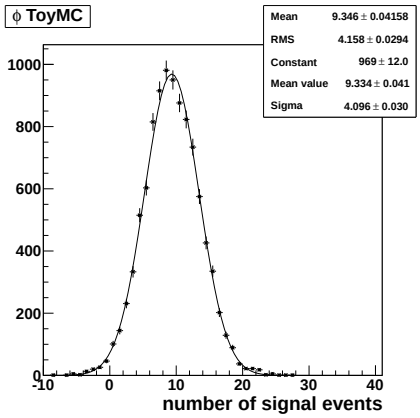

(i) $B^0 \to \phi \nu\bar{\nu}$ signal yield

Figure A.14.: The mean of the signal yield of the simulated Monte Carlo counting study with expected background and 15 signal events. Here the results for the channels (from left to right, from up to down) are sorted according to the number of expected background events.

A.4.2. Fitting

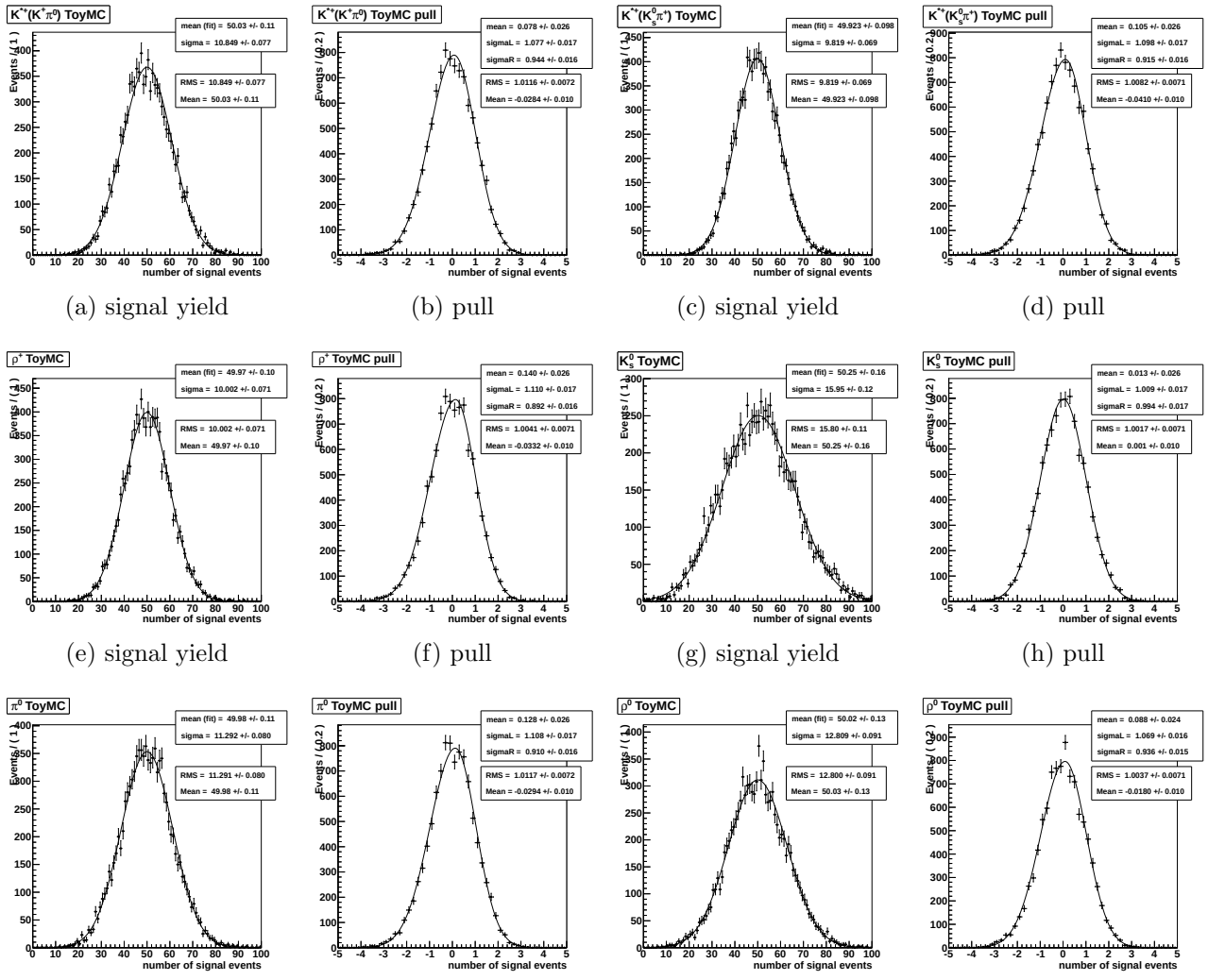

(a) signal yield (b) pull (c) signal yield (d) pull

(e) signal yield (f) pull (g) signal yield (h) pull

(i) signal yield (j) pull (k) signal yield (l) pull

Figure A.15.: The mean, fitting error and pull distributions of the simulated Monte Carlo experiments study study with 150 background and 50 signal events.

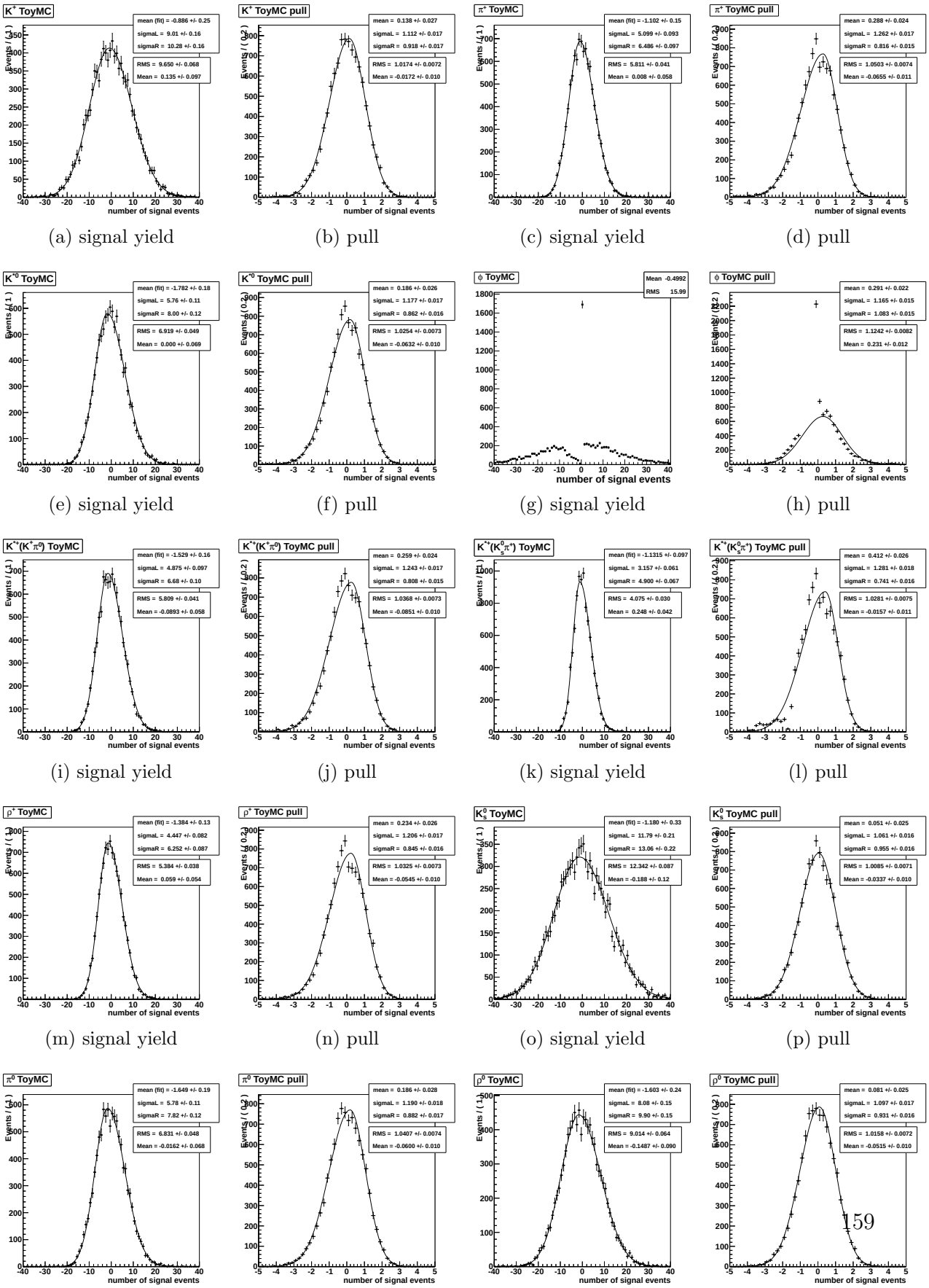

(a) signal yield (b) pull (c) signal yield (d) pull

(e) signal yield (f) pull (g) signal yield (h) pull

(i) signal yield (j) pull (k) signal yield (l) pull

(m) signal yield (n) pull (o) signal yield (p) pull

(q) signal yield (r) pull (s) signal yield (t) pull

Figure A.16.: The mean, fitting error and pull distributions of the simulated Monte Carlo experiments study with 150 background and 0 signal events.

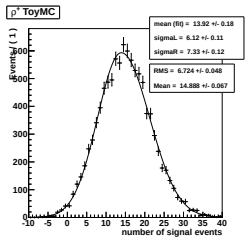

(a) $B^+ \to \rho^+\nu\bar{\nu}$ signal yield

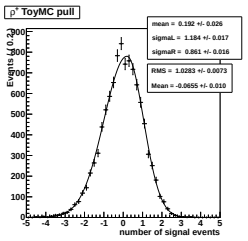

(b) $B^+ \to \rho^+\nu\bar{\nu}$ pull

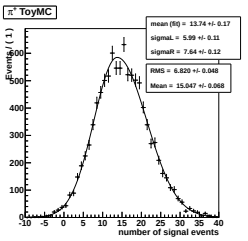

(c) $B^+ \to \pi^+\nu\bar{\nu}$ signal yield

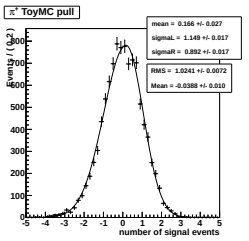

(d) $B^+ \to \pi^+\nu\bar{\nu}$ pull

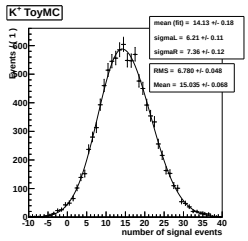

(e) $B^+ \to K^+\nu\bar{\nu}$ signal yield

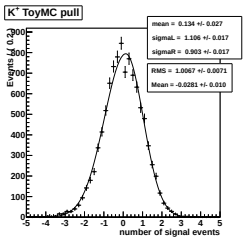

(f) $B^+ \to K^+\nu\bar{\nu}$ pull

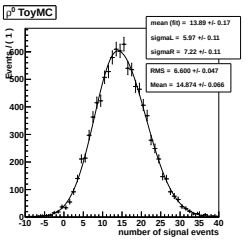

(g) $B^0 \to \rho^0\nu\bar{\nu}$ signal yield

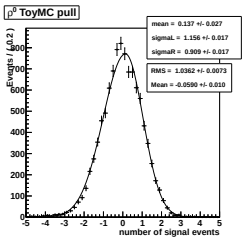

(h) $B^0 \to \rho^0\nu\bar{\nu}$ pull

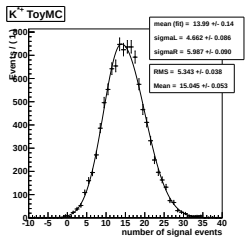

(i) $B^+ \to K^{*+}\nu\bar{\nu}$ signal yield

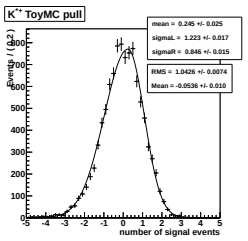

(j) $B^+ \to K^{*+}\nu\bar{\nu}$ pull

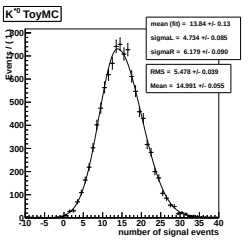

(k) $B^0 \to K^{*0}\nu\bar{\nu}$signal yield

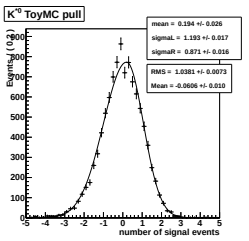

(l) $B^0 \to K^{*0}\nu\bar{\nu}$ pull

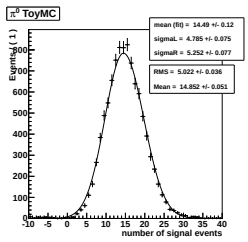

(m) $B^0 \to \pi^0\nu\bar{\nu}$ signal yield

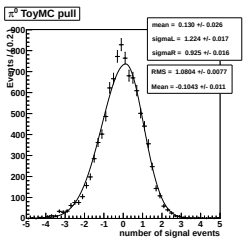

(n) $B^0 \to \pi^0\nu\bar{\nu}$ pull

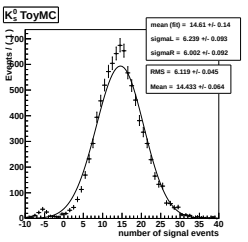

(o) $B^0 \to K^0_s\nu\bar{\nu}$ signal yield

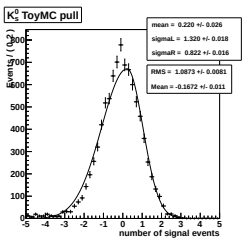

(p) $B^0 \to K^0_s\nu\bar{\nu}$ pull

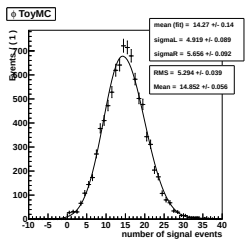

(q) $B^0 \to \phi\nu\bar{\nu}$ signal yield

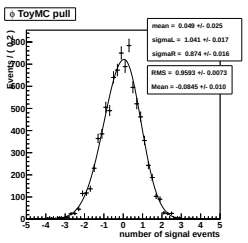

(r) $B^0 \to \phi\nu\bar{\nu}$ pull

Figure A.17.: The mean, fitting error and pull distributions of the simulated Monte Carlo experiments study with expected background and 15 signal events. Number of simulated background events (from up to down): $B^+ \to \rho^+\nu\bar{\nu}$ (117), $B^+ \to \pi^+\nu\bar{\nu}$ (102), $B^+ \to K^+\nu\bar{\nu}$ (37), $B^0 \to \rho^0\nu\bar{\nu}$ (34),$B^+ \to K^{*+}\nu\bar{\nu}$ (20), $B^0 \to K^{*0}\nu\bar{\nu}$ (14), $B^0 \to \pi^0\nu\bar{\nu}$ (7), $B^0 \to K^{0s}\nu\bar{\nu}$ (4) and $B^0 \to \phi\nu\bar{\nu}$ (2).

A.5. Investigation of the missing mass

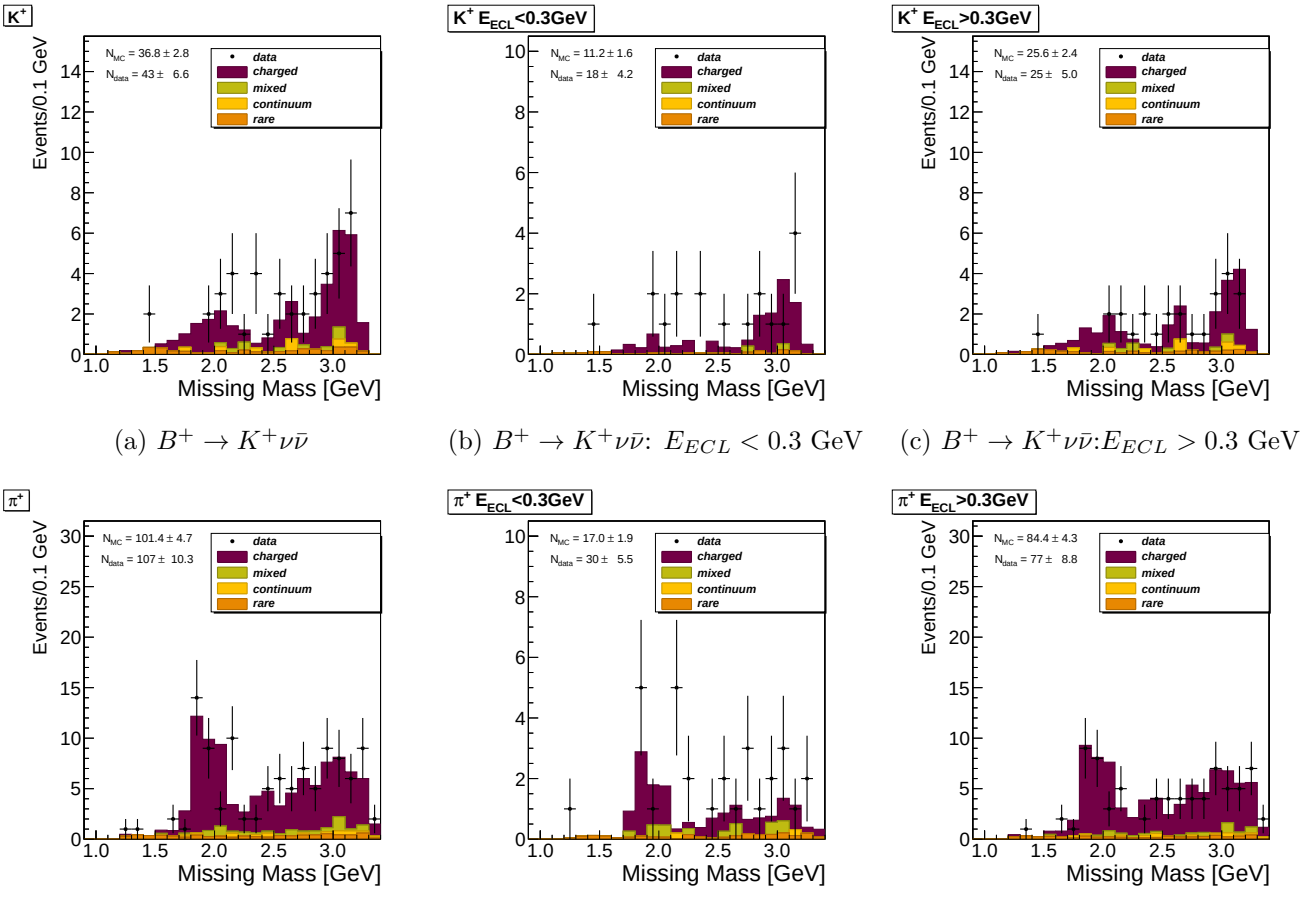

(a) $B^+ \to K^+\nu\bar{\nu}$ (b) $B^+ \to K^+\nu\bar{\nu}$: $E_{ECL} < 0.3$ GeV (c) $B^+ \to K^+\nu\bar{\nu}$:$E_{ECL} > 0.3$ GeV

(d) $B^+ \to \pi^+\nu\bar{\nu}$ (e) $B^+ \to \pi^+\nu\bar{\nu}$: $E_{ECL} < 0.3$ GeV (f) $B^+ \to \pi^+\nu\bar{\nu}$: $E_{ECL} > 0.3$ GeV

Figure A.18.: Missing mass distributions for K^+ and π^+ channels without normalisation between data and Monte Carlo. From left to right the whole E_{ECL} region, $E_{ECL} < 0.3$ GeV and $E_{ECL} > 0.3$ GeV are shown.

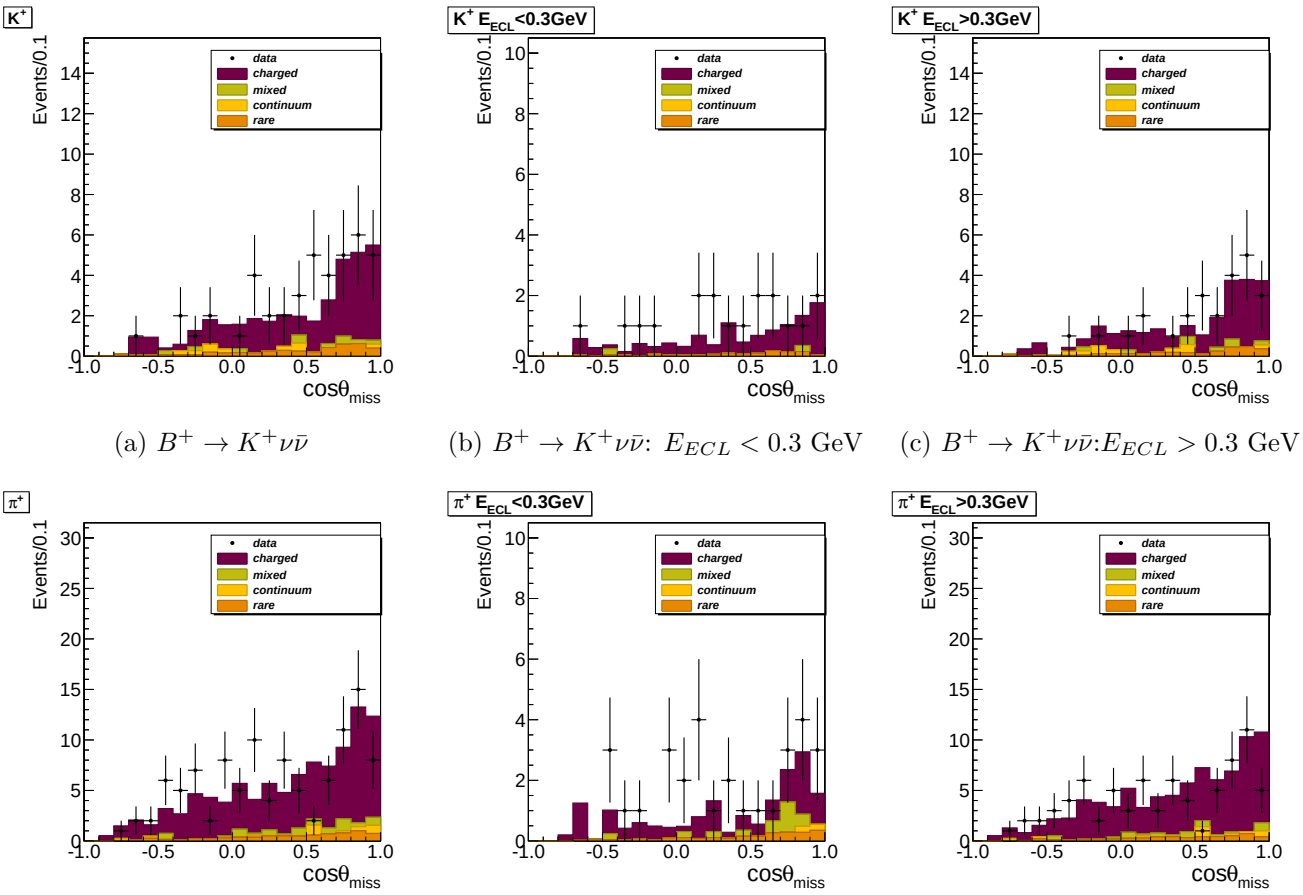

(a) $B^+ \to K^+\nu\bar{\nu}$ (b) $B^+ \to K^+\nu\bar{\nu}$: $E_{ECL} < 0.3$ GeV (c) $B^+ \to K^+\nu\bar{\nu}$:$E_{ECL} > 0.3$ GeV

(d) $B^+ \to \pi^+\nu\bar{\nu}$ (e) $B^+ \to \pi^+\nu\bar{\nu}$: $E_{ECL} < 0.3$ GeV (f) $B^+ \to \pi^+\nu\bar{\nu}$: $E_{ECL} > 0.3$ GeV

Figure A.19.: Missing momentum to beam angle distributions for K^+ and π^+ channels without normalisation between data and Monte Carlo. From left to right the whole E_{ECL} region, $E_{ECL} < 0.3$ GeV and $E_{ECL} > 0.3$ GeV are shown.

List of Figures

List of Tables

Bibliography

[1] K.-F. Chen et al. Search for $B \to h^{(*)}\nu\nu$ Decays at Belle. *Phys. Rev. Lett.*, 99(22):221802, 11 2007.

[2] J.Beringer et al. (Particle Data Group). The Review of Particle Physics. *Phys.Rev.*, D86:010001, 2012.

[3] David Griffiths. *Introduction to elementary particles.* Wiley-VCH, 2008.

[4] Nicola Cabibbo. Unitary Symmetry and Leptonic Decays. *Phys. Rev. Letters*, 10:531–533, 1963.

[5] Makoto Kobayashi and Toshihide Maskawa. CP-Violation in the Renormalizable Theory of Weak Interaction. *Progress of Theoretical Physics*, 49(2):652–657, 1973.

[6] L.Wolfenstein. Parametrization of the Kobayashi-Maskawa Matrix. *Phys.Rev.Lett.*, 51, 1983.

[7] J. Iliopoulos S.L. Glashow and L. Maiani. Weak interactions with lepton-hadron symmetry. *Phys. Rev. D*, 2:1285, 1970.

[8] Gerhard Buchalla, Gudrun Hiller, and Gino Isidori. Phenomenology of nonstandard Z couplings in exclusive semileptonic $b \to s$ transitions. *Phys. Rev. D*, 63:014015, 12 2000.

[9] C. Bird at al. Search for Dark Matter in $b \to s$ Transitions with Missing Energy. *Phys. Rev. Letters*, 93, 2004.

[10] Wolfgang Altmannshofer, Andrzej J. Buras, David M. Straub, and Michael Wick. New strategies for new physics search in $B \to K\nu\bar{\nu}$ and $B \to K^*\nu\bar{\nu}$ decays. *Journal of High Energy Physics*, 0904(04):022, 2009.

[11] H.K. Dreiner et al. Rare meson decays into very light neutralinos. *Phys. Rev. D*, 80, 2009.

[12] Christopher Smith Jernej F. Kamenik. Tree-level contributions to the rare decays $B^+ \to \pi^+\nu\bar{\nu}$,$B^+ \to K^+\nu\bar{\nu}$ and $B^+ \to K^{*+}\nu\bar{\nu}$ in the Standard Model. *Physics Letters B*, 680:471–475, 2009.

[13] Andrzej Buras, Bjoern Duling, Thorsten Feldmann, Tillmann Heidsieck, Christoph Promberger, and Recksiegel. Patterns of flavour violation in the presence of a fourth generation of quarks and leptons. *Journal of High Energy Physics*, 2010:1–74, 2010.

[14] G. Buchalla. Precision flavour physics with $B \to K\nu\bar{\nu}$ and $B \to Kl^+l^-$. *Nuclear Physics B*, 209:137–142, 2010.

[15] Bernard Aubert et al. Search for $B^+ \to K^+\nu\bar{\nu}$ decays. *Physical Review Letters*, 94:101801, 2005.

[16] T.E. Browder et al. A Search for $B \to \tau\nu$. *Phys.Rev.Lett.*, 86:2950–2954, 2001.

[17] P.H. Frampton and P.Q. Hung. Quarks and leptons beyond the third generation. *Phys.Rep.*, 330:263, 2000.

[18] Yosef Nir Yuval Grossman and Riccardo Rattazzi. CP Violation Beyond the Standard Model. *Heavy flavours II*, 1997.

[19] P. Langacker and N. Pluemacher. Flavor Changing Effects in Theories with a Heavy Z' Boson with Family Non-Universal Couplings. *Phys.Rev. D*, 62:013006, 2000.

[20] G. Buchalla et al. GIM Violation and New Dynamics of the Third Generation. *Phys. Rev. D*, 53:5185, 1996.

[21] M. Blanke et at. Rare and CP-violating K and B decays in the Littlest Higgs model with T-Parity. *JHEP*, 01:066, 2007.

[22] B. Duling K. Gemmler M. Blanke, A.J. Buras and S. Gori. Rare K and B Decays in a Warped Extra Dimension with Costodial Protection. *JHEP*, 108:0903, 2009.

[23] P. del Amo Sanchez et al. Search for the Rare Decay $B \to K\nu\bar{\nu}$. *Phys.Rev.*, D82:112002, 2010.

[24] Bernard Aubert et al. Search for $B \to K^*\nu\bar{\nu}$ decays. *Phys.Rev.*, D78:072007, 2008.

[25] A.Abashian et al. The Belle detector. *Nuclear Instruments and Methods, Section A*, 479.1:117–232, 2002.

[26] Belle II collaboration. Belle II Technical Design Report. Technical report, High Energy Accelerator Research Organization KEK, 2010.

[27] T. Aushev et al. Physics at Super B Factory. *KEK Report*, 2009.

[28] S. Kurokawa and E. Kikutani. Overview of the KEKB Accelerators. *Nuclear Instruments and Methods, Section A*, 499(1):1–7, 2003.

[29] D. Besson et al. Upsilon Spectroscopy: Transitions int the Bottomonium System. *Annual Review of Nuclear and Particle Science*, 43.1:333–378, 1993.

[30] Sebastian Neubauer. *Search for $B \to K^{(*)}\nu\bar{\nu}$ Decays Using a New Probabilistic Full Reconstruction Method*. PhD thesis, Karlsruhe Insitute of Technology, 2011.

[31] KEK Report. Machine Parameters of the KEKB. Technical report, KEK, 2009.

[32] Miyuki Fujikawa. *Measurement of Branching Fraction and Tme-dependent CP Asymetry Parameters in $B^0 \to K^0\pi^0$ Decays*. PhD thesis, Nara Women's University, 2009.

[33] F. Sauli. Principles of Operation of Multiwire Proportional and Drift Chambers. *CERN-77-09*, 1977.

[34] Belle II collaboration. Belle II documents. http://belle2.kek.jp/. http://belle2.kek.jp/.

[35] M. Kreps T. Kuhr S. Neubauer D. Zander A. Zupanc M. Feindt, F. Keller. A hierarchical NeuroBayes-based algorithm for full reconstruction of B mesons at B factories. *NIM*, 654:432–440, October 2011.

[36] M.Feindt et al. The NeuroBayes neural network package. *NIM*, 559.1, 2006.

[37] Gerhard Buchalla et al. Phenomenology of nonstandard Z couplins in exclusive semileptonic $b \to s$ transitions. *Phys.Rev.*, D63:014015, 2000.

[38] Particia Ball et al. $B_{d,s} \to \rho, \omega, K^*$ decay form factors from light-cone sum rules reexamined. *Phys.Rev.*, D 71:014029, 2005.

[39] Particia Ball et al. New results on $B \to \pi, K, \eta$ decay form factors from light cone sum rules. *Phys.Rev.*, D 71:014015, 2005.

[40] S.H. Lee et al. Evidence for $B^0 \to \pi^0\pi^0$. *Phys.Rev.Lett.*, 91.26:261801, Dec. 2003.

[41] Kevin Varvell Alexei Sibidanov. Exclusive $B \to \pi l\nu$, $B \to \rho l\nu$ and $B \to \omega l\nu$ Decays using Full Reconstruction Tagging. *internal note*, BN1206, 2011.

[42] Laha Chakravarti and Roy. Handbook of Methods of Applied Statistics. 1:392–394., 1967.

[43] Bipul Bhuyan. High PT Tracking Efficiency Using Partially Reconstructed D^* Decays. *Internal Note*, BN1165.

[44] Eric White. Determination of K_s^0 Efficiency and Systematic Uncertainty. *Internal Note*, BN1207.

[45] S.H.Lee et al. Evidence for $B^0 \to \pi^0\pi^0$. *Phys.Rev.Lett.*, 91.26:p.261801, Dec.2003.

[46] T. Aushev et al. Physics at Super B factory. *KEK Report*, 12, 2009.

[47] P.V.C. Hough. Machine Analysis of Bubble Chamber Pictures. *International Conference on High Energy Accelerators and Instrumentation*, 1959.

[48] Rainer Mankel. Pattern recognition and event reconstruction in particle physics experiments. *Rept.Prog.Phys.*, 67(DESY-04-008):553, 2004.

[49] R.E. Kalman. A new approach to linear filtering and prediction problems. *Transactions of the ASME-Journal of Basic Engineering Series D*, 82:35, 1960.

[50] R. Fruehwirth. Application of Kalman filtering to track and vertex fitting. *Nuclear Instruments and Methods, Section A*, 262:444, 1987.

[51] A. Strandlie R. Fruehwirth. Track fitting with ambiguities and noise: a study of elastic tracking and nonlinear filters. *Computer Physics Communications*, 120:197, 1999.

[52] B. Ketzer S. Paul C. Hoeppner, S. Neubert. A novel generic framework for track fitting in complex detector systems. *Nuclear Instruments and Methods, Section A*, 620:518–525, 2010.

Danksagung

Ich möchte mich als erstes bei Prof. Dr. Thomas Müller bedanken, der mir bereits in der Diplomarbeit den Einstieg in das aufregende Belle-II-Projekt ermöglichte. Für die Möglichkeit, den Themenbereich für die Promotion zu wechseln und die Unterstützung bei den Dienstreisen zu zahlreichen Meetings bin ich sehr dankbar. Bei Prof. Dr. Michael Feindt möchte ich mich für die fachliche Betreuung in den zahlreichen Gruppenmeetings und die Übernahme des Korreferats bedanken.

Für die gute Betreuung in allen Phasen dieser Doktorarbeit möchte ich mich bei Dr. Thomas Kuhr und Dr. Martin Heck bedanken.

Bei meinen Bürokollegen Michael Prim und Christian Pulvermacher möchte ich mich für die angenehme Arbeitsatmosphäre und die zahlreichen technischen Hilfestellungen bedanken. Großer Dank geht an die beiden sowie an Bastian Kronenbitter für das Korrekturlesen dieser Dissertation.

Ich möchte mich auch herzlich bei der ganzen B-Gruppe für die schöne und lustige Zeit und Unterstützung bedanken.

Herzlichen Dank auch an Frau Bräunling für die kompetente und freundliche Hilfe in allen verwaltungsbezogenen Fragestellungen.

Ein großer Dank gilt auch mehreren Mitgliedern der Belle- und Belle-II-Kollaborationen, die mich während der 3 Jahre bei dieser Arbeit unterstützt haben und von denen ich viel lernen konnte. Besonderer Dank gilt dabei Jeremy Dalseno, der mir in dieser Zeit in vielerlei Hinsicht zur Seite stand.

Ich danke auch meinen Eltern, die mir das Studium ermöglicht haben und immer Rückhalt boten. Ein großer Dank gilt meinem Mann Benny, der mich auch in den weniger rosigen Zeiten der Promotion immer unterstützt und immer an mich geglaubt hat.